Contemporaneous Multi-Wavelength Observations of the Gamma-Ray Emitting Active Galaxy IC 310

New Clues on Particle Acceleration in Extragalactic Jets

Dissertation zur Erlangung des naturwissenschaftlichen Doktorgrades der Julius-Maximilians-Universität Würzburg

vorgelegt von

Dorit Glawion

aus Mühlhausen/Thüringen

Würzburg 2014

Eingereicht am: 18.12.2014
bei der Fakultät für Physik und Astronomie.

1. Gutachter: Prof. Dr. Karl Mannheim
2. Gutachter: Prof. Dr. Matthias Kadler
3. Gutachter: Prof. Dr. Jan Conrad
der Dissertation.

Vorsitzende(r) Prof. Dr. Thomas Trefzger

1. Prüfer: Prof. Dr. Karl Mannheim
2. Prüfer: Prof. Dr. Matthias Kadler
3. Prüfer: Prof. Dr. Friedrich Röpke
im Promotionskolloquiums.

Tag des Promotionskolloquiums: 08.05.2015

Doktorurkunde ausgehändigt am: .....

I remember once I was walking on a street
far away from any big cities.
It was dark and many stars were shining.
I was trying to count them.
I was seven years old.
Many years have passed.
I am still looking at the stars
with slightly different eyes
and I am still fascinated.

Abstract

In this thesis, the broad band emission, especially in the gamma-ray and radio band, of the active galaxy IC 310 located in the Perseus cluster of galaxies was investigated. The main experimental methods were Cherenkov astronomy using the MAGIC telescopes and high resolution very long baseline interferometry (VLBI) at radio frequencies (MOJAVE, EVN). Additionally, data of the object in different energy bands were studied and a multi-wavelength campaign has been organized and conducted. During the campaign, an exceptional bright gamma-ray flare at TeV energies was found with the MAGIC telescopes. The results were compared to theoretical acceleration and emission models for explaining the high energy radiation of active galactic nuclei. Many open questions regarding the particle acceleration to very high energies in the jets of active galactic nuclei, the particle content of the jets, or how the jets are launched, were addressed in this thesis by investigating the variability of IC 310 in the very high energy band.

It is argued that IC 310 was originally mis-classified as a head-tail radio galaxy. Instead, it shows a variability behavior in the radio, X-ray, and gamma-ray band similar to the one found for blazars. These are active galactic nuclei that are characterized by flux variability in all observed energy bands and at all observed time scales. They are viewed at a small angle between the jet axis and the line-of-sight. Thus, strong relativistic beaming influences the variability properties of blazars. Observations of IC 310 with the European VLBI Network helped to find limits for the angle between the jet axis and the line-of-sight, namely $10^\circ - 20^\circ$. This places IC 310 at the borderline between radio galaxies (larger angles) and blazars (smaller angles).

During the gamma-ray outburst detected at the beginning of the multi-wavelength campaign, flux variability as short as minutes was measured. The spectrum during the flare can be described by a simple power-law function over two orders of magnitude in energy up to $\sim$10 TeV. Compared to previous observations, no significant variability of the spectral shape was found. Together with the constraint on the viewing angle, this challenges the currently accepted models for particle acceleration at shock waves in the jets. Alternative models, such as stars moving through the jets, mini-jets in the jet caused, e.g., by reconnection events, or gap acceleration in a pulsar-like magnetosphere around the black hole were investigated. It was found that only the latter can explain all observational findings, which at least suggests that it could even be worthwhile to reconsider published investigations of AGN with this new knowledge in mind.

The first multi-wavelength campaign was successfully been conducted in 2012/2013, including ground-based as well as space-based telescopes in the radio, optical, ultraviolet, X-ray, and gamma-ray energy range. No pronounced variability was found after the TeV flare in any energy band. The X-ray data showed a slightly harder spectrum when the emission was brighter. The long-term radio light curve indicated a flickering flux variability, but no strong hint for a new jet component was found from VLBI images of the radio jet. In any case, further analysis of the existing multi-wavelength data as well as complimentary measurements could provide further exciting insights, e.g., about the broad band spectral energy distribution.

Overall, it can be stated that IC 310 is a key object for research of active galactic nuclei in the high-energy band due to its proximity and its peculiar properties regarding flux variability and spectral behavior. Such objects are ideally suited for studying particle acceleration, jet formation, and other physical effects and models which are far from being fully understood.

Zusammenfassung

Für diese Arbeit wurde die Breitbandemission des Aktiven Galaxienkerns IC 130, der sich im Perseus Galaxienhaufen befindet, speziell im Gammastrahlen- und Radiobereich untersucht. Die experiementellen Methoden, die dabei verwendet wurden, sind Tscherenkow Astronomie mit den MAGIC Teleskopen, und hochauflösende Interferometrie (englisch: very long baseline interferometry, kurz VLBI) bei Frequenzen im Radiobereich (MOJAVE, EVN). Zusätzlich wurden Daten des Objektes in verschiedenen Energiebändern studiert und eine Multiwellenlängen-Kampagne organisiert und durchgeführt. Während der Kampagne wurde ein außergewöhnlicher, heller Gammastrahlenausbruch bei TeV-Energien mit den MAGIC Teleskopen gefunden. Die Ergebnisse wurden mit theoretischen Beschleunigungs- und Emissionsmodellen verglichen, die zur Erklärung von Hochenergiestrahlung in Aktiven Galaxienkernen herangezogen werden. Viele offene Fragen bezüglich der Teilchenbeschleunigung zu sehr hohen Energien in Jets von Aktiven Galaxienkernen, den Teilcheninhalt der Jets, und der Jetentstehung, wurden in dieser Arbeit anhand der Variabilitätseigenschaften von IC 310 im sehr hohen Energiebereich diskutiert.

Es stellt sich heraus, dass IC 310 bisher fälschlicherweise als sog. “head-tail” Radiogalaxie klassifiziert wurde. Stattdessen zeigt sich, dass das Variabilitätsverhalten im Radio-, Röntgen-, und Gammastrahlenbereich demjenigen von Blazaren ähnelt. Diese Objekte sind Aktive Galaxienkerne, bei denen Variabilität des Flusses in allen beobachteten Energiebändern und auf allen beobachteten Zeitskalen gemessen werden kann. Bei Blazaren wird ein kleiner Winkel zwischen Jetachse und Sichtlinie vermutet. Die dadurch enstehenden relativistische Aberration und Verstärkung nehmen Einfluß auf die Variabilitätseigenschaften. Beobachtungen von IC 310 mit dem Europäischen VLBI Netzwerk halfen, den Winkel zwischen der Jetachse und der Sichtline auf $10^\circ - 20^\circ$ einzuschränken. Damit ist IC 310 ein Objekt, das sich nicht klar als Radiogalaxie (größere Winkel) oder Blazar (kleinere Winkel) definieren lässt.

Während des Gammastrahlenausbruchs, der zu Beginn der Multiwellenlängen-Kampagne detektiert wurde, konnten Flussveränderungen auf Zeitskalen von wenigen Minuten gemessen werden. Das während diesem Ausbruchs gemessene Spektrum kann beschreiben werden mit einem einfachen Potenzgesetz über zwei Dekaden in Energie bis 10 TeV, ohne dabei Hinweise auf ein Abbrechen zu zeigen. Beim Vergleich mit früheren Beobachtungen konnten keine signifikanten Veränderungen der spektralen Form festgestellt werden. Zusammen mit der Einschränkung des Winkels stellt diese Beobachtung die derzeit weit verbreiteten Modelle der Teilchenbeschleunigung durch Stoßwellen in den Jets grundlegend in Frage. Alternative Modelle, die auf Einflüssen von Sternen, die sich durch den Jet bewegen, oder auf sogenannten Mini-Jets im Jet, die z.B. durch Rekonnektion entstehen, beruhen, wurden diskutiert. Außerdem wurde die Gap-Beschleunigung in einer pulsarähnlichen Magnetosphäre um ein Schwarzes Loch herum studiert. Es zeigte sich, dass nur das letztgenannte Modell alle beobachteten Eigenschaften erklären kann, was mindestens nahelegt, dass es sich lohnen könnte, selbst bereits veröffentlichte Untersuchungen von Aktiven Galaxienkernen unter diesem Wissen neu zu beleuchten.

Die erste Multiwellenlängen-Kampagne mit erd- sowie weltraumgebundenen Teleskopen im Radio, optischen, Ultraviolett, Röntgen und Gammastrahlenbereich wurde 2012/2013 erfolgreich durchgeführt. Keine signifikant ausgeprägten zeitlichen Flussveränderungen in den

beobachteten Energiebändern konnten nach dem Gammastrahlenausbruch gefunden werden. Die Röntgendaten zeigten ein geringfügig härteres Spektrum mit zunehmenden Fluss. Die Langzeitlichtkurve im Radiobereich wies ein Flackern des Flusses auf, allerdings wurde kein starker Hinweis auf eine neue Jetkomponente in dem VLBI-Radiojet gefunden. In jedem Fall könnten eine weitere Analyse der vorhandenen Daten genauso wie ergänzende Messungen weitere, spannende Einblicke zum Beispiel in die spektrale Energieverteilung auf breiter Skala liefern.

Insgesamt lässt sich sagen, dass IC 310 durch sein Nähe und durch besondere Eigenschaften bezogen auf Flussänderungen und spektrales Verhalten ein Schlüsselobjekt für die Erforschung von Aktiven Galaxienkernen im Hochenergiebereich ist. Solche Objekte sind ideale Kandidaten, um Teilchenbeschleunigung, Jetentstehung und andere physikalische Prozesse zu studieren, die noch nicht vollständig verstanden sind.

Contents

List of Figures

List of Tables

1

Introduction

The Elegant Universe

According to general relativity, the ultimate fate of matter that collapses under its own gravity is a black hole. Only from regions outside the event horizon information can be measured in a finite time. The astrophysical evidence for black holes is overwhelming even if the physics behind them is still matter of debate. Black holes with masses of the order of 10^{6-10} times the solar mass are commonly found in the center of galaxies. By accreting surrounding matter, the luminosity of the active galactic nuclei can outshine the emission of their host galaxies. Some of the active galactic nuclei eject powerful outflows composed of plasma, called jets. Those jets can produce a non-thermal energy distribution across the entire electromagnetic spectrum, from radio to gamma-ray energies. The low-energy emission can be explained with synchrotron radiation whereas the emission process at the higher frequencies is still not understood. It is believed that the jets of the active galaxies contribute to the production of the cosmic rays at the highest energies. However, the search for the responsible acceleration mechanism keeps astrophysicists busy. Shock acceleration known from shocks in supernova remnants is the commonly accepted process. Those shocks can be observed as moving knots with very long baseline interferometry (VLBI), but a closer look to the base of the jet remains difficult due to synchrotron self-absorption. Observations at higher radio frequencies where the core becomes transparent could provide information about the jet base. However, the yet insufficient angular resolution achieved at higher radio frequencies prohibits the imaging of the environment of black holes due to their cosmological distances.

An alternative way to obtain information about structures at this scale is to observe the highly variable gamma-ray emission of the accelerated particles. The size of the emitting region is related to the distance that the light can travel during the characteristic flux variability time scale. Recently, variability as short as minutes has been observed by Cherenkov telescopes from active galactic nuclei in which the jet is pointing towards us, called blazars. Due to relativistic motion of the particles in the jet the emission is strongly boosted. Therefore, the observed rapid variability is related to larger, time-dilated emission regions. Unfortunately, the effect of the boosting is a quantity that is not constrained well. Instead, in case of radio galaxies which are

viewed at a larger angle, the flux boosting and time-scale shortening for the approaching jet is only moderate. Nevertheless, gamma-ray emission of a few radio galaxies has been observed in the very high energy range. A prominent example is M87, the central galaxy in the Virgo cluster of galaxies. The daily-scale variability found in the gamma-ray range is marginally consistent with the scale of the event horizon.

Another active galaxy is IC 310, located in the outskirts of the Perseus cluster of galaxies. Originally classified as a head-tail radio galaxy, recent studies show a blazar-like radio structure and a peculiar variability behavior. Thus, in this thesis the object IC 310 is investigated in the gamma-ray band with the Cherenkov telescopes MAGIC. These measurements are complemented by VLBI radio observations as well as measurements in the remaining energy bands. It turns out that IC 310 shows unique and fascinating properties which question the standard scenario for explaining the high-energy emission in such objects, as well as pose critical tests to new, state-of-the-art models for rapid variability. This becomes particularly evident for an unprecedented, exceptionally bright TeV outburst occurring in November 2012. During this flare, ultra-rapid changes of the flux corresponding to $\sim 20\,\%$ of the scale of the event horizon were found. This provides, for the first time, a glimpse at the jet formation process in the plasma surrounding a supermassive black hole.

Outline of the Thesis

The thesis is structured as followed: Chapter 2 gives an introduction to the topic of active galactic nuclei and in particular to broad-band emission properties of their radio-loud subclass. In Chapter 3, an overview of the multi-wavelength instrumentation used in this thesis can be found, whereas in Chapter 4 the basics of Cherenkov telescopes, the MAGIC telescopes, and the analysis methods are introduced in detail. The emission of the active galactic nucleus of IC 310 is investigated in Chapter 5 using data from different energy bands, and the AGN classification is being discussed. In Chapter 6, the observations of the TeV flare and the first deep high-resolution high-sensitivity VLBI images are presented, and a variety of theoretical models are discussed. Chapter 7 gives a summary of the results from the first multi-wavelength campaign, and the monitoring in the gamma-ray and radio band organized by the author. The thesis ends with a short summary and outlook in Chapter 8.

2

Radio-Loud Active Galactic Nuclei

The Grand Design

2.1 Overview

Active Galactic Nuclei (AGN) are among the most luminous extragalactic objects in the universe. The broad-band emission indicates thermal and non-thermal processes associated with particle acceleration and accretion. The first hint for relativistic particle acceleration in extraterrestrial objects was provided by the discovery of cosmic rays in 1912 by Victor Hess (Hess 1912). However, it took about fifty years until the development of new astronomical techniques, the radio telescopes, to address the astrophysical role of highly energetic particles and cosmic magnetic fields.

Nowadays, it is believed that AGN are powered by supermassive black holes in the center of the host galaxy. These black holes accrete the surrounding matter, the vicinity becomes very bright ($\sim 10^{45-49}\,\mathrm{erg\,s^{-1}}$), and may outshine the normal stellar emission of their galaxies ($\sim 10^{44}\,\mathrm{erg\,s^{-1}}$). Galaxies that host AGN are also called *active galaxies* and they make up 3% of all known galaxies. For a more complete review of those objects, see Robson (1999) and Longair (2011). The basic components of an AGN are shown in Fig. 2.1, and will be introduced and motivated in the following.

The supermassive black hole and the surrounded accretion disk are enclosed by a dusty torus. This system comprises regions, the so-called broad- and narrow-line regions, BLR and NLR, respectively, which contain fast and slow moving gas clouds. Perpendicular to the accretion disk and torus, sometimes plasma outflows extend from the central region of the AGN, called *jets*. Typical dimensions of the individual components are summarized in Table 2.1.

- **Black holes in AGN:** A black hole accretes surrounding matter, also including light. It is believed to be rotating. This has been confirmed directly for one AGN in a recent publication of Reis et al. (2014). The mass of black holes in AGN can be inferred from the motion of nearby stars and gas clouds by measuring the velocity dispersion of the host galaxy (Gültekin et al. 2009) or the kinematics of masers (Woo & Urry 2002). Masses

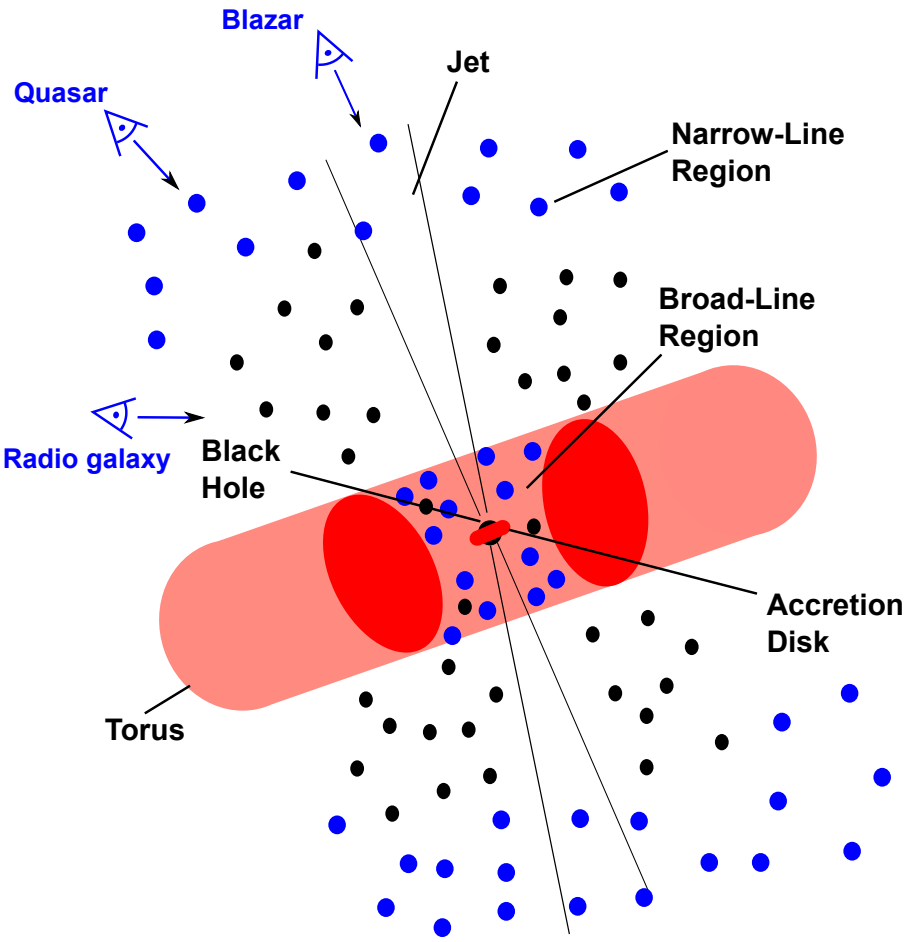

Figure 2.1: Illustration of a radio loud active galactic nucleus. The center of an AGN is believed to be a supermassive black hole. It is surrounded by an accretion disk (red) and torus (pink). The black and blue circles indicate the gas clouds of the broad- and narrow-line region. The jets extent perpendicular to the system. The figure also illustrates the unification scheme of radio-loud active galactic nuclei. See text for more information. Image adapted from Urry & Padovani (1995).

Table 2.1: Dimensions of individual components of an AGN. Table adapted from Rosswog & Brüggen (2007).

Component	Typical size		
	[pc]	[ly]	[cm]
Black hole[a]	10^{-4}	3.3×10^{-4}	3.1×10^{14}
Accretion disk	10^{-2}	3.3×10^{-2}	3.1×10^{16}
Broad-line region	10^{0}	3.3×10^{0}	3.1×10^{18}
Torus	10^{1}	3.3×10^{1}	3.1×10^{19}
Narrow-line region	10^{3}	3.3×10^{3}	3.1×10^{21}
Host galaxy	10^{4}	3.3×10^{4}	3.1×10^{22}
Jet	$\lesssim 10^{6}$	3.3×10^{6}	3.1×10^{24}

Notes. [(a)] The dimension of the black hole is given by the Schwarzschild radius for a black hole with a mass of $10^9 M_\odot$

in a range of $M_{\rm BH} \sim 10^{6-10}\,{\rm M}_\odot$ were found for AGN. Due to the nature of black holes, their size and their volume can not be measured. Therefore, the event horizon of the black hole is commonly estimated from the Schwarzschild radius for a non-rotating, or from the gravitational radius $R_{\rm S} = 2R_{\rm G} = 2GM_{\rm BH}/c^2$, for a maximally rotating black hole[1].

- **Accretion disk:** The hot accretion disk is located around the black hole and can be observed, e.g., in the optical band. The formation of the disk is caused by conservation of the angular momentum. The emitted energy spectrum is thermal, i.e., it can be described by a superposition of Planck distributions of different temperatures. Temperatures of $\sim 10^5\,{\rm K}$ give rise to spectra peaking in the ultraviolet (UV) range of the electromagnetic spectrum. Hotter temperatures can be found closer to the black holes, whereas cooler regions are farther away. The mass-dependent temperature of accretion disks has been investigated, e.g., by Bonning et al. (2007). Additional radiation is caused by Bremsstrahlung of free electrons. In case of an advection-dominated accretion flow the accretion disk is assumed to present a rather low accretion rate (Abramowicz et al. 1996). This rate is assumed to be as small as a few percent of the Eddington rate, causing a low luminosity of the disk. Such a low accretion rate might be present in the object IC 310 discussed in this thesis.

- **Broad- and Narrow-line region:** The BLR as well as the NLR include fast and slow moving clouds. Lines in spectra of the AGN are due to atomic transitions broadened by the Doppler effect. The broadening is related to the speed of the cloud. The speed of the clouds in the BLR is typically of the order of $\sim 10^{3-4}\,{\rm km\,s^{-1}}$, and $\sim 10^{2-3}\,{\rm km\,s^{-1}}$ in the NLR. Forbidden transitions can be used to measure the density of the clouds.

- **Torus:** The torus around the disk is mainly formed by dust. The radiation is mostly emitted in the infrared regime. The torus may hide the emission from the vicinity of the black hole.

- **Jets:** Jets are collimated relativistic plasma outflows. The extension of the jets can be very different. Sometimes no or only weakly extended jets are found. The jets can emit

[1] G is the Gravitational constant, and c is the speed of light.

their radiation in all energy bands, showing a non-thermal, power-law energy spectrum. They can be directly viewed in the radio, optical, X-ray, and gamma-ray band, see, e.g., the jet of M87 (Acciari et al. 2009) and Centaurus A (Abdo et al. 2010c). For the latter, one of the highest spatial-resolution radio images of a jet has been obtained using the Very Long Baseline Interferometry technique by Müller et al. (2011) showing several smaller structures, called *knots*. In addition, radio and optical observations show a highly polarized emission from the jet. The radio images of nearby radio-loud AGN often show lobes generated by the ram pressure equilibrium between the jet plasma and the ambient thermal plasma.

Jets can be found in many astronomical objects, e.g., in the solar system (e.g. Enceladus) or on galactic scales (e.g. microquasar). There are still several open questions regarding how jets extract energy from the black holes and why they do not emerge in all objects. It is also not understood how they form. In Blandford & Znajek (1977), it has been proposed that the jets of rotating black holes carrying large amounts of magnetic energy and angular momentum are created by a gravito-magnetic mechanism. On the other hand, Blandford & Payne (1982) discuss the possibility that the angular momentum is extracted magnetically via field lines from the surface of the disk. Due to absorption processes, the region where the jet is formed is opaque. The best resolved image close to this region could be obtained by Doeleman et al. (2012) with VLBI at a frequency of 230 GHz, revealing a structure with a size of $11.0 \pm 0.8\, R_{\mathrm{G}}$. Furthermore, the composition of the plasma and the origin and location of the high-energy emission is a matter of debate, compare Mannheim (1993b) versus Maraschi et al. (1992). Simultaneously, the physical mechanism for the acceleration of the particles in the jet and the jet collimation in a turbulent vicinity is still not fully understood.

2.2 The Unified Model

AGN show a zoo of morphological types and behavior regarding, e.g., the variability or their broad band emission. Originally, properties like strength of emission lines in spectra (Baldwin et al. 1981; Veilleux & Osterbrock 1987) led to different classifications of various AGN. Generally, AGN are divided into radio-loud and radio-quiet objects according to the ratio of the radio to optical flux (Kellermann et al. 1989). Interestingly, objects that fall into the radio-loud category typically exhibit jets that are not observed in radio-quiet sources. Radio-quiet AGN are typically found in spiral galaxies with no or only marginally extended jets. They are further divided into different classes of Seyfert galaxies. Radio-quiet AGN will not be further discussed in this thesis (see Longair (2011) for an overview). The focus of this thesis will be on radio-loud AGN which are mainly located in elliptical galaxies. In the unified model introduced by Urry & Padovani (1995), the various diagnostics of radio-loud AGN can be interpreted mainly as a product of different viewing angles of intrinsically the same type of object. This viewing angle is characterized by the angle between the jet-axis and the line-of-sight. The diverse classes of radio-loud AGN illustrated in Fig. 2.1 will be reviewed, following the arguments of Punsly (2001).

- **Radio galaxies:** Two types of radio galaxies are found, which are called Fanaroff-Riley (FR) type I, and II, after Fanaroff & Riley (1974). The former have intrinsic extended radio luminosities of $\lesssim 10^{43}\,\mathrm{erg\,s^{-1}}$ in a frequency range of 10 MHz to 250 GHz. The

radio jets end with diffuse, “edge darkened” plume-like structures (called *lobes*) after a few hundred kiloparsec. Figure 2.2, left, shows an overlay of optical and radio images of Hercules A, a FR I proxy.
Instead, FR II are more powerful with an intrinsical radio luminosity of $\sim 10^{43-47}$ erg s^{-1}. Additionally, they differ from the FR I by showing “edge brightened” lobes, and often “hot spots”. Those are strong and bright regions in the jet. FR II jets are more collimated, and may extend up to a few megaparsecs, see, e.g., the radio image of Cygnus A in Fig. 2.2, right. In the unified model it is believed that radio galaxies are AGN in which the jet-axis has a large angle to the line-of-sight.

- **Quasars:** Quasars are divided into subclasses according to whether they are dominated by their lobe or core. Lobe-dominated quasars have similar morphology and features as FR II radio galaxies regarding the luminosity of the lobe and the jet. However, the luminosity ratio of the jet to its counter-jet is sometimes larger, causing the detection of only one jet. According to the unified model, this can be explained in terms of the viewing angle which is smaller for quasars compared to those of radio galaxies. The viewing direction with a smaller angle between the jet-axis and the line-of-sight leads also to a different optical/UV emission and broad emission lines.
  In core-dominated quasars, as the name implies, the emission, especially at high radio frequencies, is dominated by the core instead of the lobes. The core is an unresolved, often flux-variable structure in the radio jet from which a flat power-law spectrum $\propto \nu^{-\alpha}$ with $\alpha < 0.5$ in the frequency range of 1–5 GHz is measured. Instead, the lobes show a steeper power-law index of $\alpha \approx 0.5$.

- **Blazars:** These objects are characterized mostly by non-thermal emission, often over 19 decades of the electromagnetic spectrum, and flux variability on time scales from years down to minutes. There are two special types of blazars: Flat Spectrum Radio Quasars (FSRQ) and BL Lac objects. They are distinguished based on the equivalent width ($\gtrless 5$Å) of the emission lines. In case of BL Lacs, the accretion phenomena and emission lines are sometimes outshined which complicates the determination of their redshift. It is believed that blazars are viewed at a very small angle to the jet-axis. The small viewing angle leads to a strong beaming of the radiation, making them the most common population of extragalactic gamma-ray objects (Weekes 2003).

2.3 Particle Acceleration mechanisms

The observation of non-thermal radiation from AGN up to the highest energies indicates efficient acceleration processes of the particles in the jet. Theoretical models for acceleration need to explain the typically observed power-law spectra up to energies of $\sim 10^{20}$ eV, similar to what has been observed from the spectrum of the cosmic rays.

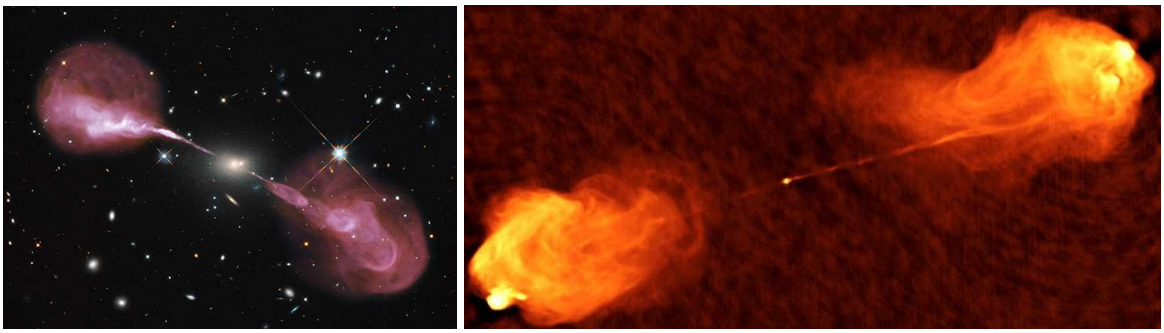

Figure 2.2: Radio galaxies. *Left:* Image of a typical FR I radio galaxy, Hercules A, obtained by a combination of an optical observation by the Hubble Space Telescope and a radio measurement of the Very Large Array (VLA). Image credit: NASA, ESA, S. Baum and C. O'Dea (RIT), R. Perley and W. Cotton (NRAO/AUI/NSF), and the Hubble Heritage Team (STScI/AURA) *Right:* Radio image of the prototypical FR II radio galaxy Cygnus A. Image credit: NRAO/AUI.

2.3.1 Fermi Acceleration

In the original work of E. Fermi (Fermi 1949), charged particles are accelerated stochastically in order to explain how cosmic rays are accelerated in interstellar clouds. A simplified, qualitative derivation of this process will be described following Stanev (2004).

A relativistic particle with an energy E_0 encounters a turbulent magnetized plasma cloud, which moves in the opposite direction in the lab frame with a certain velocity $v_{\rm cl}$. Inside the cloud, the particle suffers several elastic (energy and momentum conserved) scattering processes. If the particle leaves the cloud in the opposite but parallel direction as it entered, it gains energy. Its energy can be calculated to be proportional to the velocity of the cloud in the frame of the cloud. For the particle, the energy at exit is E_1. It can be shown that the particle gained an energy of:

$$\frac{\Delta E}{E} = \frac{E_1 - E_0}{E_0} = \gamma_{\rm cl}^2(1+\beta_{\rm cl})^2 - 1 \equiv \eta, \tag{2.1}$$

with $\beta_{\rm cl} = v_{\rm cl}/c$ and $\gamma_{\rm cl} = (1-\beta_{\rm cl}^2)^{-1/2}$. Hence, the energy gain is dependent on the square of the velocity of the cloud.

However, with a different angle of entry and exit relative to the cloud, this may result in no energy gain or even an energy loss. Therefore, any angle between the particle and the cloud needs to be taken into account. Furthermore, the direction of the particle inside the cloud is expected to be isotropized. When averaging over all angles, this will lead to an average energy gain which is proportional to the square of the velocity of the particle.

After n such encounters, the energy will be $E_n = E_0(1+\eta)^n$. Then, it can be shown that the number of particles N in the region of acceleration is given by:

$$N(>E_n) = N_0 \sum_n^{\infty} (1-P_{\rm esc})^m \propto A(E_n/E_0)^{\gamma} \tag{2.2}$$

where $P_{\rm esc}$ is the probability of the particle to escape the acceleration region and the power-law index $\gamma \simeq P_{\rm esc}/\eta$. Hence, the produced particle energy spectrum follows a power-law. Since η depends on the square of the velocity of the particle, this process is called second-order Fermi acceleration. This acceleration process in its original idea has some difficulties in explaining

the processes in an AGN jet. It takes a long time to reach high energies because

$$\frac{\mathrm{d}E}{\mathrm{d}t} = \frac{\eta E}{T_{\mathrm{enc}}} \tag{2.3}$$

where T_{enc} is the characteristic time per encounter.

A more efficient energy gain is explained with the so-called first-order Fermi acceleration. Here, η is proportional to the velocity of a shock β_{S} . This process refers to the particle acceleration in strong non-relativistic shocks created by density jumps in the plasma. Therefore, it is also called diffuse shock acceleration. It will be described in the following only quantitatively according to Longair (2011). Here, high energy particles with a velocity of $v_{\mathrm{p}} \sim c$ with a randomized velocity vector are assumed to be present in front of and behind the shock. The shock itself moves with the velocity v_{S} which is smaller than the velocity of the particle v_{p}. Further, the velocity of the shock wave is much higher than the sound speed in the ambient medium. Thus, the Mach number is $\gg 1$. The advantage of shock acceleration is that every time a particle crosses the shock, from upstream to downstream the shock and vice versa, it gains a small amount of energy. This energy gain is proportional to the velocity of the shock. This is more efficient, as no energy loss occurs. Furthermore, assuming different angles at which the particles arrive at the shocks it can be shown that the average energy gain when crossing from the upstream to the downstream side of the shock is proportional to the particle velocity upstream and proportional to the velocity of the shock. After another crossing downstream to upstream, the average energy gain is now doubled. After a few more steps, Eq. 2.2 can be written in a modified way:

$$N(E)\mathrm{d}E \propto E^{-1+(\ln P_{\mathrm{esc}}/\ln\beta)}\mathrm{d}E, \tag{2.4}$$

with $\ln\beta$ proportional to the velocity of the particle or the shock. Finally, it is found that the index $-1 + (\ln P_{\mathrm{esc}}/\ln\beta)$ equals -2. Thus, shock acceleration of high-energy particles leads to a power-law spectrum with an index of -2. This is valid for non-relativistic shocks where the magnetic field is parallel to the shock normal, and the Mach number $\gg 1$. Those conditions are not found in AGN. According to Longair (2011), the maximal energy that can be achieved is given by:

$$E_{\mathrm{max}} \propto B v_{\mathrm{S}} L \tag{2.5}$$

thus, proportional to the magnetic field flux density B, the velocity of the shock v_{S}, and its scale L.

The implications for particle acceleration processes in ultra-relativistic shocks are discussed in Kirk et al. (2000) or Reville & Bell (2014).

2.3.2 Acceleration by Magnetic Reconnection

Magnetic reconnection is usually used to explain powerful events such as solar flares (Gordovskyy et al. 2010). But it may also be considered for acceleration phenomena within magnetic reconnection sites of AGN (de Gouveia Dal Pino et al. 2011; Zenitani & Hoshino 2001). For the latter, large amounts of energy are present in magnetic fields, e.g., in regions close to a black hole. A finite electrical conductivity of the plasma enables the field lines to diffuse relative to it. This results in a dissipation of energy of the magnetic field line by heating the plasma. Thus, energy can be released. In particular, this is effective in current sheets as there the magnetic field lines are orientated in the opposite direction. Then, the lines can reconnect under resistive dissipation of the energy. The microphysics of such an effect is not yet fully

understood. Further, the large values of the electric conductivity in the plasma and the large scales where dissipation takes place cause problems. The acceleration is explained similarly to the first-order Fermi acceleration by frequent bouncing of charged particles back and forth across the reconnection site see de Gouveia dal Pino & Lazarian (2005). This results in an energy gain of $\Delta E/E \propto v_{\mathrm{rec}}/c$, where v_{rec} is the reconnection velocity carrying flow of the magnetic flux with opposite polarity. In case of fast reconnection, i.e., v_{rec} is of the order of c, the resulting particle spectrum is $N(E) \propto E^{-5/2}$, see de Gouveia Dal Pino et al. (2011). The physical conditions of the plasma, e.g., on charge carriers necessary to achieve this result are described in de Gouveia dal Pino & Lazarian (2005).

2.3.3 Acceleration by Electric Fields

Acceleration of particles up to the highest energies might occur in a magnetosphere around the black hole similar to acceleration and emission models for pulsars. A comprehensive introduction to the physics behind these processes can be found in Punsly (2001). For pulsars, mainly two scenarios have been proposed: the “polar cap” and the “outer cap model”. In the former, particles are accelerated in gaps near the magnetic poles of the rotating neutron star. The latter places the acceleration region between open field lines and the null charge surface (occurring between positively and negatively charged regions) of the magnetosphere (Weekes 2003).

In case of an AGN, it is assumed that the rotating black hole is surrounded by an external poloidal magnetic field B. The black hole itself is characterized by its angular velocity $\Omega = a(c/2R_{\mathrm{H}})$, which depends on the radius of the event horizon $R_{\mathrm{H}} = R_{\mathrm{S}}/2(1+\sqrt{1+a^2})$ and the Kerr parameter for which $0 \leq a \leq 1$ applies. R_{S} is the Schwarzschild radius. The rotation induces an electric field of $|\vec{E}| \sim (\Omega R_{\mathrm{H}})B/c$ that yields a voltage drop of $\Phi \sim R_{\mathrm{H}}E = (a/2)R_{\mathrm{H}}B$. The resulting potential drop is of the order of:

$$\Phi \sim 2 \times 10^{19} a \left(1+\sqrt{1-a^2}\right) \left(\frac{M}{10^8 \mathrm{M}_\odot}\right) \left(\frac{B}{10^4 \mathrm{G}}\right) [\mathrm{V}]. \tag{2.6}$$

In principle, a charged particle, e.g., electrons can tap this potential entirely in such a way that energies of $E = e\Phi \sim 3 \times 10^{19}(M/10^8 \mathrm{M}_\odot)(B/10^4 \mathrm{G})$ eV are reached. For a full review of the underlying physical processes and necessary conditions, see, e.g., Rieger (2011).

2.4 Non-thermal Emission and Absorption Processes

There are many radiation and absorption processes relevant in astronomical (and atmospheric) phenomenons, but only those that are of particular interest for this thesis will be covered in the following section. Comprehensive descriptions of all processes can be found in Weekes (2003), Longair (2011), and Stanev (2004).

Here, the following parameters are used: σ_{T} the Thompson cross section, μ_0 the vacuum permeability, h the Planck constant, ν the frequency, m_{e} the mass of an electron, and thus, $m_{\mathrm{e}}c^2$ the rest mass of the electron, and γ the Lorentz factor.

Compton Scattering

Compton scattering occurs if a photon with energy $h\nu$ approaches an unbound electron. The photon will change its energy and the direction of movement by a certain angle. The electron gains energy by this process. However, the more important process appearing in relativistic jets of AGN is the inverse Compton effect that produces radiation up to the very high energy (VHE, 100 GeV-100 TeV) regime. Here, a high-energy electron collides with a low-energy photon. Two regimes are distinguished: the Thompson regime is valid if the photon energy is small compared to the rest mass of the electron; In the opposite case, the Klein-Nishina regime is valid (Klein & Nishina 1929). For relativistic electrons with Lorentz factor γ_e following a power-law spectrum ($\propto E^{-\Gamma_\mathrm{e}}$), inverse Compton scattered on low-energy photons $h\nu$, the produced gamma rays have energies of $(\gamma_\mathrm{e})^2 h\nu$ in the Thompson regime and $\gamma_\mathrm{e} h\nu$ in the Klein-Nishina range. In the first case, the emitted photons follow the spectrum similar to the one of the seed photons; in the later, the spectrum is proportional to $E_\gamma^{-\Gamma_\mathrm{e}+1/2}$ up to the energy of the incident electron. Above this, energy the spectrum is cut off.

Pair Production

Pair production plays an important role in the atmosphere as it causes the production of electromagnetic air showers. It may also cause the absorption of gamma rays in compact dense emission regions. Basically, this process describes the absorption of radiation taking place in the field of, e.g., a nucleus with atomic number Z. The process leads to the complete transfer of energy of gamma rays to electron-positron pairs, i.e, $h\nu \rightarrow \mathrm{e}^+ + \mathrm{e}^-$. This occurs at a certain threshold of > 1.022 MeV that corresponds to the sum of the rest masses of two electrons.

The quantity λ_Pair characterizes the mean distance that a photon can travel in a number of target nuclei per unit volume N_V before the initiation of the absorption:

$$\lambda_\mathrm{Pair} = 1/(N_\mathrm{V}\sigma_\mathrm{Pair}) = 9/7 X_0 \tag{2.7}$$

where σ_Pair is the pair production cross section (Weekes 2003), and X_0 is the radiation length corresponding also to an energy loss by a factor e.

In case of high-energy photons E_γ and a high density of lower energetic photons $h\nu$, this process is responsible for the absorption of the high-energy photons. In this case, the pair production cross section has a maximum at:

$$E_\gamma h\nu (1 - \cos\Phi) \sim 2(m_\mathrm{e}c^2)^2 = 0.52\,(\mathrm{MeV})^2 \tag{2.8}$$

where Φ is the angle between the trajectories of the colliding photons. For example, for gamma-ray photons of an energy 1 TeV the cross section peaks for collisions with photons in the near infrared regime at wavelengths of $\sim 2\,\mu$m. Such a photon field is provided, e.g, by dust and stars distributed in the Universe, and is called the extragalactic background light (EBL). For more distant objects, the density of the low-energy photon field increases. Hence, pair-production becomes more relevant. The probability for detecting objects at high redshifts in the VHE range is limited.

Over a distance d the optical depth τ can be expressed by[2]:

$$\tau(E) = d/\lambda_\mathrm{Pair}(E) \tag{2.9}$$

[2]The attenuation for IC 310 is shown in Appendix B Fig. 5 for different EBL models.

Pion Production

If protons of energy >290 MeV interact, e.g., in the jets of AGN by collision with hydrogen gas, excited states lead to the emission of pions:

$$p + p \rightarrow \mathrm{N} + \mathrm{N} + n_1(\pi^+ + \pi^-) + n_2(\pi^0) \tag{2.10}$$

where N could either be a proton or a neutron and $n_{1/2}$ are integers. Due to a very short lifetime of $\sim 10^{-16}$ s, the neutral pions almost immediately decay into two gamma rays. The charged pions in contrast decay under the production of muons and neutrinos as follows:

$$\begin{aligned} \pi^+ &\rightarrow \mu^+ + \nu_\mu \\ \pi^- &\rightarrow \mu^- + \bar{\nu}_\mu \end{aligned} \tag{2.11}$$

and those muons decay as follows:

$$\begin{aligned} \mu^+ &\rightarrow \mathrm{e}^+ \nu_\mathrm{e} + \bar{\nu}_\mu \\ \mu^- &\rightarrow \mathrm{e}^- \bar{\nu}_\mathrm{e} + \nu_\mu. \end{aligned} \tag{2.12}$$

Hence, the detection of the neutrinos by telescopes is an indicator for the presence of protons in AGN jets. The two gamma rays resulting from the decay of a neutral pion have an energy of 70 MeV in the pion rest frame. With a power-law distribution with index Γ_p of the original protons the gamma-ray spectrum will follow a power-law with an index of $\Gamma_\gamma = 4/3(\Gamma_\mathrm{p} - 1/2)$ (see Weekes (2003)).

Electron Bremsstrahlung

This process describes the radiation of electromagnetic waves due to acceleration/deflection of electrons in the electric field of a nucleus, e.g., in an electromagnetic air shower. Typically, for this radiation, the amplitude is proportional to the acceleration.

Synchrotron Radiation

Under the influence of a homogeneous magnetic field $B = \mu H$ non-relativistic charged particles, e.g. electrons, will be accelerated in the direction of the field lines, causing a helical movement with an angular frequency of $\omega = 2\pi\nu = eH/m_\mathrm{e}$. An ultra-relativistic electron (with a Lorentz factor γ) losses energy through the emission of radiation that is called synchrotron radiation. The radiation is beamed into a cone of opening angle $\phi \approx m_\mathrm{e}c^2/E \sim 1/\gamma$. This radiation will only be observable in the direction of the cone and hence, the motion of the electron. The power distribution of the synchrotron radiation P shows a continuum spectrum with a characterizing critical frequency:

$$\omega_\mathrm{c} = 2\pi\nu_\mathrm{c} = (3/2)(eH/m_\mathrm{e}c)\gamma^2 \sin\theta_\mathrm{P}. \tag{2.13}$$

The power peaks at this frequency. θ_P is the angle between the velocity vector of the electron and the local magnetic field also known as the so-called pitch angle. At $\omega < \omega_\mathrm{c}$ the power is distributed with $\propto (\omega/\omega_\mathrm{c})^{1/3}$ and at $\omega > \omega_\mathrm{c}$ with $\propto (\omega/\omega_\mathrm{c})^{1/2}\exp[-2\omega/3\omega_\mathrm{c}]$.

Let us assume now an initial power-law distribution of electron energies, $N(E)\,\mathrm{d}E = \kappa E^{-p}\mathrm{d}E$ where the electrons with number density $N(E)\,\mathrm{d}E$ in an energy range E to $E+\mathrm{d}E$ radiate away

the energy at ν_c. The energy radiated in the frequency range ν to $\nu+\mathrm{d}\nu$ can be written according to the electrons' energy as:

$$J(\nu)\mathrm{d}\nu = -\left(\frac{\mathrm{d}E}{\mathrm{d}t}\right) N(E)\,\mathrm{d}E \tag{2.14}$$

with the energy loss rate:

$$-\left(\frac{\mathrm{d}E}{\mathrm{d}t}\right) N(E) = \frac{4}{3}\sigma_\mathrm{T} c\gamma^2 \frac{B^2}{2\mu_0}. \tag{2.15}$$

The final emissivity $J(\nu)$ is therefore a power-law $\propto \kappa B^{(p+1)/2}\nu^{-(p-1)/2}$. This can be simplified to $J(\nu) \propto \nu^{-\alpha}$, where $\alpha = (p-1)/2$ is the spectral index depending on the slope p of the electron spectrum.

At low frequencies this dependence vanishes due to synchrotron self-absorption. This happens in the case of a very compact object which absorbs its own emitted synchrotron radiation. Therefore, at a certain frequency (*turnover* frequency) the spectrum breaks, following a power-law of index $5/2$. This effect is more accurately described in Longair (2011).

One important property of the synchrotron radiation is the polarization behavior. For non-relativistic electrons, the radiation is circularly polarized in the direction parallel to the magnetic field lines. In any direction, an elliptical polarization can be observed. It can be shown that for an index of $p = 2.5$ of the electron energy spectrum, the polarization is expected to be 72%, i.e., highly polarized.

Curvature Radiation

Curvature radiation occurs if relativistic electrons move, e.g., in a black hole or pulsar magnetosphere where the magnetic field is strongly curved (Rieger 2011). The electron moves along an arc of radius $R_c \sim \gamma m_\mathrm{e} c^2/(eB\sin\theta_\mathrm{P})$, for which actual acceleration equals the centripetal one. The critical frequency is given by:

$$\nu_c \sim \frac{3c}{4\pi R_c}\gamma^3. \tag{2.16}$$

For $\nu < \nu_c$, analogous to synchrotron radiation, the curvature emission spectrum of a single particle follows a power-law of $\propto \nu^{1/3}$, and for $\nu > \nu_c$, it decreases exponentially. The energy loss rate or radiation power P_c for a single particle is given by:

$$P_c = \frac{2}{3}\frac{e^2 c}{R_c^2}\gamma^4. \tag{2.17}$$

It can be shown that under certain conditions prevalent in the magnetosphere close to supermassive black holes, acceleration by electric fields may account for Lorentz factors of the electrons up to $\gamma_{c,\mathrm{max}} \sim 10^{10}$ (Rieger 2011).

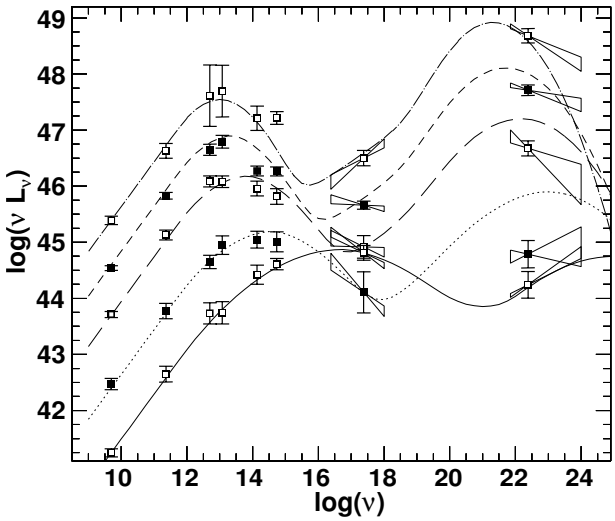

Figure 2.3: Spectral energy distribution of blazars averaged for many sources and binned in five classes according to different radio fluxes. The data points were connected with phenomenological curves. Image adapted from Fossati et al. (1998).

2.5 Spectral Energy Distribution of Radio-Loud AGN

Radio-Loud AGN can emit radiation over the entire electromagnetic spectrum, from the radio band up to the VHE regime. The spectral energy distribution (SED) of this radiation is typically shown as the energy flux $\mathrm{d}N/\mathrm{d}E$ per interval of the logarithmic energy:

$$E^2 \frac{\mathrm{d}N}{\mathrm{d}E} = E \frac{\mathrm{d}N}{\mathrm{d}(\log E)}, \tag{2.18}$$

comparable to an application of νF_ν. The integral of the SED represents the total energy output in each energy band.

2.5.1 Emission Models

The SED of radio-loud AGN shows two main broad humps, see Fig. 2.3. The first maximum is usually observed in the infrared, optical/UV or X-ray band, whereas the second can be found in the MeV/GeV/TeV range. This low-energy hump can be explained by synchrotron radiation of electrons and positrons assuming that the jet of an AGN consists of a plasma of electrons and positrons (Hartman et al. 1992; Sikora 1994). The acceleration of the particles is usually explained by shocks. Those shocks propagate down the jet (at different velocities), and originate from colliding inhomogeneities in the jet plasma. This can be observed as blobs in the VLBI images. Due to the magnetic field in the jet, the electrons emit synchrotron radiation, as confirmed by the measurement of highly polarized radio and optical emission from these objects. Linear polarization also results from Compton scattering or plasma emission processes. The position of the first hump is determined by the efficiency of the acceleration process and the cooling via synchrotron and Compton scattering.

The origin of the second, high-energy hump is still a subject of debate. Two basic mechanisms are discussed: leptonic and hadronic models. Leptonic models are based on the inverse Compton scattering of low-energy photons which could be the photons of the synchrotron radiation. This Synchrotron-Self-Compton (SSC) process has been proposed by Marscher & Gear

(1985), Maraschi et al. (1992), and Bloom & Marscher (1996). The photons in this process will be boosted to energies $\approx \gamma^2 h\nu$ in the Thomson regime and $\approx \gamma m_\mathrm{e} c^2$ in the Klein-Nishina range. The simplest version of such a model assumes a single component (zone) in which synchrotron and inverse Compton radiation is produced. The seed photons may also originate from external radiation. Possible sources could be the optical to X-ray emission from the accretion disk (Dermer & Schlickeiser 1994), the line emission from the BLR or NLR (Ghisellini & Madau 1996), infrared emission from the dust (Arbeiter et al. 2002), or the cosmic microwave background (Harris & Krawczynski 2002). Additionally, models with a different geometry are considered, e.g., multi-component jet scenarios such as the model by Georganopoulos & Kazanas (2004). In Weidinger (2011), a spherical acceleration zone surrounded by a larger but also spherical emission zone is assumed. In contrast, Tavecchio & Ghisellini (2008) suggested a cylindrical geometry, with a fast *spine* and a slower *sheath*. This model has been used to explain the broad band SED of the radio galaxies M87 (Tavecchio & Ghisellini 2008) and NGC 1275 (Tavecchio & Ghisellini 2014). The fitting of the SEDs of those objects with emission models originally build for blazars is complicated. The reason is that the radio to X-ray band is often dominated by additional sources of radiation external to the jet such as the host galaxy. Further contributions may originate from the surrounding galaxy cluster, or star forming regions, see, e.g., NGC 1275 (Aleksić et al. 2014a)

Leptonic models typically require low values for the magnetic field (Tavecchio et al. 2010), or a magnetic collimation of the jet. Such magnetic field strengths are insufficient for the acceleration of protons to high energies. However, if large magnetic field strengths are present, the high energy emission, i.e., the second hump, may originate from, e.g., proton synchrotron radiation (Mücke et al. 2003; Mannheim 1993b), or photo-pion production initiating electromagnetic cascades (Mannheim 1993a,b). Those models are summarized as hadronic models. They are motivated by the observed cosmic-ray spectrum up to energies of 10^{20} eV. To confirm the acceleration of hadrons in AGN jets, neutrinos need to be detected from these objects. In Mannheim (1995), the neutrino flux from AGN jets was predicted to exceed the atmospheric flux at energies of ~ 100 TeV, in agreement with recent measurements (IceCube Collaboration 2013; Aartsen et al. 2014). Due to the interaction of the protons with soft photons in the jet, pion production cascades with neutrinos as decay products are initiated. The significant detection of individual neutrino sources is still pending (IceCube Collaboration 2013; Aartsen et al. 2014).

2.5.2 Classification of Blazars

As explained in the previous section, blazars show two broad humps in their SED. According to the frequency of the peaks and additionally to their luminosity (among other properties), the blazars are divided into subclasses. More luminous blazars tend to be “redder”, having their synchrotron peak at lower frequencies. This statement is however strongly biased by the variable behavior of these objects. The most luminous and most powerful objects found are usually associated with quasars which show emission lines greater than $5\,\text{Å}$ (Urry & Padovani 1995). This criteria may lead to misclassification, as an intense continuum (during flaring activities) can hide broad emission lines, see, e.g., the case of BL Lac (Vermeulen et al. 1995). The synchrotron peak of red blazars is typically located in the sub-mm band (Ghisellini 2013). FSRQs also often show a so-called big blue bump located in the optical and UV range (Shang et al. 2005). It is believed that this emission originates from the accretion disk. Hence, for those objects the black hole mass and its accretion rate can be estimated, see Ghisellini (2013) for a review.

"Bluer" objects are associated with the BL Lac objects which show no emission or less strong (< 5 Å) broad emission lines in their optical spectra (Urry & Padovani 1995). Those objects are further distinguished into classes characterized by the location of the synchrotron peak in the SED: low-frequency peaked BL Lacs (LBLs), intermediate-frequency peaked BL Lacs (IBLs) and high-frequency peaked BL Lacs (HBLs). Those objects seem to be less powerful compared to FSRQs and, hence, have lower luminosities. For LBLs the synchrotron emission peaks at infrared frequencies and the high-energy peak is found at MeV energies. For HBLs, the former lies in the UV to X-ray band and the latter at GeV ($\lesssim 100$ GeV) energies. Since the gamma-ray flux (> 100 GeV up to ~ 10 TeV) of HBLs is rather high, those objects are preferably detected by ground-based gamma-ray telescopes. For some HBLs, the synchrotron emission even extends to > 1 keV and the second peak is found at TeV energies. This is typically observed during flaring activities of the object. Those objects are called extreme HBLs (EHBLs) (Costamante et al. 2001a,b). Ghisellini (1999) suggested that those objects dissipate the jet power in a most efficient way, associated with very efficient acceleration close to the limit.

2.5.3 The Blazar Sequence

The general trend, from red to blue blazars, is illustrated in Fig. 2.3 by averaged SEDs for many objects. The objects were divided into five categories according to their radio fluxes (Fossati et al. 1998). Generally, three characteristics could be inferred: the bolometric luminosity follows the radio luminosity; with decreasing radio luminosity (and the bolometric one) the synchrotron and high energy peaks shift to higher frequencies, and simultaneously the dominance of the second hump becomes less important. This *Blazar sequence* was first reported by Fossati et al. (1998) and Ghisellini et al. (1998) and updated by Donato et al. (2001). Ghisellini et al. (1998) interpreted the blazar sequence as an effect of different amounts of radiative cooling in the different objects. Less powerful BL Lacs could carry a weaker magnetic field. Assuming a SSC mechanism, the cooling will be limited, electrons can be accelerated to higher energies, producing preferably radiation at higher frequencies. With overall higher luminosity the magnetic field in the jets gets stronger. Then, the cooling becomes more important, so that the electrons attain lower energies. In parallel, the probability for electron scattering on external photon fields (disk, torus, BLR) increases, leading to a dominating high energy bump.

Cavaliere & D'Elia (2002) and Ghisellini & Tavecchio (2008) suggested that the blazar sequence is an implication for cosmic evolution of blazars. The classification into different subclasses of blazar populations might be due to the same object at different stages of development. Red blazars (FSRQ), believed to be at the beginning of an AGN life, have a low black hole mass of $M_{\rm BH} \sim 10^6 {\rm M}_\odot$ and they are still equipped with a high amount of material that can be accreted, thus the accretion rate is high. With accretion of more and more material (e.g. from the disk) the amount of available photons decreases. This results in a lower luminosity and at the same time, an increase of the black hole mass to higher values ($M_{\rm BH} \lesssim 10^{9-10} {\rm M}_\odot$). This is in agreement with measurements of the black hole masses from BL Lac and FSRQs (Ghisellini & Tavecchio 2008).

According to the blazar sequence, no low-peaked low-luminosity as well as high-peaked high-luminosity objects exist. But those were claimed to be detected (Padovani et al. 2002, 2003; Giommi et al. 2007; Bassani et al. 2007; Padovani et al. 2012). Recent studies by, e.g., Giommi et al. (2012a,b) using Monte Carlo simulations and larger samples of blazars, respectively, suggest that the blazar sequence might be affected, or even triggered, by selection effects mostly due to shallow radio and X-ray surveys and non-measurable redshifts of high-peaked

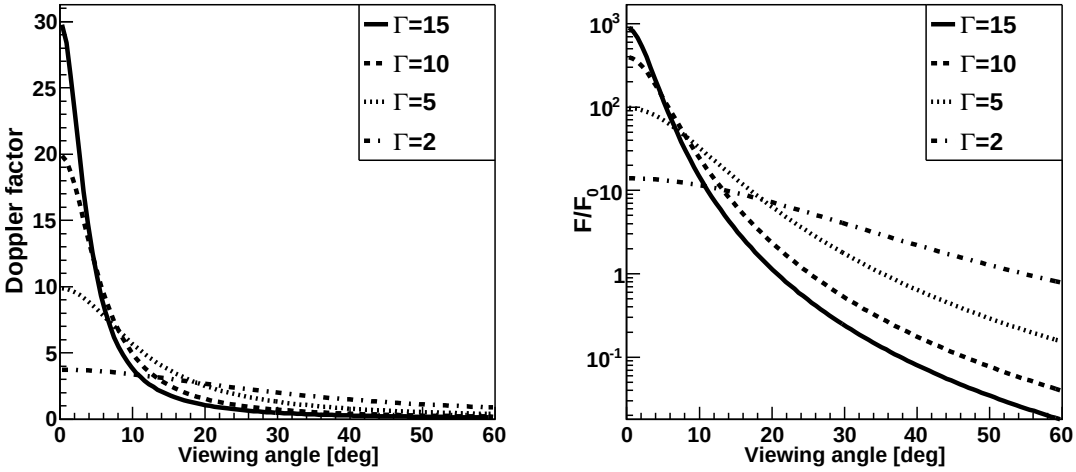

Figure 2.4: Effect of the Doppler boosting. *Left panel:* Dependence on the Doppler boosting factor on the angle between the jet-axis and the line-of-sight. *Right panel:* Ratio between the observed (boosted) flux F to the unbeamed flux F_0 as a function of the Doppler factor. Image adapted from Urry & Padovani (1995).

high-luminosity objects.

2.6 Relativistic Beaming

The relativistic motion of particles in jets is characterized by the bulk Lorentz factor:

$$\Gamma = (1 - \beta^2)^{-1/2}, \tag{2.19}$$

where β is defined as the velocity v/c. Assuming that an object, e.g., an AGN is observed under a viewing angle θ, the Doppler factor δ is given by:

$$\delta = \frac{1}{\Gamma(1 - \beta \cos\theta)}. \tag{2.20}$$

Generally, for $\Gamma >> 1$ the Doppler factor depends only on the combination of Γ and θ. Assuming $\theta = 0$, the maximal Doppler factor is determined by 2Γ. Figure 2.4 (left) shows the dependence of the Doppler factor on the angle between the jet-axis and the line-of-sight for different values of the Lorentz factor.

Doppler boosting has several effects on the physical parameters of the emitted emission. In the co-moving frame of an AGN jet, the frequency of the photons is ν'. In the observers frame, the frequency ν then equals to $\delta\nu'$. Therefore, the energy of the observed photon is larger than the emitted photon in the co-moving frame by a factor of δ. The observed luminosity L at a given frequency amplifies to $\delta^p L'$, compared to the luminosity in the co-moving frame L'. The index p depends on the index α of a power-law spectrum, $F(\nu) \propto \nu^{-\alpha}$, whether a moving sphere ($p = 2 - \alpha$) or a continuous jet ($p = 3 - \alpha$) is assumed (Urry & Padovani 1995). The flux amplification, dependent on the viewing angle for different Lorentz factors, is shown in Fig. 2.4, right panel.

The importance of the Doppler boosting is evident for the explanation of various observational properties. One particular effect is fast variability of the radio flux. Kellermann &

Pauliny-Toth (1969) found that there must be a limit for the apparent variability brightness temperatures of $T_{\mathrm{B}} \sim 10^{12}$ K. If this limit is exceeded, catastrophic energy losses due to inverse Compton scattering occur that lead to a decrease of the brightness temperature back to the value of the limit. At this limit, the amount of inverse Compton losses equals the synchrotron losses. However, higher values for the brightness temperature were observed. This *Compton limit* or *Compton catastrophe* can be explained by taking into account the beaming effect. Similarly, it can be explained why the observed luminosities in the X-ray band are found to be lower and not consistent with the theoretical predictions from Compton scattering in isotropic sources (Marscher et al. 1979; Ghisellini et al. 1993).

In addition, without assuming the beaming, the fast variability would be in conflict with the Eddington limit which limits the luminosity of an accreting object. This limit is achieved if the radiative force due to Thomson-scattering of the radiation at free electrons equals the gravitational force. Analogously, in Fabian (1979) a limit for the change of the luminosity ΔL in a certain time τ_{var} was estimated to be $\Delta L < 2 \times 10^{41} \epsilon \tau_{\mathrm{var}}\,\mathrm{erg\,s^{-1}}$ assuming an efficiency ϵ for conversion of matter to energy of 10%.

One-sided jets

The effect of the Doppler boosting on the emission becomes obvious in high spatial-resolution images of either radio, optical or X-ray emission of jets (e.g. M87 (Acciari et al. 2009)). The radio morphology of one-sided jets (especially on the parsec scales) typically shows a bright compact component at the beginning of the jet, called *core*, where the optical depth to synchrotron emission is of the order of unity, or a standing shock further downstream the jet (Marscher 2008). Starting from the core the brightness along the jet then usually decreases, but sometimes shows stronger components further away from the core.

Due to the beaming the intensity of the jet pointing into the direction towards the observer gets amplified, whereas the counter-jet in the opposite direction gets diluted. Hence, for some of the radio-loud AGN only one of the jets is visible and the counter-jet remains undetected. This can be described by the ratio of the flux density of the jet and its counter-jet according to Urry & Padovani (1995):

$$R = \frac{S_{\mathrm{jet}}}{S_{\mathrm{counter-jet}}} = \left(\frac{1 + \beta \cos\theta}{1 - \beta \cos\theta} \right)^{2-\alpha}. \tag{2.21}$$

By measuring β and α, the angle between the jet-axis and the line-of-sight can be obtained. In case of a non-detection of the counter-jet, a limit can be estimated. Note, however, that a non-detection of the counter-jet or an observation of only the core component in 1-3% of the objects, e.g., in the MOJAVE survey could also be a result from an insufficient dynamic range or disturbances in the jet flow (Boettcher et al. 2012).

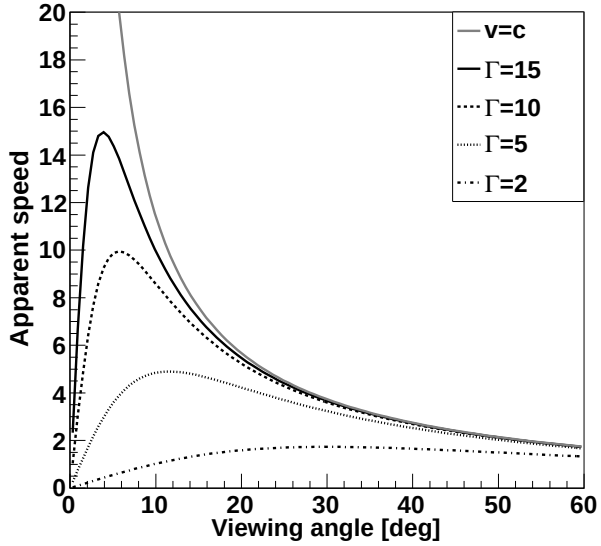

Figure 2.5: Superluminal motion. Dependence of the apparent speed on the angle between the jet-axis and the line-of-sight shown for different Lorentz factors (black lines) and for the case $v = c$ (gray line). Image adapted from Urry & Padovani (1995).

Superluminal motion

Superluminal motion was predicted by Rees (1966) and first measured with kinematic analysis of radio knots in jets in VLBI radio maps of objects with small viewing angles. Due to a geometrical effect the emitting material in the jet appears to be mowing with a velocity larger than the speed of light. This is characterized by the apparent speed $\beta_{\rm app}$:

$$\beta_{\rm app} = \frac{\beta \sin\theta}{1 - \beta\cos\theta} < \Gamma\beta. \tag{2.22}$$

Thus, by measuring the apparent superluminal motion a lower limit on the bulk Lorentz factor can be obtained. Figure 2.5 shows the apparent speed as a function of the viewing angle.

The apparent speed can be also connected to the jet-to-counter-jet ratio (Eg. 2.21) with:

$$R = \left(\beta_{\rm app}^2 + \delta^2\right)^{2-\alpha}. \tag{2.23}$$

Statistical studies on the superluminal motion can be found, e.g., in Vermeulen & Cohen (1994), or Lister et al. (2013). In the latter survey, the MOJAVE blazar monitoring program at 15 GHz, the fastest apparent motion was found to be 41.8 c observed from the FSRQ PKS 0805–07. Jorstad et al. (2005) reported an even higher value of ~ 45 c for the FSRQ PKS 1510−089. The authors also estimated the Lorentz factors for a number of blazars. They found values in a range of $\Gamma \sim 5 - 40$. For quasars a typical value of $\Gamma \sim 16 - 18$ has been inferred, while for BL Lacs objects the values are more widely spread.

For most TeV bright BL Lacs (mainly HBLs), however, no pronounced superluminal motion was reported, see, e.g., Piner & Edwards (2004); Giroletti et al. (2004a); Piner et al. (2010); Lico et al. (2012); Blasi et al. (2013). Typically, the kinematic analysis of the radio components in those jets show an apparent speeds of $\lesssim 1$ c. This observation, along with other properties such as brightness temperatures and core dominance, reported by Giroletti et al. (2004b); Lister et al. (2011), suggest rather small Lorentz factors for these objects. In contrast to this, high

bulk Lorentz factors are necessary to explain the strong variability observed in the TeV band for these objects (e.g. Begelman et al. (2008); Nalewajko et al. (2011); Narayan & Piran (2012)) as well as in the modeling of the overall broad band emission (e.g. Tavecchio et al. (2010)). This discrepancy is called *Doppler Factor Crisis*. One plausible explanation could be that the radio and gamma-ray emission originate from different locations with different bulk Lorentz factors in the jet. Possible alternative scenarios to explain this phenomenon could be spine-sheath structures (Ghisellini et al. 2005), decelerating jets (Georganopoulos & Kazanas 2003), the 'jets-in-the-jet' model (Giannios et al. 2009), or fast moving leading edges of radio components which are highly magnetized and non-stationary (Lyutikov & Lister 2010).

Size of the emission region

Generally, variability allows to infer the size of the region where the radiation is emitted by using causality arguments. As long as the source of the emission is transparent, any fast variable emission is diluted due to the finite time in which light can travel (Boettcher et al. 2012). Assuming R (radius of a sphere) characterizes the size of the emission region, this time can be given by $\Delta t' \sim R/c$ in the co-moving frame of the jet[3]. If the emitting source moves relativistically, the observed time scale $\Delta t_{\rm obs}$ is a result of contraction $\Delta t_{\rm obs} = \Delta t'/\delta$. Therefore, the smallest observed variability time scale is $\tau_{\rm var,min} \geq \delta^{-1} R/c$. The size of the emission at a redshift z is constrained by the variability time scale $\Delta t_{\rm obs} = \tau_{\rm var}$:

$$R \leq c\tau_{\rm var}\delta\,(1+z)^{-1}\,. \tag{2.24}$$

The measurement of this size obviously requires the knowledge of the Doppler factor. For $z = 0$, an observed variability time scale of $\tau_{\rm var} = 1$ day gives a constrain of $R \leq 2.6 \times 10^{16}(\tau_{\rm var}/1\,{\rm day})(\delta/10)$ cm. This value is consistent with the sizes of components found in high spatial-resolution radio maps of pc-scale jets, and those found by modeling of the broad-band spectral energy distribution (Tavecchio et al. 2010). Extreme cases are the observation of minute variability where R is smaller than the event horizon of the black hole. To achieve $R \geq R_{\rm G}$ for $M \sim 10^9 M_\odot$, a large Doppler factor of $\delta \sim 80$ has to be considered.

Opacity problem

One particular effect is the absorption of high-energy gamma rays in a compact dense emission region via pair-production effects. Originally, in Cavallo & Rees (1978) the authors proofed that a compact source which can emit non-thermal radiation up to the highest energies becomes opaque at those energies when a certain limit of compactness is exceeded. Then, more frequent photon-photon collisions lead to electron-positron pairs and hence, absorb the gamma rays. This problem has been further discussed in Begelman et al. (2008) for the minute-scale variability of TeV gamma rays observed from the objects Mrk 501 and PKS 2155−303, where the variability time scale is shorter than the time scale corresponding to the event horizon of the black hole. Consequently, due to the enhanced emission in such a small region the gamma rays would be absorbed if no Doppler boosting of the emission would be present. The dependency of the Doppler factor on this effect will be derived similarly to Dondi & Ghisellini (1995).

Assume that the gamma rays and the target photons originate from a single, spherical region of radius R' moving with a velocity βc and Lorentz factor Γ with an angle to the line-of-sight

[3] All values marked with a prime indicate quantities in the co-moving frame of the jet.

of θ. The absorption takes place if the gamma rays of energy E' collide with the target photons of energy $\epsilon'_{\rm t}$ under an angle Φ. This is given by:

$$(1-\cos\Phi)E'\epsilon'_{\rm t} \simeq 8(m_{\rm e}c^2)^2 \tag{2.25}$$

For simplicity, the factor $(1-\cos\Phi)$ shall equal 1 for the most frequent scattering where $\cos\Phi = 0$ applies. The cross-section $\sigma_{\gamma\gamma} \simeq \sigma_{\rm T}/5$ for this process is maximized under this condition and hence the optical depth can be calculated, see Heitler (1960), and Zacharias (2014):

$$\tau_{\gamma\gamma}(E') = \frac{\sigma_{\rm T}}{5} n'(\epsilon'_{\rm t})\epsilon'_{\rm t} R', \tag{2.26}$$

where $n'(\epsilon'_{\rm t})$ is the density of the target photons, given by

$$n'(\epsilon'_{\rm t}) = \frac{L'_{\rm syn}}{4\pi(R')^2 c\epsilon'_{\rm t}}, \tag{2.27}$$

with the luminosity $L'_{\rm syn}$ of the synchrotron target photons. The radius of the emission region is constrained by the variability time scale $\tau_{\rm var}$ by causality arguments:

$$R' = c\tau_{\rm var}\frac{\delta}{1+z} \simeq c\tau_{\rm var}\delta. \tag{2.28}$$

The second equality is valid for objects at low redshifts. To rewrite Eq.2.26 in terms of observed quantities, the luminosity of the target synchrotron photons is transformed from the co-moving frame into the observer frame with:

$$L_{\rm syn} = L'_{\rm syn}\delta^4. \tag{2.29}$$

Generally, the observed photons of energy E are emitted with energy $E' = E/\delta$ and, the target photons have an energy of $\epsilon'_{\rm t} = \delta/E$ in the co-moving frame. The latter are observed at energies $\epsilon_{\rm t} = \epsilon'_{\rm t}\delta = \delta^2/E$.

To avoid the $\gamma\gamma$ pair production and hence allowing for an escape of the gamma rays, the optical depth is required to be $\tau_{\gamma\gamma} < 1$, so

$$\tau_{\gamma\gamma}(E') = \frac{\sigma_{\rm T}}{5}\frac{L_{\rm syn}}{\delta^4 4\pi R' c\epsilon'_{\rm th}} < 1. \tag{2.30}$$

With Eq. 2.25 and Eq. 2.28 this leads to:

$$\tau_{\gamma\gamma} = \frac{\sigma_{\rm T}}{5}\frac{L_{\rm syn}E'}{\delta^5 4\pi c^2\tau_{\rm var}8(m_{\rm e}c^2)^2} = \frac{\sigma_{\rm T}}{5}\frac{L_{\rm syn}E}{\delta^6 4\pi c^2\tau_{\rm var}8(m_{\rm e}c^2)^2} < 1. \tag{2.31}$$

Finally, a lower limit for the Doppler factor can be obtained:

$$\delta \geq \left[\frac{L_{\rm syn}\sigma_{\rm T}E}{160\pi c^2\tau_{\rm var}(m_{\rm e}c^2)^2}\right]^{1/6}. \tag{2.32}$$

2.7 Variability of Radio-Loud AGN

2.7.1 Observations

The topic of variability observed from AGN is being investigated basically since the discovery of the first quasars by Matthews & Sandage (1963). The authors claimed that the observed variability constrained the size of the emission region by causality arguments (described in Section 2.6) to be of the order of lightweeks. This implies high-energy densities which rule out stellar emission processes like fusion. Since then, variability has been found in all observed frequency bands and on all observed times scales from years to minutes (Wagner & Witzel 1995).

The first optical observations of fast, intra-day variability of AGN has been claimed by, e.g., Racine (1970); Bertaud et al. (1973); Grauer (1984). In the X-ray and radio band variability as fast as 100 s and 10^3 s (de Bruyn 1988), respectively, were found.

The detectability of fast variability is naturally limited by the sampling time scale as well as the amplitudes reaching the noise level, plus insufficient photon statistics and the accuracy of the measurement as stressed by Wagner & Witzel (1995). That limited statistics affect the minimal variability time scale measured in the high energy (HE, 100 MeV-100 GeV) range by *Fermi*-LAT has also be mentioned by Vovk & Neronov (2013). Hence, faster variability is expected in this energy range, but not resolvable by the *Fermi*-LAT instrument. Therefore, the authors have found only variability times scales which are not shorter than the black hole horizon light-crossing time $T_{\rm G} = R_{\rm G}/c$.

As mentioned in Section 2.1, there are several open questions, e.g., regarding the connection between the jet and the black hole, the jet base, the acceleration and radiation physics in the jet, its matter content, and the origin and location of the gamma-ray emission. Studying some of these topics requires a high angular resolution. The highest spatial resolution can be obtained with the VLBI technique in the radio band, see Müller et al. (2011). Those observations allow for a direct imaging of the region close to the black hole (Doeleman et al. 2012). However, due to the synchrotron self-absorption, the region of the jet base is usually opaque. Fortunately, rapid variability indirectly provides information about this region. To illustrate this, the spatial scales inferred from fast variability will be compared to the VLBI angular resolution. Müller et al. (2011) achieved a resolution of $0.4\,\mathrm{mas\,x\,0.7\,mas}$ at 8.4 GHz, corresponding to $\lesssim 0.013$ pc at $z = 0.0018$ which equals to $\sim 4 \times 10^{16}$ cm. The same scale is already achieved by observing a variability time of 15 days at $z = 0.0018$.

To investigate variability, especially fast variability, in general several questions can be studied as indicated by Wagner & Witzel (1995).

- Is the appearance of fast variability connected to an overall long-term variation of the flux? This could indicate a similar physical mechanism responsible of both types of variability.

- Can periodicity be inferred? This can be studied, e.g., by the structure function (Hughes et al. 1992), the power spectrum (Vaughan et al. 2003), or the Lomb-Scargle periodogram (Lomb 1976; Scargle 1982).
  The "power" of variability as a function of temporal frequency can be calculated by the power spectral density, see Vaughan et al. (2003). Applying this method to X-ray light curves of Seyfert galaxies, it was found that they follow a simple power-law ($P(f) \propto f^{-k}$) with a typical slope k between 1 and 2 (see e.g. Lawrence et al. (1987);

McHardy & Czerny (1987)). Such slopes characterize the so-called “red noise”. A “flickering” light curve has more power in short-term variability, leading to a flatter slope of 1. A steeper slope indicates variability on longer time scales (Vaughan et al. 2003). Further features that can be discovered in power spectra are, e.g., piece-wise power-laws behavior with breaks (e.g. Uttley et al. (2002); Markowitz et al. (2003)), or peaks denoting periodicity (e.g., Belloni & Altamirano (2013)). The same red-noise property of the power-spectra seen in AGNs and X-ray binaries may refer to a similar underlying physical process of the X-ray variability (e.g., Edelson & Nandra (1999); Uttley et al. (2002); Markowitz et al. (2003)). In contrast, the so-called “white noise” shows a flat spectrum with a slope of 0 resulting from, e.g., a Gaussian or Poissonian process (Bernardini & Cackett 2014). Those processes contribute roughly with the same amount of power to all time scales and frequencies.
However, the results of these analysis methods often suffer from an insufficient observational sampling and duration causing unresolved individual flares and poor coverage over several periods.

- Is the shape of flares, either symmetric (same timescales for rise and decay) or asymmetric (different timescales for rise and decay) following an exponential or Gaussian course? This may give hints of the physics behind the flare.

- Are objects for which fast variability has been observed specific ones in terms of their classification? For example, in the TeV gamma-ray regime the most rapid flux variations (on time scales of minutes) have been measured from the HBLs Mrk 501 and PKS 2155-304 (Albert et al. 2007c; Aharonian et al. 2007). However, these objects are assumed to be viewed under a small angle between the jet-axis and the line-of-sight, hence the beaming effect is strong (see Fig. 2.4). In case of radio galaxies, like M87, the viewing angle is larger and in general, no strong beaming should be present. Therefore, the variability time scale as long as a day as reported in Acciari et al. (2009) can be considered to be fast.

- What is the flux amplitude of a flare compared to the quiescent state? Assuming an isotropic emission of $10^{45}\,\mathrm{erg\,s^{-1}}$ and a change of the luminosity by a factor of 2 for 24 h requires a total energy of the order of $\sim 10^{50}$ erg.

- Is the flux variability connected to a spectral variability? Here, flux as well as spectral variability during flares needs to be compared to the low activity states of the objects over the entire electromagnetic spectrum. Often, correlations during outbursts are found between different energy bands, e.g., for HBLs in the X-ray and VHE band (Fossati et al. 2008; Acciari et al. 2011a,b). This follows the expectations from the SSC mechanism, where the particle population that produces the X-ray emission is the same as the one that produces the VHE emission. At the same time, a change of the spectra in these bands has been observed. During flaring periods the spectra become harder. This is visible in the SED by a movement of the synchrotron as well as the inverse Compton peak to higher frequencies. Further correlations between the optical and VHE fluxes, X-ray and HE regime have been reported by Wehrle et al. (1998) and Reinthal et al. (2012), respectively. In contrast, in very rare cases no correlation between TeV flares and the low energy band, e.g., in X-rays has been observed, see Krawczynski et al. (2004). These are called *orphan* flares. In the case of S5 0716+714 an orphan flare has been observed in the X-ray band

(Rani et al. 2013). Generally, orphan flares may also be misidentified due to an insufficient multi-wavelength (MWL) coverage. Therefore, a dense and simultaneous MWL coverage is crucial for the understanding of variability. Wagner (1997) mentioned that fast variability has been observed in combination of fast changes of the polarization. The similar time scales indicate small turbulences of the magnetic field on scales comparable to the one of the emitting region. A particular case of correlation, the study of gamma-ray activity and the connection with newly outcoming radio blobs in the VLBI jets, has been presented by Jorstad et al. (2001); Marscher et al. (2008); Kovalev et al. (2009); Arlen et al. (2013). Typically, a time lag between gamma-ray flare and ejection of one month to several months could be measured. Such an ejection may also lead to an increase of the overall radio flux density, see, e.g., the case of NGC 1275 (Aleksić et al. 2014a).

- Are different flux states consistent with arrival times of neutrinos? In terms of the multi-messenger approach, it might also be considered to search for correlations between flares and arrival times of neutrinos (Adrián-Martínez et al. 2012; Sánchez Losa & ANTARES Collaboration 2013) according to models of Mannheim (1993a) or Bednarek & Protheroe (1999).

It should be mentioned that several authors use a different nomenclature to characterize rapid variability. Some authors quote the doubling time (Gaidos et al. 1996; Aharonian et al. 2007; Rani et al. 2013). This time scale, however, does not fully constrain the size of the emission region as this size is defined by the complete time span in which the flux changes from a low state to a high state or vice versa. This requires a full coverage of the flare from the rise to the decaying phase, which is often not achieved. In this case, the doubling time can be considered. Other authors may call the entire time span (rise and decay) the variability time scale. For example, this might be used because of a flickering behavior where several short-term flares are observed, and individual rise and decay periods can barely be distinguished. Those various notations makes it difficult to compare different observations.

2.7.2 Physical mechanisms

To explain variability, it is commonly assumed that particles are accelerated on shock fronts in the jet. For a review on this *shock-in-jet model* it is referred to Wagner & Witzel (1995). This model was originally suggested by Blandford & Königl (1979) and in-depth studies can be found in works of Marscher (1980); Marscher & Gear (1985); Jones (1988); Melia & Konigl (1989); Marscher (1992). It has been suggested by analogy to pulsar winds and supernova remnants that shocks located in turbulent jets cause changes in the local emissivity and activate flaring periods. As mentioned by Hughes et al. (1985), and Koenigl & Choudhuri (1985), those changes connected with compression of the magnetic field configuration lead to variability of the polarization degree and angle. Blandford & Eichler (1987) has shown that shocks in jets might accelerate particles to ultrarelativistic energies by the *in situ* Fermi mechanism of diffusive shock acceleration.

The shock-in-jet models may have difficulties in explaining the rapid variability as those observed by Albert et al. (2007c); Aharonian et al. (2007); Acciari et al. (2009). The variability time scales in those cases were found to be smaller than the event horizon light crossing time T_{G}. In terms of the shock-in-jet model, however, the shortest possible time scale for incoherent radiation is the one that corresponds to the light travel time across the shock which is the size

of the diameter of the jet. The lowest limit of the jet diameter is the black hole event horizon, in contrast to the observed minute variability if no Doppler boosting is assumed. Rather large Lorentz factors of $\Gamma_{\rm j} \sim 50$ are suggested by Begelman et al. (2008) to explain the minute variability, e.g., observed from PKS 2155−304 in order to avoid the opacity problem (see Section 2.6). Alternative models are based, e.g., on the interaction of the jets with clouds or stars (Bednarek & Protheroe 1997a; Barkov et al. 2010, 2012b; Araudo et al. 2013) as originally proposed by Blandford & Königl (1979). Other authors suggested *jets-in-jet* models assuming that large Lorentz factors are produced by several subregions, *mini-jets*, moving relative to the main jet (Giannios et al. 2009, 2010; Narayan & Piran 2012).

The observation of rapid variability in the gamma-ray band may provide information about where the high-energy emission is located (Vovk & Neronov 2013). As explained by Liu & Bai (2006), gamma-rays can be absorbed by production of electron-positron pairs within the dense BLR. Hence, the gamma-ray emission may originate from a region outside the BLR which lies parsecs away from the black hole. Instead, Celotti et al. (1998) calculated the distance of the gamma-ray emission from the black hole $D \sim \Gamma^2 R$ with $\Gamma \sim 3 - 30$ and R being of the order of the size corresponding to the black hole horizon light-crossing time $T_{\rm G} \sim 10^3\,[R/2\,{\rm AU}]$. It has been suggested that a correlation/non-correlation between the minimal variability time scale and the mass of the black hole can be used to distinguish whether the location is close to the black hole or not (Vovk & Neronov 2013). If the minimal time scale is determined by the mass, the location is expected to be close to the central engine. If not, the minimal time scale might be related to a compact region at large distances from the black hole. The rapid time scale may then possibly be caused by intrinsic instabilities of the jet.

2.8 The Active Galaxy IC 310

IC 310 is a nearby lenticular galaxy[4] (Hubble scheme: S0) and one of the brigthest objects at radio and X-ray frequencies in the Perseus cluster of galaxies. The galaxy was first discovered by Edward Swift on November 3, 1888[5]. The redshift was measured to be $z = 0.019$, e.g. by Shaw et al. (2013) and hence a luminosity distance of $D_L = 81\,$Mpc to the object can be estimated[6].

Originally, IC 310 has been classified as a head-tail radio galaxy (HTRG) (Ryle & Windram 1968), more specifically as narrow-angle tail radio galaxy (Sijbring & de Bruyn 1998; Feretti et al. 1998; Miley 1980). Those radio galaxies can be naturally found in clusters of galaxies. Their characteristic radio structure arises from the motion of the galaxy through the intra-cluster medium (ICM) resulting in a bending of the jets on a bow shock which are then pointing away from the center of the cluster. The classification of IC 310 as a HTRG followed due to the direction of the extended radio jet of IC 310 which points, however, only marginally in the direction to the center.

The object became of interest with its discovery in the gamma-ray regime in 2010 at energies above 30 GeV in the data of the *Fermi*-LAT instrument (Neronov et al. 2010) as well as above 260 GeV by the MAGIC telescopes (Aleksić et al. 2010b), see Fig. 2.6. The authors found first hints for variability of the gamma-ray flux, arguing against the classification as HTRG. A bow shock in a HTRG is large and therefore, variability shorter as a human-life time is not expected (Neronov et al. 2010).

[4] IC 310 is located at right ascension R.A.: 3h16m42.978s and declination Dec: +41d19'29.616", epoch J2000.
[5] `http://cseligman.com/`
[6] A cosmology model of $\Omega_{\rm m} = 0.27$, $\Omega_\Lambda = 0.73$ and $H_0 = 71\,{\rm km\,s^{-1}\,Mpc^{-1}}$ has been adapted.

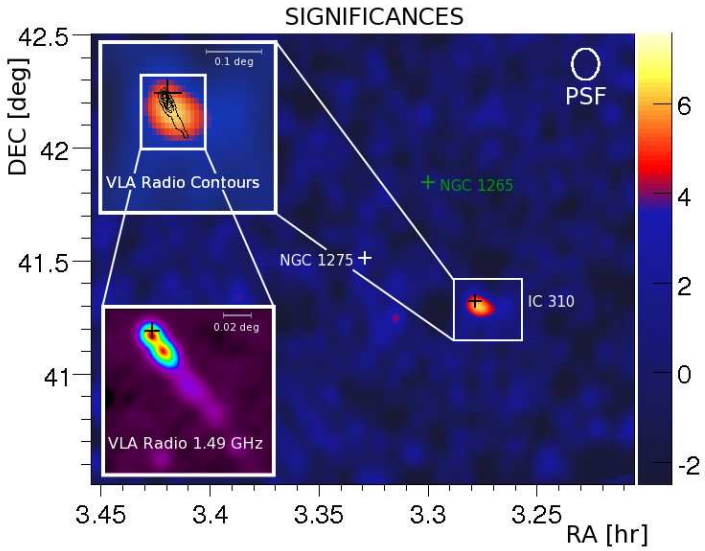

Figure 2.6: Detection of IC 310 with the MAGIC telescopes. The significance map of the Perseus cluster of galaxies above 400 GeV measured by MAGIC in 2009/2010 is shown. The insets show the kpc scale jet measured at 1.4 GHz with the Very Large Array (VLA) as part of the NVSS (NRAO VLA Sky Survey) (Condon & Broderick 1988). Image taken from Aleksić et al. (2010b).

A transitional behavior of IC 310 between a radio galaxy and a blazar has been found in various energy bands, e.g., Rector et al. (1999). Owen et al. (1996) found weak optical emission lines similar to those usually observed in FR I radio galaxies. In the X-ray band, IC 310 shows a blazar-like non-thermal point-like emission (Schwarz et al. 1992; Rhee et al. 1994; Sato et al. 2005). Observations with higher angular resolution by the *Chandra* satellite yielded a faint X-ray halo which points in the same direction as the kpc radio jet (Dunn et al. 2010).

3

Multi-wavelength Instrumentation

... in a Nutshell

Radio-loud AGN emit over the entire regime of the electromagnetic spectrum. Due to their often different variable behavior in various energy ranges, observations with telescopes in all bands are crucial and should be carried out simultaneous or quasi-simultaneous. In this chapter, the different multi-wavelength instrumentation is introduced from which observational data will be presented in this thesis. Further information and details on the performance of the telescopes can be found in the corresponding references.

3.1 Radio observations

Besides the permeable transmission window at optical frequencies there exists a broad window in the radio band, making direct ground-based observation in this regime possible. The continuous improvements of the radio telescopes techniques since its birth in 1933 (Jansky 1933) established the radio astronomy as the domain in which the highest angular resolution can be achieved. One of the currently best resolution provides information of structures of a size of ~ 0.018 pc in the closest AGN Centaurus A achieved by Müller et al. (2011). A comprehensive description on radio astronomy and its various techniques is provided, e.g., by Thompson et al. (2001), Burke & Graham-Smith (2002), and Rohlfs & Wilson (2004).

Radio telescopes can work as single antennas or as combination of several telescopes spread all over the world (or space-based instruments) in an interferometric array, using the so-called Very Long Baseline Interferometry (VLBI) method. The achieved angular resolution θ_{ang} depends on the wavelength λ, as well as the diameter of the telescope dish in case of a single telescope, or the maximal distance between the telescopes in an array both denoted as D. The Rayleigh criterion implies:

$$\sin\theta_{\mathrm{ang}} \approx 1.22\frac{\lambda}{D}. \tag{3.1}$$

By combining the telescopes a resolution of < 1 mas can be obtained.

Figure 3.1: Multi-wavelength instruments. Shown are the space-based instruments *INTEGRAL*, *XMM-Newton*, *Swift*, *Chandra*, *Fermi*, and ground-based telescopes VLBA, OVRO, EVN, KVA, Magic, Effelsberg 100 m. Image credits: NASA `http://heasarc.gsfc.nasa.gov`, ESA `http://www.esa.int`, NASA `http://swift.gsfc.nasa.gov/`, Chandra X-ray Observatory, NASA `http://fermi.gsfc.nasa.gov`, NRAO `http://www.cv.nrao.edu`, `http://www.astro.caltech.edu/`, EVN, Operations manual for the KVA-telescope (L.O. Takalo and E. Lindfors), Max Planck Institute for Physics/R. Wagner, MPIfR (N. Junkes)

Even if the performance of single-dish telescope in terms of angular resolution is less adequate, long-term monitoring data and spectral properties at larger scales in this regime can be provided for astronomical objects, e.g., AGN and therefore, provided crucial scientific information. Detailed structural studies of these objects can be performed with the VLBI arrays.

3.1.1 Single-Dish

Effelsberg 100-m

The Effelsberg telescope[1], located next to Bad Münstereifel in the Eifel in Germany, is operated by the Max Planck Institute for Radio Astronomy in Bonn. With its 100 m in diameter, it is one of the largest single-dish radio telescopes in the world. With several receivers of different wavelength, the Effelsberg telescope can provide spectral measurements in the range from 0.3 to 86 GHz on a monitoring basis, e.g., in the framework of the F-GAMMA program (Fuhrmann et al. 2014). Basic information on the telescope system can be found in Beuchert (2013).

OVRO

The Owens Valley Radio Observatory (OVRO, near Bishop, California, USA) 40 m telescope provides radio data since 2008 for a list of AGN at 15 GHz nearly twice per week[2]. The targets were selected from the Candidate Gamma Ray Blazar Survey, CGRaBs (Healey et al. 2008), as well as from the *Fermi*-LAT AGN catalogs (Abdo et al. 2010a; Ackermann et al. 2011) with the restriction to the declination of $> -20°$. Details on the observing strategy and the calibration procedures are summarized in Richards et al. (2011).

3.1.2 Very Long Baseline Interferometric arrays

VLBA/MOJAVE

The Very Long Baseline Array[3] (VLBA) of the National Radio Astronomy Observatory (NRAO) is an array of 10 identical 25 m (in diameter) antennas with a baseline up to 8000 km. It is controlled by the Science Operations Center in Socorra, New Mexico where the correlation of the data from the individual telescopes is performed. VLBI observations at eight frequency bands between 1.2 GHz to 96 GHz as well as two narrow sub-GHz ranges are accessible with this array.

The "Monitoring Of Jets in Active galactic nuclei with VLBA Experiment" (MOJAVE) project is a long-term VLBI monitoring program at 15 GHz conducted with the VLBA[4]. All known northern hemisphere AGNs with a galactic latitude of $> 2.5°$, a declination of $> -30°$ (now $> -20°$) have been included in the program. The first target list has been restricted to a total flux density of at least 1.5 Jy during the epochs 1994 to 2010 at the observation frequency (Lister & Homan 2005). Later, all objects from the *Fermi*-LAT catalog (Nolan et al. 2012) with a gamma-ray spectral index of harder than 2.1, and with a flux limitation at 15 GHz of > 100 mJy were selected, see, e.g., Arshakian et al. (2012). Extra 20 AGN from the first

[1] http://www.mpifr-bonn.mpg.de/effelsberg
[2] http://www.astro.caltech.edu/ovroblazars/
[3] https://science.nrao.edu/facilities/vlba
[4] http://www.physics.purdue.edu/MOJAVE/

list were added due to large, significant changes in the jet speed or its direction. Furthermore, gravitational lensed objects were excluded in both samples.

Due to the detection in the gamma-ray range with *Fermi*-LAT and MAGIC, and the modified radio flux limit, IC 310 has been included in the monitoring target list of MOJAVE.

The TANAMI project[5] presents a complementary AGN VLBI program on the southern hemisphere.

EVN

The European VLBI Network (EVN) is a consortium of several radio-astronomical institutes and telescopes from Europe, Asia, and South Africa[6]. Currently, the network consist of 21 individual telescopes which are combined to an array three times per year for 3-4 weeks operating at different frequencies. Due to the large collection area of its telescopes the EVN provides one of the best sensitivities so far. The number of antennas used and therefore its final resolution during a specific observation, depends, however, on the availability of the telescopes and on the existing receiver frequency. Typically, an observation is carried out by $\sim$10 telescopes.

3.2 Optical telescopes

In the optical regime ground-based as well as space-based telescopes are possible, depending on the frequency window.

KVA

The Kungliga Vetenskaps Akademien (KVA) telescopes are located at the Observatorio del Roque de los Muchachos on the island of La Palma, Spain, and are being led by the Tuorla observatory[7]. They consist of two optical telescopes of different size, one with a mirror diameter of 60 cm and one with 35 cm. Filters in the R-band (640 nm), B-band (550 nm), and V-band (440 nm) are available.

Observations mentioned in this thesis were conducted with the latter in the R-band (640 nm) in photometry mode in close collaboration with the MAGIC telescopes (Takalo et al. 2008).

Swift-UVOT

The UltraViolet/Optical Telescope (UVOT) on board the *Swift* satellite performs measurements in the ultraviolet (UV) range (Gehrels et al. 2004; Krauß 2013). Therefore, the telescope is equipped with the filters: V (547 nm), B (439 nm), U (347 nm), UVW1 (260 nm), UVM2 (225 nm), and UVW2 (193 nm).

[5] http://pulsar.sternwarte.uni-erlangen.de/tanami/
[6] http://www.evlbi.org/
[7] http://www.astro.utu.fi/

3.3 X-ray regime

In the X-ray range, the atmosphere is opaque. Thus, satellite-based observations are necessary.

Chandra

The *Chandra* X-ray Observatory was launched in summer 1999 and is equipped with the High Resolution Camera (HRC), the Advanced CCD Imaging Spectrometer (ACIS, 0.2 keV-10.0 keV), and further high-resolution spectrometers, see Garmire et al. (2003); Weisskopf et al. (2002).

XMM-Newton

In 1999, the X-ray Multi-Mirror Mission (XMM-Newton) started its operation in the energy range of 0.3–10.0 keV (Jansen et al. 2001). The European Photon Imaging Camera-PN (EPIC-PN), and the two EPIC-MOS and the Reflection Grating Spectrometers (RGS) are the main instruments on-board the satellite. Additionally, the optical monitor (OM) allows for observation at optical wavelengths.

Swift-XRT/BAT

The *Swift* satellite has been launched in late 2004. Besides UVOT, it harbors several other telescopes covering the soft as well as the hard X-ray range. Continuous observations in the hard X-ray range (15-150 keV), mainly for detecting gamma-ray bursts, are provided by the Burst Alert Telescope (BAT). The X-Ray Telescope (XRT) operates in the soft X-ray regime from 0.2 to 10.0 keV (Burrows et al. 2005; Krauß 2013). Together with the UVOT instrument, it provides pointed follow-up observations of the gamma-ray bursts. Observations of other objects can be organized, e.g., via Target of Opportunity (ToO) proposals besides normal proposals.

INTEGRAL

The International Gamma-Ray Astrophysics Laboratory (*INTEGRAL*) satellite operates since late 2002 (Winkler et al. 2003; Grinberg 2013). It is equipped with several instruments in the hard X-ray to soft gamma-ray range: the high resolution spectrometer SPI (20 keV-8 MeV, Vedrenne et al. (2003)), and two high angular resolution gamma-ray imagers, called IBIS (15-1000 keV, 0.175-10.0 MeV, Ubertini et al. (2003)). In addition, the JEM-X monitor (Lund et al. 2003), and the Optical Monitoring Camera (OMC) (Mas-Hesse et al. 2003) provide spectral and imaging observation in the optical and X-ray regime.

3.4 Gamma-ray energies

The gamma-ray range relevant for this thesis is divided into the High Energy (HE, $\sim 0.1 - 100$ GeV), and the Very High Energy (VHE, $\sim 0.1 - 100$ TeV) range. The former is accessible by space-based instruments by direct measurements and the latter via ground-based telescopes using an indirect detection method described in Chapter 4.

3.4.1 Fermi-LAT

Fermi has been launched in June 2008 and since August 5, 2008 it has operated primarily in the sky survey mode, scanning the entire sky every three hours (Atwood et al. 2009; Krauß 2013). The *Fermi*-Large Area Telescope (LAT) is a pair-conversion telescope mostly sensitive to photons between 20 MeV and several hundred GeV (Ackermann et al. 2012). Furthermore, the Gamma-ray Burst Monitor (GBM) exists on-board, designed for observations of transient objects such as gamma-ray burst.

For this thesis, two catalogs have been used: the “Fermi Large Area Telescope Second Source Catalog”, designated 2FGL (Nolan et al. 2012), and the “The First Fermi-LAT Catalog of Sources Above 10 GeV”, 1FHL (Ackermann et al. 2013). The former covers the first two years of observation (August 4, 2008 - August 1, 2010) at an energy range above 100 MeV. The latter is dedicated to a higher energy range above 10 GeV and covers the first three years.

3.4.2 MAGIC telescopes

The MAGIC telescopes are two telescopes based on the Imaging Air Cherenkov Technique assigned to measure gamma-rays in the energy range from 50 GeV up to 50 TeV (Aleksić et al. 2012b). It is located at the Observatorio del Roque del los Muchachos on the Canary island of La Palma. Further information of the working principle of an Imaging Air Cherenkov telescope as well as on MAGIC can be found in Chapter 4.

4

Gamma-Ray Astronomy at Very High Energies

A Brief History of MAGIC

4.1 Introduction to Gamma-Ray Astronomy

Ground-based instruments used in astronomy are naturally restricted by the transparency of the atmosphere. Apart from windows in the optical as well as in the radio band, the atmosphere is opaque to radiation in the other parts of the electromagnetic spectrum. Hence until the mid of the 20th century, only these band were accessible to astronomers. With the development of the first rockets and balloons, the situation changed gradually, making, e.g., the X-ray and other frequency bands available.

The study of the highest energy radiation became important already in 1912 with the discovery of the cosmic rays by Victor Hess. He measured an increasing ionization of the atmosphere with increasing height (Hess 1912). This "radiation" remarkably follows an almost stable power-law distribution with an index of ~ 2.7 over about 10 decades in energy. Pronounced features in the spectrum like the "knee" at 3×10^{15} eV and the "ankle" at 3×10^{18} eV allow to draw conclusions on the origin of these ionized particles. However, the measurement of the "sources" is difficult. Apart from the cosmic rays at the highest energies, the information of the arrival direction gets lost on the way to the Earth due to turbulent magnetic fields, e.g., in the interstellar medium. Since gamma rays, which are rather unaffected by those, are produced during various radiation processes of cosmic rays, one can use the gamma-ray astronomy to identify the sources.

The direct measurement of gamma rays in the high energy (HE) range at 20 MeV–100 GeV is covered by space-based instruments like the *Fermi*-LAT. At higher energies in the very high energy (VHE) band between 50 GeV and 50 TeV, the atmosphere can be used as a part of the detector. The underlying physical processes and the so-called Imaging Air Cherenkov technique (IACT) will be introduced below, following the description by Weekes (2003).

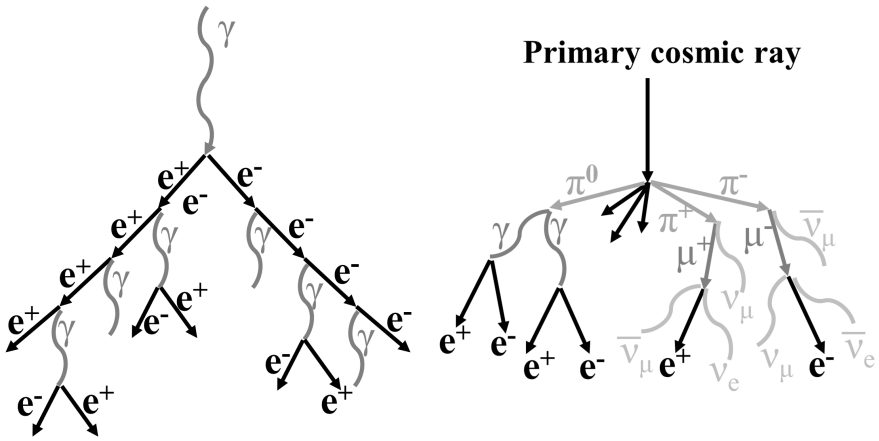

Figure 4.1: Schematic development of air showers. *Left panel:* Electromagnetic cascade introduced by a gamma ray. *Right panel:* Hadronic cascade induced by a cosmic ray, e.g, a proton. Image adapted from Weekes (2003).

4.2 Observational Techniques at TeV Photon Energies

4.2.1 Extensive Air Showers

The absorption of gamma-ray photons in the atmosphere is composed of different processes, e.g., Compton scattering, the photoelectric effect, and pair production. Which of those processes dominates the absorption, depends on the energy of the incoming photon. If a gamma ray with more than 10 MeV enters the atmosphere the production of an electron-positron pair dominates (see Fig. 4.1 left and Section 2.4). The first interaction takes place at an altitude of about 20 km above sea level. For energies >10 GeV, primary gamma rays split into one electron and one positron. Those then travel in approximately the same direction as the primary. Generally, after the pair has roughly traveled a length equal to the radiation length X_0 (more accurate 7/9 X_0 with a radiation length in air of $X_0 = 37.2\,\mathrm{g\,cm^{-2}}$), secondary gamma rays are produced by Bremsstrahlung due to an interaction with molecules in the air. The secondaries again may produce $\mathrm{e^+e^-}$ pairs after moving another radiation length towards the ground. The resulting electromagnetic cascade continues until the average energy reaches the value at which ionization losses of the e^+e^- pairs and the losses due to Bremsstrahlung are equal. At this height ($\sim$10 km, depending on the initial gamma-ray energy), the maximum of the produced electrons is reached, indicating also the maximum of the shower. The secondary electrons in those showers, if energetic enough, i.e. above the threshold for Cherenkov radiation (see below), can activate the atmosphere for emission of Cherenkov photons in a cone of with a small opening angle.

Besides showers introduced by gamma rays, showers induced by hadrons (e.g., protons) exist (see Fig. 4.1 right). Those showers form the dominating background and hence are the limiting factor for ground-based gamma-ray astronomy. They can be considered as a combined collection of electromagnetic showers and pion decays. The neutral pions can produce gamma rays which may release additional electromagnetic showers. The charged pions on the other hand decay into muons under the production of neutrinos. The muons may decay into neutrinos, electrons and positrons. The exact shape of the shower depends on the nature of the primary particle. For more details on the modeling of hadronic showers, see Sokolsky (1989).

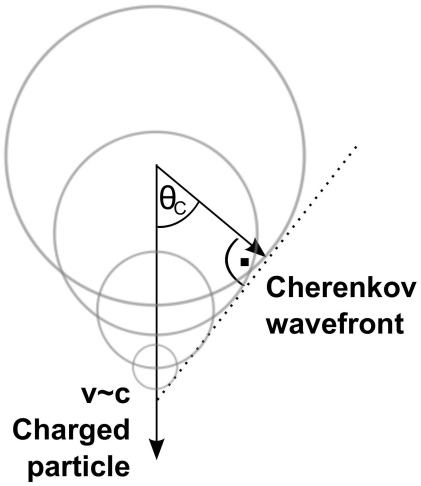

Figure 4.2: Illustration of the Cherenkov angle θ_{C}. Image adapted from Weekes (2003).

The different properties of the showers (lateral elongation, maximal height etc.) can later be used for the background suppression by separating the gamma and hadron introduced showers. Generally, the latter are broader and more scattered.

4.2.2 The Cherenkov Effect and its Radiation Properties

If a charged particle as produced in an electromagnetic shower exceeds a certain threshold speed, the so-called Cherenkov radiation can be observed. This happens when the velocity v of the particle is larger than the speed of light c_n in a dielectric medium (here: atmosphere) with refraction index n. The so-called Cherenkov angle θ_{C} at which the radiation will be emitted can be calculated from:

$$\cos\theta_{\mathrm{C}} = \frac{1}{n\beta}, \tag{4.1}$$

where $\beta = v/c$ (see Fig. 4.2). The radiation is then emitted at a certain angle as individual wavefronts will interfere constructively.

Figure 4.3 shows how charged particles interact with molecules in a dielectric medium by inducing polarization depending on their velocity. This releases the molecules to radiate in the case of $v > c_n$. Then, the disturbance is asymmetric which causes a net electric field (Fig. 4.3, right). This field is not created if the disturbance is symmetric as in Fig. 4.3 on the left, where $v < c_n$.

A maximal Cherenkov angle is reached when v approaches c_n, and the energy of the particle is at least $m_e c^2/\sqrt{1-n^{-2}}$, with m_e the rest mass of an electron. This forms a cone with a typical opening angle of $\sim 1^\circ$ in the atmosphere. At a height of $\sim 2000\,\mathrm{m}$ above sea level, this "light pool" will have a radius of $\sim 120\,\mathrm{m}$ (see also Fig. 4.4).

Since the lifetime of the Cherenkov light from an electromagnetic shower is very short ($\sim 3-5\,\mathrm{ns}$) fast sampling electronics are necessary for detection and for limiting the contamination by the night sky background. The photon density on the ground which depends roughly linearly on the energy of the progenitor photon is marginally affected by scattering processes (e.g., Rayleigh or Mie scattering) and amounts to $\sim 100\,\mathrm{ph\,m^{-2}}$ in the light pool for a 1 TeV photon. The spectrum of the Cherenkov light covers the UV to optical range, hence it is mostly located

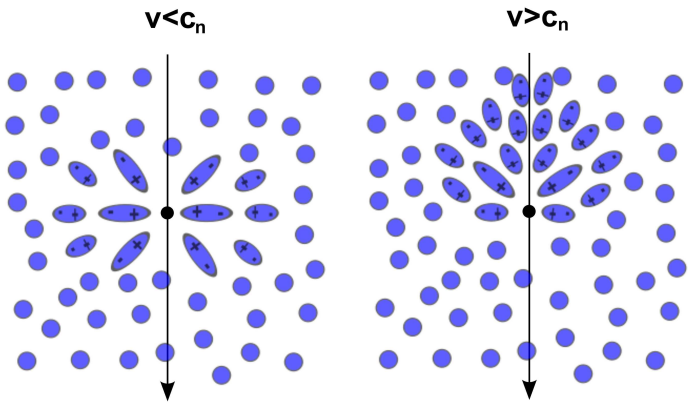

Figure 4.3: Influence of a charged particle in a dielectric medium such as an atmosphere. *Left panel:* Particle with velocity $v < c_n$. The disturbance is symmetric. No net electric field is created. *Right panel:* Illustration for $v > c_n$. The disturbance is asymmetric which causes a net electric field. Image adapted from Weekes (2003).

in the visible area of the electromagnetic spectrum. However, due to the faintness, sensitive detectors are needed for its observation.

4.2.3 Imaging Air Cherenkov Technique

The imaging air Cherenkov technique uses the production of Cherenkov light in extensive air showers, thus the atmosphere is an essential component of this technique. An Imaging Air Cherenkov Telescope (IACT) consists of a light collector and the detector, i.e., the camera which is connected to a fast readout system, see Fig. 4.4. For the energy calibration of the entire instrument, Monte Carlo simulations of the atmospheric showers and their effect on the telescope are important because man made or natural sources of this energy are missing.

Maximizing the incoming Cherenkov light and hence lowering the energy threshold can be facilitated by large mirrors. One possibility for a cheap enlargement of the reflection area is to use a parabolic tessellated array of mirrors in a structure with the same radius of curvature as the focal length, known as Davis-Cotton design (Davies & Cotton 1957). As such large mirror structures are usually made out of glass, no protection dome or cover is used for financial reasons. This, however, may cause degradation of the mirror reflectivity. Possible counteractions are, e.g., applying anodized aluminum surfaces or regular cleaning. Additionally, the large Cherenkov light pool of $\sim 120\,\mathrm{m}$ allows a huge shower collection area of $\sim 5 \times 10^4\,\mathrm{m}^2$ and a good photon statistic. This makes the technique superior compared to instruments in other frequency bands as the collection area is limited by the dimensions of the telescope. This fact is important for observations of fast variability of AGNs.

The cameras used in IACTs must be sensitive to detect the faint Cherenkov light and sensitive to its wavelengths. This can be achieved, e.g., by photomultipliers (PMTs) used by the MAGIC telescopes, or Geiger-mode avalanche photodiodes (G-APDs) introduced by the FACT project (Anderhub et al. 2013).

Turbulence in the atmosphere, changes in temperature, pressure, humidity, and clouds can distort the measurements, limiting the angular resolution and the reliability of the data. Hence, monitoring the atmospheric parameters during data acquisition is necessary. In addition, background light of either natural (moon, stars, ...) or artificial origin (cities, cars, ...) can influence

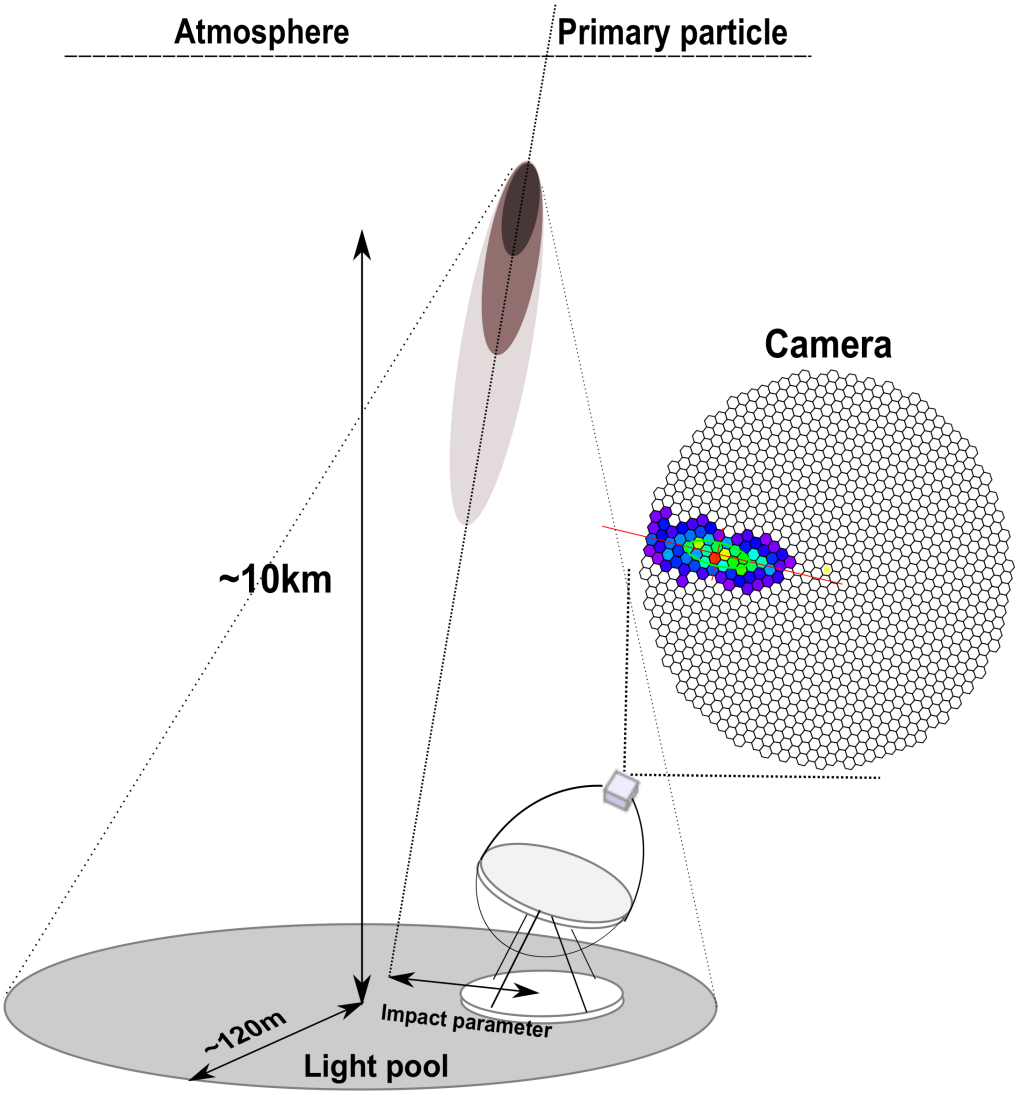

Figure 4.4: Principle of the IACT technique. An incoming gamma photon causes the development of an electromagnetic air shower with a shower maximum at about 10 km and the production of faint Cherenkov light flashes. This Cherenkov light develops into a cone with a radius of $\sim$ 120 m at an altitude of $\sim$ 2000 m above sea level. Those photons will be reflected by a mirror onto a camera. In the camera plane, the "image" of a gamma induced shower appears as an ellipse. Different colors indicate different signal amplitudes in the pixels of the camera.

Table 4.1: Imaging Air Cherenkov Telescopes.

IACT	Nr. of telescopes	FoV[a] [°]	Energy range [TeV]	Reference
FACT	1	5	>0.4	Anderhub et al. (2013)
H.E.S.S.	4(+1)[b]	5	0.1-100	Aharonian et al. (2006)
MAGIC	2	3.5	0.05-50[c]	Aleksić et al. (2012b)
VERITAS	4	3.5	0.1-30	Holder et al. (2011)

Notes. [(a)] Field-of-view. [(b)] Recently, a fifth telescope with a mirror diameter of 28 m has been commissioned, allowing for measurement down to < 50 GeV. [(c)] This is the energy range that is accessible with the current standard trigger chain. Using the newly developed Sum-Trigger, the threshold will be significantly lower at around 0.03 GeV.

the data and detection efficiency. The optimal site for an IACT is therefore a dark site far away from man-made lights. Fortunately, the minimum of the night sky background (NSB) is located close to the optimal Cherenkov band at 300-450 nm. This is also the sensitive region of the PMTs whereas G-APDs are also sensitive at longer wavelengths.

Even under the best observational conditions (dark night, no moon, no clouds, etc.) the hadronic showers which produce Cherenkov light as well influence the sensitivity of the observation of the gamma rays. This background is a factor of $\sim$1000 times larger and hence must be discriminated. The properties of the different kinds of showers are reflected in the images in the camera plane. Therefore, the discrimination can be made based on the geometry and the temporal properties of showers. Images from gamma-ray showers comprise single elliptical shapes in the camera plane. The orientation of those ellipses reflects the position of the discrete source. Hadronic showers, however, form more irregular, randomly orientated images with several islands.

Particular shower images from the background mainly below 100 GeV form rings in the camera plane. Those are generated by muons. Their time duration of the Cherenkov pulse is different, and they are produced close to the ground. To control the background from the muons, usually arrays of at least two IACTs are used because such muons may only trigger one telescope. Stereoscopic observations with a telescope array significantly improve the performance of the observation. Furthermore, a stereoscopic system allows for a three-dimensional reconstruction of showers. Some muons produce very compact images in the camera plane, similar to those produced by gamma-ray photons. These muons can be filtered out due to a different maximal height of the showers. The advantages are a larger effective area, a better flux sensitivity since a better background suppression is possible, a reduced energy threshold due to the muon separation, and an improved energy and angular resolution.

A collection of currently operating IACTs and their characteristics is given in Table 4.1. The MAGIC telescopes will be described in greater detail in the next section.

4.3 The MAGIC Telescopes

The MAGIC telescope system is an array of two 17 m diameter IACTs situated on the Canary Island of La Palma at an altitude of 2200 m above sea level, at the Observatorio del Roque de los Muchachos ($28°$N, $18°$W). MAGIC-I and MAGIC-II are located 80 m apart from each other. The construction of MAGIC-I was completed in 2004 and five years later MAGIC-II was commissioned. Since then, they mainly have been operated in stereoscopic mode in an energy range from 50 GeV to 50 TeV (Aleksić et al. 2012b).

Due to a parabolic shape of the mirrors, the information of the arrival time of the showers is conserved, hence making it possible to use this information in the data analysis. Additional advantages of MAGIC in comparison to other IACTs are the fast drive system (Bretz et al. 2009) and the light structure out of carbon fiber epoxy tubes (Biland et al. 2008), enabling the observation of transient objects like gamma-ray bursts (Albert et al. 2007b).

The system underwent a major upgrade in 2011/2012. This included the replacement of the already matured MAGIC-I camera as well as the exchange of the readout electronics, and the digital trigger in both telescopes (Mazin et al. 2013; Aleksic et al. 2014a).

Until 2012, the MAGIC-I camera consisted of 577 PhotoMultiplier Tubes (PMTs) each with a quantum efficiency[1] of $\sim$30% (Paneque et al. 2004). 397 pixels were located in the inner part of the camera, with a diameter of 1 inch each. The remaining 180 pixels formed the outer part, with a diameter of 2 inch each. The total trigger area was $\sim 1.0°$. With the upgrade, MAGIC-I received a new camera similar to the one used in MAGIC-II. The number of pixels was increased to 1039, with a diameter of 1 inch each (Aleksic et al. 2014a). Therefore, also the number of the readout channels had to be increased. The resulting trigger area in both telescopes is $1.2°$. The telescopes have a field of view of $3.5°$.

Signals registered in the PMTs are converted into optical pulses by vertical-cavity surface-emitting lasers (VCSELs) and then passed to the counting house by optical fibers for digitization. There, the receiver boards convert the optical pulses into electric ones via photodiodes, the signal is split into the branch of the readout and the trigger, and a first-order trigger condition is applied. This trigger is the so-called Level-0 trigger and is based on the amplitude of the signal in a trigger channel ("discriminator threshold"). The receiver boards in MAGIC-I were changed to be equal to the one used in MAGIC-II.

Before the upgrade, the readout system in MAGIC-I consisted of multiplexed FADCs, MUX-FADCs (Flash Analog to Digital Converters). The readout in MAGIC-II was based on the Domino Ring Sampler 2 (DRS2) chip. The MUX-FADCs were robust and allowed a great performance, but their costs were high and the system was very bulky. In contrast, DRS2 chips were cheap but showed a large dead time, non-linearities, and high intrinsic noise. Hence, both readout systems were replaced by a new generation of the Domino Ring Samplers chip, the DRS4. These chips allow the same sampling frequency of 2 Gsamples/s. Furthermore, they are cheaper and show better performance in terms of dead time, linear behavior, and cross talk between channels.

With the upgrade of the MAGIC-I camera, a trigger system of larger area in MAGIC-I was installed. Such a system is responsible for a fast (< 5 ns) discrimination of Cherenkov showers from the NSB. They involve several neighboring pixels in a short time interval surviving the Level-0 trigger criteria. Therefore, the Level-1 trigger is based on the X-next neighbor (XNN) topology. In case of mono/stereo observations, a 4NN/3NN configuration is used in each tele-

[1] The quantum efficiency reflects the percentage of detected photons in a device.

scope, respectively. The Level-3 trigger, also called stereo trigger, finally rejects those events which were only triggered by one telescope in a certain coincidence window. Furthermore, a specific trigger chain of MAGIC, the so-called Sum-Trigger, allows for observations down to energies of ~ 30 GeV (Garcia et al. 2013).

4.4 Observation Procedure and Quality

The data obtained from an IACT are strongly dominated by background. Typically, only one out of one thousand shower events is generated by a gamma photon. Measuring events is influenced by many aspects, e.g., the ambient light (zodiacal light, moon, or stars) or the weather, as well as the telescope performance (e.g., noise of electronics).

4.4.1 Data Acquisition

During each observation, different kinds of data acquisition are performed. This includes pedestal, pedestal subtraction, calibration, and the actual data runs. The first measures the amount of the ambient light, i.e., the NSB in the field-of-view (FoV) during observation, as well as the noise of the detector and electronics. Additionally, since the upgrade of the telescopes with a new readout system, the base line of the readout chips needs to be calibrated with a pedestal subtraction run, usually done once per night. The calibration run, performed with the artificial light pulses from the calibration box in each telescope, is responsible for the calibration of the detector and the electronics. The data runs (typically with a duration of ~ 20 min) are divided into sub runs of ~ 1 min. In addition to the pedestal and calibration run before each data run of an observation of an object, interleaved pedestal and calibration events are recorded at a rate of 25 Hz each during the data acquisition, to account for changes of the detector/electronics on a short time scale.

4.4.2 Observation Modes

The standard observation mode of the MAGIC telescopes is the so-called wobble mode (Fomin et al. 1994). The advantage of this mode is the simultaneous observation of the object (ON) and the background (OFF). During data acquisition, the telescopes do not point directly to the celestial coordinates of the object that should be observed but track positions which are usually 0.4° away from it. There are typically two or four wobble positions centered around the object of interest. These positions are sometimes chosen in order not to have bright stars in the FoV that might influence the trigger rate. Usually every 20 min, the wobble position is changed to eliminate possible inhomogeneities of the cameras. This also allows for an uniform observation of events from the ON and OFF regions in terms of the background (NSB and weather condition) and the zenith distance.

For the results presented in this thesis, different wobble observations have been performed in which sometimes the object of interest, IC 310, appeared in the FoV of a different observation target. Hence, the wobble offsets varied in different observation cycles from 0.25° and 1.0° to 0.4° and 0.938°. The individual wobble positions are shown in the respective chapters.

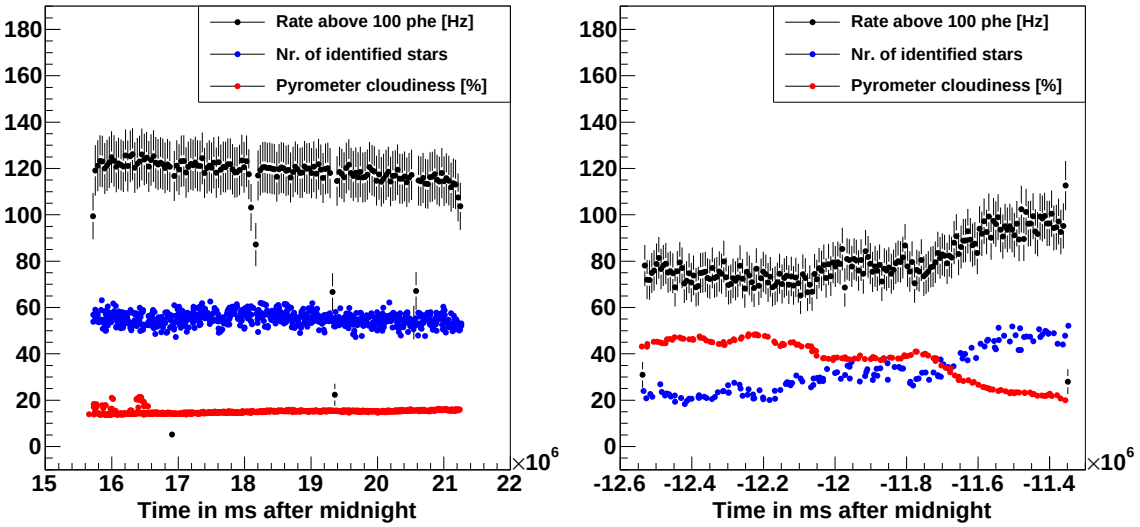

Figure 4.5: Quality check of data. Rate trend (black) during two observations together with the number of identified stars (blue) measured by the starguider, and the cloudiness (red) measured by the pyrometer. *Left panel:* Observation of the Perseus cluster on October 09, 2013 (Zd: 18°-35°). The drops of the rate are artifacts of the script caused by the start and stop of the data acquisition at different wobble positions. *Right panel:* Observation of the Perseus cluster on December 08, 2013 (Zd: 13°-19°).

4.4.3 Quality of the Data

To verify the reliability of the data and their results, the observational conditions (e.g., the weather) and the hardware functionality need to be checked. In the following, some aspects and their influence on the quality of the data will be addressed.

Several auxiliary instruments for monitoring the atmosphere were installed at the MAGIC site. Non-optimal weather conditions, result, e.g., in biases in the energy and flux reconstruction of the gamma-ray emission. The MAGIC weather station is located on the roof of the counting house and continuously measures typical atmospheric variables, e.g, temperature, wind speed and direction, humidity, and pressure. The dish of MAGIC-I is further equipped with a pyrometer measuring the “cloudiness” of the sky (Fuchs 2008). This parameter is calculated by measuring temperatures and the humidity and taking into account the zenith distance. Further weather stations are placed close to the other telescopes located on the Roque de los Muchachos.

For visual inspection of the sky during data acquisition, a web camera and an AllSky camera were mounted on-site. The latter takes long-exposure pictures of the sky every two minutes so that clouds passing the sky can be identified. Such information in addition to technical problems can be written down by the shifters in the electronic runbook.

Additionally, from the starguider which works as an online monitor for the tracking system information on clouds or the sky brightness can be extracted, e.g., from the number of stars that have been identified by comparison with a star catalog. The prior function of the starguider, however, is to monitor the pointing of the telescopes. A mispointing can distort the final physical result.

During the observation, a so-called LIDAR, LIght Detection And Ranging, is operating every five minutes. This device consists of a laser mounted on a robotic, optical telescope, and a Hybrid Photo Detector (HPD) as detector. It records the time profiles of back-scattered photons. Hence, it provides the transparency (ratio between cloud/aerosol scattering and molecular scat-

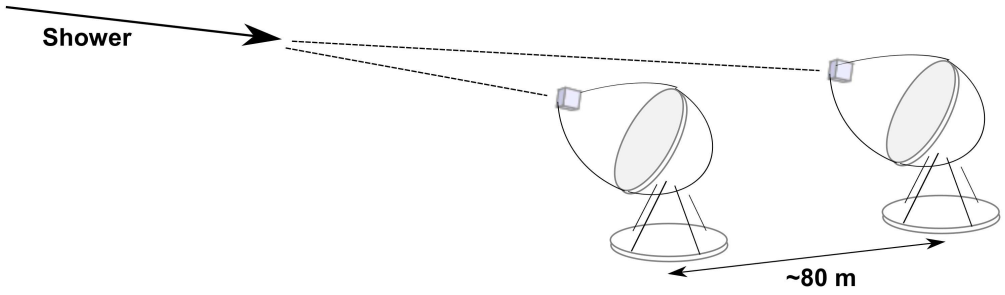

Figure 4.6: Sketch of the dead zone problem. In some cases depending on the zenith and azimuth, the telescopes point almost parallel into on direction. Then, a shower triggers one telescope. The second telescope must receive the trigger within a certain time range, otherwise the event is lost due to the stereo coincidence condition.

tering which is close to unity in a typical case). This information can be used to correct for an energy bias and the effective area due to atmospheric extinction as shown in Fruck et al. (2014).

An example of a correlation of weather indicators on the trigger rate for an observation affected by good and bad weather is shown in Fig. 4.5. The observation shown in the left panel reflects a stable weather condition with a low cloudiness, a high number of identified stars and a high rate. The right panel shows an unstable weather condition possibly due to clouds, as the number of identified stars as well as the cloudiness is changing in time. This effect is also visible in the variable, lowered rate distribution. A low trigger rate might also be due to an observation at high zenith distances or result from ambient light (moon, twilight) that increases the trigger threshold.

In addition to measures to cope with weather conditions, a good hardware functionality during the observation must be ensured. Especially before the upgrade, the MAGIC-I camera suffered from many dead and unreliable pixels. Those have to be treated in the analysis by interpolating the signal from neighboring pixels. A clustering of those pixels may bias the result as showers might be wrongly reconstructed. Furthermore, some part of the readout electronics may fail which could produce holes in the camera, e.g., affecting its homogeneity. This could result in a wrong flux estimation, as the treatment of the background could be biased.

In stereoscopic mode, the observation of objects in a certain zenith and azimuth region in the sky is limited by the so-called “dead zone” due to limitations of the trigger hardware. A sketch of such a situation is illustrated in Fig. 4.6. If the telescopes are pointing in almost parallel direction, one Cherenkov event may trigger the first telescope but may not be stored in the readout of the second telescope. This is on the one hand due to to physical separation of the two telescopes ($\sim 80\,\mathrm{m}$), and on the other hand due to a limited size of the readout buffer. Since the trigger system in stereoscopic mode is based on coincidence, those events are not recorded at the end, affecting the physical result of the observation. Data affected by this problem need to be rejected in the analysis.

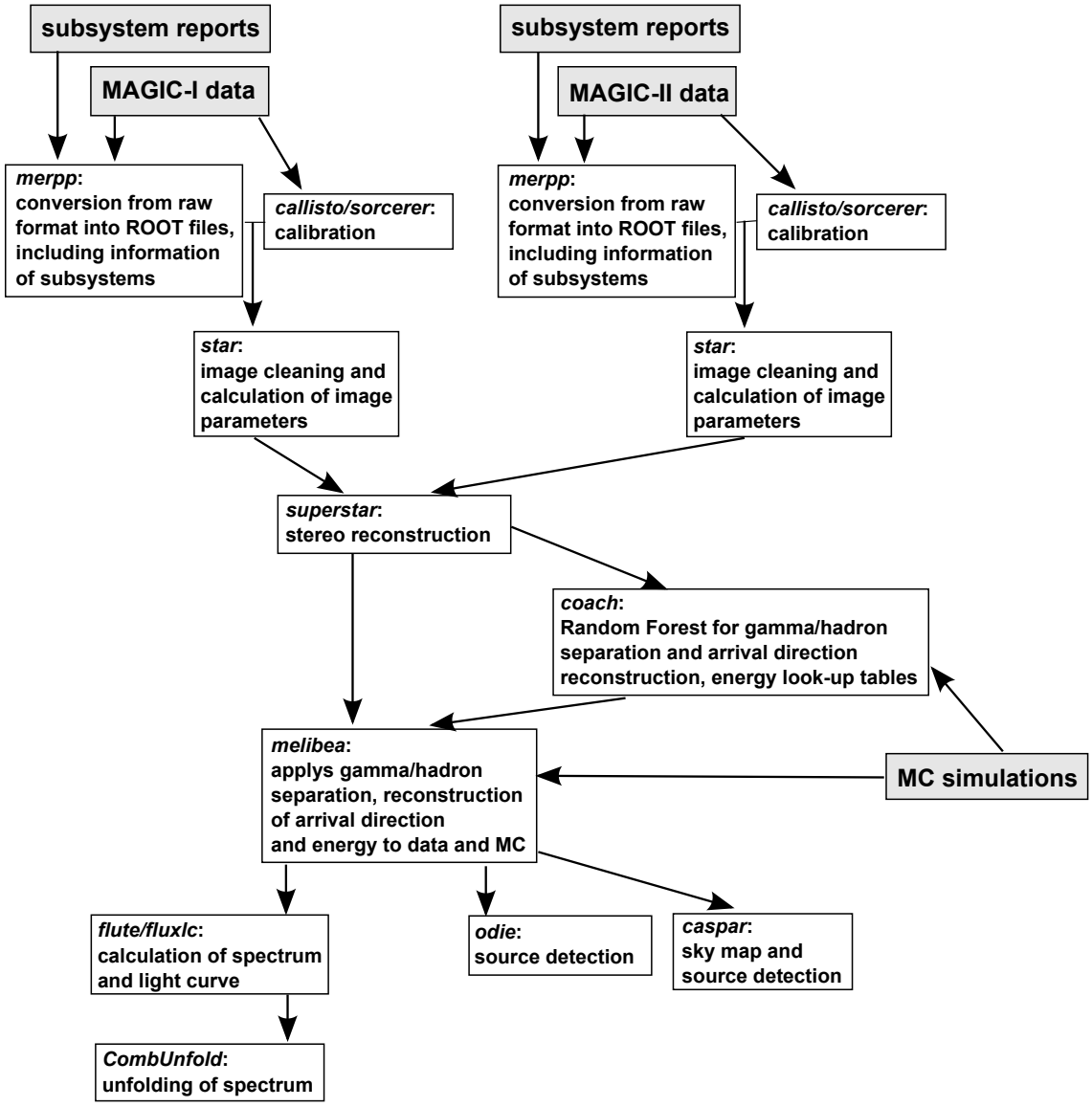

Figure 4.7: Analysis chain of the MARS software. Details can be found in the corresponding sections.

4.5 Analysis and Reconstruction Software

The MAGIC Analysis and Reconstruction Software (MARS) provides tools based on the software framework ROOT[2] for the analysis of MAGIC data (Zanin et al. 2013). It is assigned to select the gamma from the hadron-initiated showers, to reconstruct the arrival direction, and the energy. This information is needed for the signal detection, the calculation of the energy spectra of the gamma-ray emission, and to produce light curves.

In the following, the individual steps in the analysis chain are described based on an example analysis of $\sim$ 7h data taken in standard wobble mode in October 2013 to December 2014 from the Crab Nebula at a zenith distance (Zd) range of 6° to 41°. The Crab Nebula is the brightest steady source of VHE gamma-ray emission in the Northern sky and therefore, is referred as "standard candle" for VHE gamma-ray astronomy. Although it should be noted that frequent

[2] `http://root.cern.ch/drupal/`

activity in the gamma-ray regime (albeit at lower energies) has been observed by *Fermi*-LAT and *AGILE* (Tavani et al. 2011; Abdo et al. 2011). In the VHE range no significant enhancement during such a period could be measured yet (Aliu et al. 2014).

4.5.1 Calibration

At the very first stage of the analysis, the raw data are converted into a ROOT readable format and combined with the information from the different subsystems (e.g., weather station, readout, camera, etc.) by the program *merpp* or *sorcerer*. Then, the calibration of the raw data is done with the program *sorcerer* in order to extract the information of the charge measured in photoelectrons (phe) from individual pixels in the camera and the arrival time of the signal. For older data, e.g. MAGIC-I data from the MUX-FADC based readout, the program *callisto* was used. The exact methods and algorithms for the calibration depend on the particular camera-readout configuration, see Albert et al. (2008a) for MAGIC-I and Aleksić et al. (2012b) for MAGIC-II data (before the upgrade 2011/2012). The basics are given here for the currently working system as most of the data presented in this thesis were taken under this configuration.

In the raw format, a single event in each pixel consists of a waveform, i.e., a signal in a number of time samples with a sampling frequency of 2 Gsamples/s and a time span of 30 ns. From each pixel and each event, the charge and the arrival time are extracted. The extraction of the signal is based on the algorithm described in Albert et al. (2008a). Currently, a maximal integral of six time slices (3 ns) are searched in a readout window of 30 ns. Before the upgrade, the MAGIC-II data had to be linearized first (Tescaro et al. 2009). The conversion into phe is then based on the so-called "F-Factor" method (Mirzoyan & Lorenz 1997). For example, ~ 100 readout counts corresponds to 1 phe on average. The DRS4 used now needs some additional steps to eliminate inhomogeneities of the domino ring as explained in Sitarek et al. (2013b). Furthermore, at this stage a correction for malfunctioning pixels or pixels illuminated by bright stars is applied by interpolation from neighboring pixels.

4.5.2 Image Cleaning and Parameter Calculation

The next step in the analysis is carried out with the program *star*. It provides a "cleaning" of the image of the air shower (event). Examples of such a cleaning process on different events (gamma, hadron, muon) are shown in Fig. 4.8. A shower is registered by all pixels in the camera as shown in the left panel of the figure. Most of the pixels colored in blue and violet measure a signal introduced from the NSB and the noise from the electronics rather than from the Cherenkov light of showers. Usually, only a few tens of pixels, marked in green, yellow, and red, contain the signal that is of interest. To cut away the NSB and noise introduced signals that do not belong to the shower images, different cleaning algorithm can be used.

The standard algorithm before the upgrade (applied to the data presented in Chapter 5) was based on the charge and timing information of individual pixels as criteria for rejection. Here, two charge threshold levels for the pixels are defined, the *core*, containing at least 6/9 phe (for MAGIC-I/-II) and the *boundary* with at least 3.5/4.5 phe. For this, all pixels with higher numbers of phe than the *core* are selected first. Those are marked as *core* pixels if a neighboring pixel satisfied the same condition as well. Directly neighboring pixels that fulfill the *boundary* condition are then marked as *boundary* pixels. The charge of the remaining pixels is set to zero. To further improve the sensitivity to the lowest energies an additional constraint is applied using the arrival time, see Fig. 4.8 center panel. As shown in this figure, different showers have

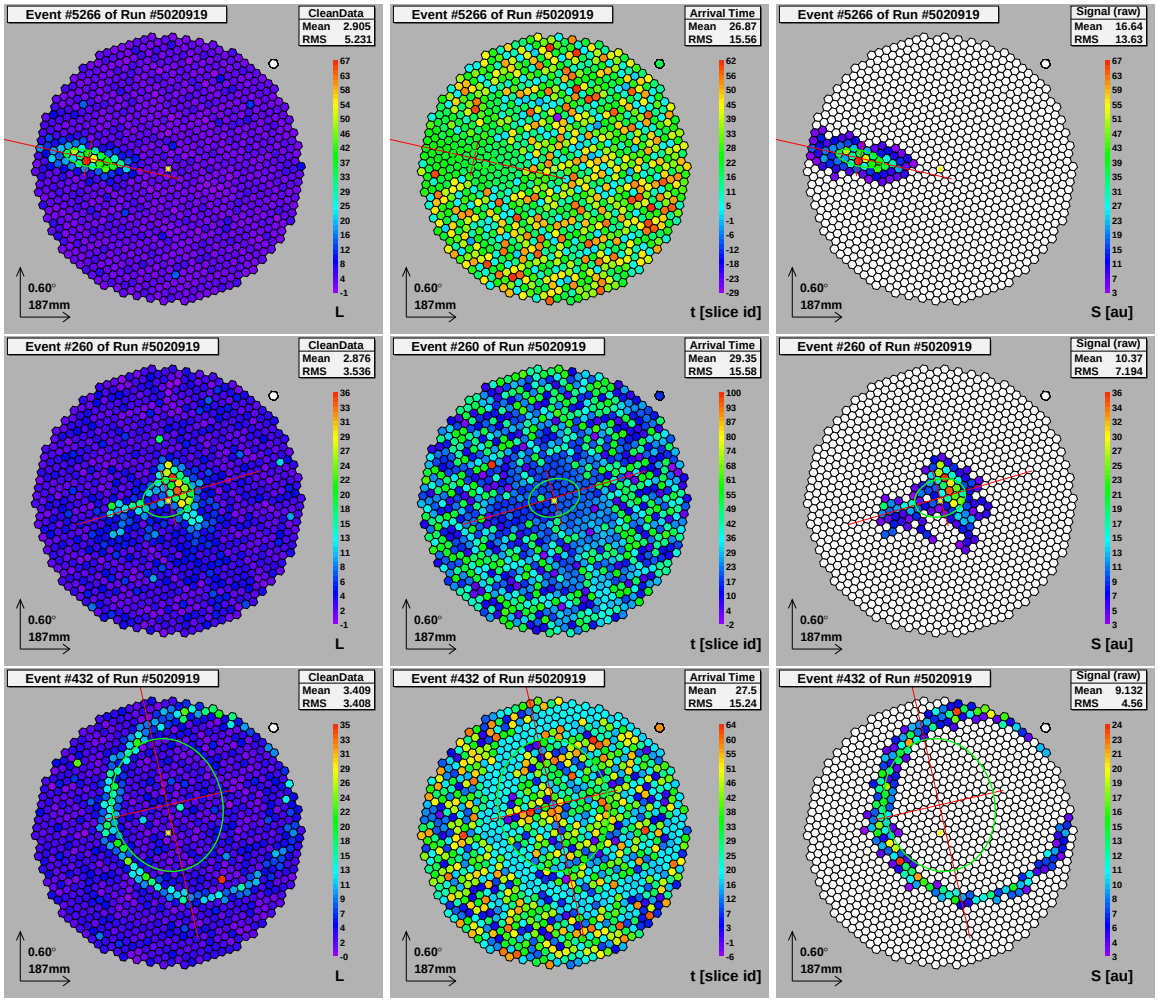

Figure 4.8: From top to bottom: example for a gamma, hadron and muon event in MAGIC-I camera. Calibrated signal before image cleaning (*left panel*), arrival time information of individual pixels (*middle panel*), and after image cleaning (*right panel*).

different arrival times on the pixels. Therefore, in addition to the charge criterion, the signal in the *core* pixels needs to arrive within 4.5 ns with respect to the mean arrival time of all *core* pixels. For the *boundary* pixels, a maximum time spread of 1.5 ns with respect to neighboring core pixels is set. The remaining events after cleaning are shown in right panel of Fig. 4.8.

Another cleaning approach currently used is the so-called "sum-image cleaning" explained in Aleksic et al. (2014b). Here, the signals are clipped in amplitude. The *core* pixels are selected from a search for groups of 2, 3, or 4 neighboring (2NN, 3NN, 4NN) pixels whose charge summed up exceeds a certain threshold, and in addition arrived in a time interval of ~ 1 ns (0.5, 0.7, and 1.1 ns for 2NN, 3NN, and 4NN). The charge thresholds for the individual groups are $2 \cdot 10.8$ phe (2NN), $3 \cdot 7.8$ phe (3NN), and $4 \cdot 6$ phe (4NN). Those thresholds were optimized as described in Aleksic et al. (2014b). For the *boundary* pixels, the same conditions are used as those in the standard cleaning, i.e., 3.5 phe for charge and 1.5 ns for arrival time.

The data of the flare of IC 310 presented in Chapter 6 were cleaned with a modified version, the so-called "dynamical sum-image cleaning". In addition to the sum image cleaning, the cleaning thresholds are dynamically increased for showers with total charge above 750 phe (Sitarek et al. 2013a). This ensures that image parameters (described below) calculated from only well reconstructed shower cores are used in the later stages of the analysis chain.

After the cleaning process, characteristic parameters of the images are calculated. Originally, those parameters consisted of the so-called "Hillas parameters" (Hillas 1985). Those and further defined image parameters are listed below; some of them are illustrated in Fig. 4.9.

- SIZE: total number of phe in a shower image, containing information of the primary particle energy.
- LENGTH: half length of the major axis of the ellipse, characterizing the longitudinal development of the shower.
- WIDTH: half width of the minor axis of the ellipse, characterizing the transverse development of the shower.
- CoG position: Center of Gravity of the image.
- DIST: angular distance between the CoG and the expected source position.
- DISP: angular distance between the CoG and the reconstructed source position used for the reconstruction of the arrival direction.
- α: angle between major axis of the ellipse and DIST direction.
- θ: angular distance between the reconstructed and the expected source position. It can be calculated when the arrival direction of the shower is reconstructed.
- CONC-N: fraction of SIZE in the N brightest pixels describing the compactness of the shower core.
- TimeGradient: amplitude of the time profile of an event along the main axis of the image.
- TimeRMS: spread of the arrival time of Cherenkov photons belonging to the cleaned image.

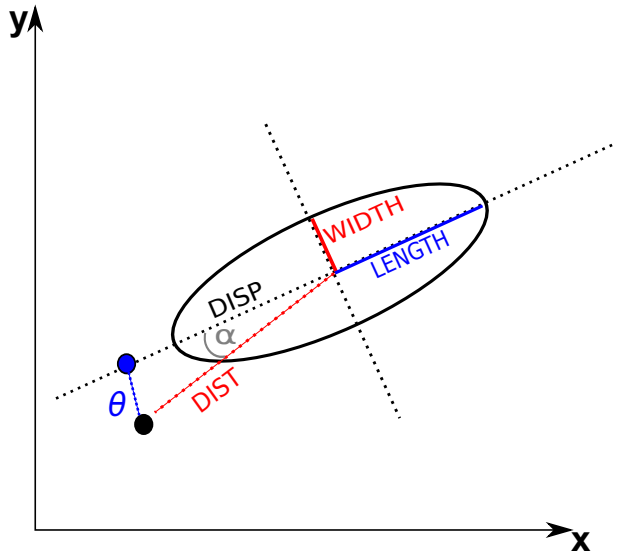

Figure 4.9: Definition of some important image parameters shown on a gamma-like, elliptical event.

- M3LONG: third longitudinal momentum along the major axis depending on whether the head (part of the image with higher charge concentration) is closer to/further away from the camera center than the tail (part of the image with lower charge concentration).
- ASYMMETRY: distance, positive or negative, (analog to M3LONG) between CoG and the pixel with highest phe.
- LEAKAGE: estimated fraction of signal in the outer rings of pixels of the camera.
- Number-of-Islands: number of separated islands (groups of pixels) in the shower image.

These parameters give either geometrical, source-dependent, or time-related information of the cleaned events. Those can be used for the background suppression and/or the energy and arrival direction reconstruction.

4.5.3 Stereo Reconstruction

Up to this point, the data are treated individually for each telescope. Now, the data from both telescopes are combined with the program *superstar*. Events that are recorded only by one telescope are rejected. Typically, about $\sim 80\%$ of the cleaned events survive.

By comparing the single events seen by MAGIC-I and the same events seen by MAGIC-II, a first tentative direction of the shower can be calculated applying the “crossing-point” method described in Aharonian et al. (1997); Hofmann et al. (1999). The axis of the air shower follows the direction of the gamma source in the sky, and the major axis of the image follows that as well. But two telescopes see a different position of the shower in the sky, hence their major axes cross at the point towards the incoming direction. This method induces problems as soon as the axes become more and more parallel to each other in the camera plane, or the ellipses are very small (small LENGTH and WIDTH) which is especially relevant for low energy events.

The stereo observation also allows for a 3D reconstruction of the shower so that the so-called “stereo parameters” can be calculated (Kohnle et al. 1996).

- IMPACT: corresponds to the distance of the shower axis and the telescope pointing position, see also Fig. 4.4.
- MaxHeight: defines the height of the shower maximum. It can be calculated by knowing the shower direction using the angle at which the CoG is viewed from individual telescopes. This parameter depends strongly on the energy of the incident particle. Showers from higher-energy particles penetrate deeper into the atmosphere and reach their maximum closer to the telescopes, see also Aleksić et al. (2012b).
- Cherenkov radius: radius of the Cherenkov light pool, see Fig. 4.4.
- Cherenkov density: photon density on the ground.

Knowing MaxHeight, one can calculate further properties on the Cherenkov light depending on the zenith distance, e.g., the light pool on the ground (see Fig. 4.4) characterized by the Cherenkov radius, and the Cherenkov density, i.e., the density of the Cherenkov light on the ground. Those calculations are based on a normalization that Cherenkov light is produced by a single electron of the shower at MaxHeight and the critical energy of 86 MeV, at which the ionization energy losses of electrons equals the radiative losses.

4.5.4 Monte Carlo Simulations

Since artificial sources of gamma rays are missing, the energy calibration must be introduced in the analysis based on Monte Carlo simulations (MCs, see also Lopez (2013)). They are needed for simulating the development of showers in the atmosphere produced by a particle of certain energy, and their production of Cherenkov light including also different attenuation processes, that influence the travel of the photons in the atmosphere. Those simulations are provided for different incident particles (gammas, protons, etc.) by a modified version of CORSIKA (Heck et al. 1998). As explained at the beginning of this chapter, protons or other hadrons produce showers with irregular structures and sub-showers, hence the computing time of such showers is long compared to the one for gammas. As reported in Lopez (2013) in more detail, an important step in the generation of MC data is the implementation of the entire detector response (reflectivity of the mirrors, camera layout, readout electronics etc.). In the end, such simulations contain information how an image of a certain shower with particular energy and direction of the incident particle is recorded by the camera. The same calibration and cleaning analysis is applied to the MCs.

In particular, the simulations are needed for the calculation of the effective area and hence for the determination of the energy spectrum. The effective area depends on the observation mode, either the ON-OFF mode or the wobble mode. For the latter, the wobble offset is essential. The standard offset during wobble observations for MAGIC is $0.4°$. Due to the rotation of the Earth, the expected source position in the camera plane follows a ring with a radius of $0.4°$. Therefore, the standard gamma MCs used in MAGIC contain only those events and are called ring-wobble MCs. In this thesis, however, data where the source did not appear within this ring will be presented (e.g., in the case of IC 310 appearing in the FoV of the observation of NGC 1275). One possibility is to generate MCs with a different wobble offset. Due to the importance of the flare observed from IC 310, this has been done. Another possibility is to use so-called “diffuse MCs” which are generated for gammas arriving from all directions in the camera plane (see Chapter 5). To select only MCs events with a certain offset between the camera center and the source position, an auxiliary program of MARS can be used, called *selectmc*.

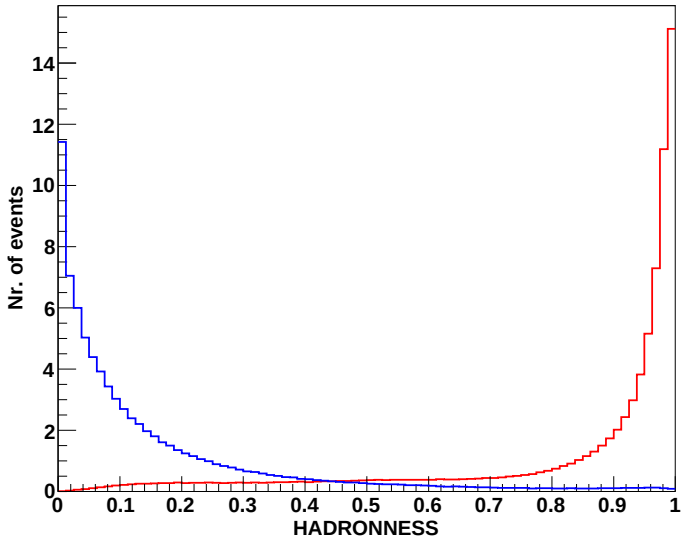

Figure 4.10: Example for HADRONNESS distribution of gamma Monte Carlo events simulated for a spectrum with a photon index of 2 (blue) and hadron events from real data (red).

4.5.5 Background suppression, Direction and Energy Reconstruction

For a gamma-ray source like the Crab Nebula, the fraction of gamma compared to background events in the stage of the raw data is only 10^{-3}. Therefore, the background suppression requires powerful algorithms. Such an algorithm is provided by the Random Forest (RF) approach, a multi-dimensional classification algorithm of construction of decisional trees (Albert et al. 2008b). It can be based on any set of parameters, e.g., the image shape of an event, the time, and the reconstruction direction, to determine the probability for gamma and hadron initiated showers. In the analysis presented here, those are SIZE, WIDTH, LENGTH, IMPACT, MaxHeight, TimeGradient, and Zd. In case of the flare analysis, the parameters WIDTH and LENGTH were substituted with the parameters calculated from the dynamical sum-image cleaning. Further improvements are allowed by applying the parameter TimeRMS (root mean square of the arrival time) in the RF approach.

Out of these parameters a combined parameter is calculated, called “HADRONNESS”. It ranges from 0 to 1 for each event and indicates how likely it is that the event is a hadron-like event. If the HADRONNESS is $0/1$ the event is gamma/hadron-like, respectively (see Fig. 4.10).

The production of the RFs is done with a set of gamma MC simulations and a hadron sample. The latter is a set of observational data in which no gamma-emission is detected. Both, MCs and the hadron sample, need to be selected properly (depending on Zd, light condition and telescope configuration) according to data that should be analyzed. Generally, proton/hadron MCs can be used as a hadron sample as well. However, those are time-consuming in their production.

The training of the background suppression of certain parameters is quantified by the *Gini index* (Gini 1921) which is defined as:

$$Q_{\mathrm{Gini}} = 4 \cdot \frac{N_\gamma}{N} \cdot \frac{N_{\mathrm{bg}}}{N}, \tag{4.2}$$

where N_γ and N_{bg} are the number of gamma and background events, and N is the a total number of events after a cut in a parameter. This index has to be minimized in the RF. The parameter

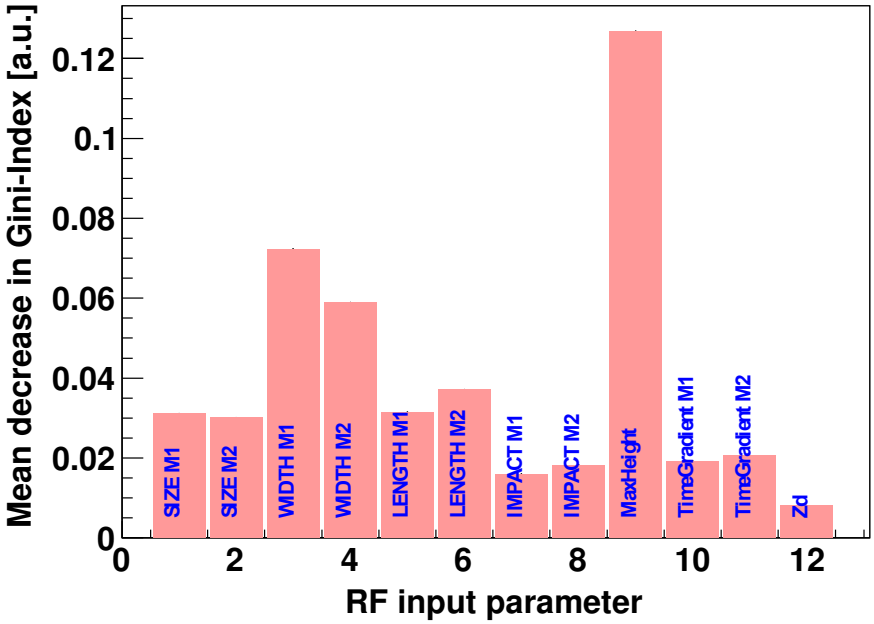

Figure 4.11: Gini index for a set of parameters used in the background suppression. The most important parameter in this analysis is MaxHeight as it provides the highest Q_{Gini} decrease. However, this is an energy-dependent effect. At the lowest energies, MaxHeight has a very strong contribution, whereas at higher energies, the WIDTH parameter has a higher contribution.

with the highest Q_{Gini} decrease indicates the parameter with the highest separation power, see Fig. 4.11.

An additional separation of gamma and background events is provided by the direction of the shower since hadron-like showers (as well as gamma showers not originating from the source) arrive from different directions in the sky. In principle, the direction of a shower can be obtained from the crossing-point method mentioned above. In MARS, another improved method is used for the direction reconstruction as well. This method is based on RF including the image shape and the timing information parameters (SIZE, IMPACT, Zd, MaxHeight, TimeGradient, WIDTH, LENGTH, DIST), see Aleksić et al. (2010a). Originally, the distance between the CoG and the source position DISP was calculated for each telescope according to:

$$\mathrm{DISP} = A(\mathrm{SIZE}) + B(\mathrm{SIZE}) \cdot \frac{\mathrm{WIDTH}}{\mathrm{LENGTH} + \eta(\mathrm{SIZE}) * \mathrm{LEAKAGE}}. \tag{4.3}$$

The coefficients A, B, and η are optimized on MC events. The leakage term in the equation accounts for large truncated images at the edge of the camera. The equation has two solutions on either side of the CoG, both lying on the major axis of the ellipse indicated by A and B in Fig. 4.12. In principle, the correct solution can be found by using the ASYMMETRY parameter along the major axis (Domingo-Santamaria et al. 2005) or by the crossing-point method. At low energies, the determination of ASYMMETRY may fail due to the small images. The crossing-point method may also fail in case of (almost) parallel images. Therefore, all four distances (two solutions A and B of each telescope I and II) are calculated (Fig. 4.12). Then, the pair of solutions is selected with the smallest distance, I-B and II-B. Nowadays, the DISP is calculated from RF which are trained on gamma MCs. Thus, hadron events give incompatible

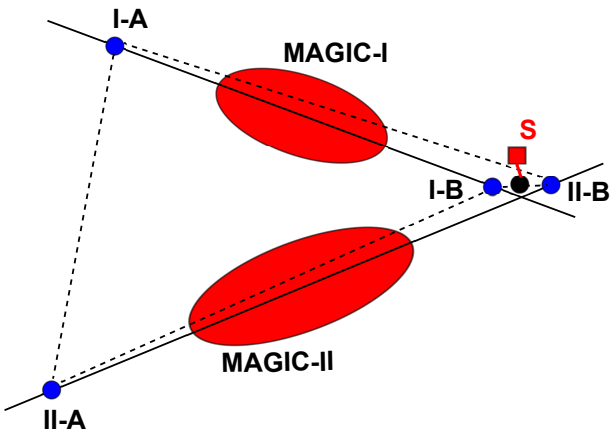

Figure 4.12: Reconstruction of the arrival direction of an event using the information of two telescopes. A and B indicate the two solutions of the DISP calculation. The reconstructed and expected source position is marked as black circle and red square, respectively. Image adapted from Aleksic et al. (2014b).

results, providing an additional gamma/hadron separation. The final source position is found by averaging the position from both telescopes (black dot in Fig. 4.12) taking into account the number of pixels involved in each image.

The energy estimation of the events is provided by look-up tables (LUTs) generated from gamma MCs (Aleksić et al. 2012b) using the information of the IMPACT, the Cherenkov density, and SIZE parameter as the energy of the primary particle is related to the amount of Cherenkov photons produced in an air shower. The amount of Cherenkov light also depends on the azimuth, zenith, MaxHeight, and the position in the camera. The LUTs are multi-dimensional tables of every energy bin considering these parameters. For gamma events in the data, the energy can then be estimated by comparing it with the contents in the LUTs.

First, the LUTs are filled with values of energy/SIZE$\times$Cherenkov density. The number of electrons in a shower and hence the energy is roughly proportional to the ratio between SIZE and Cherenkov density. Next, IMPACT and the Cherenkov radius are taken into account, as the Cherenkov density depends with the IMPACT parameter. Further, the energy dependence of the SIZE is included. Some corrections are applied, e.g., for the geomagnetic field (as electrons and positrons are affected by this and hence the Cherenkov density might be lowered), for the Zd (as the amount of Cherenkov light depends on $\cos^2$ (Zd) as Cherenkov light from larger Zd travels through a larger atmospheric depth) and for LEAKAGE (producing an underestimation of the energy due to truncated images if not taken into account). The final reconstructed energy is the average of the estimated energy from both telescopes weighted by the inverse of the errors.

In the analysis chain of MARS, the RF for the background suppression direction reconstruction, and the energy LUTs are calculated with *coach*. The generated RF and LUTs are then applied to the data and a test sample of MCs (statistically independent from the MCs sample used for the training) in *melibea*.

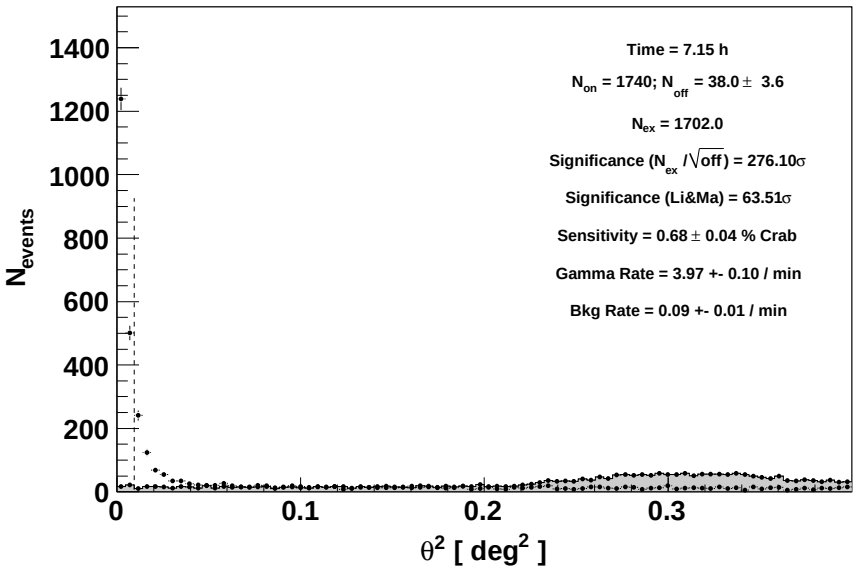

Figure 4.13: θ^2 distribution of the Crab data calculated above 220 GeV. The black points/the gray area show the number of ON/OFF events, respectively. The excess events are calculated from the region left from the dashed line (θ^2 cut). Applied cuts: HADRONNESS < 0.16, SIZE > 300 phe, energy > 220 GeV, $\theta^2 = 0.0093$, and using three OFF regions. At around $\theta^2 \sim 0.3$ a bump is visible influenced by the strong signal.

4.5.6 Signal Detection

With the programs *odie* (simple signal determination) and *caspar* (production of sky maps), the signal in the data can be evaluated on the basis of cuts in different parameters calculated before. Usually, those are HADRONNESS, SIZE, and reconstructed energy. They select the gamma-like events of certain energy from a certain direction in the sky where the source of interest is located (ON position). Further cuts in other image parameters can be applied as well, e.g., the NumberOfIsland, or LEAKAGE. However, those have minor effects on the result, as the HADRONNESS parameters has a strong impact already.

θ^2 Distribution

In *odie*, a simple distribution of the events versus the θ^2 parameter is generated that is determined by the reconstructed DISP. Figure 4.13 shows an example of such a distribution obtained from data taken from the Crab nebula. If the event arrived from the direction of the analyzed source position, the θ^2 equals to zero and results in a peak at this position. Further away, the distribution is mostly determined by background, if no additional gamma-ray source appeared in the FoV. In case of a strong signal, a fraction of the signal may appear as a bump in the θ^2 distribution when the signal region is too close to an OFF region. The distance between the ON and OFF region depends on the number of OFF regions used for the calculation of the background as well as on the wobble offset used during the observation.

After applying cuts to discriminate the gamma from the hadron-like events, the number of events (N_{ON}) are counted in the ON region, defined by the signal cut in θ^2. The remaining events consist of gamma and hadrons. To evaluate this fraction of background after cuts in the ON region, the amount of background events (N_{OFF}) has to be measured from a region where

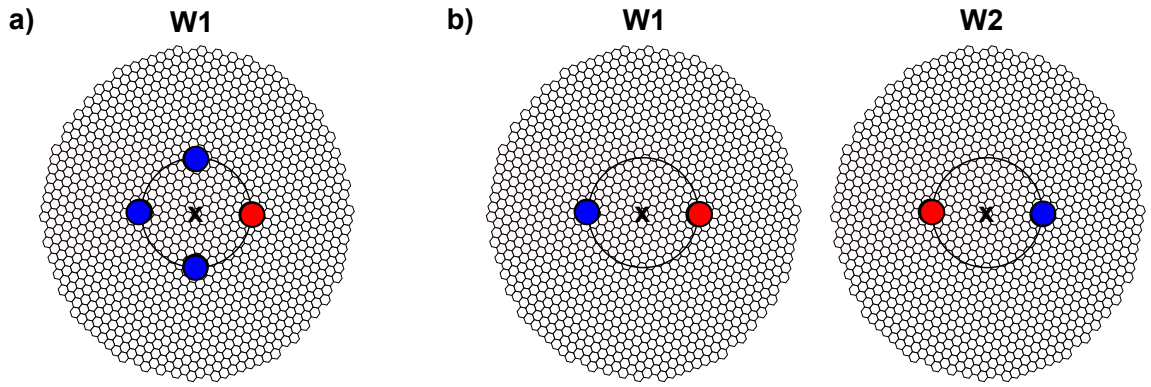

Figure 4.14: Methods for background determination: (a) the simultaneous ON-minus-OFF and (b) the OFWP method. The red and blue markers correspond to the source (ON) and OFF positions in the camera plane, respectively. In case of the ON-minus-OFF method the background is determined from the same wobble data W1 (here from three OFF regions). In case of the OFWP method, the background at the position of the ON region in W1 is determined from OFF region in W2.

no signal is expected. The number of excess events can be calculated according to:

$$N_{\mathrm{ex}} = N_{\mathrm{ON}} - \alpha \cdot N_{\mathrm{OFF}}, \tag{4.4}$$

where α is a normalization factor given by the fraction of ON events over OFF events in a region far away from the signal. The significance of a signal S_σ that this signal is not comparable with the background is calculated by Eq. 7 in Li & Ma (1983):

$$S_\sigma = \sqrt{2}\left(N_{\mathrm{ON}} \cdot \ln\left[\frac{1+\alpha}{\alpha}\left(\frac{N_{\mathrm{ON}}}{N_{\mathrm{ON}}-N_{\mathrm{OFF}}}\right)\right] + N_{\mathrm{OFF}} \cdot \ln\left[(1+\alpha)\left(\frac{N_{\mathrm{OFF}}}{N_{\mathrm{ON}}-N_{\mathrm{OFF}}}\right)\right]\right)^{1/2}. \tag{4.5}$$

In Fig. 4.13, N_{ON} were measured to be 1740 and $N_{\mathrm{OFF}} = 38.0$ in the region $\theta^2 < 0.0093$, corresponding to $S_\sigma \sim 63\,\sigma$.

In case of wobble observations, there are currently two possibilities in determining the background from the OFF region. As shown Fig. 4.14 a one can calculate the OFF (blue markers) from positions far away from the ON simultaneous from the same data (simultaneous ON-minus-OFF method). Using only one OFF, this means the background will be calculated from the opposite position with respect to the camera center. The distance of the OFF region from the camera center is determined by the distance between the source and the camera center, hence the ON and the OFF lie on a circle centered around the camera center with a radius $0.4°$ in case of a standard wobble observation. Generally, a number of n (1, 2, 3, or 5) OFFs are used, then $\alpha = 1/n$. More OFF regions are favored especially for higher energy signals due to their lower statistical error. However, ON and OFF should not be too close to each other to avoid a contamination by the source.

Another possibility is to calculate the OFF from the "wobble partner" (OFWP). This method is illustrated in Fig. 4.14 b. If the signal is calculated from the red position in W1, then the background is determined at the same position in the camera in the data from the second, counter wobble position W2. This enables to overcome possible inhomogeneities in the camera which is particularly important for retrieving low-energy events. For sources appearing in the FoV during a wobble observation, the asymmetry in the camera may be more serious resulting in

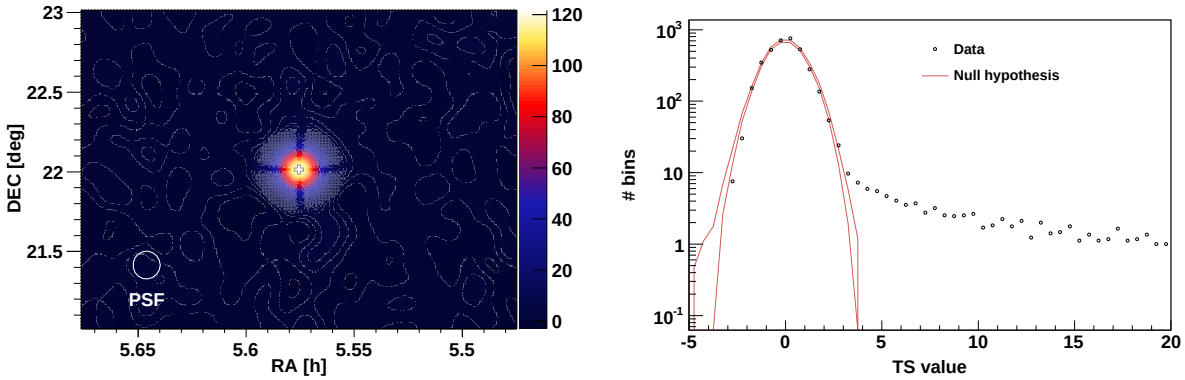

Figure 4.15: TS value map of the Crab data in the medium energy range ($\gtrsim 250\,\mathrm{GeV}$). The following cuts have been applied: HADRONNESS < 0.16, SIZE $> 300\,\mathrm{phe}$. *Left:* TS value distribution in coordinates of the sky. *Right:* Distribution of TS value measured from the data and the null hypothesis.

a significant mismatch between the ON and the OFF in the background region. Hence, the OFWP approach can handle this special situation better. However, the number of the available OFF regions depends on the number of wobble pairs used during observation. If only one wobble pair was observed, only one OFF can be used for the calculation of the background.

Sky Maps

A signal can be also detected by producing a sky map. This is a histogram of the arrival directions calculated from the DISP in coordinates of the sky (RA and DEC) after applying cuts for the background suppression and energy. In Fig. 4.15 (left) the TS (test statistics) value as sky map from Crab Nebula data is shown. The TS value is a similar statistical way to determine the significance of a detection based on Eq. 4.5, taking into account a smoothing process and a model for an estimated background. The null hypothesis distribution of TS can be described by a Gaussian function in most of the cases. Sky maps are in particular important to find objects appearing in the FoV. In this way, also IC 310 has been detected. The calculation of sky maps is described in Lombardi (2010).

4.5.7 Spectrum and Light Curve

The last step in the analysis is the calculation of the spectral distribution of the events and the light curve done with *flute* or *fluxlc*.

The differential energy spectrum is calculated with:

$$\frac{\mathrm{d}N}{\mathrm{d}E} = \frac{\mathrm{d}N_{\mathrm{ex}}(E)}{t_{\mathrm{eff}} A_{\mathrm{eff}}(E) \mathrm{d}E} \left[\mathrm{TeV}^{-1}\,\mathrm{cm}^{-2}\,s^{-1}\right], \tag{4.6}$$

where N_{ex}, t_{eff}, and A_{eff} are the number of excess events, the effective time, and the effective area. The first is obtained from creating individual θ^2 distributions for a certain number of small energy intervals (bins). Generally, this number of bins should not be smaller than the energy resolution of the system, and depends on the strength of the gamma-ray signal. The calculation of the background can be performed with the simultaneous ON-minus-OFF or OFWP method. The background suppression is mainly applied by energy dependent HADRONNESS and θ^2

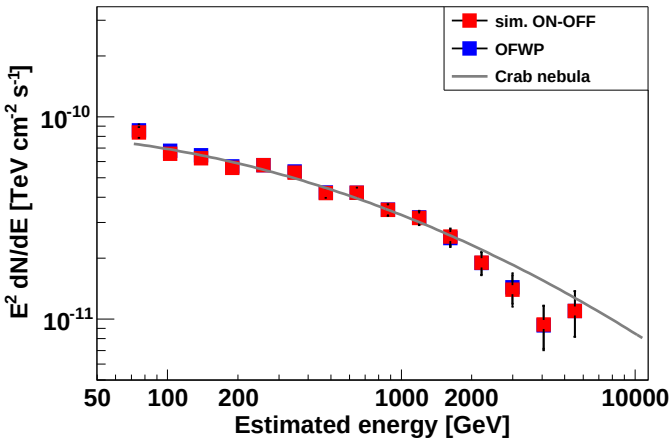

Figure 4.16: Spectral distribution of estimated energy from Crab nebula data. Red/blue data points show the SED from the simultaneous ON-minus-OFF/OFWP method, respectively. The gray line represents the Crab nebula spectrum extracted from Aleksić et al. (2012b). For the calculation, the spectral shape found in Aleksić et al. (2012b) for the Crab nebula data was assumed.

cuts for the individual energy bins. Those cuts are determined, e.g., by the efficiency of the cuts. Since only significant bins are used for the final spectrum, each of the θ^2 distributions should contain at least ten ON. Otherwise, the evaluated significance might be biased, see Li & Ma (1983).

The effective time takes into account the dead time of the system and hence can differ from the elapsed observation time. It can be calculated by $t_{\text{eff}} = N/\lambda$, where N is the total number of measured events, following a Poissonian distribution, and λ gives an average event rate obtained from a fit to the exponential distribution of time differences of sequentially recorded events. The calculation is simplified by subtracting a fixed dead time (0.5 ms/26 μs for the system before/after the upgrade) from the elapsed time. Before the upgrade, a fraction of $\sim 10\,\%$ of the time was lost due to the DRS 2 readout. After the upgrade, this was only 1 % thanks to the DRS 4.

The calculation of the effective area requires MCs with events of known energy (E_{true}) to simulate a given area in which a fraction of showers trigger the telescopes. This calculation also takes into account the efficiency of the analysis for detecting events, mostly depending on Zd and their energy. At low energies, not all events trigger the telescopes due to a small amount of light in the light pool, hence A_{eff} is small. With increasing energy, the probability for a trigger increases and therefore, A_{eff} becomes larger until saturation.

Typically, the spectrum is presented as the spectral energy distribution (SED):

$$E^2 \cdot \frac{\mathrm{d}N}{\mathrm{d}E}[\mathrm{TeV\,cm^{-2}\,s^{-1}}] = E \cdot \frac{\mathrm{d}N}{\mathrm{d}(\ln E)}, \tag{4.7}$$

which is comparable to the $\nu F \nu$ representation shown in Section 2.5.1.

First, the SED is calculated with respect to the estimated energy E_{est} obtained from data taken from the Crab nebula as shown in Fig. 4.16, using the simultaneous and the OFWP method for the background estimation.

The final spectrum calculated with respect to the true energy E_{true} is obtained by an unfolding. Here, the distribution of an *observable*, here E_{est}, is transformed into the physical quantity

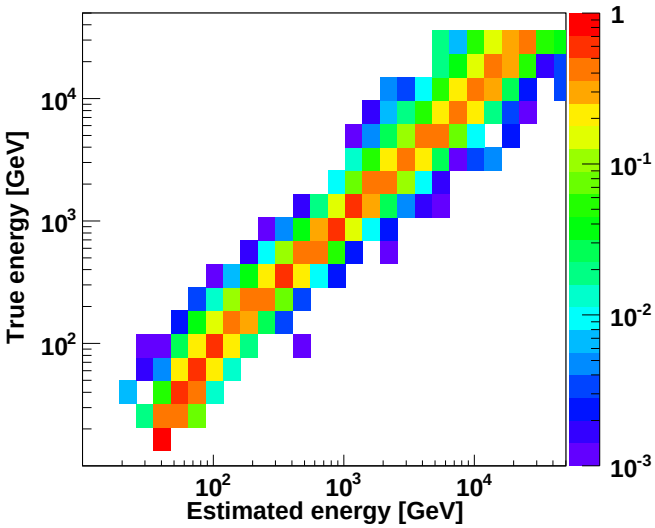

Figure 4.17: Discretized migration matrix from estimated and true energy.

E_{true}. The former is affected by the resolution of the instrument and therefore biased, as the collection area strongly depends on energy especially at low energies.

The relation between the estimated spectrum $g(y)$ and the true spectrum $f(x)$ is given by:

$$g(y) = \int M(x,y) f(x) dx + b(y), \tag{4.8}$$

where x and y correspond to the E_{true} and E_{est}, respectively. $M(x,y)$ is a two-dimensional matrix of E_{true} and E_{est} called "migration matrix" (see Fig. 4.17). The matrix determines the response of the instrument. The equation is not analytically (easily) solvable for large matrices. Therefore, in order to obtain $f(x)$ the equation must be discretized:

$$y_i = M_{i,j} x_j + b_i. \tag{4.9}$$

In this way, the migration indicates that the event of true energy j is measured in the finite resolved energy bin i.

There are several unfolding algorithms for the matrix inversion available in MARS (see Albert et al. (2007a) and references therein). The spectra from different algorithms differ due to, e.g., different approximations and number of parameters to solve the problem numerically. Due to the discretization a smoothing is applied by regularization based on methods described in Tikonov & Arsenin (1979); Schmelling (1998); Bertero (1989).

In Fig. 4.18, the resulting spectrum in true energy is shown for different unfolding methods. The red shaded area shows the "forward-folded" spectrum determined without the need of a regularization. It is calculated by assuming a certain spectral shape by parametrization of the true energy with an analytical function. This function is folded by the response matrix yielding a predicted distribution in estimated energy. The forward-folded spectrum is then the result from a minimization of the χ^2 depending on the parameters comparing the distribution of the predicted and observed ones.

The unfolding program in MARS allows to combine spectra from, e.g., data with different offsets from the source to the camera center, as it is required for off-axis objects.

Notice, the binning center in the final spectrum in MARS is not the logarithmic center but follows an approach described in Lafferty & Wyatt (1995). This method takes into account the

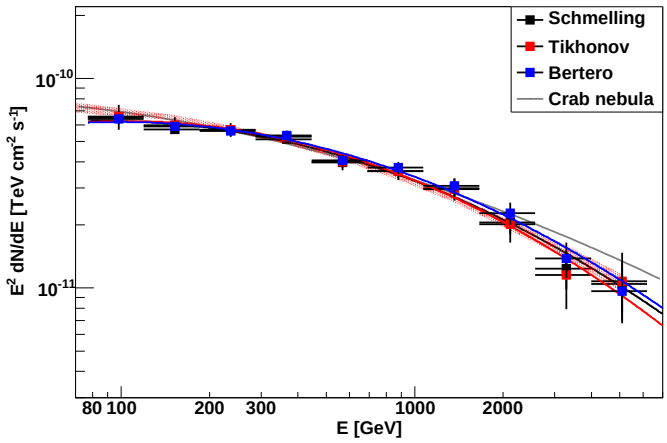

Figure 4.18: Spectral energy distribution from Crab nebula data applying different unfolding methods. Shown are the resulting spectral points and fit lines from the Schmelling (black), Tikhonov (red), and Bertero (blue) method. In addition, the forward-folded spectrum is shown by the red shaded area as well as the Crab Nebula spectrum as gray line (Aleksić et al. 2012b).

spectral index of the spectral distribution. Therefore, the errors of the energy in the spectrum become asymmetric.

The light curve is usually defined as the integral flux in an energy range $[E_1, E_2]$ versus time. For a given time interval $[T_1, T_2]$, the integral flux can be calculated as:

$$F = \int_{T_1}^{T_2} \int_{E_1}^{E_2} \frac{\mathrm{d}N_{\mathrm{ex}}(E)}{\mathrm{d}t A_{\mathrm{eff}}(E) \mathrm{d}E} \mathrm{d}E \mathrm{d}t \ \ [\mathrm{cm}^{-2}\mathrm{s}^{-1}]. \tag{4.10}$$

The number of excess events N_{ex} is obtained from a θ^2 distribution calculated for the energy range in that time interval. The cuts are either the energy-dependent cuts set for the spectrum calculation (in the case of *flute*), or applied with fixed values (in *fluxlc*). Generally, for the background estimation both methods, the simultaneous ON-OFF or OFWP, can be used. For the light curve calculation, A_{eff} is obtained from MC simulations weighted with Zd (and azimuth angle) that is covered by the data in that time interval, see Zanin (2011) for more detail.

Generally, the time intervals in the light curve are determined by the strength of the signal. Alternatively, the light curve can also be binned in a way that each flux point has a certain number of events, as shown in this thesis.

If the signal is too weak to be detected or, e.g, the flux calculation is negative (or comparable with zero) due to a negative statistical fluctuation of the excess events, upper limits (UL) can be estimated. Those can be either integral or differential ULs. They are calculated with a confidence level of usually 95% reflecting the statistical precision of the measurement, and assuming a certain systematic uncertainty of, e.g., 30%. The calculation is similar to the calculation of the spectrum/light curve, just uses an upper limit to the number of excess events N_{UL} as described in Rolke & López (2001); Rolke et al. (2005) and references therein. For this, a differential spectrum $\mathrm{d}N/\mathrm{d}E = \mathrm{K} * S(E)$ following, e.g., a power law with photon index Γ is assumed. The emission is considered to be constant in time. The upper limit of the flux in the energy

Table 4.2: Performance. Adapted from Aleksić et al. (2012b) and Aleksic et al. (2014b).

	Before upgrade	After upgrade
Sensitivity	0.76% C.U. above 290 GeV	0.66% C.U. above 220 GeV
Energy threshold	50-60 GeV	$\sim$50 GeV
Energy resolution[a]	16%	15%
Angular resolution[b]	0.07° at 300 GeV	0.07° at 250 GeV, 0.04° at $\sim$ 1 TeV

Notes. [(a)] Valid in the most sensitive energy region at a few hundred GeV. [(b)] The values depend strongly on the method used for the calculation of the angular resolution, see Aleksic et al. (2014b).

range E_1 to E_2 for an effective time interval of T_{eff} can be estimated with:

$$K^{\text{UL}} < \frac{N_{\text{UL}}}{T_{\text{eff}} * \int_{E_1}^{E_2} S(E) A_{\text{eff}}(E) \mathrm{d}E}, \tag{4.11}$$

calculated by weighting the average of the effective area.

4.6 Performance and Systematic Uncertainties

Over more the ten years, the hardware of the MAGIC telescopes was upgraded from time to time and the analysis techniques improved. A complete investigation of the performance and systematic effects can be found in Aleksić et al. (2012b) as well as Aleksic et al. (2014b).

The sensitivity is used to compare the performance of different experiments. A simple treatment of the sensitivity especially working for weakly emitting objects is computed from the number of excess events over the square root of the background events:

$$S = \frac{N_{\text{ex}}}{\sqrt{N_{\text{bgd}}}}. \tag{4.12}$$

The sensitivity is then defined as the flux of the object for which S equals to 5 in 50 hours of observation. Similarly, this can be calculated by applying Eq. 4.5. In this case, the sensitivity depends on the number of OFF regions. In MAGIC, two further criteria are applied in the calculation: $N_{\text{ex}} > 10$ and $N_{\text{ex}} > 0.05 N_{\text{bgd}}$. The first allows an approximation of the Poisson-like distribution of the excess events with a Gaussian distribution, and the latter overcomes possible small systematic differences between ON and OFF. The integral sensitivity is typically calculated from a Crab-like spectrum and hence is given in units of the flux of the Crab nebula (C.U.). The performance, independent of the power-law index, can be received by the differential sensitivity curve, see (Aleksić et al. 2012b). The evolution of the integral sensitivity obtained during the different phases of the instrument over time is shown in Fig. 4.19. The improvement from the single to the stereoscopic system is best visible at low energies due to the rejection of background events in the stereo mode. After the upgrade, an integral sensitivity of 0.66% (before 0.76%) of C.U. in 50 h at a few hundred GeV could be achieved.

Further performance parameters are given in Table 4.2.

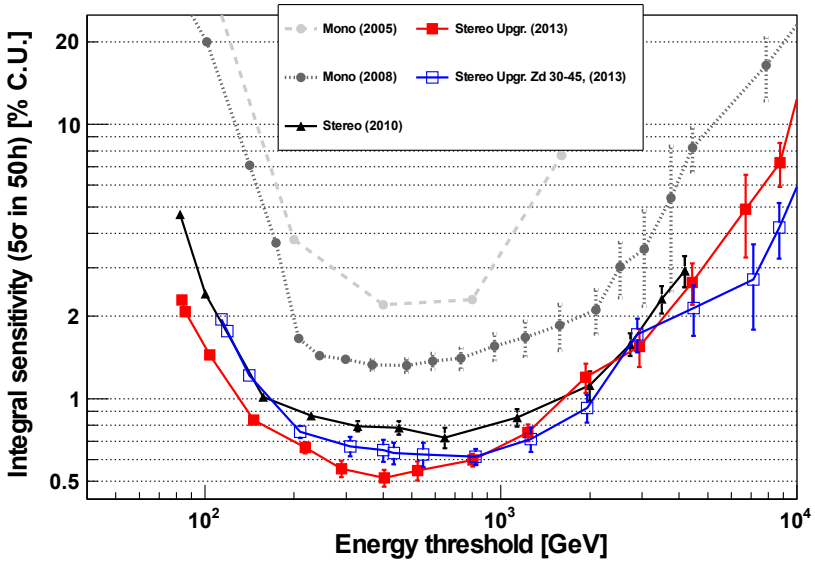

Figure 4.19: Evolution of the integral sensitivity of the MAGIC telescopes given in units of the Crab nebula flux (C.U.): MAGIC-I single telescope with Siegen readout (light gray, Albert et al. (2008c)), with MUX readout (dark gray, Aleksić et al. (2012b)), stereo system before (black, Aleksić et al. (2012b)), and after the upgrade (red/blue for low/high zenith distance observation, Aleksic et al. (2014b)). Image taken from Aleksic et al. (2014b).

Off-axis performance

One important point for this thesis is the off-axis performance of the telescopes since the object IC 310 is often observed with a non-standard wobble configuration (standard: $0.4°$) with larger or smaller distances to the camera center. To study this effect, Crab Nebula observations at different wobble offsets were performed (Aleksić et al. (2012b) and Aleksic et al. (2014b)). With the upgrade 2011/2012, an improvement in the sensitivity of about 25% at an offset of $1°$ could be achieved compared to 15% at a standard offset (see Fig. 4.20). In contrast, it was found that the gamma rate at different offsets did not change much. This may be due to an improved image reconstruction due to the new MAGIC-I camera with smaller pixels.

Systematic uncertainties

Besides statistical errors, the results from Cherenkov telescopes are affected by different systematic effects. Those need to be considered, e.g., when the energy spectra or the light curves are discussed. Some of the effects arise from observational and atmospheric conditions, some from the instrument and its limited performance, and others from the analysis methods. They can either have an effect on the energy scale, on the flux normalization, or the spectral slope. Table 4.3 summarizes the total errors in the flux normalization, the spectral slope, and the energy scale before (Aleksić et al. 2012b) and after the upgrade 2011/2012 (Aleksic et al. 2014b).

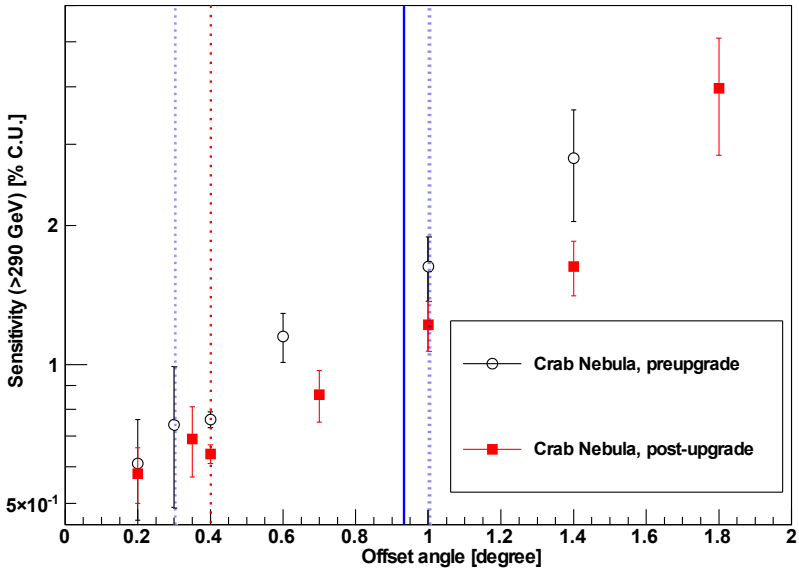

Figure 4.20: Integral sensitivity of the MAGIC telescopes at different offsets from the camera center. The pre-upgrade data are taken from Aleksić et al. (2012b). The lines indicate the offsets at which IC 310 has been observed (red: standard offset, dashed blue: October 2009 to February 2010, solid blue: in case of NGC 1275 mode, see Section 6.1). Image adapted from Aleksic et al. (2014b).

Table 4.3: Systematic uncertainties. Adapted from Aleksić et al. (2012b) and Aleksic et al. (2014b).

Systematic uncertainty	Before upgrade	After upgrade
Flux normalization	19% / 11%^{a}	18% / 11% / 15%^{b}
Spectral slope	± 0.15	unchanged
Energy scale	17% / 15%^{a}	$< 15\%$

Notes. $^{(a)}$ The values are given for low ($\lesssim 100$ GeV) and medium/high energies (>300 GeV), respectively. $^{(b)}$ The values are given for low ($\lesssim 100$ GeV), medium (>300 GeV), and high energies (>1 TeV), respectively.

5

Study of Multi-Band Data

The Character of IC 310

The discovery of IC 310 in the gamma-ray band with *Fermi*-LAT and MAGIC was very surprising. Due to its original classification as HTRG this would have been the first detection of gamma-ray emission for this kind of radio galaxies. Deep multi-wavelength studies of this object were required. Therefore, the aim of this chapter is to investigate the general "character" of IC 310 in the gamma-ray as well as the other energy bands. For that purpose, multi-band data were used which was available at the beginning of this thesis. This includes the gamma-ray data from *Fermi*-LAT and MAGIC as well as X-ray data from *Chandra*, *XMM-Newton* and *Swift*-XRT, all of which were examined in terms of flux and spectral variability. In addition, archival VLBI data from the VLBA were studied.

The studies presented here resulted in two publications in the journal Astronomy & Astrophysics, Vol 538, L1, and Vol 563, A91. Some of the findings are based on first results in the author's Diploma thesis while other parts of this work has been done in the course of the author's PhD work.

5.1 MAGIC Observations and Data Analysis

Form October 2009 to February 2010, the Perseus cluster has been observed with the previous MAGIC-I camera, the FADC readout in MAGIC-I and the DRS 2 chip in MAGIC-II (Aleksić et al. 2012b). IC 310 was discovered during this observations for the first time by chance in the field of view. Hence, no dedicated wobble positions with a standard wobble offset were made. As seen in Fig. 5.1, two pointings with 0.4° away from the center of the cluster, NGC 1275, were used. In this configuration, IC 310 appears at an offset of 0.25° and 1° from the center of the cameras. Since two different Monte Carlo simulation sets are needed for the analysis only the closer wobble position has been analysed in Aleksić et al. (2010b). However, for the present study, the complete data set was studied using improved analysis settings which can handle the data of both wobble positions. This provides a higher statistic for a daily binned light curve making variability studies on shorter time scales more accurate.

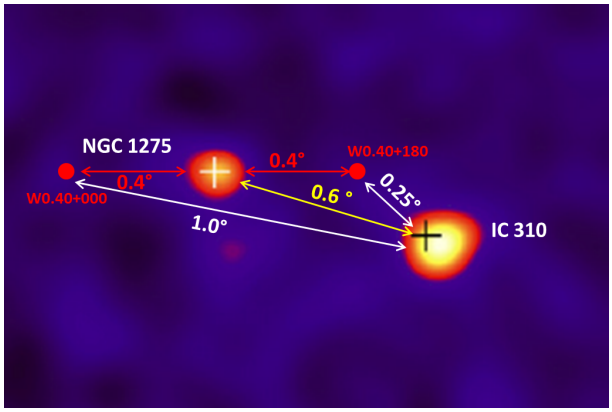

Figure 5.1: Configuration of the wobble positions during Perseus observations in 2009/2010. Two positions centered around NGC 1275 were used, W0.40+000 with an offset of 1° and W0.40+180 with 0.25° distance to IC 310.

The data were taken under small zenith distances (Zd $< 35^\circ$) during dark time in the so-called *soft stereo* mode. In this case, MAGIC-I was triggering and read out. In addition, the data of the second telescope were read-out. Only data during non-optimal atmospheric and hardware conditions have been rejected, see Appendix B Fig. 3, Table 2, and 3. The distribution of a few typical quality parameters (Zd, number of identified stars, currents in the camera, trigger rate after cleaning) is shown in Appendix B Fig. 3. The overall data sample corresponds to 43.3 h of effective time, t_{eff}. The effective time of single MAGIC observations is reported in Appendix B Table 2.

The low level analysis of the data from the calibration up to *superstar* was performed using the standard analysis as described in (Aleksić et al. 2012b) and Chapter 4 applying an image cleaning of 6-3 for MAGIC-I and 9-4.5 for MAGIC-II data. For the generation of energy LUTs and the DISP RF, diffuse gamma Monte Carlos (MCs), with gamma events distributed over the entire camera plane were used. The production of the background suppression RF, the diffuse gamma MCs as well as OFF data from the MAGIC sources OffCrab7, 3C 454.3, ON 325 and Cygnus Loop (see Appendix B Table 4) have been used, covering a Zd range of $1^\circ - 49^\circ$ ($t_{\text{eff}} = 10.4$ h). However, the diffuse gamma Monte Carlos were generated for the full stereo mode observation with both telescopes triggering. This produces a discrepancy between the SIZE distribution of data and the MCs at low values (SIZE $<$ 150 phe). Therefore, a cut in SIZE $>$ 150 phe has been applied in the analysis.

The estimation of the background was performed separately for data with different wobble offset. For the wobble position closer to IC 310, two OFF regions at 0.25° away from the camera center were used, whereas for the distant one five OFFs with an offset of 1° were chosen. The gamma-ray signal N_{ex} for each wobble set is calculated by subtracting the estimated background from the ON-source region in each wobble set individually (simultaneous ON-minus-OFF method). As explained in Chapter 4, the effective area A_{eff} strongly depends on the distance from the camera center. Therefore, A_{eff} was estimated separately for each wobble position using diffuse gamma MCs cut to the corresponding distance from the camera center to the source position (see Fig. 5.2). The cuts applied in the light curve and spectra analysis can be found in Appendix B Section 3.

The light curve of both wobble positions was combined by calculating the total number of excess events N_{ex}, measured during both wobble observation weighted by the sum of the corre-

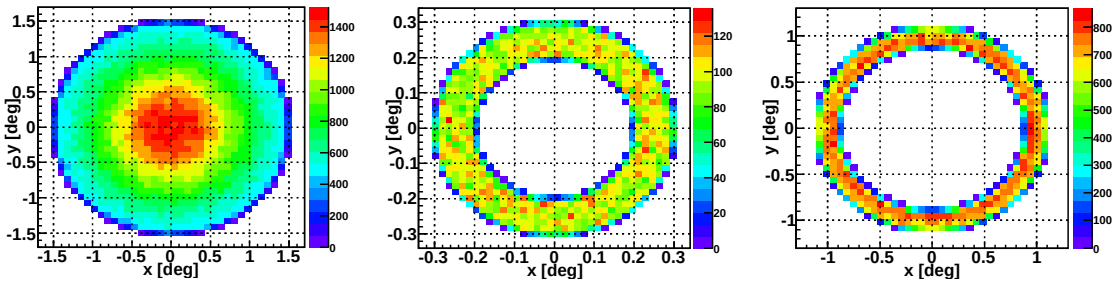

Figure 5.2: Monte Carlo simulations for the wobble positions configuration in 2009/2010. *Left:* Raw diffuse gamma MCs. *Middle:* Cutted diffuse gamma MCs between 0.2 to 0.3°. *Right:* Cutted diffuse gamma MCs between 0.9 to 1.1°.

sponding effective area times the effective time t_{eff}:

$$F_{\mathrm{Combined}} = \frac{\sum N_{\mathrm{ex}}}{\sum A_{\mathrm{eff}} \cdot t_{\mathrm{eff}}}. \tag{5.1}$$

The flux upper limits were calculated according to:

$$UL = F_{\mathrm{Combined}} \cdot \left(\frac{N_{\mathrm{UL}}}{\sum N_{\mathrm{ex}}} \right). \tag{5.2}$$

The spectra of the different wobble positions can be combined within the unfolding process.

To test this analysis chain and to calculate the systematic errors, data from the Crab Nebula taken with a wobble offset of 0.2° on February 9, 2010 and with 1° offset on February 22, 2011 were used, see Fig. 5.3. No data with a wobble offset of 0.25° were taken, hence, a dedicated test fitting the wobble configuration of IC 310 with this offset was not possible.

Even though the statistics is limited due to a short observation time the spectra are in good agreement with the results obtained from standard observation with 0.4°.Therefore, the systematic errors on the flux normalization and photon index are evaluated to be below ∼17% and ∼0.2, respectively (instead of 11% and 0.15 for standard wobble observations (Aleksić et al. 2012b)). The systematic uncertainty on the energy scale is estimated to be 15% similar to the value reported in Aleksić et al. (2012b).

5.2 *Fermi*, X-ray, and Radio Data

The *Fermi*-LAT data shown in this chapter were taken during the period August 4, 2008 - August 1, 2010 published in the "The Second Fermi-LAT Catalog" 2FGL catalog (Nolan et al. 2012) and, during August 5, 2008 - July 31, 2011 (MJD 54683–55773). Both periods are contemporaneous to the MAGIC observation described above. The analysis of the latter period is a dedicated high energy analysis above 10 GeV for "The First Fermi-LAT Catalog of Sources Above 10 GeV", designated 1FHL catalog (Ackermann et al. 2013). The details of the analysis are described in the corresponding paper from the *Fermi* Collaboration.

Since the angular resolution degrades with a lower energy (Ackermann et al. 2012) the analysis of the region of the Perseus cluster is complicated. A strong signal originating from NGC 1275 is contaminating the signal and background region around IC 310. At GeV energies NGC 1275 is ∼20 times brighter than IC 310. However, the point-spread function of the LAT instrument is about $0.2°$, so that the signal of both objects can be well resolved.

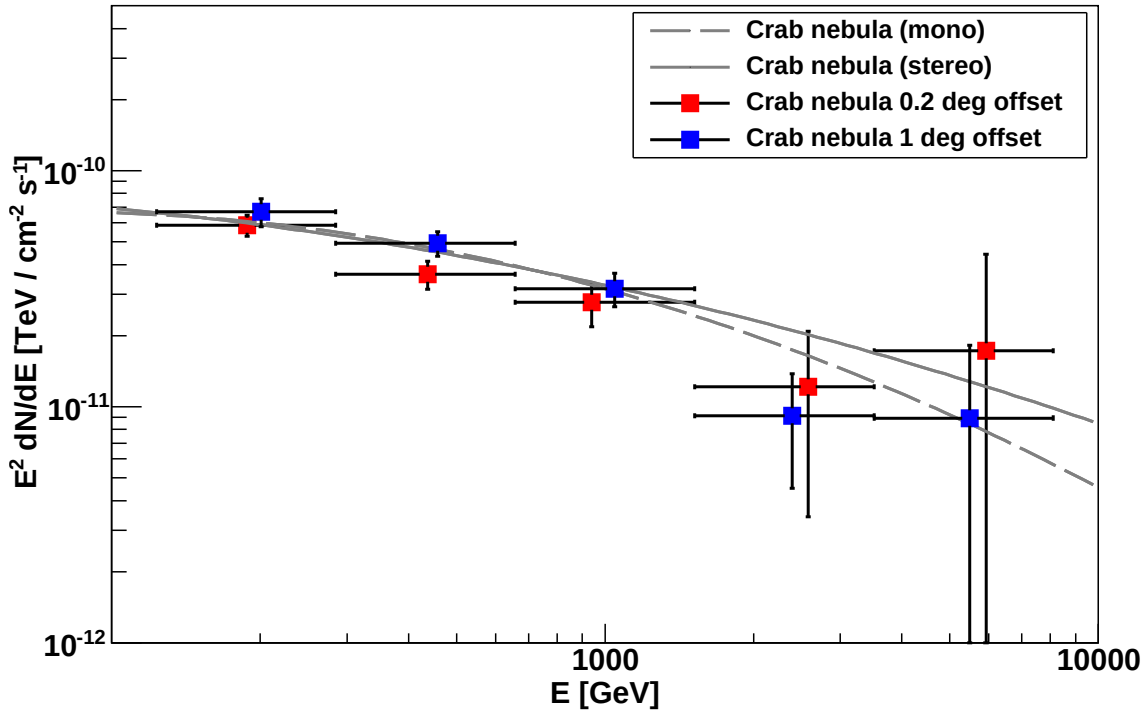

Figure 5.3: Spectra of the Crab Nebula data taken with wobble offsets of 0.2° and 1° offset, respectively. For reference the spectra from mono (Albert et al. 2008c) and stereo observations (Aleksić et al. 2012b) are shown.

For the characterization of the spectra for the 1FHL data a binned likelihood method and simple power-law model has been applied (see Ackermann et al. (2012)) with ten bins per energy decade starting at 10 GeV. From this, three energy bins were extracted, 10–30 GeV, 30–100 GeV, and 100-500 GeV. Due to low statistics, the errors are asymmetric as the flux uncertainties are strongly dominated by Poisson fluctuations. Further analysis details of the 2FGL data are given in (Nolan et al. 2012) and for the 1FHL data in (Ackermann et al. 2013) and in Aleksić et al. (2014c), respectively.

In the X-ray regime, data of the *Chandra*, *XMM-Newton* and the *Swift*-XRT telescopes of IC 310 were found in the archive and investigated.

The *XMM-Newton* observation on February 26, 2003 had an exposure time of 22.6 ks (Obs. ID 0151560101). It was performed with the pn detector of the European Photon Imaging Camera in an energy range of 0.2–15 keV (Strüder et al. 2001).

With the *Chandra* satellite using the Advanced CCD Imaging Spectrometer (ACIS), two measurements in intervals of four months were performed, on December 26, 2004 with an exposure of 25.2 ks (Obs. ID 5597) and on March 23, 2005 with 1.5 ks (Obs. ID 5596).

The *Swift*-XRT observation of IC 310 in an energy range of 0.2–10 keV was performed on February 19, 2007 lasting for 4.1 ks.

For the spectral fitting between 0.5 keV and 10 keV with a reasonable signal-to-noise criteria, the *Interactive Spectral Interpretation System* (Houck & Denicola 2000) was used . The column density N_{H} and the photon index Γ were calculated with the fitting procedure. Note, that the Perseus cluster is a bright X-ray emitter. Part of this thermal radiation originates from the intercluster medium. However, as IC 310 is located on the outer part of the cluster. The contribution of this emission was neglected.

Radio observations have been performed with the Effelsberg 100 m single-dish telescope. Furthermore, some VLBI measurements are available in the archive. The former took place on July 23, 2011 at frequencies between 2.64 GHz and 14.60 GHz. As calibrators 3C 286, NGC 7027, and 3C 48 were chosen. The analysis applied is presented in Kraus et al. (2003). The VLBI measurements were carried out with the Very Long Baseline Array (VLBA) as part of an observing program for 2MASS galaxies (Condon et al. 2011), with the experiment codes BC196Q and BC196R. On May 16 and 30, 2011 one observation of 5 min each in a range of 7.9 GHz and 8.9 GHz were conducted. The analysis of this data is described in Kadler et al. (2012).

5.3 Light Curve and Spectra in Different Energy Bands

5.3.1 MAGIC Light Curve

In order to produce a light curve the differential spectrum and hence the effective area must be assumed for the calculation of integral fluxes. Here, a simple power-law distribution, $\propto E^{-\Gamma}$, with a photon index of $\Gamma = 2.0$ has been applied as reported in Aleksić et al. (2010b). The dependence of the photon index of the power-law spectrum on the calculation of the integral flux is only minor. The resulting light curve computed above 300 GeV between October 2009 and February 2010 is shown in Fig. 5.4. The individual flux measurements can be also found in Appendix B Table 6. In case the flux was comparable with zero within one standard deviation (1σ) or smaller, upper limits (ULs) were calculated using the model four of Rolke et al. (2005). All ULs were determined using a confidence level (c.l.) of 95% and assuming a systematic uncertainty of 30%.

Above 300 GeV the mean flux was calculated to be $F_{\mathrm{mean}} = (3.62 \pm 0.40) \times 10^{-12}\,\mathrm{cm^{-2}s^{-1}}$. This is in agreement with the findings in Aleksić et al. (2010b) of $F_{\mathrm{mean}} = (3.1 \pm 0.5) \times 10^{-12}\,\mathrm{cm^{-2}s^{-1}}$ calculated from the data from the closer wobble position. All light curve points were fitted with a constant ignoring the ULs (dashed line in Fig. 5.4). The obtained flux fit is $F_{\mathrm{CstFit}} = (2.52 \pm 0.37) \times 10^{-12}\,\mathrm{cm^{-2}s^{-1}}$ and has a χ^2 of 102 for 32 degrees of freedom. This corresponds to a very small probability of 3.10×10^{-9} that the light curve is not variable. Therefore, non-variability can be excluded on a confidence level of $5.8\,\sigma$.

Figure 5.5 shows the distribution of the deviation of the flux measurements from the constant fit given in σ. Clearly, three days deviate by $\gtrsim 3\,\sigma$. Those days, November 16, 2009 (MJD = 55151), January 8 (MJD = 55204) and February 9, 2010 (MJD = 55236)[1], have a mean flux of $(1.60 \pm 0.17) \times 10^{-11}\,\mathrm{cm^{-2}s^{-1}}$. This is six times higher than the flux obtained from the fit with a constant. If these days are not included in the fit the probability for a constant light curve is 36%. A zoom-in to the light curve in November 2009 is shown in Fig. 5.6. On the last day on which MAGIC took data on Perseus the most significant high flux was detected. Due to limited statistics no variability within this observation could be measured.

Even if no observations followed[2], the variability can be studied by measuring the characteristic flux doubling time τ_{D}. This is done by fitting the data points with the function

$$F = F_0 + F \cdot \mathrm{e}^{\tau_{\mathrm{D}}}. \tag{5.3}$$

[1] Observations were taken around midnight in UTC time. Exact observation times are given in Appendix B Table 6.

[2] IC 310 was an un-known TeV source at that time and no skymap tool in the Online Analysis was available to detect off-axis sources.

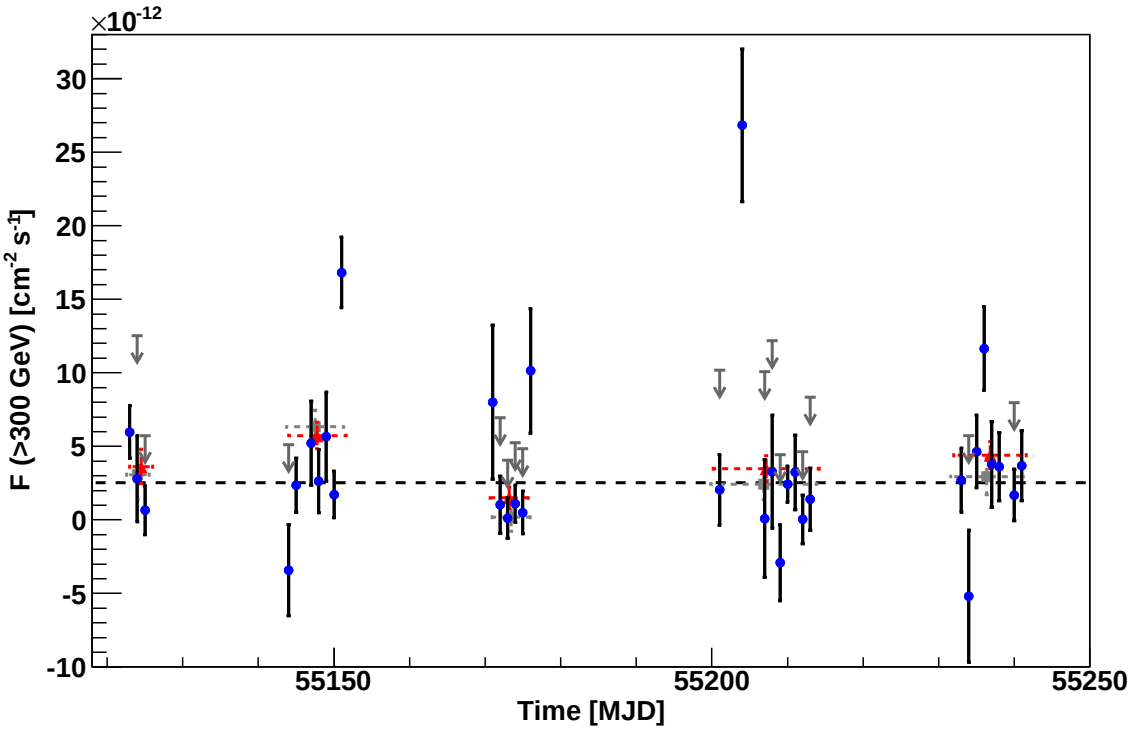

Figure 5.4: Daily (blue markers) and monthly (red markers) binned light curve of IC 310 above 300 GeV from October 2009 to February 2010. The arrows show the 95% confidence level upper limits calculated for individual measurements compatible with no signal. The dashed line shows the constant fit to the light curve with a χ^2/d.o.f of 102/32. Note, that the fit does not take into account the upper limits. For comparison, the monthly binned light curve (grey markers) from Aleksić et al. (2010b) is shown.

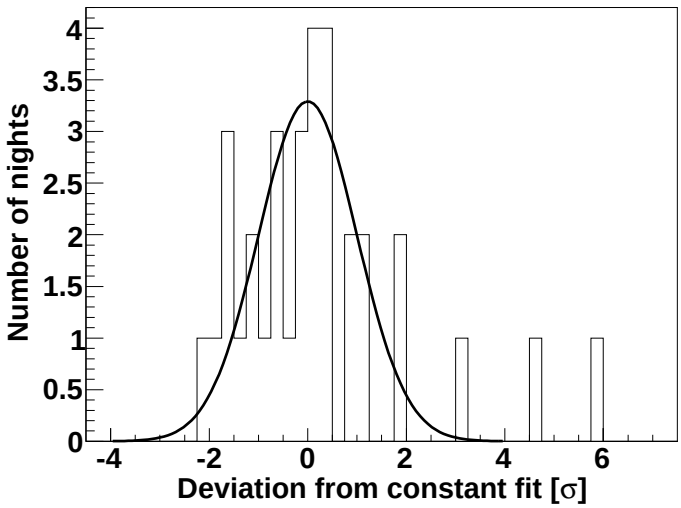

Figure 5.5: Distribution of the number of flux measurements deviating from a fit with a constant in σ.

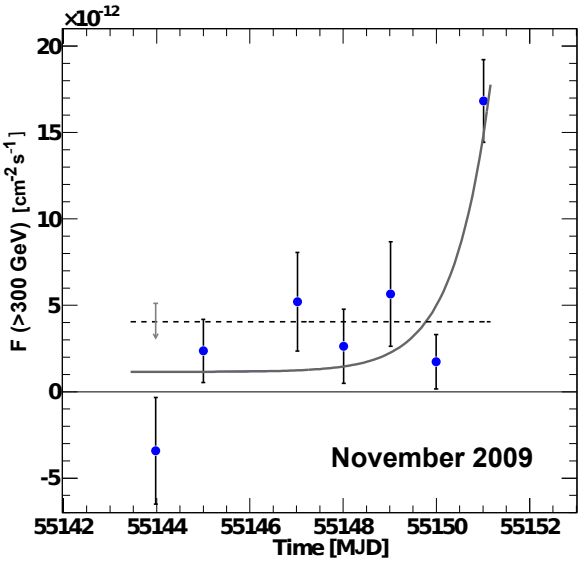

Figure 5.6: Zoom into the light curve above 300 GeV in November 2009. The dashed line shows a constant fit to the data and the thick gray line a fit of a constant plus an exponential rise with a doubling time of $\tau_{\mathrm{Nov,UL}} = 0.55\,\mathrm{d}$. Image adapted from (Aleksić et al. 2014c).

The best fit with this function yields a doubling time of zero due to a very low flux measured in the night prior the flare. In order to find a larger doubling time, the data were fitted with a fixed τ_{D} and the probability of each hypothesis with the χ^2 method was compared. The largest doubling time with a fit probability above 5% was obtained with $\tau_{\mathrm{Nov,UL}} = 0.55\,\mathrm{d}$. This fit is displayed by the thick line in Fig. 5.6.

The other two flares in January and February 2010 provide less constraining results due to a sparse observational time coverage and a much less significant flare in February.

5.3.2 Very High Energy Spectra

For the calculation of the spectra, the data were now split into two data sets corresponding to the different flux states. The "high state" set includes the data from the days with $F_{\mathrm{E>300\,GeV}} > 1.1 \times 10^{-11}\,\mathrm{cm^{-2}\,s^{-1}}$: MJD 55151, 55204 and 55236 ($t_{\mathrm{eff}} = 4.5\,\mathrm{h}$). The "low state" set consist of the remaining data with a total observation time of $t_{\mathrm{eff}} = 38.8\,\mathrm{h}$. Figure 5.7 shows the reconstructed spectral energy distribution $E^2\mathrm{d}N/\mathrm{d}E$ as well as the distributions corrected for the EBL absorption. The spectra between 120 GeV and 8.1 TeV for both states follow a simple power-law function:

$$\frac{\mathrm{d}N}{\mathrm{d}E} = f_0 \times \left(\frac{E}{1\mathrm{TeV}}\right)^{-\Gamma} \left[\frac{10^{-12}}{\mathrm{cm^2 s\,TeV}}\right]. \tag{5.4}$$

The results of the flux normalization at 1 TeV and the photon index Γ are given in Table 5.1. The individual data points in the spectra are also given in Appendix B Table 7. For the correction of the spectra for EBL absorption, the models by Domínguez et al. (2011), Franceschini et al. (2008) and Kneiske & Dole (2010) were applied. Due to the proximity of IC 310 the effect is only minor (see also Appendix B Fig. 5) reducing the flux normalization at 1 TeV by 15–20 % and the photon index by ∼0.1. The observed (and EBL corrected) high and low spectra show no spectral variability as the photon index does not change significantly. In contrast, f_0 varies by a factor of ∼7.

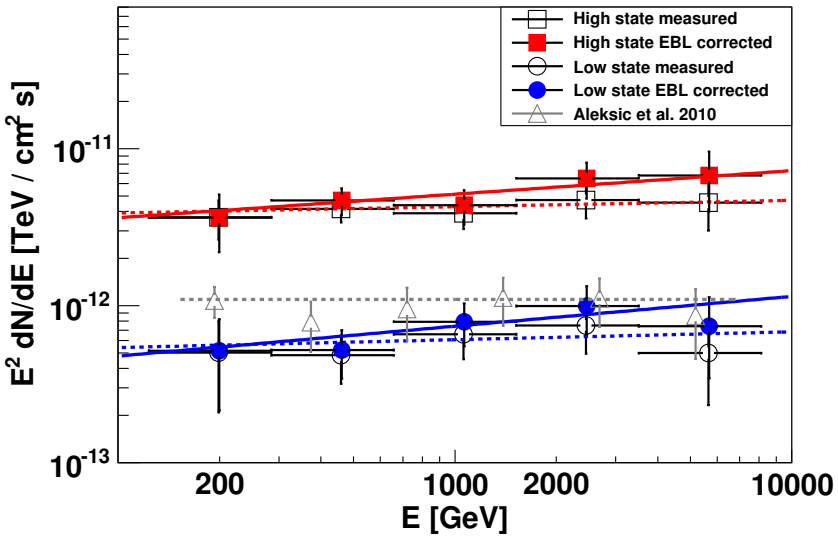

Figure 5.7: High and low state spectral energy distribution of IC 310 measured from October 2009 to February 2010. Open markers show the measured distribution and filled markers the spectra corrected for EBL absorption. Also shown are the power-law fits as dashed line (measured) and solid line (EBL corrected). Fit parameters are given in Table 5.1. For comparison, the result from (Aleksić et al. 2010b) (gray triangles, without EBL de-absorption) for the same time period is shown. Image adapted from Aleksić et al. (2014c).

Table 5.1: Power-law fit parameters of the spectra between 0.12–8.1 TeV. The measured and the EBL corrected (Domínguez et al. 2011) results are listed. Table taken from Aleksić et al. (2014c).

State		$f_0 \pm f_{\mathrm{stat}} \pm f_{\mathrm{syst}}$ $\times 10^{-12} [\mathrm{TeV}^{-1}\,\mathrm{cm}^{-2}\,\mathrm{s}^{-1}]$	$\Gamma \pm \Gamma_{\mathrm{stat}} \pm \Gamma_{\mathrm{syst}}$
High	observed	$4.28 \pm 0.21 \pm 0.73$	$1.96 \pm 0.10 \pm 0.20$
	intrinsic	$5.14 \pm 0.28 \pm 0.90$	$1.85 \pm 0.11 \pm 0.20$
Low	observed	$0.608 \pm 0.037 \pm 0.11$	$1.95 \pm 0.12 \pm 0.20$
	intrinsic	$0.741 \pm 0.045 \pm 0.14$	$1.81 \pm 0.13 \pm 0.20$

Table 5.2: Arrival times and energies of gamma events above 10 GeV measured within a circle around IC 310 with a radius of 0.3° in the first three years by *Fermi*-LAT. Table taken from Aleksić et al. (2014c).

MJD	Energy [GeV]
54720.03	96.4
54833.95	112.1
54846.64	22.2
54972.38	12.6
55081.11	39.0
55118.56	148.3
55247.01	12.1
55462.98	46.3

Table 5.3: Results of the archival X-ray observations. Table taken from Aleksić et al. (2014c).

Instr.	Date [MJD]	Expo. [ks]	$F_{0.5-2\,\mathrm{keV}}{}^{a}$ [$10^{-3}\,\mathrm{keV\,s^{-1}\,cm^{-2}}$]	$F_{2-10\,\mathrm{keV}}{}^{b}$ [$10^{-3}\,\mathrm{keV\,s^{-1}\,cm^{-2}}$]	Γ^{c}	$N_{\mathrm{H}}{}^{d}$ [$10^{22}\,\mathrm{cm^{-2}}$]	χ^2/d.o.f.
XMM	52697	22.6	1.007 ± 0.012	$0.828^{+0.026}_{-0.040}$	$2.55^{+0.07}_{-0.04}$	$0.146^{+0.016}_{-0.008}$	124/104
Chandra	53456	1.5	1.77 ± 0.13	2.5 ± 0.4	2.01 ± 0.20	$0.07^{+0.08}_{-0.07}$	62/78
Chandra	53363	25.2	0.656 ± 0.019	1.39 ± 0.08	1.76 ± 0.07	$0.089^{+0.028}_{-0.027}$	97/78
XRT	54152	4.1	0.82 ± 0.10	$1.2^{+0.6}_{-0.5}$	$2.0^{+0.5}_{-0.4}$	$0.07^{+0.13}_{-0.07}$	12/16

Notes. $^{(a)}$ Flux between 0.5 and 2 keV determined by a simple power-law fit. $^{(b)}$ Flux between 2 and 10 keV determined by a simple power-law fit. $^{(c)}$ Photon index ($\propto E^{-\Gamma}$). $^{(d)}$ Absorption with an equivalent column of hydrogen.

5.3.3 Results from the High Energy Band

In three years of data taking, *Fermi*-LAT detected IC 310 above 10 GeV with a test statistic of $\mathrm{TS} = 27.0$ which corresponds to 4.5 σ. The measured integral flux in this time period between 10 and 500 GeV was $(6.9 \pm 3.3) \times 10^{-11}\,\mathrm{cm^{-2}\,s^{-1}}$. The spectrum was fitted with the following power-law function with a photon index of $\Gamma = 1.3 \pm 0.5$:

$$\frac{\mathrm{d}N}{\mathrm{d}E} = \frac{F_{10-500}(-\Gamma+1)E^{-\Gamma}}{E_{\mathrm{max}}^{-\Gamma+1} - E_{\mathrm{min}}^{-\Gamma+1}} \left[\frac{1}{\mathrm{cm^2 s\,GeV}}\right]. \tag{5.5}$$

E_{min} and E_{max} are the lower and the upper boundary of the energy bins quoted in GeV, respectively. The spectral energy distribution is shown in Fig. 5.8. For comparison, the distribution from the 2FGL catalog (two years of data taking) is displayed in the same figure.

The energy and arrival times of the photons detected by LAT above 10 GeV are given in Table 5.2. Interestingly, seven of the eight photons arrived within the first 1.5 years (see also Appendix B Fig. 4). However, firm conclusions on variability or connection between LAT detected photons and MAGIC high states can not be drawn. The time coverage of MAGIC is limited and the statistics of LAT detected events is too low.

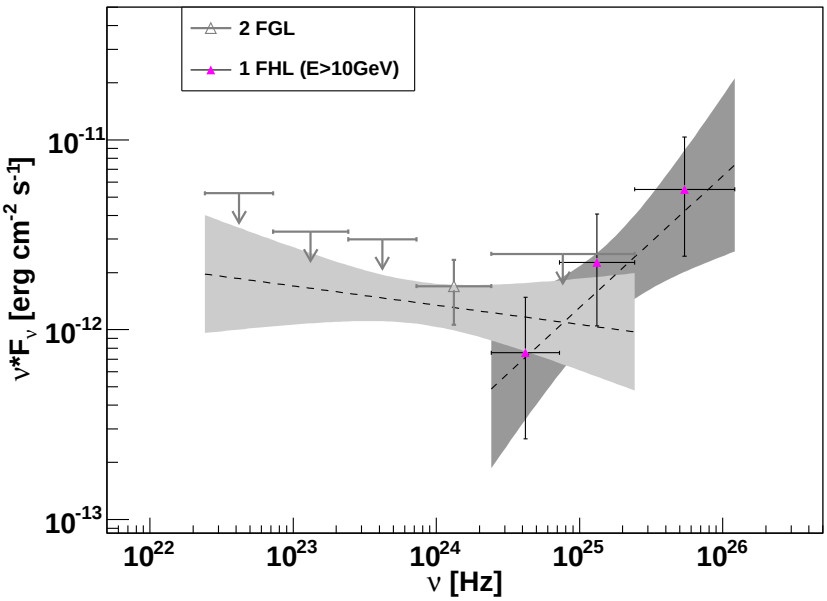

Figure 5.8: Spectral energy distribution measured with the *Fermi*-LAT instrument. The gray, open triangle and the gray upper limits are obtained from the 2FGL catalog (Nolan et al. 2012). Filled triangles and the dark gray butterfly depict the results from the 1FHL catalog (Ackermann et al. 2013; Aleksić et al. 2014c).

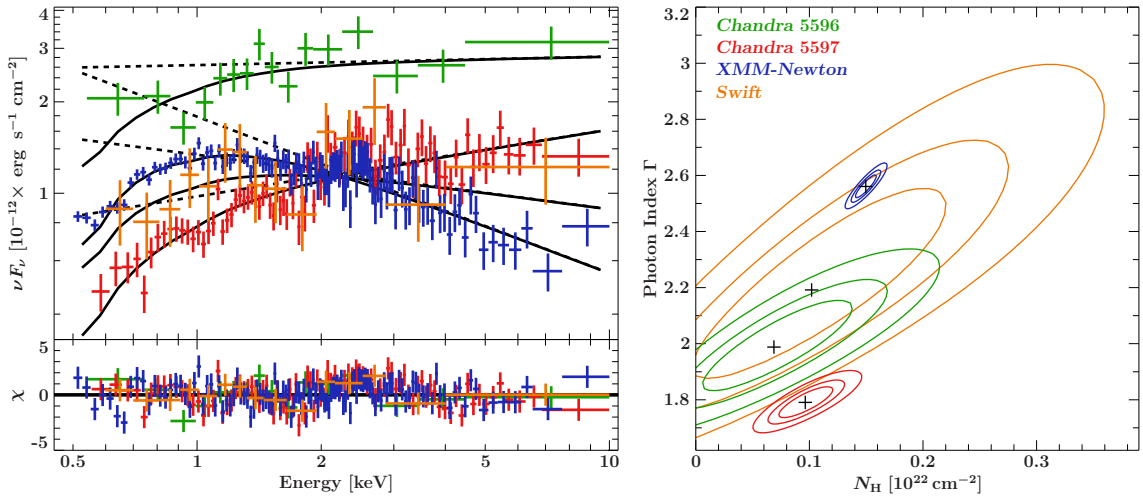

Figure 5.9: *Top left panel:* Archival X-ray spectra of IC 310 in different time periods. *Chandra* Obs. ID 5596 (green), *XMM-Newton* (blue), *Chandra* Obs. ID 5597 (red) and *Swift*-XRT (orange). Solid/dashed lines show the absorbed/de-absorbed power-law fit. *Bottom left panel:* Residuals of the χ^2 fit. *Right panel:* Contour plot of the intrinsic column density N_H versus the X-ray photon index Γ for the spectra depicted in the left panel. The contours are given at 68%, 90%, and 99% confidence level. For comparison, the galactic N_H value is $0.12 \times 10^{22}\,\mathrm{cm}^{-2}$ (Kalberla et al. 2010). Image taken from Aleksić et al. (2014c).

Table 5.4: Effelsberg flux density measurements on July 23, 2011. Table taken from Kadler et al. (2012).

Band	λ^a [cm]	ν^b [GHz]	I^c [mJy]	P^d [mJy]	m^e [%]	χ^f [deg]
S	11	2.64	383 ± 3	17 ± 4	4.5 ± 1.1	-2 ± 7
C	6	4.85	238 ± 4	10 ± 4	4.0 ± 1.7	-29 ± 9
X	3.6	8.35	148 ± 3	< 10	...	...
X	2.8	10.45	155 ± 15	< 10	...	...
U	2	14.60	103 ± 6	...	...	...

Notes. $^{(a)}$ Observing wavelength. $^{(b)}$ Observing frequency. $^{(c)}$ Total flux density. $^{(d)}$ Linearly polarized flux density. $^{(e)}$ Polarization degree. $^{(f)}$ Electric vector position angle.

5.3.4 X-ray Behavior

Table 5.3 and Fig. 5.9 summarize the results of the analysis of archival X-ray data for one *XMM-Newton*, two *Chandra* and one *Swift*-XRT observation. The absorption column $N_{\rm H}$ and the photon index Γ were determined from fits of simple power-law models in the energy range of 0.5–10 keV. Both parameters were left free during the fitting procedure. In comparison with the other results, the obtained $N_{\rm H}$ from the *XMM-Newton* data differs from the neutral galactic absorption towards IC 310 which is $N_{\rm H} = 0.12 \times 10^{22}\,{\rm cm}^{-2}$ (Kalberla et al. 2010).

Between 2003 and 2007, the flux changed in the low energy regime (0.5–2 keV) as well as in the higher energy range (2–10 keV). This is accompanied by changes in Γ and $N_{\rm H}$. The former varies between $\Gamma = 2.5$ (soft) and $\Gamma = 1.8$ (hard). Γ and $N_{\rm H}$ are strongly correlated parameters. The confidence contours are shown in the right hand panel in Fig. 5.9. Due to a low signal-to-noise ratio of the *Swift* data, the contours allow no firm conclusions on variability. Comparing the results of the *XMM-Newton* and *Chandra* observation, one can see a significant change of the spectral slope. Furthermore, the $N_{\rm H}$ in the *XMM-Newton* observation is higher than the *Chandra* Obs. ID 5597. An increased intrinsic absorption in the object might be caused by the presence of material close to the black hole. Such variability of the intrinsic $N_{\rm H}$ was observed for Centaurus A over a long (Benlloch et al. 2001) and short (Rivers et al. 2011) period.

5.4 Radio Results

The results of the flux density (S) measurements with the Effelsberg 100 m telescope are summarized in Table 5.4.

The radio spectrum of IC 310 can be described by a steep simple power-law ($S \propto \nu^{-\alpha}$) with $\alpha = 0.75$. At high frequencies (≥ 14.6 GHz), the object appears compact with a rather flat spectrum. At lower frequencies, the spectrum is dominated by the optically thin emission of the kpc-scale radio jet as previously reported by Sijbring & de Bruyn (1998); Feretti et al. (1998). Comparing this with the VLBI measurements shown below, the total flux density at 8.3 GHz was found to be (148 ± 3) mJy. Therefore, > 80 % of the emission at this frequency can be assumed to be originating from scales < 1 mas.

The analysis of the two VLBA observations at 8.3 GHz resulted in the detection of an one-sided blazar-like core-jet morphology with a ~ 20 mas jet pointing in the direction towards a

Table 5.5: VLBA map parameters of the images shown in Fig 5.10 and 5.11. Table taken from Kadler et al. (2012).

Epoch	$S_{\rm tot}$ [mJy]	$S_{\rm peak}$ [mJy/beam]	rms [mJy/beam]	Beam [mas $\times$ mas , deg]
2011/05/16	118.8 ± 6.0	88.7 ± 4.4	0.20	2.50×0.94 , -28.4
2011/05/30	115.0 ± 6.1	85.1 ± 4.6	0.21	2.39×0.94 , -13.5
Combined	115.6 ± 7.9	84.8 ± 5.7	0.16	2.34×0.93 , -21.5
Combined Taper	113.6 ± 7.7	94.5 ± 6.4	0.17	2.63×1.76 , -21.5

position angle (PA) $-135°$, see Fig. 5.10. The parameters belonging to the images are listed in Table 5.5. No hint for a counter-jet could be observed.

The flux densities measured from the two observations are comparable within the errors. Therefore, the data have been merged in order to achieve a higher signal-to-noise ratio. The resulting image is shown in the inset of Fig. 5.11. In addition, the kpc-scale (resolution of 45 arcsec) radio jet from the NRAO VLA Sky Survey obtained on December 15, 1993 is viewed. The VLBA beam size projected along the direction of the jet of ~ 2 mas could been achieved. From the core, a flux density has been measured to be $80 - 90$ mJy, and a size of (0.3 ± 0.4) mas yielding a brightness temperature of $\sim 1.5 \times 10^{10}$ K. Additionally, tow jet components were found, one with 14 mJy at 0.8 mas (PA $-144°$) and one with 10 mJy at $3 - 8$ mas away from the core. Hence, a compactness at 8.3 GHz of ~ 70 % was measured.

5.5 Influence on Physical Processes and AGN Classification

The observational results presented in this chapter have strong impact on the classification of the active nucleus of IC 310. The classification will be now discussed along with implications on the underlying physical processes.

5.5.1 Misclassification as HTRG and Viewing Angle

As mentioned in Section 2.8, IC 310 was originally classified as HTRG. However, the high resolution VLBI images of the object show an one-sided core-jet structure in the direction of the large scale structure, see Fig. 5.11. There seems to be no indication for a jet bending process, neither on large nor on small scales. The difference between the directions of the kpc and pc-scale jets is about $\lesssim 10°$. Therefore, the direction of the kpc scale jet is more likely to be determined by the small scale structure rather than by a bow shock. Hence, IC 310 was probably misclassified.

The observed variability in the X-ray to TeV band is another indicator for the misclassification. If the gamma-rays would be associated with the bow shock driven into the ICM an almost steady-state emission would be produced as explained by Neronov et al. (2010). However, with the day-to-day variability measured with MAGIC in October 2009 to February 2010 this scenario can be ruled out. More likely, the VHE emission observed originates from the blazar-like central engine.

The one-sidedness of the radio jet might be caused by relativistic bulk motion along a small angle between the jet-axis and the line-of-sight, similarly to a blazar. This leads to a Doppler

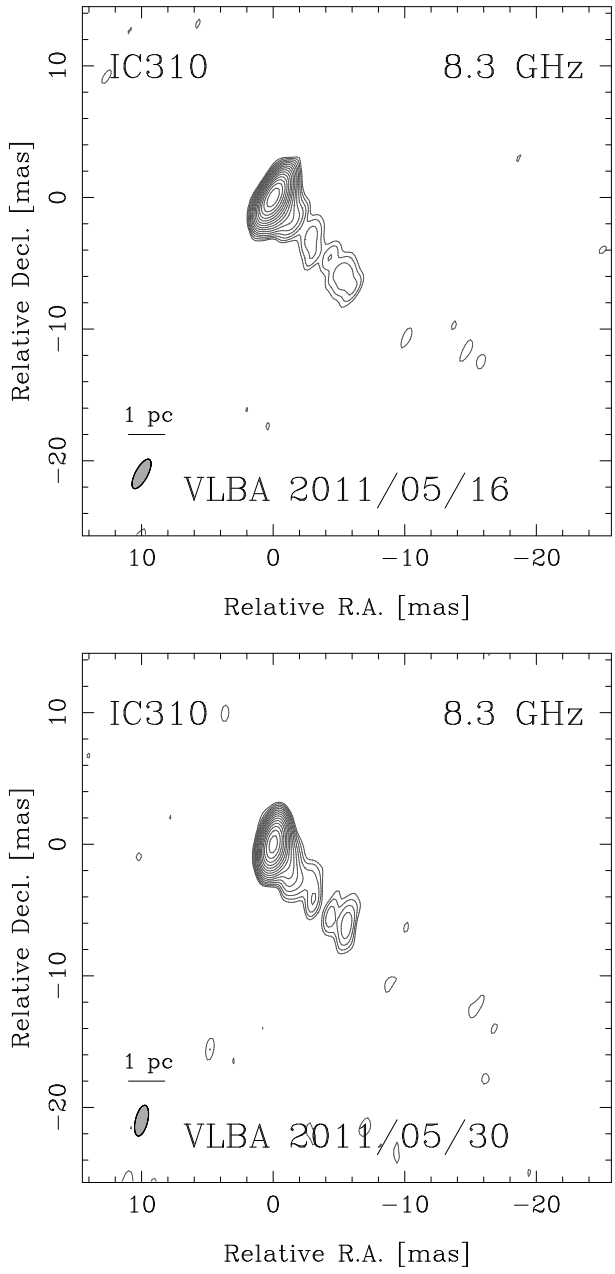

Figure 5.10: VLBA images of IC 310 obtained on May 16 (*top*) and May 30 (*bottom*), 2011. Lowest contours are 2.5× the rms level. Further images paramters are given in Table 5.5. Image adapted from Kadler, Eisenacher et al. (2012).

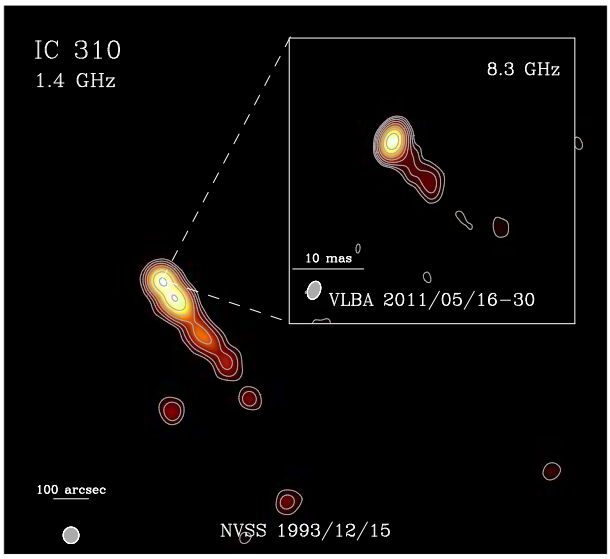

Figure 5.11: Kpc-scale jet measured at 1.4 GHz with the VLA and the pc-scale jet at 8.4 GHz with the VLBA of IC 310. Image parameters of the VLBI map are given in Table 5.5. Image taken from: Kadler, Eisenacher et al. (2012).

boosting of the approaching jet and a deboosting of the counter-jet. Measuring the ratio between the flux densities of the jet and its counter-jet allows the estimate of the angle to the line-of-sight θ according to Eq. 2.21. Since no signal from the counter-jet (below $3\,\sigma$) could be found in the VLBI measurements at 8.3 GHz, only an upper limit to the angle can be calculated. From the VLBI image, a ratio of $R > 177$ was found. Assuming a flat spectrum with $\alpha = 0$ and letting $\beta \to 1$ yields an upper limit[3] of $\theta < 31°$.

The lower limit can also be derived from the emission maximum 3 arcsec away in the jet direction of the 49 cm image in Sijbring & de Bruyn (1998) assuming one-sidedness on all scales. The local peak of ~ 400 mJy together with the $3\,\sigma$ noise on the other side of the core gives $R > 500$. Applying further the measured spectral index of $\alpha = 0.75$ yields $\theta < 36°$.

A more conservative estimate yields $\theta < 38°$ when applying a ratio of $R = 162/0.8 = 202$ inferred from the first jet maximum in the 1.4 GHz image of VLA at ~ 23 kpc, and assuming a spectral index of $\alpha = 0.5$ at this position.

Using Eq. 2.23 and assuming further an apparent speed of $\beta_{\rm app} = 1$ as measured by Piner & Edwards (2004); Piner et al. (2010) for TeV loud BL Lac objects, yields a constraint for the Doppler factor of $\delta > 3.5$ ($R > 177$, $\alpha = 0$), $\delta > 2.9$ ($R > 500$, $\alpha = 0.75$), and $\delta > 2.7$ ($R > 202$, $\alpha = 0.5$). For comparison, typical Doppler factors for Centaurus A, M87, and NGC 1275 are $\delta_{\rm Cen\,A} < 3.8$ (Abdo et al. 2010b), $\delta_{\rm M87} \sim 3.9$ (Abdo et al. 2009b), and $\delta_{\rm NGC\,1275} \sim 2.3$ (Abdo et al. 2009a), respectively.

Furthermore, the linear size of the projected extended kpc jet enables an estimate of a lower limit of the angle. Sijbring & de Bruyn (1998) measured an extension of the jet of ~ 350 kpc at a wavelength of 49 cm. De-projecting of the jet with simple geometrical arguments using the largest limit quoted above of $\theta < 38°$ yields a jet length of ~ 570 kpc. This is already larger than the peak of the distribution of jet lengths obtained from FR II radio galaxies which lies at about 150 kpc-300 kpc, see Fig. 5.12 from Neeser et al. (1995).

The length of a radio jet may extent up to 4.7 Mpc which is the record up to now observed

[3] This calculation can be also found in Kadler et al. (2012).

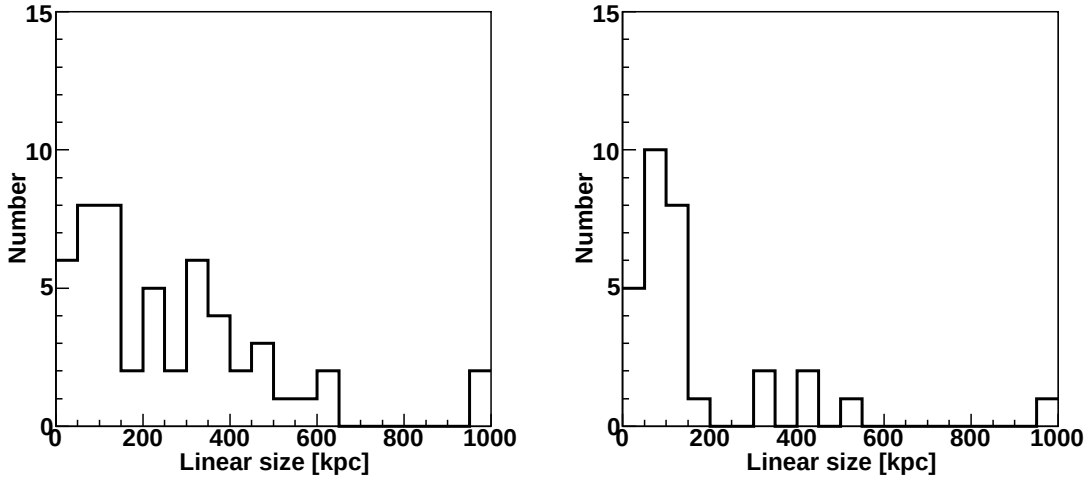

Figure 5.12: Distribution of linear sizes of FR II radio galaxies. The linear sizes were calculated assuming $\Omega_0 = 1$. *Left panel:* Objects of the 3C source catalog. *Right panel:* Objects of the 6C source catalog. Image adapted from Neeser et al. (1995).

from the giant radio galaxy J1420-0545 (Machalski et al. 2008). Assuming such a long jet for IC 310 would imply an angle of only $\sim 4°$. However, J1420-0545 is an extreme case making a limit of $\theta \sim 10°$ more likely. Large linear sizes of jets may result in inconsistencies of the advance speed of jets into the intergalactic medium, the mass of an AGN and its lifetime. For example, an advance speed is of the order of 0.01 c (Parma et al. 2002) and a lifetime of 10^8 yr (Sijbring & de Bruyn 1998; Feretti et al. 1998) would produce a ~ 300 kpc long jet. The lifetime has been inferred from the space density of AGN and their host galaxies (Sijbring & de Bruyn 1998) or estimated directly for IC 310 from the calculation of the electron aging along the kpc jet of $2 - 2.5 \times 10^8$ yr (Feretti et al. 1998). However, the latter is only a lower limit since it strongly depends on the sensitivity of the instrument. Applying this lifetime would imply a jet length of > 800 kpc corresponding to a limit of $\theta \sim 26°$. Interestingly, the mass grow in this time span is consistent with the mass of the black hole of IC 310 (Appendix A Section 1) if assuming an accretion with an Eddington rate of several solar mass per year.

An angle of the jet-axis to the line-of-sight of $10° \leq \theta \leq 38°$ places IC 310 at the borderline between radio galaxies and BL Lac objects. As seen in Fig. 2.4, this range of the angle allows only low values of the Doppler factor. Therefore, for the later discussion $\delta \sim 3 - 4$ is used.

5.5.2 Localization and Size of the TeV Emission Region

According to Eq. 2.24, the variability time-scale $\tau_{\rm var}$ allows an estimation of the radius of a spherical emission region R. For $\tau_{\rm var} = 1$ d and $z = 0.0189$ the radius of the emission region must be $R \lesssim \delta \times 2.5 \times 10^{15}$ cm. Using the upper limit for the doubling time $\tau_{\rm Nov,UL} = 0.55$ d (see Section 5.3.1) the radius is calculated to be $R \lesssim \delta \times 1.4 \times 10^{15}\,{\rm cm}$. Assuming a mass of the black hole of $M_{\rm BH} \simeq 3 \times 10^8\,{\rm M}_\odot$ (see Appendix A Section 1), the radius can be compared with the Schwarzschild radius of IC 310 yielding:

$$R \lesssim 16\,\delta\,R_{\rm S}. \tag{5.6}$$

Adopting a Doppler factor of $\delta \sim 3 - 4$ known from radio observations (see Section 5.5.1)

the radius becomes $R \lesssim (47 - 63)\, R_{\rm S}$.[4]

This rather small emission region (compared to the dimension of the jet) implies high local photon densities and thus might be incompatible with the observed VHE spectrum up to $\sim 10\,$TeV. This could be caused by absorption of gamma-rays via pair production on the low-energy photon field with a synchrotron luminosity $L_{\rm syn}$ produced by electrons (see Chapter 2.6). Equation 2.32 can be used to estimate a limit for $L_{\rm syn}$ in the local near-infrared (NIR) region associated with the gamma-ray spectrum up to $\sim 10\,$TeV. This leads to

$$L_{\rm syn} \sim 1.8 \times 10^{39}\, \delta^6\, \tau_{\rm var}\, {\rm erg\,s^{-1}}. \tag{5.7}$$

Assuming $\tau_{\rm var} \approx 0.55\,{\rm d}$ ($\approx 1\,{\rm d}$) this becomes $L_{\rm syn} \sim \delta^6 \cdot 8.4 \times 10^{43}\,(1.5 \times 10^{44})\,{\rm erg\,s^{-1}}$. The observed NIR luminosity of the host galaxy was found to be $L_{2\,\mu{\rm m}} = 2 \times 10^{44}\,{\rm erg\,s^{-1}}$ measured by Skrutskie et al. (2006). Hence, $L_{\rm syn} < L_{2\,\mu{\rm m}}$ applies if no Doppler boosting is assumed. Assuming a Doppler boosting with $\delta = 4$, the non-thermal NIR emission may reach a weak luminosity of $L_{\rm syn} \approx 1\%\, L_{2\mu{\rm m}}$. If this emission component extends up to the X-ray regime, this would still be consistent with the observed X-ray luminosity. Measurements with IRAS (Beichman et al. 1988) showed a infrared (IR) luminosity of $L_{12\,\mu{\rm m}} < 9.8 \times 10^{42}\,{\rm erg\,s^{-1}}$ and $L_{100\,\mu{\rm m}} = 4.7 \times 10^{43}\,{\rm erg\,s^{-1}}$. Interpolating this to a wavelength of $20\mu{\rm m}$ yields $L_{20\,\mu{\rm m}} \sim 10^{43}{\rm erg\,s^{-1}}$. This leads to an optical depth of

$$\tau_{\gamma\gamma}(10\,{\rm TeV}) \simeq \left(\frac{L_{20\,\mu{\rm m}}}{10^{43}{\rm erg\,s^{-1}}}\right)\left(\frac{r_{\rm dust}}{1{\rm kpc}}\right)^{-1} \sim 1, \tag{5.8}$$

for isotropic infrared photons from the gas and dust torus with radius $r_{\rm dust}$. Therefore, some TeV photons can still escape the torus freely and hence may also originate from a region close to the central engine. The photons of a possible present accretion disk would not significantly increase the optical depth at VHE energies because of the decrease of the pair production cross section above the threshold.

The day-scale TeV variability and the VHE spectrum are hence still consistent with the scenario that the high-energy emission is produced by a shock in the jet.

5.5.3 IC 310 seen as a Blazar and the Blazar Sequence

Figure 5.13 shows the non-simultaneous observed spectral energy distribution (SED) extending from X-ray to VHE. Typically, the νF_ν graph of a blazar features two bumps. As explained in Chapter 2.5.1 the low energy bump is produced by synchrotron emission. The origin of the high energy emission maximum is still a matter of discussion.

The shape of the multi-wavelength SED (even if the entire frequency range can not be covered) of IC 310 supports the notion that the high-energy emission especially in the HE and VHE regime is associated with a blazar-type jet. It is notable however, that the apparent VHE luminosity of $10^{42-43}\,{\rm erg\,s^{-1}}$ is a few orders of magnitude lower than for typical TeV blazars (see Fig. 2.3) even in a higher emission state of the object. Since the X-ray and VHE data are not simultaneous, the conclusions also with respect to the blazar sequence listed in the following have to be drawn with caution.

- In Giommi et al. (2012a) the authors show that within a redshift of $z < 0.07$, i.e., in the local universe in which also IC 310 is located, low luminosity AGNs might be originally

[4] The numbers given in this differ from those given in Aleksić et al. (2014c) as a different value for the black hole mass of IC 310 was used.

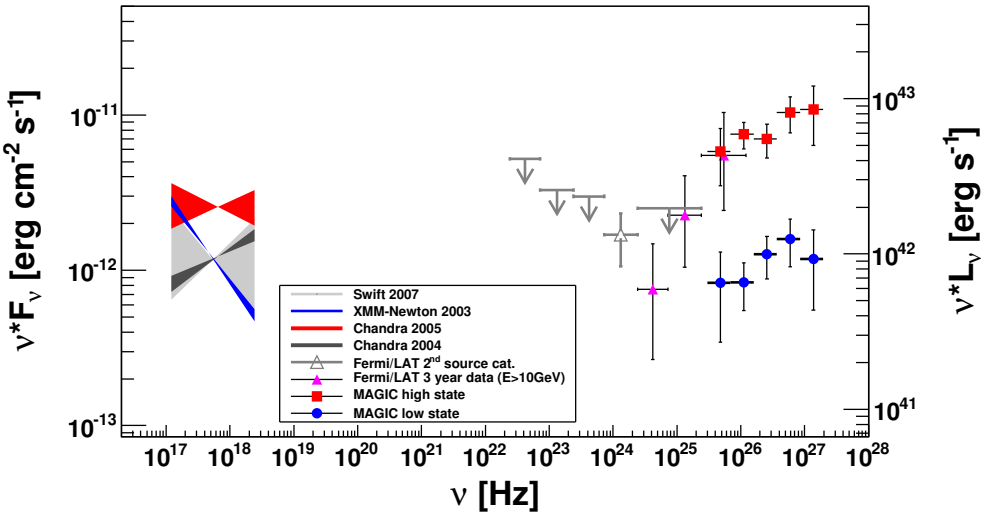

Figure 5.13: Historical measurement of the spectral energy distribution from X-rays to VHE gamma rays. In the X-ray range, butterflies of the observations are shown. Colors are explained in the legend. The gray, open triangle and the gray upper limits are taken from the 2FGL catalog (Nolan et al. 2012). Filled, pink triangles depict the results from the dedicated high-energy analysis above 10 GeV from the 1FHL catalog (Ackermann et al. 2013). The MAGIC results (EBL corrected) for the high (red) and low (blue) states are marked with full squares and full circles, respectively. The corresponding apparent luminosity is given at the right axis and has been calculated from the luminosity distance of 81 Mpc. Image adapted from Aleksić et al. (2014c).

misinterpreted as radio-galaxy. The jet points roughly towards the Earth, thus having a small angle to the line-of-sight. But the blazar-like emission gets outshined by the strong emission of their own host galaxy. This could also be the case for IC 310.

- The blazar sequence (Fossati et al. 1998; Ghisellini et al. 1998) suggests a lower apparent luminosity of the overall SED as the synchrotron and the high-energy peak shift to higher frequencies. Remembering the *Chandra* measurement in 2004 with a hard spectrum still rising in the νF_ν graph and the VHE spectra, IC 310 might then be a candidate for a very extreme high frequency peaked BL Lac object (VEHBL). The first bump would lie in the hard X-ray regime, and the second at multi-TeV energies. However, such objects have not been detected yet. This is probably due to the limited sensitivity of the telescopes, but tracing the blazar sequence such a population may exist.

- The previous point is also in line with the idea of the cosmic evolution of blazars as explained in Chapter 2.5.3. Blazars with low accretion rates, i.e., low luminosities and high masses of the central black hole are at the end of the stage of development. The accretion process of the surrounding matter of IC 310 might be advanced, explaining the relatively high black hole mass and low luminosity.

- The low luminosity problem could be a consequence of a small misalignment, i.e., a larger angle to the line-of-sight of an extreme HBL like 1ES 1426+428, an object with an synchrotron peak measured around 100 keV (Wolter et al. 2008). A discrepancy of, e.g, $\sim$100 in luminosity corresponds to an angle of $\sim$8.5° assuming a typical Lorentz factor of $\Gamma_\mathrm{b} = 15$, and $\delta \sim 5$ consistent with the Doppler factor obtained from the radio

measurements (Section 5.5.1). Indeed, Ghisellini & Tavecchio (2008) predicted a large population of weak blazars with relatively small viewing angles of $\theta = 4 - 7°$. However, such an angle would be in contradiction with variability of shorter (< 1 d) time scales (see Chapter 6) and a large extension of the kiloparsec radio jet (see Section 5.5.1). It should also be noted that jets of TeV emitting HBLs typically lose their structure after a few kiloparsecs as presented in Rector et al. (2003) which is surely not the case for IC 310 with a projected jet of ~ 350 kpc (Sijbring & de Bruyn 1998).

In summary, IC 310 may be considered as a representative of a transitional population between low-luminosity blazars and FR I radio galaxies.

6

An Exceptional Bright TeV Flare

A Cosmic Treasure Hunt

This chapter is based on a measurement of an exceptional TeV flare detected by MAGIC announced in The Astronomer's Telegram #4583, #4581 (Cortina 2012; Krauß et al. 2012). The observational results were connected with high-resolution radio measurements from EVN. These observations were part of an intense multi-wavelength program described in Chapter 7. The analysis results and the theoretical interpretation can be found in the publication *Science*, Vol. 346, 1080.

6.1 MAGIC Observation and Data Analysis

In the night of November 12 to 13, 2012 (MJD 56243.95–56244.11) MAGIC started the observation of the Perseus cluster after the commissioning phase of the fully upgraded system had ended. The data was taken with the wobble mode "NGC 1275" illustrated in Fig. 6.1. Here, four wobble positions are used with an offset of $0.4°$ centering around the center of the cluster, NGC 1275. This mode allows for a homogeneous camera illumination, i.e., a better control of the background subtraction is possible. This is important for measuring the lowest energies ($E < 100\,\mathrm{GeV}$). For the analysis of the emission from NGC 1275 this is necessary due to its very soft power-law spectrum ($\Gamma \sim 4$). In case of IC 310, however, this requires dedicated MCs for the data which has a wobble offset of $0.938°$ (W0.40+058, W0.40+337). The remaining data from the wobble positions W0.40+157, and W0.40+238 can be analyzed with the standard MCs with the default wobble offset of $0.4°$.

The total observation time in that night was 3.7 h. Due to a nearly perfect weather condition and the absence of technical problems, no data needed to be rejected. The signal extraction, calibration, and image parametrization was applied as described in Chapter 4. For the image cleaning, the 6-3.5 dynamical sum-cleaning algorithm was used (see Section 4.5.2). In addition to the standard analysis, the dynamical parameters were calculated within *star* and *superstar*. Some of those (WIDTH and LENGTH) were used in the training of the RF for the gamma-hadron separation and DISP method. For the training, data from M87, PKS1222+21, 2FGLJ1410+74

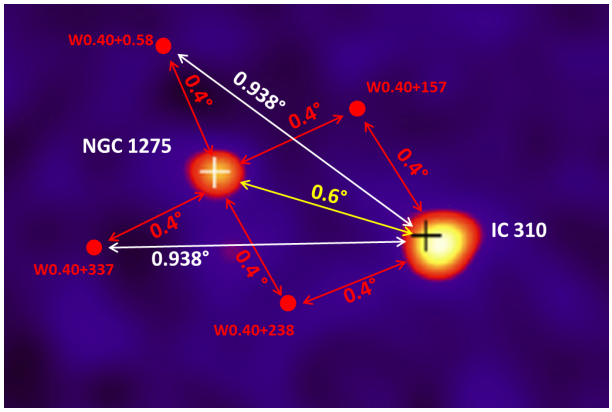

Figure 6.1: Configuration of the wobble positions during the flare. This mode is called "NGC 1275 mode". Here, four position were used centered around NGC 1275, W0.40+058 and W0.40+337 each with an offset of $0.938°$, and W0.40+157 and W0.40+238 with $0.4°$ distance to IC 310.

and from Dark Patches 2, 4, 6, 11, 18, 22, 25, 28, 29, and 31 was applied as Off sample (see Appendix B Table 8) covering a Zd range of $9° - 56°$ ($t_{\text{eff}} = 11.0\,\text{h}$). The reconstruction of the energy and DISP was performed in the standard way (see Section 4.5.5). To calculate the effective area of the data with $0.938°$ offset, special MCs in addition to the standard MCs were generated and used in this analysis.

The study of the light curve was performed with the classical method consisting of time bins of fixed width. In addition, a new approach with time bins of fixed number of ON events was implemented. The latter is commonly used by the X-ray community for the calculation of spectra. Finding variability on shorter time scales is less affected by limited statistics of the gamma-ray and background events. The program first identifies time gaps shorter than $\lesssim 1$ min (resulting from, e.g., changes of the wobble position). Then, the remaining time is sampled on a certain number of ON events. As one can see from Fig. 6.4, the ratio between the signal and the background is $\gg 1$. Thus, the precision of individual data points in the light curves is $\lesssim 3\sigma$.

To test this approach, a light curve from Crab nebula data taken on January 9, 2013 has been rebinned according to 16 and 9 ON events per bin (see Fig. 6.2). It can be seen that the 16 ON events light curve represents the light curve with fixed time bins very well. A constant fit to the 16 ON events light curve gives a $\chi^2/\text{d.o.f.} = 32.6/29$. Applying the 9 ON events binning to the light curve produces a few outlier which deviate by $\lesssim 2\sigma$ from the light curve with fixed time binning. However, the constant fit to the 9 ON events light curve still shows a reasonably good $\chi^2/\text{d.o.f.}$ of $50.6/51$.

Furthermore, a toy MC study was performed comparing this method with the classical one (see Fig. 6.3). From this study, one can see that a low number of events in a fixed time width bin ($\lesssim 10$) may result in an underestimation of the error in the flux because of down fluctuations of the number of events. This explains the tail in the distribution of the residua, bias in the mean, and the RMS of the resulting distribution. For comparison, examples are shown for Mean = -0.1 to -0.2 and RMS = 1.05 to 1.15. The characteristic, discrete shape follows from an integer, Poissonian statistic of the events in a bin of fixed time. In contrast, the method with fixed number of ON events permits a continuous distribution of the residuals without a net bias (Mean $= 0$, RMS $= 1$). To correct the asymmetry of the residua distribution in both approaches, an assumption of the unknown shape of the light curve must be applied. However, this was not

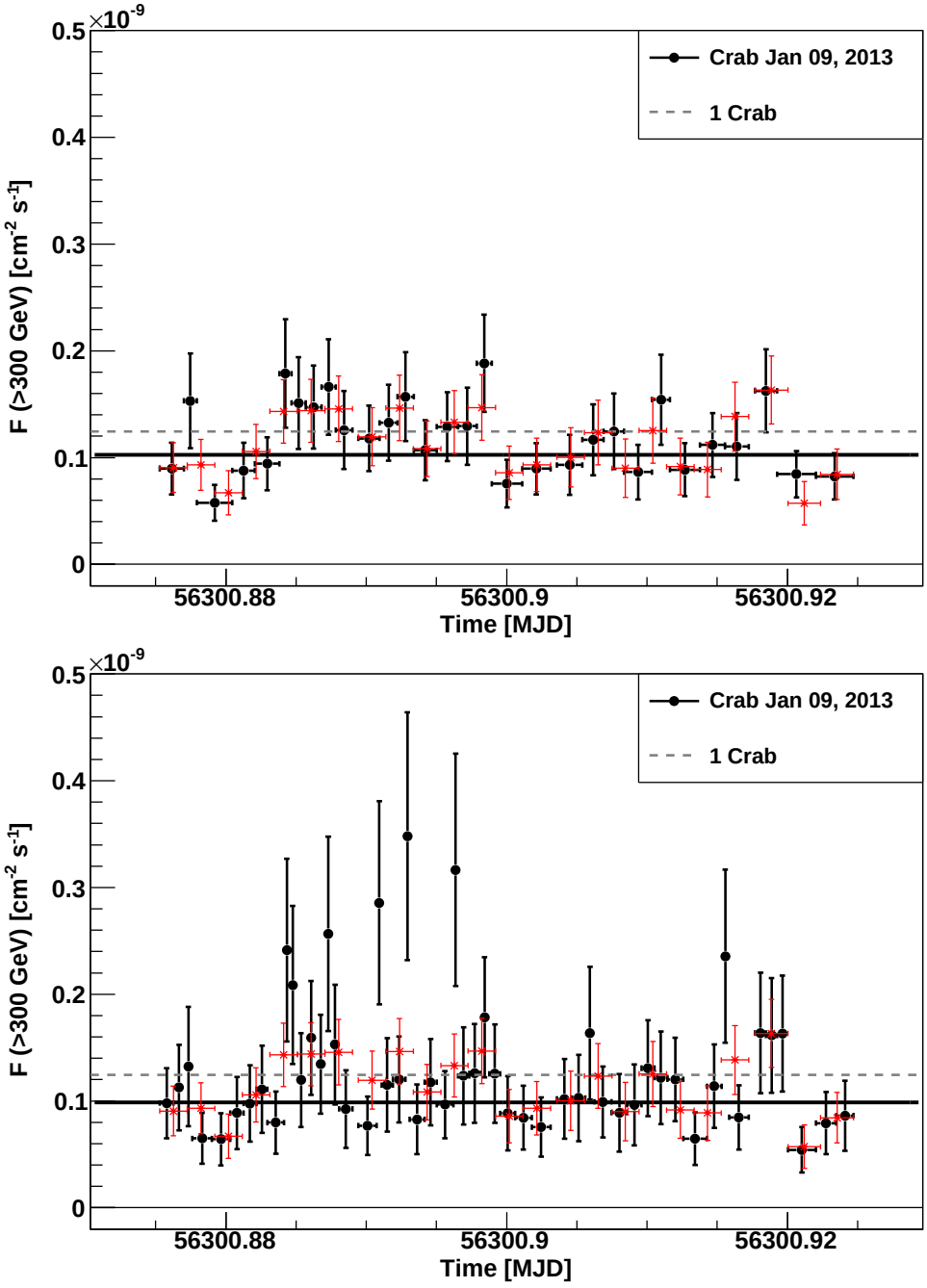

Figure 6.2: Light curve of the Crab Nebula in the night of January 09, 2013 above 300 GeV. The black and red data points show the light curve with fixed ON events and fixed time (3 min) binning, respectively. A fit to the light curve with fixed time binning has a $\chi^2/\mathrm{d.o.f.}$ of $27.5/23$. For comparison, the dashed line shows the 1 C.U. level (Aleksić et al. 2012b). *Top panel:* Light curve with 16 ON events binning. Fitting this light curve (thick black line) with a constant gives $\chi^2/\mathrm{d.o.f.} = 32.6/29$ with a constant flux of $(10.28 \pm 0.53) \times 10^{-11}\,\mathrm{cm}^{-2}\,\mathrm{s}^{-1}$. *Bottom panel:* Light curve with 9 ON events binning with a constant flux fit of $(9.86 \pm 0.52) \times 10^{-11}\,\mathrm{cm}^{-2}\,\mathrm{s}^{-1}$ and $\chi^2/\mathrm{d.o.f.} = 50.6/51$.

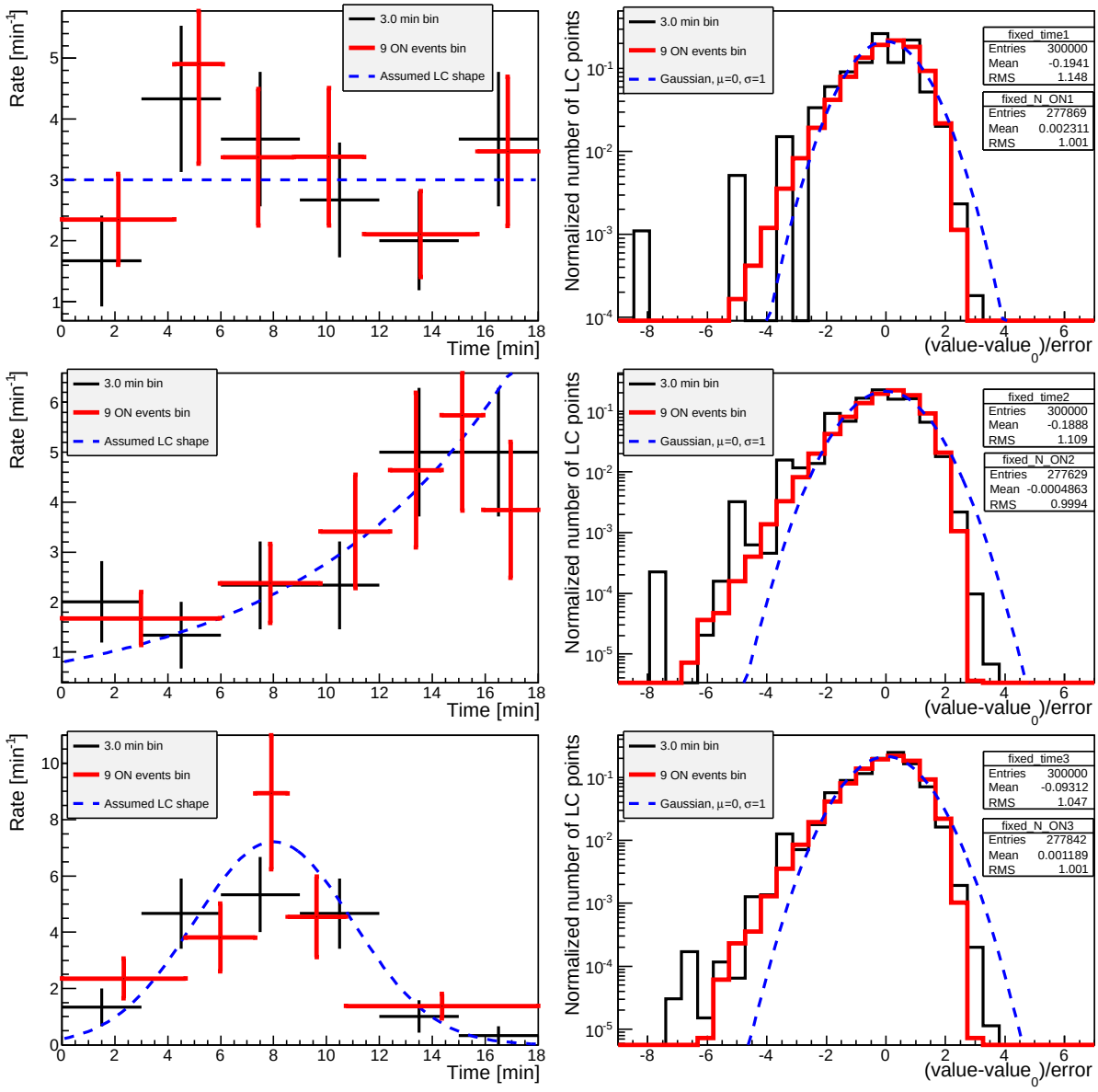

Figure 6.3: Comparison of toy MC light curves obtained with fixed time binning (black) and with fixed number of ON events (red) for different assumed shapes of the light curve (dashed blue line). *Top panel:* Constant flux. *Middle panel:* Exponential rise. *Bottom panel:* Gaussian peak. The panels on the left show an example of each of those light curves, while the right panels show the distributions of light curve residua with respect to the assumed shape obtained from 50000 random light curves. Figure adapted from Aleksić et al. (2014b).

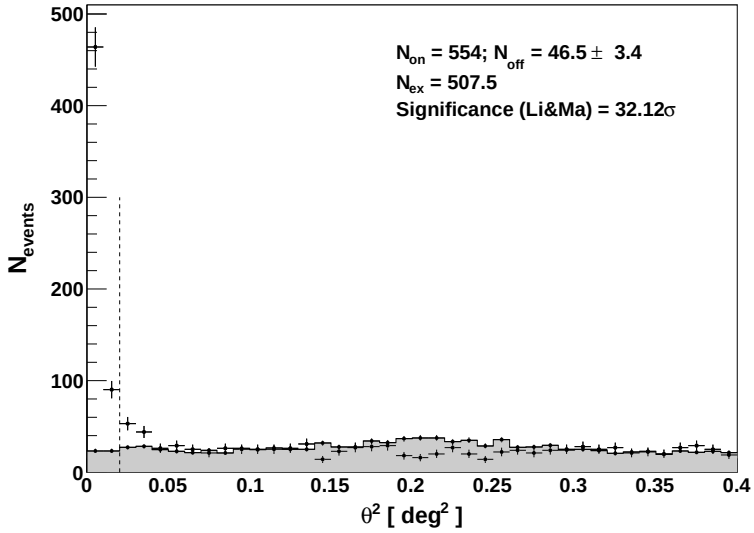

Figure 6.4: θ^2 distribution of ON (black points) and OFF events (gray shaded area) in the night of November 12-13, 2012 above 300 GeV. The distribution shown here is the stacked result of individual wobble pointings. The number of excess events is calculated in the region left from the dashed line. Figure adapted from Aleksić et al. (2014b).

done in the analysis.

6.2 Signal Evaluation

In the night of November 12-13, 2013 a clear signal could be measured. This signal was already seen in the skymap of the Online Analysis of MAGIC (Tescaro et al. 2013). The corresponding θ^2-distribution is shown in Fig. 6.4. This distribution was calculated by stacking the ON and OFF distributions from the individual data sets with different wobble offsets. In the standard analysis described in Chapter 4, the evaluation of the signal is typically calculated above a dedicated energy after a certain HADRONNESS and SIZE cut. Here, an energy-dependent HADRONNESS cut (used for the calculation of the spectra as well) was applied for the determination of the ON and OFF. This guarantees the compatibility of the number of ON events also used in the light curve with variable time binning. In total, 554 ON and 46 OFF events resulting in 507 excess events above 300 GeV could be reconstructed. This corresponds to a significance of 32 standard deviations.

6.3 Light Curve

The light curve has been calculated with two methods. First, the standard fixed time binning was applied (here: 3 minutes). Afterwards, the variable time binning based on a fixed number of ON events (here: 16 and 9 ON events) was used. Figure 6.6 shows the flux above 300 GeV measured in the time range of MJD 56243.95–56244.11.

Both approaches yield comparable results. However, the new, variable time bin method provides a more sensitive search for ultra-fast (< 1 minute) flux variations.

The mean flux in the night could be measured to be $F_{\mathrm{mean}} = (6.08 \pm 0.29) \times 10^{-11}\,\mathrm{cm}^{-2}\mathrm{s}^{-1}$. This is four times higher than the mean flux of the high state of $(1.60 \pm 0.17) \times 10^{-11}\,\mathrm{cm}^{-2}\mathrm{s}^{-1}$ (see Chapter 5). A constant fit to the light curve with 9 ON events over the entire observa-

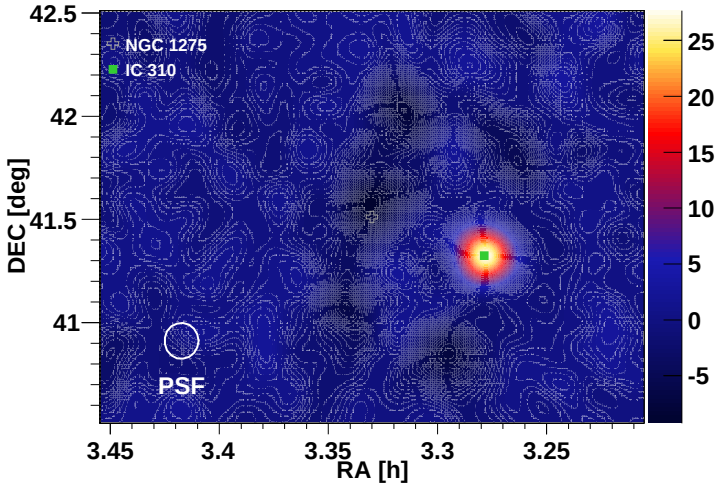

Figure 6.5: Significance map (in TS value) of the Perseus cluster above 300 GeV measured on November 12-13, 2012. The white cross and the green square mark the position of NGC 1275 and IC 310, respectively. Figure adapted from Aleksić et al. (2014b).

tion time range reveals $F_{\text{const.}} = (3.52 \pm 0.22) \times 10^{-11}\,\text{cm}^{-2}\text{s}^{-1}$ with a $\chi^2/\text{d.o.f.}$ of 198.8/58 corresponding to a probability of 2.6×10^{-17} for the constant flux. For comparison, the constant fit to the 16 ON events light curve has a $\chi^2/\text{d.o.f.}$ of 179.3/33 and the 3 min light curve $\chi^2/\text{d.o.f.} = 309.9/74$.

To find periods with the fastest flux variation, the evolution of the doubling time is shown in the bottom panels of Fig. 6.6. This doubling time is calculated by computing the flux difference between each two consecutive points and taking into account the time lapse between these two points. It is important to note, that non of the individual flares in the light curve are restricted to changes in the wobble position.

6.3.1 Fractional Variability and Power Spectrum

A common way to quantify the variability amplitude in AGN light curves is the estimation of the fractional root mean square (rms) variability amplitude F_{Var} (Vaughan et al. 2003). For N individual flux points x_i with error $\sigma^2_{\text{err},i}$ and a mean flux of $\bar{x}$ the fractional variability can be estimated with:

$$F_{\text{Var}} = \sqrt{\frac{S^2 - \overline{\sigma^2_{\text{err}}}}{\bar{x}^2}} \tag{6.1}$$

with the sample variance

$$S^2 = \frac{1}{N-1} \sum_{i=1}^{N} (x_i - \bar{x})^2 \tag{6.2}$$

and the mean square error

$$\overline{\sigma^2_{\text{err}}} = \frac{1}{N} \sum_{i=1}^{N} \sigma^2_{\text{err},i}. \tag{6.3}$$

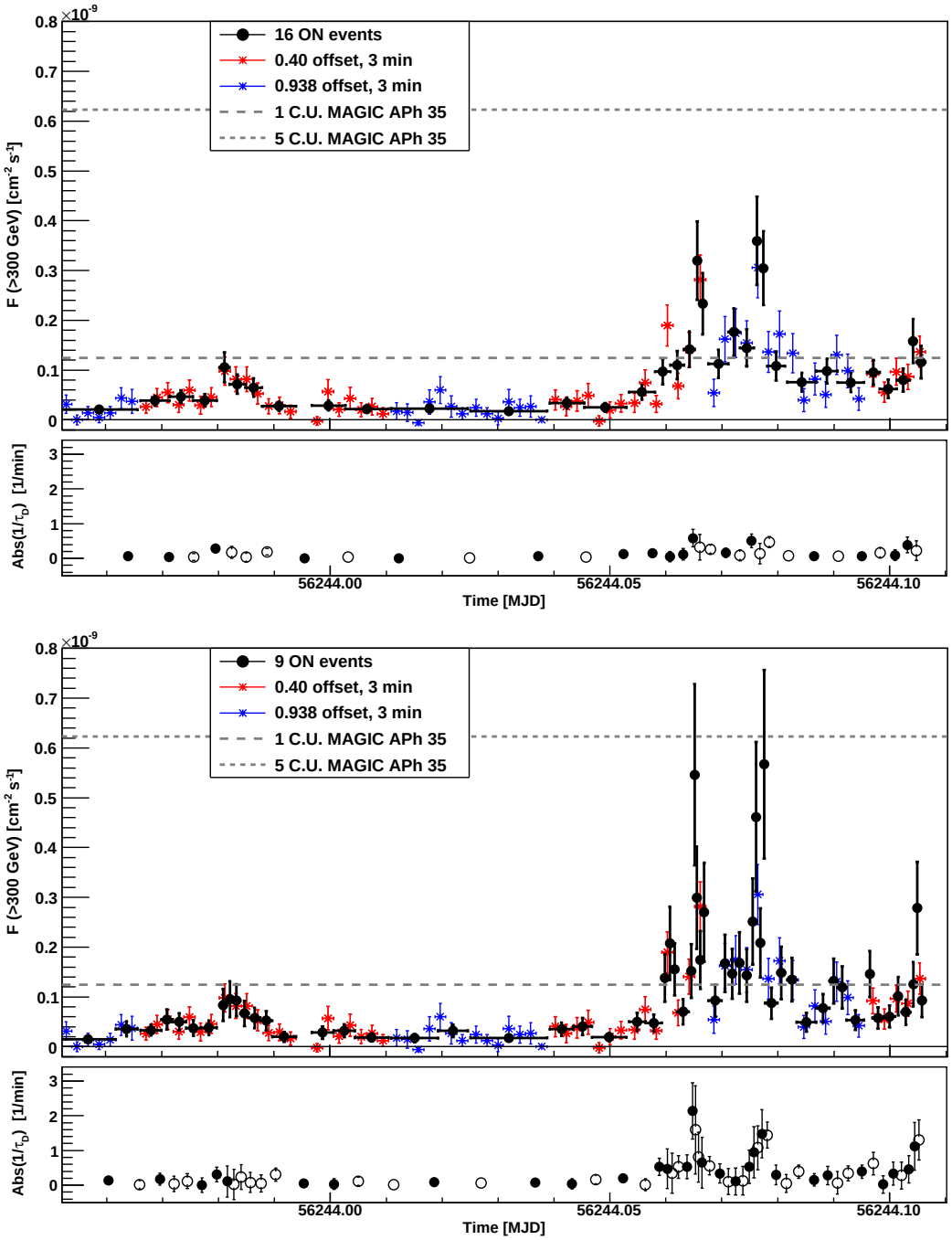

Figure 6.6: Light curve of IC 310 as measured in the night of November 12-13, 2012 above 300 GeV. *Upper panels:* The black points show the results obtained from a fixed binning of ON events (top: 16, bottom: 9 events). The colored light curve presents the result from a fixed time binning (here: 3 minutes), red from the data of the wobble pointing with 0.4°, and blue with 0.938° offset, respectively. The two gray lines correspond to the flux level of the Crab nebula (Crab) and 5 Crab, respectively (Aleksić et al. 2012b). *Bottom panels:* Temporal curve of the absolute inverse doubling time during the flare. Positive doubling times are shown with filled markers, negative doubling times with open markers. Figure adapted from Aleksić et al. (2014b).

The error of $F_{\rm Var}$ can be calculated according to Eq. B2 in Vaughan et al. (2003):

$$\mathrm{err}(F_{\rm Var}) = \sqrt{\left(\sqrt{\frac{1}{2N}}\frac{\overline{\sigma^2_{\rm err}}}{\bar{x}^2 F_{\rm Var}}\right)^2 + \left(\sqrt{\frac{\overline{\sigma^2_{\rm err}}}{N}}\frac{1}{\bar{x}}\right)^2}. \tag{6.4}$$

For the light curve with fixed time binning, $F_{\rm Var}$ was calculated to be $F_{\rm Var,3\,min} = 0.92 \pm 0.05$ and for the variable time binning $F_{\rm Var,9\,ON} = 0.87 \pm 0.07$ ($F_{\rm Var,16\,ON} = 0.78 \pm 0.06$). Note however, these values should not be compared to each other as they result from a different number of light curve data points, i.e, the tested variability time scale is not equal. This calculation was applied to the light curve from the Crab nebula (see Fig. 6.2) resulting in $F_{\rm Var,3\,min} = 0.08 \pm 0.12$ and $F_{\rm Var,9\,ON} = 0.30 \pm 0.07$ ($F_{\rm Var,16\,ON} = 0.01 \pm 2.25$). In case of the light curve from the Crab nebula, an object with constant flux, $F_{\rm Var}$ is poorly defined and may result in a larger mean square error than the sample variance, hence the square root becomes negative. Therefore, the absolute value of $S^2 - \overline{\sigma^2_{\rm err}}$ was used.

Another approach to investigate the variability is to analyze the "power" of variability as a function of temporal frequency by calculating the power spectral density, see Vaughan et al. (2003).

The power spectrum is defined as modulus-squared of the discrete Fourier transformation (DFT). This method is only well defined for an evenly sampled light curve with flux point at discrete times t_i ($i = 1, 2, .., N$). Therefore, it was only applied to the fixed time binned light curve. The power is being calculated according to:

$$P(f_i) = A|\mathrm{DFT}(f_i)|^2 \tag{6.5}$$

and

$$|\mathrm{DFT}(f_i)|^2 = \left[\sum_{i=1}^{N} x_i \cos(2\pi f_i t_i)\right]^2 + \left[\sum_{i=1}^{N} x_i \sin(2\pi f_i t_i)\right]^2 \tag{6.6}$$

at frequencies $f_i = j/N/\Delta T$, with $j = 1, 2, .., N/2$.

The normalization A of the power spectrum was chosen to be:

$$A = \frac{2\Delta T}{N}, \tag{6.7}$$

taken from Appendix A in Vaughan et al. (2003).

The resulting power spectra for the flare of IC 310 and for comparison, PKS 2155–304 (Aharonian et al. 2007) are shown in Fig. 6.7.

The power spectrum of IC 310 was fitted with a power-law function. The index was found to be $k = 0.64$. For comparison, the index for the light curve of PKS 2155–304 is $k = 2.05$. Thus, IC 310 showed a flickering behavior with more power at shorter time scales. Note however, due to the 3 min sampling, the higher frequencies can not be reached as in the case of the 1 min binned light curve from PKS 2155–304. One could argue that the fractional variability shows a similar result. For PKS 2155–304, $F_{\rm Var,PKS\,2155-304} = 0.58 \pm 0.03$ was found (Aharonian et al. 2007) which is smaller than the value found for IC 310.

In general, no distinguished feature as those mentioned in Section 2.7 could be found in the power spectrum of IC 310.

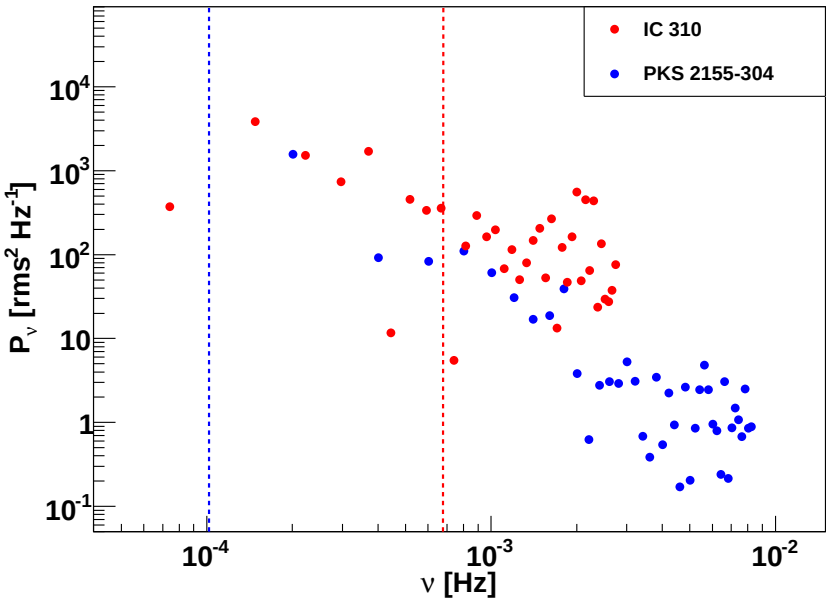

Figure 6.7: Power spectrum of the flare of IC 310 (red, spectral slope: 0.64) and of PKS 2155–304 (blue, spectral slope: 2.05). The dashed lines show the frequency corresponding to the gravitation radius of the objects. For PKS 2155-304 a black hole mass of $1 \times 10^9\,\mathrm{M_{Sun}}$ has been assumed (Bettoni et al. 2003).

6.3.2 Individual Substructures in the Light Curve

In the following, substructures in the light curve were fitted in order to determine the doubling time $\tau_\mathrm{D} = \tau \times \ln 2$. First, an exponential fit was applied:

$$F(t) = F(t_0) * e^{-\frac{t-t_0}{\tau}} \tag{6.8}$$

with $F(t)$ and $F(t_0)$ being the fluxes at the time t and t_0, respectively. The results of the fits are shown in Fig. 6.8, 6.9 and, summarized in Table 6.1.

In addition, the conservative, slowest doubling time was computed from the first big flare. The light curve in the range MJD 56244.062–56244.0652 was fitted with many exponential functions, each time fixing τ to a different value. From computing the probability of the fit, the doubling time of $4.88\,\mathrm{min}$ was found with a fit probability of 5% (95% C.L.).

The doubling times are very different, ranging from $\sim 1-9$ minutes. The shortest time scale in Table 6.1, however, may not be reliable, e.g., due to 0 degrees of freedom. Since the pre-flare showed similar time scales for the rising and the decaying period, the time scale covering the pre-flare was fitted with a Gaussian (see Fig. 6.8). The full-width half-maximum (FWHM) expressing the time period in which the maximal flux raised/decayed by $1/2$ is $(22.3 \pm 4.4)\,\mathrm{min}$.

For the theoretical discussion, the doubling time of $4.88\,\mathrm{min}$ will be used. The corresponding time scale in the frame of reference of IC 310 is therefore: $4.88\,\mathrm{min}/(1+z) = 4.8\,\mathrm{min}$.

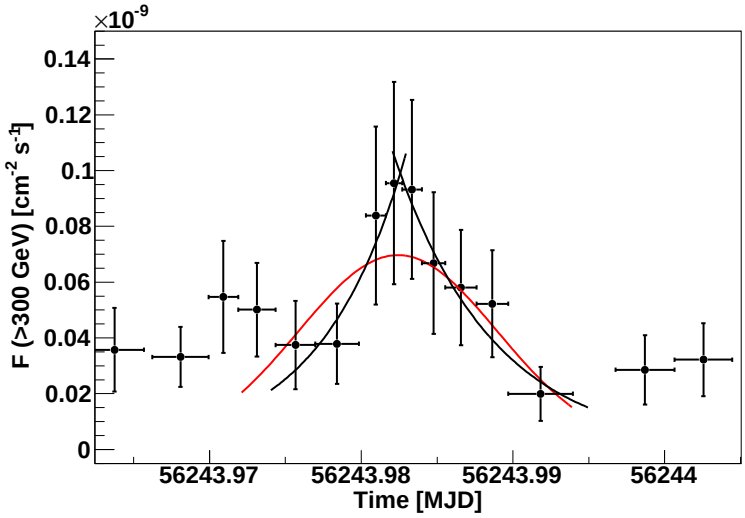

Figure 6.8: Zoom to the pre-flare with exponential fits to the rising and decaying edge (black lines) as well as a Gaussian fit (red line). Figure adapted from Aleksić et al. (2014b).

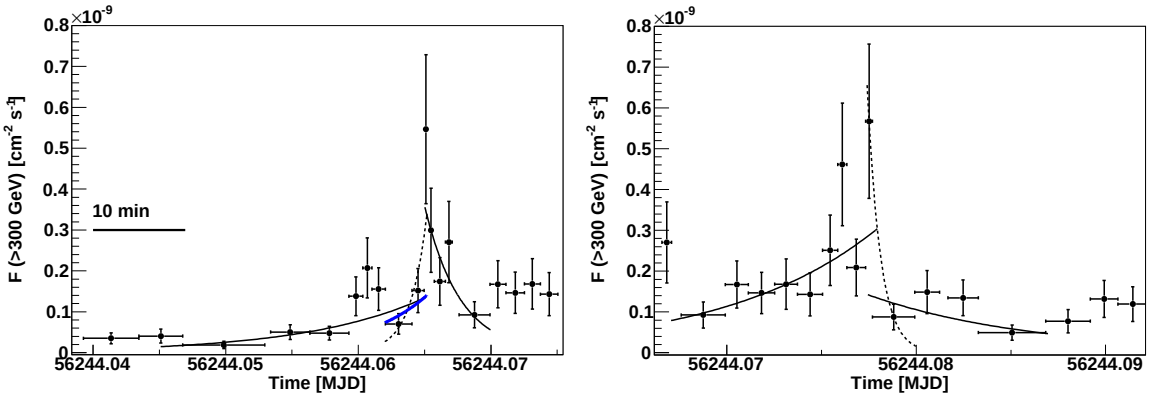

Figure 6.9: Zoom to the first (*left panel*) and the second (*right panel*) big flare with exponential fits to the rising and decaying edge. The blue line shows the exponential fit with the doubling time of 4.88 min. Figure adapted from Aleksić et al. (2014b).

Table 6.1: Fit results from individual substructures in the light curve. Table adapted from Aleksić et al. (2014b).

state	time range [MJD]	t_0 fixed [MJD]	$F(t_0) \cdot 10^{-11}$ [cm^{-2} s^{-1}]	τ [min]	$\tau_{\mathrm{D}}{}^{a}$ [min]	χ^2/ d.o.f.
pre:						
rise	56243.974–56243.983	56243.983	10.7 ± 4.3	8.0 ± 4.4	5.5	0.8/2
decay	56243.982–56243.995	56243.982	10.8 ± 2.5	9.5 ± 2.9	6.6	0.8/4
1. Flare						
fast rise	56244.062–56244.0652	56244.0652	34.5 ± 13.6	1.8 ± 0.7	1.3	2.4/1
95% C.L.	56244.062–56244.0652	56244.0652	34.5 ± 13.6	< 7.04	< 4.88	-
slow rise	56244.045–56244.0652	56244.0652	13.7 ± 2.9	13.0 ± 3.2	9.0	17.2/8
decay	56244.065–56244.07	56244.065	35.9 ± 9.4	3.8 ± 1.4	2.7	3.1/3
2. Flare						
rise	56244.067–56244.078	56244.078	30.6 ± 6.9	11.6 ± 4.2	8.1	6.7/7
fast dec.	56244.0774–56244.08	56244.0774	66.8 ± 24.3	1.0 ± 0.3	0.7	2.1/0
slow dec.	56244.0774–56244.087	56244.0774	14.3 ± 4.2	12.3 ± 6.5	8.5	9.0/3

Notes. $^{(a)}$ $\tau_{\mathrm{D}} = \tau \times \ln 2$.

6.4 Spectrum

As mentioned in Chapter 5, the unfolding enables the calculation of a combined spectrum from individual spectra from data with different offsets[1]. The resulting spectrum can be described with a simple power-law with a flux normalization at 1 TeV of $f_0 = 17.6 \pm 0.7 \times 10^{-12}\,\mathrm{TeV}^{-1}\,\mathrm{cm}^{-2}\,\mathrm{s}^{-1}$ and a photon index of 1.86 ± 0.04. Note that the numbers and the data points shown here slightly differ from the ones published in Aleksić et al. (2014b). The results in this thesis were obtained by the analysis of the author.

In order to test for curvature of the spectrum, different power-law fits (simple, log-parabolic, broken power-law fit) were applied to the data. The results are shown in Appendix B Fig. 8 and summarized in Appendix B Table 10. Since the log-parabolic and broken power-law fit show no significant improvement in the χ^2-test compared to the simple power-law, all further results and discussion refer to the simple power-law.

The unfolded SED of the flare is shown in Fig. 6.10. Additionally, the SED corrected for EBL absorption with the model by Domínguez et al. (2011) is show in the same figure. The deabsorption yields to a flux normalization at 1 TeV of $f_0 = 21.3 \pm 0.9 \times 10^{-12}\,\mathrm{TeV}^{-1}\,\mathrm{cm}^{-2}\,\mathrm{s}^{-1}$ and a photon index of 1.75 ± 0.04. Comparing the SED with the one measured in 2009/2010 (compare Chapter 5 and see Fig. 6.11 as well as Table 6.2) no significant spectral variation between the flare and the high and low flux state could be found. This finding was already reported in Chapter 5.

[1]Both SEDs calculated from the data with different offset can be found in Appendix B Fig. 7.

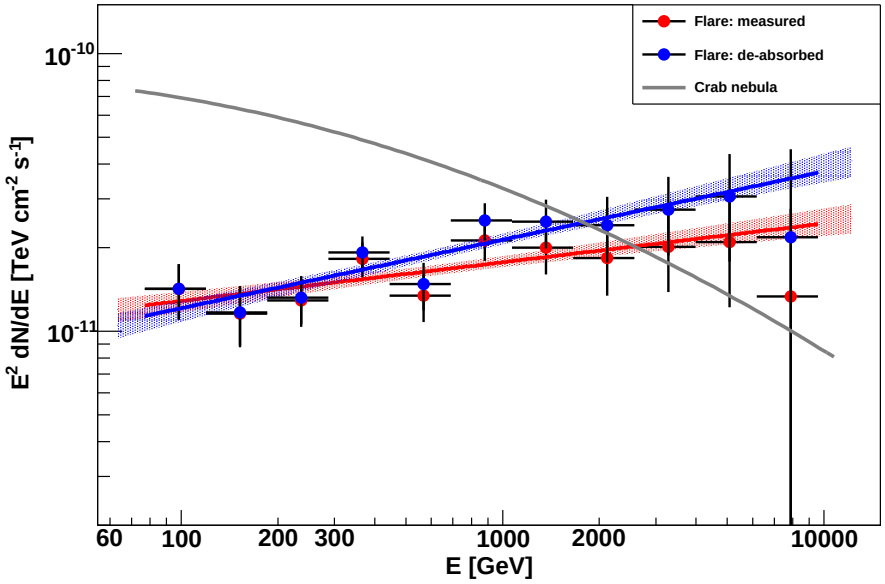

Figure 6.10: Measured SED (red) as well as corrected for EBL absorption (blue, applying the model by Domínguez et al. (2011)) of the flare. The red/blue butterfly shows the forward folded SED and the red/blue data points and the solid line the unfolded SED using the Schmelling method, respectively.

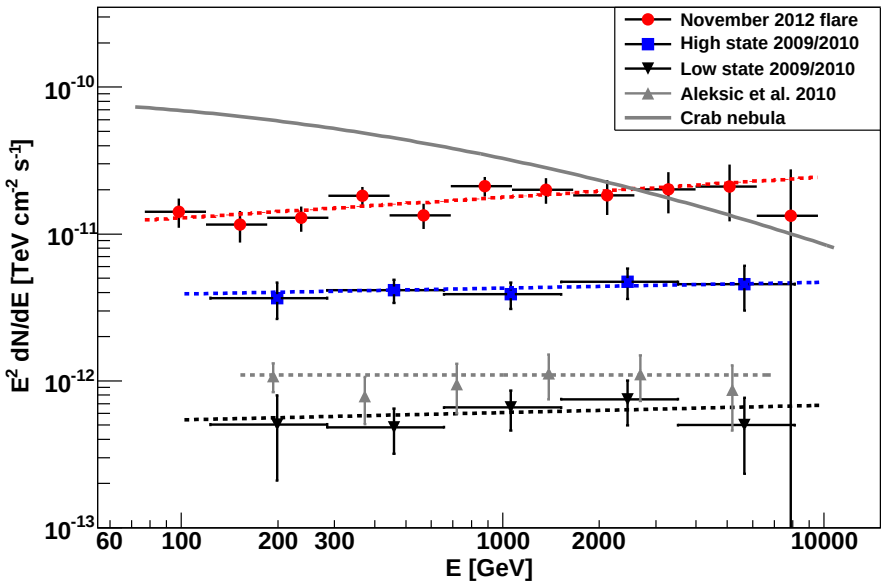

Figure 6.11: Measured SEDs obtained by MAGIC in different periods of activity of IC 310. The SED together with the power-law of the flare is shown in red. For comparison, the result from the high (blue squares) and low (black triangles) state (Chapter 5), and the average results (grey triangles) from Aleksić et al. (2010b) for the whole period are shown. In addition, the spectral power-law fit of the Crab nebula observations from Aleksić et al. (2012b) is shown (grey, solid line).

Table 6.2: Division of the data of 2013-11-13 according to different flux states.

state	run ID	time start [MJD]	time stop [MJD]
low state of flare part I	05020909	56243.951958	56243.965686
low state of flare part II	05020915-18	56243.996756	56244.052941
pre-flare	05020910-11	56243.966217	56243.993958
big flare I	05020919	56244.053380	56244.067083
big flare II	05020920	56244.067593	56244.081231
post flare	05020921-22	56244.081669	56244.095371

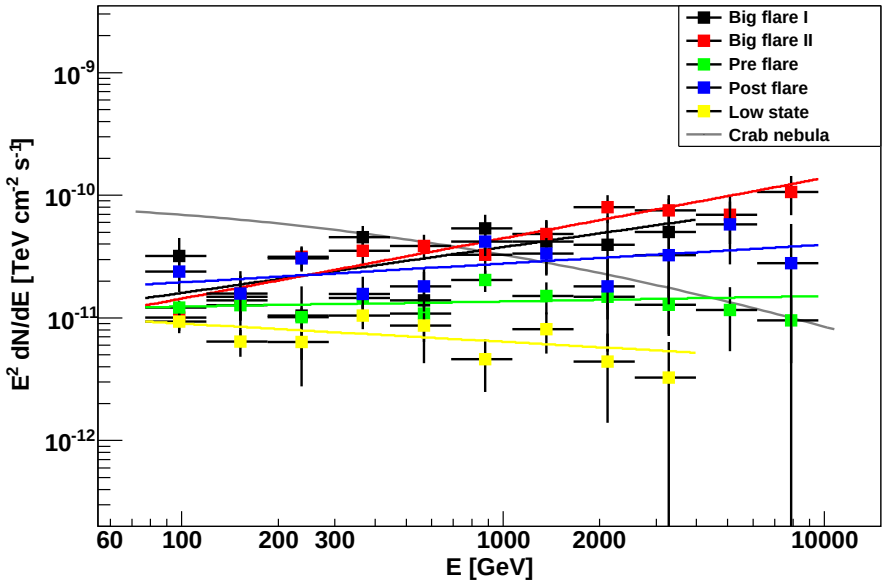

Figure 6.12: Study of spectral variability during the flare. SEDs as well as the corresponding power-law fits of diverse flux states according to Table 6.2. Intra flare I (black), intra flare II (red), pre-flare (green), post flare (blue), and low state (yellow) are shown.

6.4.1 Intra-night Spectral Variability

In the following, the spectral variability in the night during the flare will be investigated. Therefore, the data have been grouped into five sets as quoted in Table 6.2. The selection of the runs and classification was based on different flux states by eye.

All spectra have been fitted with simple power-laws. The results are tabulated in Table 6.3 and shown in Fig. 6.12.

Figure 6.13 shows the photon index versus the flux normalization and time, respectively, obtained from power-law fits to the different spectra during the flare.

From this method, one can argue for a minor, marginally significant ($\sim 1\sigma$) variation of the spectral emission during the flare. The constant fit in the left panel of Fig. 6.13 has a probability of $<$1% of the unfolded spectra (2% for the forward folding). A linear fit reveals 75% probability (68% for the forward folding).

A second approach to evaluate the spectral behavior during the flare uses the so-called "hardness ratio". Here, this ratio is defined by the integral flux above 1 TeV divided by the flux between 300 GeV and 1 TeV. Those fluxes were obtained by the calculation of the light curve

Table 6.3: Results of power-law fits of the spectra obtained with MAGIC. For the definition of individual flux states in the second part of the table, see Table. 6.2

state		energy range [TeV]	$f_0 \pm f_{\rm stat} \pm f_{\rm syst}$ $\times 10^{-12}[\mathrm{TeV}^{-1}\,\mathrm{cm}^{-2}\,\mathrm{s}^{-1}]$	$\Gamma \pm \Gamma_{\rm stat} \pm \Gamma_{\rm syst}$
flare overall night	obs.	0.07-8.3	$17.6 \pm 0.7 \pm 2.2$	$1.86 \pm 0.04 \pm 0.15$
	intr.	0.07-8.3	$21.3 \pm 0.9 \pm 2.6$	$1.75 \pm 0.04 \pm 0.15$
low state of flares	obs.	0.07-4.0	6.4 ± 0.8	2.15 ± 0.10
pre-flare	obs.	0.07-9.5	13.5 ± 0.9	1.96 ± 0.06
big flare I	obs.	0.07-4.0	37.5 ± 4.2	1.63 ± 0.11
big flare II	obs.	0.07-9.5	44.2 ± 2.1	1.51 ± 0.06
post flare	obs.	0.07-9.5	27.5 ± 2.3	1.85 ± 0.08
high 2009/2010	obs.	0.12-8.1	$4.28 \pm 0.21 \pm 0.73$	$1.96 \pm 0.10 \pm 0.20$
	intr.	0.12-8.1	$5.14 \pm 0.28 \pm 0.90$	$1.85 \pm 0.11 \pm 0.20$
low 2009/2010	obs.	0.12-8.1	$0.61 \pm 0.04 \pm 0.11$	$1.95 \pm 0.12 \pm 0.20$
	intr.	0.12-8.1	$0.74 \pm 0.05 \pm 0.14$	$1.81 \pm 0.13 \pm 0.20$
2009/2010 previous	obs.	0.15-7.0	$1.1 \pm 0.2 \pm 0.0$	$2.00 \pm 0.14 \pm 0.00$

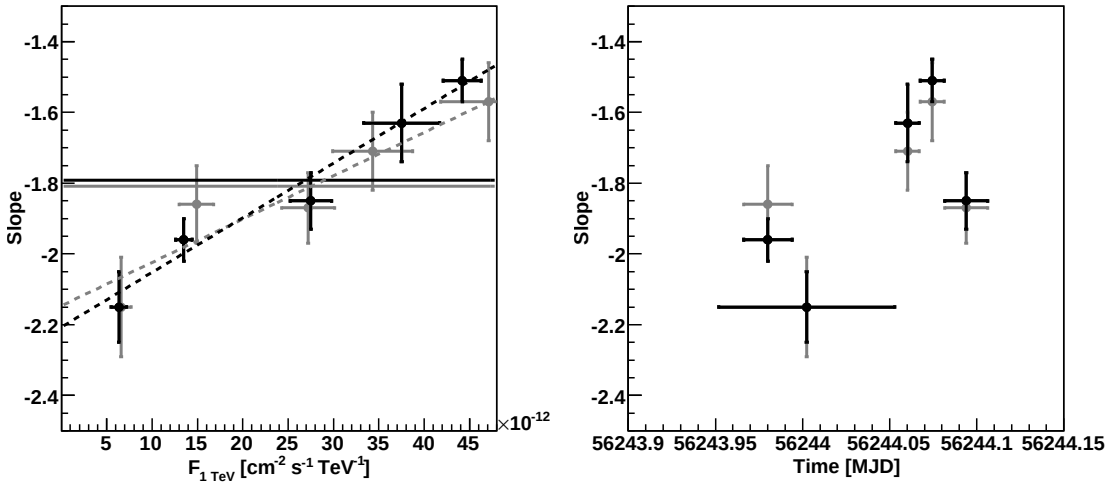

Figure 6.13: Photon indices during the flare. Black correspond to unfolded spectra using the Schmelling method and grey show the forward folded result. *Left panel:* Distribution of the slope versus the flux normalization at 1 TeV with constant (solid lines) and linear (dashed lines) fits. *Right panel:* Variation of the photon index in time.

Table 6.4: Parameters of the 5 GHz EVN image from October 29, 2012.

Configuration[a]	$S_{\rm peak}$[b] [mJy beam^{-1}]	RMS[c] [mJy beam^{-1}]	$S_{\rm total}$[d] [mJy]	$b_{\rm maj}$[e] [mas]	$b_{\rm min}$[e] [mas]	P.A.[e] [°]
EF-WB-JB-ON-MC-NT-TR-YS-ZC-BD-UR-SH	76.7	0.027	109	4.97	1.24	-8.5

Notes. [(a)] Telescope configuration: EF: Effelsberg, WB: Westerbork, JB: Jodrell Bank, ON: Onsala, MC: Medicina, NT: Noto, TR: Torun, YS: Yebes, ZC: Zelenchukskaya, BD: Badary, UR: Urumqi and SH: Shanghai. [(b)] Peak flux density in mJy/beam. [(c)] 1σ noise level in mJys/beam. [(d)] Total flux density in mJy [(e)] Major and minor axis and position angle of restoring beam.

in the corresponding energy ranges. The study was performed for two different fixed time binnings, a run-wise (i.e., 20 minutes per bin) and a five-minute binning. It should be noted that the hardness ratio for data points in which a statistical fluctuation resulted in a negative or zero flux is not physical. Those points were exclude in this study.

The results are presented in Fig. 6.14. In the top panel of the figure, a direct connection between the low and the high-energy flux is shown, while in in the bottom panel the hardness ratio is shown versus the overall flux above 300 GeV.

This study yields no significant detection of spectral variability as well neither in the run-wise nor the five-minutes binning. Spectral variability would result in a curved trend of the distribution of the high versus the low energy flux. In case of an energy-dependent spectral slope, the diagram of the hardness ratio versus overall flux would show a clear linear relationship. This, however, was not found when fitting the distributions. A constant fit to the data points in both binning methods yielded $\sim 1\sigma$ (probability of 16% for the run-wise and, 68% for five minutes) and $\sim 2\sigma$ for a linear fit (probability of 96% for the run-wise and, 94% for five minutes).

Spectral changes between the rising and decaying phase of a flare might provide information about the underlying physical processes. This has been tested by calculating two spectra (see Fig. 6.15), one for the rising edge of the pre-flare in the time range MJD 56243.966217 - 56243.979838 (data run 05020910), and one for the decaying edge MJD 56243.980301 - 56243.993958 (data run 05020911). The flux normalization at 1 TeV for the power-law spectra are measured to be $f_{0,\rm rise} = 9.7 \pm 0.8 \times 10^{-12}\,\mathrm{TeV}^{-1}\,\mathrm{cm}^{-2}\,\mathrm{s}^{-1}$ and $f_{0,\rm decay} = 16.3 \pm 1.7 \times 10^{-12}\,\mathrm{TeV}^{-1}\,\mathrm{cm}^{-2}\,\mathrm{s}^{-1}$. The indices of the spectra are comparable within the errors, 2.06 ± 0.06 for rise and 1.93 ± 0.09 for decay. Therefore, no significant spectral difference between the rising and the decaying flux phase could be found.

6.5 EVN Observation

As part of the multi-frequency campaign, high-sensitivity radio VLBI observations with the EVN had been proposed. They were performed in October and November 2012 at the frequencies 1.7, 5.0, 8.4, and 22.2 GHz. Only the data and results from the 5.0 GHz observation from October 29, 2012 with the highest dynamic range will be presented in this thesis. The analysis results of the data were provided by R. Schulz from the University of Würzburg.

The amplitude and phase calibration was applied to the data using the standard methods of the Astronomical Image Processing System (AIPS, (Greisen 2003)). For imaging and self-calibration, DIFMAP (Shepherd et al. 1994) was used.

The participating telescopes were: Effelsberg, Westerbork, Jodrell Bank, Onsala, Medicina,

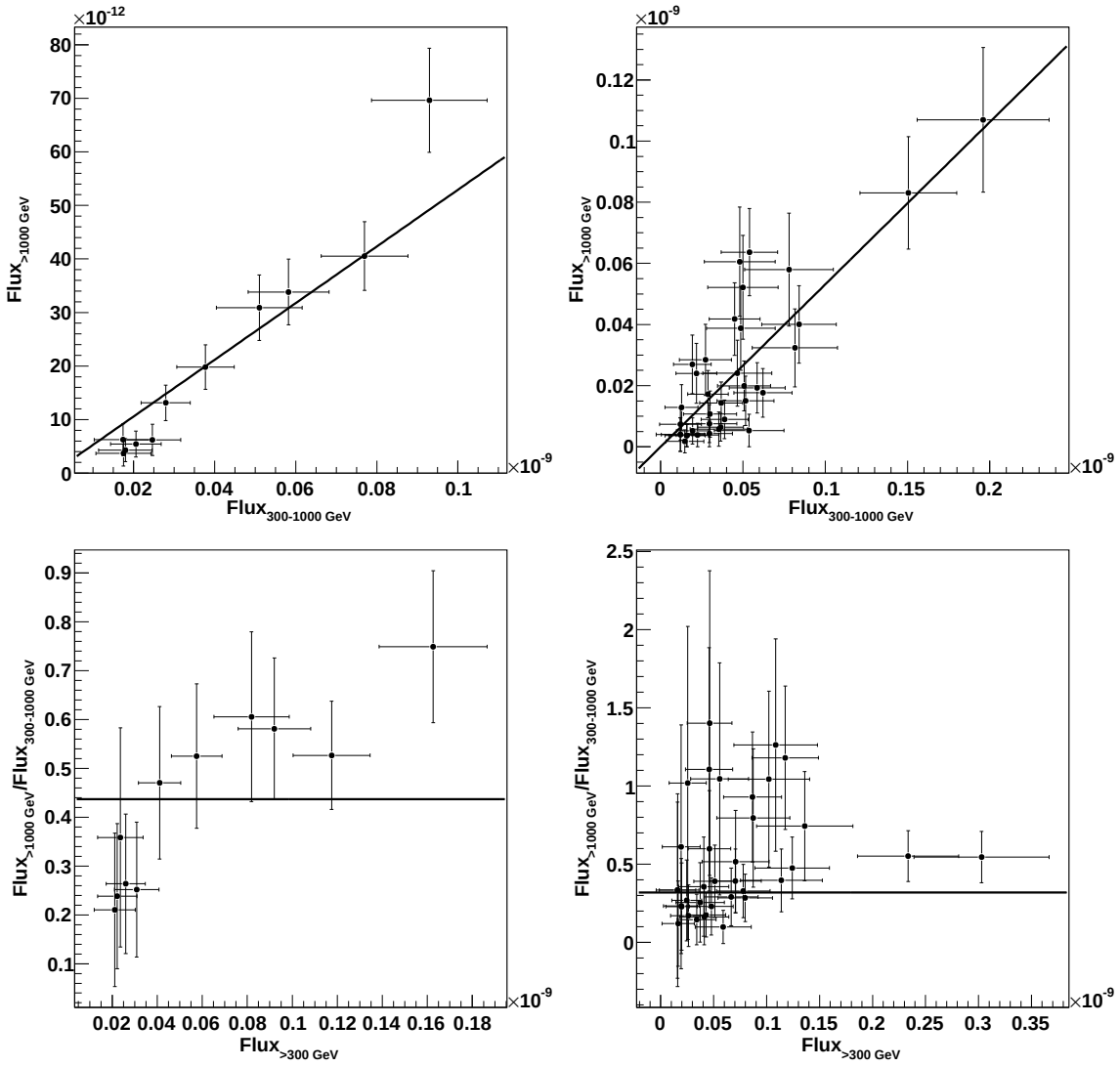

Figure 6.14: Study of spectral variability during the flare using the hardness ratio. *Top panels:* Flux above 1 TeV vs. flux in the energy range 300 GeV to 1 TeV. The linear fits have a χ^2/d.o.f. of 10.8/10 / 34.9/35 corresponding to a probability of 0.37 / 0.47. *Bottom panels:* Hardness ratio vs. flux; const fits χ^2/d.o.f. of 14.3/10 / 30.6/35 corresponding to a probability of 0.16 / 0.68. *Left panels:* Results for a run-wise division of the data. *Right panels:* Results for a five-minutes binning. Note that data points with negative or zero fluxes have been removed. Image adapted from Aleksić et al. (2014b).

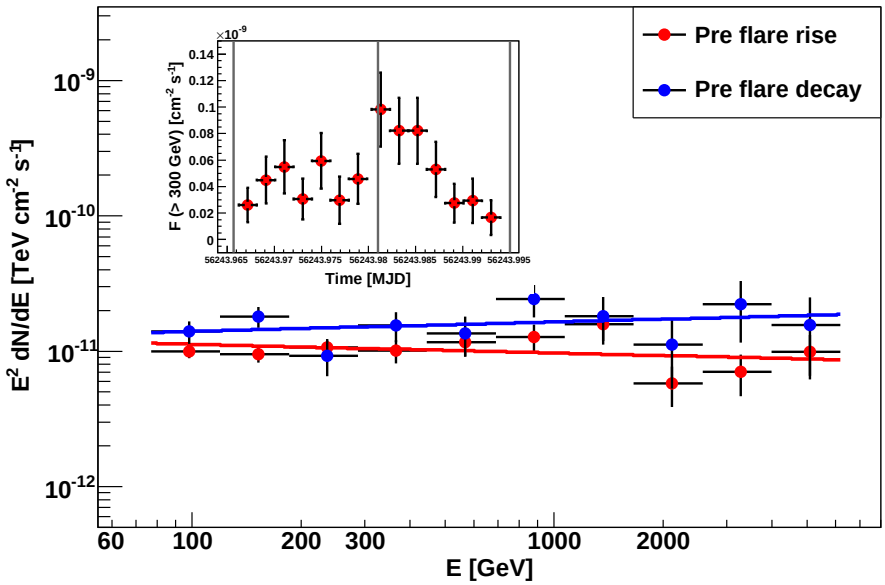

Figure 6.15: Observed spectra of the rising and decaying edge of the pre-flare. The inset shows the corresponding section of the light curve with vertical lines indicating the beginning and the end of the runs.

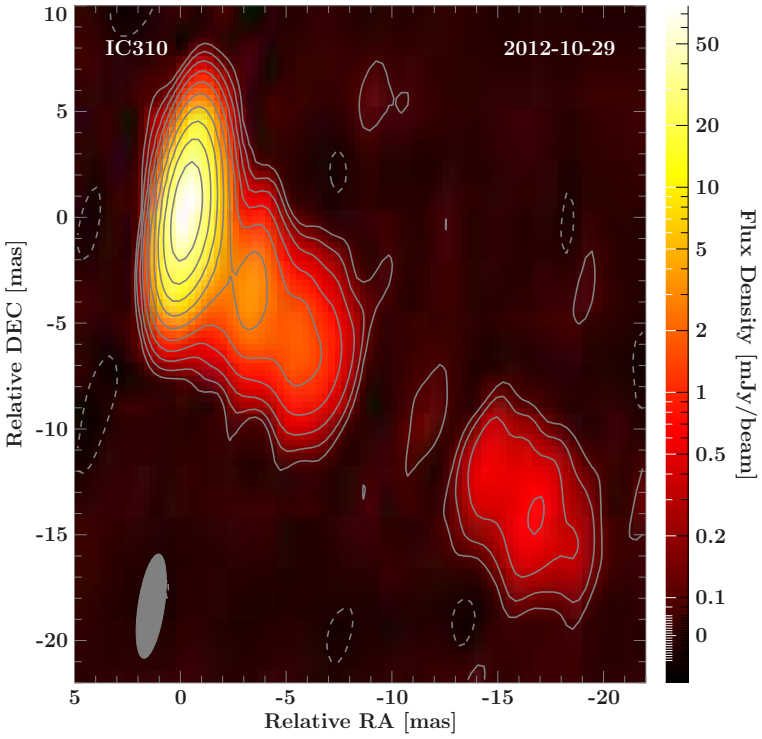

Figure 6.16: 5.0 GHz map of IC 310 obtained with the EVN on October 29, 2012. Image parameters are given in Table 6.4. Image taken from Aleksić et al. (2014b).

Noto, Torun, Yebes, Zelenchukskaya, Badary, Urumqi, and Shanghai. Information about the calibration from Jodrell Bank, Zelenchukskaya, and Badaray was missing. Therefore, an image was produced with DIFMAP first without these other telescopes. From the resulting image model, a constant amplitude correction factor was determined for each telescope. Those were applied to the amplitude calibration and imaging procedure in order to obtain the final image. The image parameter of the resulting image (see Fig. 6.16) are given in Table 6.4.

The image shows the core-jet structure and no hint for the counter-jet, similar to the image obtained from the short VLBA observations presented in Chapter 5. However, with a higher dynamic range one can further constrain the upper limit of the angle between the jet axis and the line-of-sight using the method described in Section 5.5.1. The dynamic range R of the image is given by the ratio between the flux density of the peak, $S_{\rm peak} = 76.7\,\mathrm{mJy}$, and the $3\,\sigma$ noise level ($0.081\,\mathrm{mJy\,beam^{-1}}$), resulting in $R \approx 940$.

Using Eq. 2.21 and assuming $\alpha = 0$ and $\beta \to 1$ one arrives at a limit of the angle of $\theta \lesssim 20^\circ$. Together with the lower limit resulting from the length of the radio jet, see Section 5.5.1, the possible range for the angle is found to be $10^\circ \leq \theta \leq 20^\circ$.

6.6 Fast Variability at Sub-Horizon Scales

In this chapter, the detection of a ultra-fast variable emission of IC 310 has been presented. To achieve such a detection some effort is needed, as usually the measurements are either strongly limited by the sampling time scale (short observation in a few not closely spaced nights) and/or limited event statistics, and accuracy of the instrument. In case of the data of IC 310 taken on November 12-13, 2012, those difficulties could be managed by an observation with almost no interruption, and by introducing a new method for the calculation of the light curve. The results can now be used to draw conclusions on the underlying processes. To this end, the findings will be compared also with other measurements of intra-night TeV variability (see Table 6.5).

Figure 6.17 shows the relation between the minimum variability time scale and the black hole mass. Vovk & Neronov (2013) used *Fermi*-LAT data of several blazars to investigate a possible correlation between these two parameters. No variability shorter than the light-crossing time of the black holes was found, possibly due to the limited statistics. According to the authors, a positive correlation (minimum variability time equals the light-crossing time) would suggest that the emission region responsible for the fast variability is located close to the central engine. If, however, shorter time scales are measured, compact regions at larger distances would produce the variable light curves. Such regions could develop from instabilities intrinsic to the jet.

In addition to the measurements by Vovk & Neronov (2013), the findings from the IACTs summarized in Table 6.5 are now included in the graph (Fig. 6.17). Since the time scales given in the publications were determined differently, an error of 20% is assumed for all observations. For the mass, an uncertainty of 10% is assumed.

The horizon light crossing time shall be defined following Eq. 2 in Vovk & Neronov (2013):

$$\begin{aligned} T_{\rm lc} &= 2(R_{\rm G} + \sqrt{R_{\rm G}^2 - a^2})/c \\ &\simeq \begin{cases} 10^3 \left(\frac{M_{\rm BH}}{10^8 \mathrm{M}_\odot}\right) s, & a = R_{\rm G} \\ 2 \times 10^3 \left(\frac{M_{\rm BH}}{10^8 \mathrm{M}_\odot}\right) s, & a = 0 \end{cases} \end{aligned} \tag{6.9}$$

Table 6.5: Overview of intra-night TeV flares.

Object[a]	Class[b]	Year	$\tau_{\rm min}$[c]	$M_{\rm BH}/{\rm M}_\odot$[d]	R/δ[e]	$R/(\delta \cdot R_{\rm G})$[f]
Mrk 421	HBL	1996	15 min	$\sim 6 \times 10^8$	2.6×10^{13} cm	~ 0.7
		2001	15 min			
Mrk 501	HBL	1997	10 h	$(0.9 - 3.4) \times 10^9$	1.0×10^{15} cm	7.7–2.0
		2005	2 min		3.5×10^{12} cm	0.03–0.01
1ES 1959+650	HBL	2002	1 h	$\sim 1.3 \times 10^8$	1.0×10^{14} cm	~ 5.3
PKS 2155–304	HBL	2006	3 min	$(1 - 2) \times 10^9$	4.8×10^{12} cm	0.03–0.02
PKS 1222+21	FSRQ	2010	10 min	$\sim 6 \times 10^8$	1.3×10^{13} cm	~ 0.1
BL Lac	LBL	2011	13 min	$\sim 1.7 \times 10^8$	2.2×10^{13} cm	~ 0.9
M87	RG	2008	0.9 d	$\sim 6.0 \times 10^9$	2.3×10^{15} cm	~ 2.6
IC 310	RG	2012	4.9 min	$\sim 3 \times 10^8$	8.7×10^{12} cm	~ 0.2

Notes. [a] The publications to the variability listed in this table are (form top to bottom): Gaidos et al. (1996), Fossati et al. (2008), Aharonian et al. (1999), Albert et al. (2007c), Krawczynski et al. (2004), Aharonian et al. (2007), Aleksić et al. (2011), Arlen et al. (2013), Acciari et al. (2009), this work. For the calculation of the size of the emission region R, the redshifts were extracted from the NASA extragalactic database. [b] AGN classification of the object. [c] Shortest variability time-scale reported for this object. [d] References to the black hole masses: Mrk 421: Bednarek & Protheroe (1997b), Mrk 501: Barth et al. (2002), 1ES 1959+650: Falomo et al. (2002), PKS 2155-304: Bettoni et al. (2003), PKS 1222+21: Farina et al. (2012), BL Lac: Woo & Urry (2002), M87: Gebhardt & Thomas (2009), IC 310: this work. [e] Upper scale of the corresponding emission region. [f] Upper scale of the corresponding emission region normalized to the gravitational radius $R_{\rm G} = GM_{\rm BH}/c^2$ of the object.

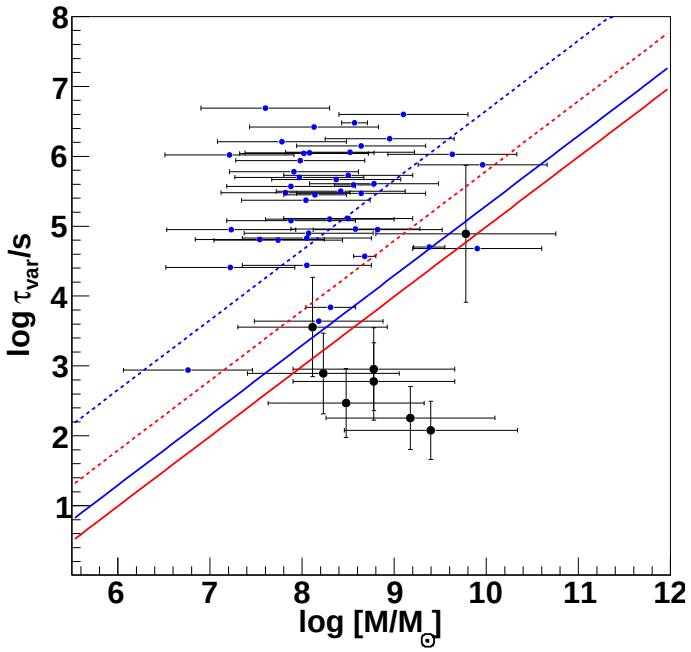

Figure 6.17: Variability time scale versus black hole mass. Blue points show the minimum variability time scales with *Fermi*-LAT and black hole masses measured by Vovk & Neronov (2013). Black data points illustrate the measurements from IACTs. The solid lines indicate the light-crossing time for maximally rotating (red) and non-rotating black holes (blue). Similarly, the dashed lines show the light-crossing time for the last stable orbit.

with $a = J_{\rm BH}/M_{\rm BH}c^2$ lying in the range $0 \leq a \leq R_{\rm G}$, where $J_{\rm BH}$ is the angular momentum of the black hole. The dashed lines in Fig. 6.17 represent the last stable orbit, defined as (Eq. 3 in Vovk & Neronov (2013)):

$$P = \begin{cases} \frac{4\pi R_{\rm G}}{c} \simeq 6 \times 10^3 \left(\frac{M_{\rm BH}}{10^8 {\rm M}_\odot}\right) s, & a = R_{\rm G} \\ \frac{12\sqrt{6}\pi R_{\rm G}}{c} \simeq 5 \times 10^4 \left(\frac{M_{\rm BH}}{10^8 {\rm M}_\odot}\right) s, & a = 0 \end{cases} \tag{6.10}$$

It is evident that for some AGN a shorter variability time is found compared to their horizon light-crossing time. This result is not compatible with the standard shock-in-jet model. It is assumed that a shock extends over the entire jet diameter. Otherwise, the observed luminosities could not be reached. The smallest diameter of the jet is present close to the base of the jet with approximately the scale of the event horizon. Shorter variability times however than the horizon light-crossing time were found.

In the following, alternative models will be discussed which could explain the observations. However, a few comments shall be made towards some previous work from different authors. Firstly, it is disputable that the emission needs to be located far away from the black hole as suggested by Vovk & Neronov (2013). For example, mini-jets produced by reconnection events (Giannios et al. (2009, 2010); Narayan & Piran (2012)) require the relatively high magnetic field close to the black hole. Secondly, the emission regions in the jet need to be very compact compared to the event horizon. The luminosity produced by such a small region is, however, limited and hence may not be able to create a flare. Another possibility represents the anisotropic acceleration of the particles.

6.7 Theoretical Aspects of the Flare

In this section, a few possible classes of gamma-ray emission models will be reviewed and their applicability to the VHE outburst observed from IC 310 will be proved. These models need to deal with the following charateristics: (i) a high state of the VHE lasting for at least 3.7 h, (ii) frequent short-time variability on time scales of minutes, (iii) a simple power law spectrum up to 10 TeV without a break, (iv) hard photon index of the order of ~ 2, (v) no strong variability of the VHE spectrum during the flare, (vi) overall weak VHE luminosity of $10^{44}\,{\rm erg\,s^{-1}}$, and (vii) no or only weak relativistic aberration.

Besides the failing standard shock-in-a-jet model, non-standard models will be introduced. Those have been invented in order to explain, e.g., to the minute-scale flares of the HBLs PKS 2155–303 or Mrk 501 (Aharonian et al. 2007; Albert et al. 2007c), or the day-scale variability of M87 (Acciari et al. 2009).

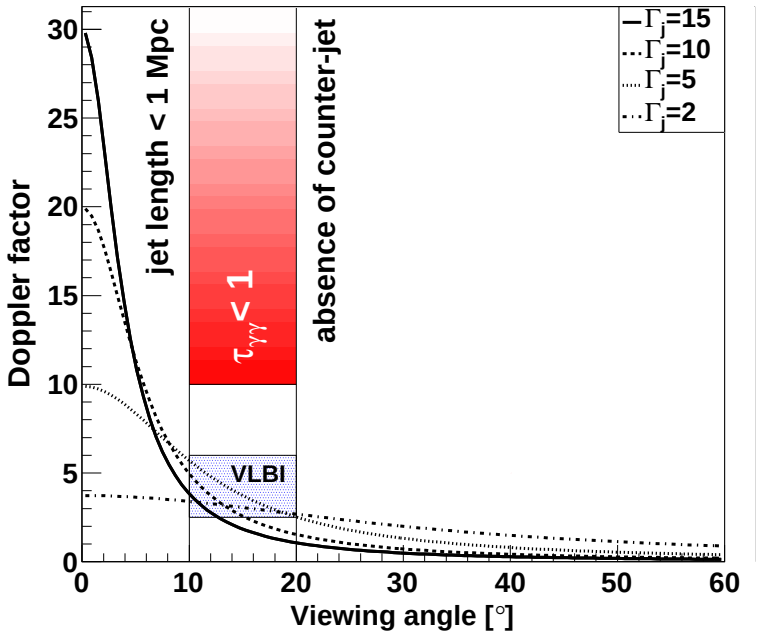

Figure 6.18: Dependence of the Doppler factor on the viewing angle constrained by the flare of IC 310. The red area indicates the valid region of the Doppler/Lorentz factor and viewing angle ($10^\circ \leq \theta \leq 20^\circ$) obtained from the observational constrains. The optical depth $\tau_{\gamma\gamma}$ restricts the Doppler factor to $\delta \gtrsim 10$. The blue shaded area shows the region for the Doppler factor which is consistent with the VLBI observation. Image taken from Aleksić et al. (2014b).

6.7.1 Shock-in-jet model

Similar to the discussion in Chapter 5, the observed fast TeV variability will be investigated in terms of the size of the emission region and the opacity problem. In Begelman et al. (2008) it was shown that in case of PKS 2155–304 the shock-in-jet model can still explain the minute-variability by considering a large Lorentz factor of $\Gamma_\mathrm{j} \gtrsim 50$ to allow for an escape of the TeV radiation. As PKS 2155–304 is a blazar the viewing angle is assumed to be small, hence the Doppler factor can be as large as $\delta \gtrsim 100$. However, for IC 310 the angle is larger. The allowed region of the Doppler factor constrained by the angle found from the radio observations is marked in Fig. 6.18. The valid Doppler factors for the boosting of the emission of IC 310 lie in a range of $1 \leq \delta \leq 6$. These values are consistent with those found in Section 5.5.1.

Following Eq. 2.24 and assuming a variability time scale of $\tau_\mathrm{var} = 4.8\,\mathrm{min}$, the size of the emission region is of the order of $R \sim \delta \cdot 8.5 \times 10^{12}\,\mathrm{cm}$. In terms of the gravitational radius of IC 310, this can be given as $R \sim \delta \cdot 0.2\,R_\mathrm{G}$. With $\delta = 4$, the one minute variability time would correspond to a size of the emission region to be as small as $\sim 80\,\%$ of the event horizon of the black hole of IC 310. In order to achieve $R \approx R_\mathrm{G}$, a Doppler factor of at least $\delta = 5$ is necessary.

The most severe condition on the explanation of the flare is set by the optical depth of $\gamma\gamma$ pair production (see Section 6.4). The observed gamma-ray spectrum attains energies up to 10 TeV. These particles need to escape the emission region without being absorbed. The optical depth is given in Eq. 2.31. Assuming a synchrotron luminosity of $L_\mathrm{syn} \sim 10^{42}\,\mathrm{erg\,s^{-1}}$, we arrive at

$$\tau_{\gamma\gamma}(10\,TeV) = \delta^6 \cdot 1.2 \times 10^5, \tag{6.11}$$

using $\tau_{\rm var} = 4.8\,$min. Thus, strong Doppler boosting is required to achieve $\tau_{\gamma\gamma}(10\,TeV) < 1$. Applying $\delta = 4$, the optical depth results in $\tau_{\gamma\gamma}(10\,TeV) \sim 29.8$ for $\tau_{\rm var} = 4.8\,$min. To achieve $\tau_{\gamma\gamma}(10\,TeV) < 1$ a Doppler factor of $\delta \gtrsim 7.1$ is needed. Since variations as short as 1 minute were observed, a Doppler factor of $\delta \gtrsim 10$ is required.

The inferred values for the Doppler factor from the fast variability are not compatible with those found from the radio observations. This might be due to the already known Doppler factor crisis (see Section 2.6). However, according to Fig. 6.18, no Lorentz factor can be found which yields a Doppler factor within the region limited by the viewing angle. Thus, the fast variability measured from IC 310 can not be explained by the shock-in-jet model. This model restricts the size of a shock at which the emission is produced to the size of the event horizon, see Section 2.7.2.

However, the lower limit on the viewing angle inferred from the jet length that challenges the shock-in-jet model might be biased by a bend in the jet. Such a bend cloud cause the jet near the black hole to point into just the right direction towards us in order to allow for large Doppler boosting. As the projected pc and kpc scale jet are almost perfectly aligned, this bend is required to be in the plane set by the pc and kpc scale jet. For a semi-opening angle of 6°, corresponding to a Lorentz factor of $\Gamma_{\rm j} = 10$, the probability for a jet randomly pointing in a certain direction is $1 - \cos 6^\circ = 0.5\%$ assuming that two jets are being in a sphere of 4π. If the bend should not affect the position angle (P.A.) of the observed jets, this would multiply another chance probability of 11%.

Jet-bending on sub-pc and pc scales was already observed in VLBI images of, e.g., Mrk 501 (Edwards & Piner 2002), BL Lac (Gabuzda & Cawthorne 2003), 3C 279 (Homan et al. 2003), and CTA 102 (Fromm et al. 2013). It has been suggested that the appearance of those bends is connected to the gamma-ray emission observed from those objects (von Montigny et al. 1995; Graham & Tingay 2014). However, Graham & Tingay (2014) studied the tendency for jet bending in gamma-ray-quiet and loud AGN, and concluded that jet bending is not a significant condition for detection of an object in the gamma-ray regime.

6.7.2 Cloud/Star-Jet Interaction Models

In literature, several models for gamma-ray emission or in particular for gamma-ray flares are based on the interaction of the jet with stars or clouds, and vice versa (Bednarek & Protheroe 1997a; Barkov et al. 2010, 2012b; Araudo et al. 2013). Such a scenario was originally proposed to explain variability observed from AGN in the radio band by Blandford & Königl (1979). Gas clouds could originate from, e.g., stellar winds of massive stars, or from the envelop of a red giant. Those clouds are known to exist in AGN as their optical emission lines can be observed.

Generally, such models needs to be critically examined. The probability that a star interacts with a jet is commonly not known due to missing measurements on, e.g., the density of stars in the vicinity of the black hole in particular objects. It is also questionably if enough massive stars (necessary, e.g., in the model by Bednarek & Protheroe (1997a)) are present in the jet in order to reproduce the observed duty cycle (ratio between the time of flaring activity and observation time). Such estimates could be done using the information about the starforming and supernova rate, respectively.

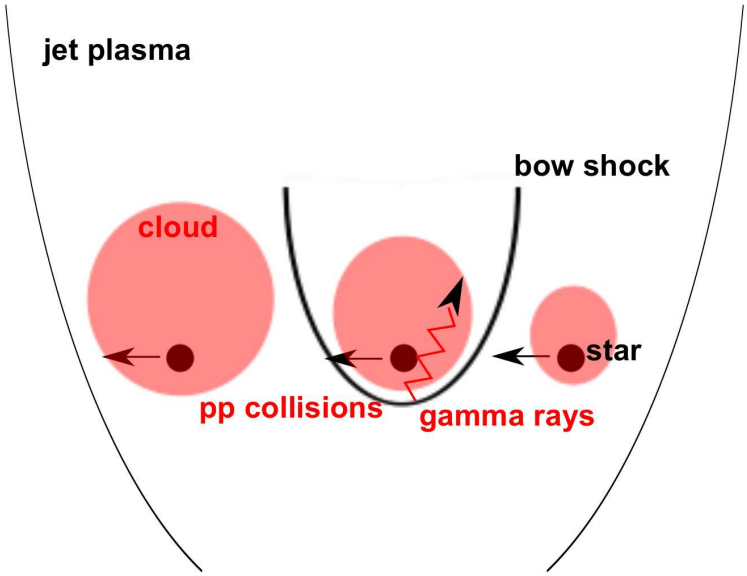

Figure 6.19: Cloud-in-jet model. As a star (red giant) travels through the jet, the envelop will be blown up to a cloud that will be accelerated and heated by the pressure of the jet. For simplicity, the evolution of a spherical cloud expansion is shown. pp collision at the bow shock between the cloud and the jet interface will lead to the production of gamma rays.

Cloud-in-jet model

Barkov et al. (2010, 2012b) introduced a model for the production of flaring gamma-ray emission for M87 based on the interaction of a red giant (solar-mass-type star) with the AGN jet. The envelop of the red giant is assumed tidally disrupted in parts already by the gravitational field of the black hole (Ivanov et al. 2003; Lodato et al. 2009). Due to the pressure present in the jet the envelop will be blown up and heated. This will form a gas cloud (see Fig. 6.19). As the external layers of red giants are less gravitationally bounded to the core of the star, clouds up to $\gtrsim 10^{29}$ g can be formed in the vicinity of the black hole. Due to a strongly magnetized base of the jet (Komissarov et al. 2007; Barkov & Komissarov 2008) electrons may not be accelerated to TeV emitting energies. On the other hand, protons are less affected by the magnetic field and hence reach the cloud. There, proton-proton (pp) interactions of accelerated protons could produce the observed gamma-ray emission at a bow shock located at the interface of the jet and the cloud. A concrete mechanism for the acceleration of the protons is not given. The authors explicitly mention that the cloud must not be accelerated in order to achieve a most effective production of the TeV emission, i.e., no Doppler boosting takes place. The day-scale variability observed from M87 can be explained by this model as well as the observed hard gamma-ray spectrum ($\Gamma \approx 2.2$).

The produced gamma-ray peak in a light curve depends on the radius of the cloud which changes with time (see Barkov et al. (2012b)). Several peaks in the light curve could be produced if the clouds gets destroyed into fragments due to the jet pressure. Barkov et al. (2012a) could show that under such condition the model can also describe the observed minute variability from blazars, e.g., PKS 2155–304. On the contrary, in case of IC 310 the large Doppler boosting due to a larger viewing angle is missing. A large beaming factor is then necessary to

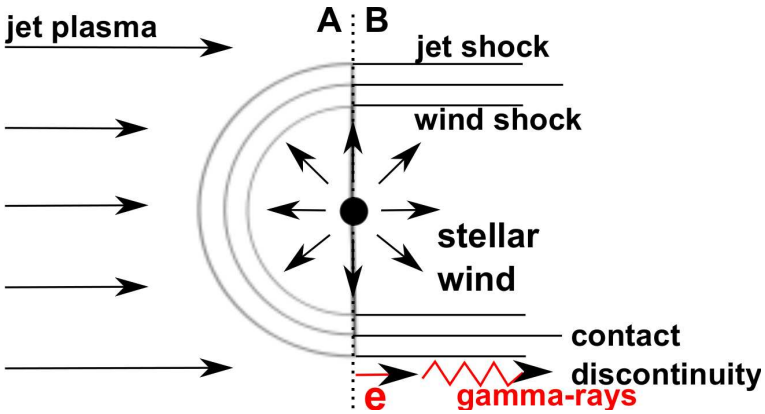

Figure 6.20: Star-in-jet model. The interaction of a massive star with strong stellar wind with the jet plasma may lead to the formation of two shocks, the jet and the wind shock, surrounded by the contact discontinuity. In region A, the jet shock is quasi-parallel. In region B, the shock in quasi-perpendicular and electrons might be accelerated along the jet shock parallel to the magnetic field direction. Gamma radiation is then produced by pair-Compton cascades. Image adapted from Bednarek & Protheroe (1997a).

reach the observed luminosity. Hence, this model can not explain the flare of IC 310.

Star-in-jet model

Bednarek & Protheroe (1997a) have developed a model for variable gamma-ray emission introduced by massive stars interacting with the jet. Based on this work, their model will be described in the following. Those stars could be Wolf-Rayet or young massive OB stars. They are characterized by a high mass-loss rate ($\dot{M} \sim 10^{-6} - 10^{-5} \mathrm{M}_\odot\,\mathrm{yr}^{-1}$) due to intense stellar winds with wind velocities of $v_{\mathrm{wind}} \sim 10^3\,\mathrm{km\,s}^{-1}$ (Lang 1992). If those stars interact with the relativistic jet, a double-shock structure with a contact discontinuity may form, as illustrated in Fig. 6.20. The jet shock will be relativistic while the wind shock remains non-relativistic. Along the relativistic jet shock electrons will be accelerated by the Fermi-I mechanism (see Section 2.3.1). In principle, protons can also be considered to be accelerated. However, the authors showed that the interaction lengths of protons in the wind plasma and stellar radiation exceed the shock radius. The accelerated electrons can trigger pair-Compton cascades in the thermal radiation field of the star which lead to the production of gamma rays. In Bednarek & Protheroe (1997a), this model was used to explain daily-scale gamma-ray variability of the blazar Mrk 421. Shorter variability time scales can be achieved in case of very unstable stellar winds and/or due to irregularities in the jet plasma.

Applying this model to the observation of IC 310 requires relatively large angles of the shock directions to the direction of the jet. The following parameters are assumed: radius of the star $R_{\mathrm{star}} = 10^{12}\,\mathrm{cm}$, mass loss rate of $\dot{M} \sim 10^{-6}\mathrm{M}_\odot\,\mathrm{yr}^{-1}$, wind speed of $v_{\mathrm{wind}} = 10^3\,\mathrm{km\,s}^{-1}$, velocity of the star $v_{\mathrm{star}} = 10^4\,\mathrm{km\,s}^{-1}$ at a distance of $l \sim 0.01\,\mathrm{pc}$ from the jet base. Assuming a jet power of $L_{\mathrm{jet}} = 2 \times 10^{42}\,\mathrm{erg\,s}^{-1}$ (see Appendix A Section 2) and a jet opening angle of $\Phi = 5°$, one can estimate the radius of the shock r_{sh} from:

$$\frac{r_{\mathrm{sh}}}{10^{12}\mathrm{cm}} \approx 103 \sqrt{\frac{\dot{M}}{10^{-5}\mathrm{M}_\odot\,\mathrm{yr}^{-1}}} \sqrt{\frac{v_{\mathrm{wind}}}{3 \times 10^8\,\mathrm{cm\,s}^{-1}}} \frac{R_{\mathrm{star}}}{10^{12}\,\mathrm{cm}} \frac{\Phi}{5°} \frac{l}{1\,\mathrm{pc}} \left(\sqrt{\frac{L_{\mathrm{j}}}{10^{46}\,\mathrm{erg\,s}^{-1}}} \right)^{-1} \tag{6.12}$$

The resulting radius of the shock would be of the order of $r_{\rm sh} \sim 10^{13}$ cm. The short variability time scales from individual flares can be explained with an unstable shock direction caused by the stellar wind. Assuming that the size of these irregularities is of the order of 3% compared to the stellar dimension, on can determine the expected time in which the shock changes its direction. This time can be calculated to be $\sim 3\,\% R_{\rm star}/v_{\rm wind} = 5\,$min, comparable to the observed variability time scale of IC 310. The maximum achieved electron energy in this model can be determined from the synchrotron energy loss rate if further losses are neglected:

$$E_{\rm e}^{\rm max} = 6 \times 10^4 \chi^{1/2} B^{-1/2}\,{\rm GeV}, \tag{6.13}$$

where χ is the acceleration coefficient, and B the magnetic field of the star in Gauss. According to Igoshev & Kholtygin (2011), one can find a surface magnetic field of the order of 1 kG for OB stars. At the distance of the shock, this would reduce to 0.01 G for a dipole structure of the magnetic field. For acceleration at a shock with velocity 0.1 c, values of $\chi \sim (0.16 - 40) \times 10^{-3}$ are found for a parallel or perpendicular shock (Protheroe 1998). This allows an acceleration of the electrons to maximum energies of $\sim 10 - 120\,$TeV consistent with the observed spectrum. The unbroken gamma-ray spectrum with a photon index of $\Gamma \sim 2$ up to 10 TeV can be explained with efficient cooling of the electrons in the Thomson and Klein-Nishina regime by scattering radiation from the massive star.

To calculate the produced gamma-ray luminosity, the power $L_{\rm sh}$ that can be extracted from the jet by the shock has to be determined. This power can be calculated from

$$L_{\rm sh} \cong L_{\rm jet}\,(r_{\rm sh}/(\Phi l))^2 \approx 1.5 \times 10^{39} \frac{\dot{M}}{10^{-5} {\rm M}_\odot\,{\rm yr}^{-1}} \frac{v_{\rm wind}}{3 \times 10^8\,{\rm cm\,s}^{-1}}\,{\rm erg\,s}^{-1}. \tag{6.14}$$

Inserting Eq. 6.12 into Eq. 6.14 one can show that the maximum power that can possibly be extracted only depends on parameters of the stellar wind, and not on the jet power. The gamma-ray luminosity can be estimated

$$L_\gamma \approx 4 \times 10^6 \mu L_{\rm sh} \left(\frac{\phi}{10^{-3}\,{\rm rad}} \right)^{-2}, \tag{6.15}$$

with μ being the efficiency of the conversion of the jet power into gamma rays at the shock, and ϕ the angle of the cone of gamma-ray emission. However, only a small fraction of the jet around the star can produce the emission. Hence, the resulting gamma-ray luminosity becomes $L_\gamma \sim 10^{38}\,{\rm erg\,s}^{-1}$ which is way lower than the observed gamma-ray luminosity of the flare of $L_\gamma \sim 2 \times 10^{44}\,{\rm erg\,s}^{-1}$. In order to achieve this luminosity, the emission has to be beamed into a narrow cone with opening angle of $< 0.4°$. Therefore, a strong beaming is necessary to explain the observation of the flare from IC 310 with this model.

6.7.3 Jets-in-a-jet models

The *jets-in-a-jet* model presents another possibility for explaining fast gamma-ray variability. Although other works have discussed this model as well (Giannios et al. (2009, 2010); Narayan & Piran (2012)) the discussion will be focused on the model by Giannios et al. (2010). In the model, the relativistic jet (with a bulk Lorentz factor of $\Gamma_{\rm j}$) contains several mini-jets with $\Gamma_{\rm mj}$ that move relative to the main jet. Those mini-jets result from dissipation of magnetic energy in strongly magnetized plasma regions (magnetic reconnection, see Section 2.3.2) caused by instabilities in the jet (Eichler 1993; Begelman 1998; Appl et al. 2000; Moll et al. 2008; Moll

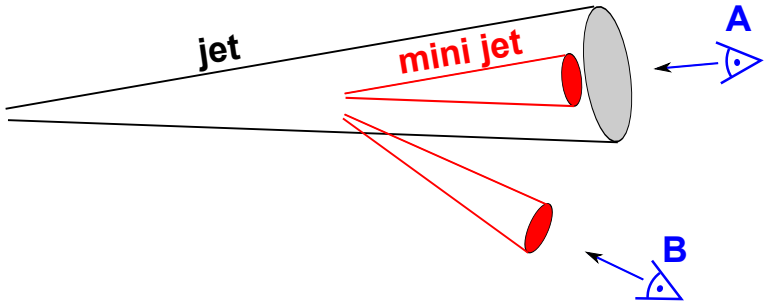

Figure 6.21: Jets-in-a-jet model. Insight the jet, several mini-jets may exist. Depending on the angle towards the observer the emission gets boosted with different Lorentz factors $\Gamma_{\rm em}$. The case A represents the situation for a blazar with a small viewing angle, while case B applies for radio galaxies. Note, that always two mini-jets pointing into an opposite direction are formed by a reconnection event.

2009), or, e.g., due to reversal of magnetic field polarity in the inner disc/black hole magnetosphere (Giannios et al. 2009). As consequence from a reconnection event, two mini-jets are formed at any time which move in random directions.

In terms of fast variability, where $R < R_{\rm G}$, the size of the emitting region is at least as large as $R_{\rm G}$ and the fast amplitude change results from a small fraction (mini-jets) of the emitting volume beamed into a narrow cone. Generally, the "emitted" Lorentz factor can be expressed as $\Gamma_{\rm em} \propto \Gamma_{\rm j}\Gamma_{\rm mj}$. Adapting $\Gamma_{\rm j} = \Gamma_{\rm mj} = 10$ yields $\Gamma_{\rm em} = 100$, which is large enough to avoid absorption of TeV photons for the case of the minute flares observed from PKS 2155–304 according to Begelman et al. (2008). However, as pointed out by Narayan & Piran (2012), $\Gamma_{\rm j}$ can not simply be replaced by $\Gamma_{\rm em}$ in the calculation of the optical depth from Begelman et al. (2008). This calculation is valid for a single radiation region. In the jets-in-a-jet model, many regions produce the emission, and if one beam escapes its emission region it may encounter other emission regions.

The resulting value for the emitted Lorentz factor depends furthermore on the viewing angle. For blazars (see case A in Fig. 6.21), we observe mini-jets pointing into the direction of the main jet ($\theta \lesssim 1/\Gamma_{\rm j}$). Instead, in case of radio galaxies (case B in Fig. 6.21), we may see emission from mini-jets "off-axis", pointing outside the jet cone ($\theta > 1/\Gamma_{\rm j}$). This off-axis observation have been considered by Giannios et al. (2010) to explain the daily-scale TeV variability of M87. According to the authors, variability time scales down to 2-3 hours can be explained by the model for M87.

The off-axis observation of a conical jet with opening angle $\sim 1/\Gamma_{\rm j}$ is defined by the angle $\alpha_{\rm off}$ by Eq. 3 in Giannios et al. (2010):

$$\theta \equiv \frac{\alpha_{\rm off}}{\Gamma_{\rm j}}, \tag{6.16}$$

where θ is the viewing angle. For $\Gamma_{\rm j}$, $\Gamma_{\rm mj} \gg 1$ and $1 \lesssim \alpha_{\rm off} \lesssim \Gamma_{\rm j}$, $\Gamma_{\rm mj}$, the emitted Lorentz factor can be expressed as:

$$\Gamma_{\rm em} \simeq \frac{2\Gamma_{\rm j}\Gamma_{\rm mj}}{\alpha_{\rm off}^2}. \tag{6.17}$$

Assuming $\alpha_{\rm off} = 2$ and $\Gamma_{\rm j}, \Gamma_{\rm mj} = 10$ gives $\Gamma_{\rm em} \sim 50$. For IC 310 this Lorentz factor easily allows for the emitting region being $R > R_{\rm G}$ assuming $\tau_{\rm var} = 4.8$ min.

The detectability of the emission originating from a mini-jet depends on the luminosity of the source. The bolometric mini-jet luminosity depends on the radiated energy of the mini-jet,

the solid angle over which the radiation takes place, and the observed duration of the emission (variability time scale). The expected measured luminosity of an off-axis blob is found to be

$$L_{\rm obs} = \frac{16 L_{\rm on}}{\alpha_{\rm off}^8}, \tag{6.18}$$

where $L_{\rm on}$ denotes the luminosity of the source which would be observed "on-axis". The luminosity of this mini-jet corrected for beaming effects is given by:

$$L_{\rm mj} = \frac{L_{\rm rad}}{\epsilon} = \frac{L_{\rm on}}{4\Gamma_{\rm em}^2 \epsilon}, \tag{6.19}$$

with ϵ being the radiative efficiency. For one mini-jet pointing towards the observer, there exist $N \sim \Gamma_{\rm mj}^2$ mini-jets in total. Therefore, the total power of the mini-jets can be calculated using Eq. 6.17:

$$L_{\rm tot} = \frac{L_{\rm obs}}{\epsilon} \frac{\alpha_{\rm off}^{12}}{256\,\Gamma_{\rm j}^2} \tag{6.20}$$

During the flare, a luminosity of $L_\gamma \sim 2 \times 10^{44}\,{\rm erg\,s^{-1}}$ was measured. For $\alpha_{\rm off} = 2$, $\Gamma_{\rm j} = 10$, and $\epsilon = 0.1$, a total luminosity of $L_{\rm tot} \simeq 3 \times 10^{44}\,{\rm erg\,s^{-1}}$ is found. Supposing that the mini-jets tap a fraction f of the entire jet power, gives:

$$L_{\rm jet} \simeq 3 \times 10^{44} f\ {\rm erg\,s^{-1}}. \tag{6.21}$$

The result is clearly higher than the jet power of IC 310 (Appendix A Section 2).

This model is based on the simple SSC mechanism (see Section 2.5.1). The result changes if an external photon field (e.g., accretion disk, broad-line region, or synchrotron emission from other locations of the jet, e.g., mini-jets) is considered. Furthermore, the observed VHE spectrum from IC 310 during the flare up to energies of 10 TeV not showing hints for a break complicates the explanation using a SSC model. The acceleration must be very efficient, assuming a small magnetic field and/or short acceleration time scale and a fast escape of the particles. Finally, the shortest possible variability time in agreement with the model will be calculated analogous to the discussion in Giannios et al. (2010) for M87 by comparing the black holes mass with the observed $\tau_{\rm var}$ of Mrk 501 and PKS 2155–304. The latter harbors a black hole of mass $M_{\rm BH} \sim 1 \times 10^9\,{\rm M_\odot}$ and shows a variable TeV emission of $\tau_{\rm var} \sim 5\,{\rm min}$. The black hole mass of IC 310 is four times smaller. The larger viewing angle which results in more pronounced off-axis observation yields a time-scale reduced by a factor of $\alpha_{\rm off}^2 = 2^2 = 4$. Therefore, a variability time as short as 5 min can still be expected from IC 310 consistent with the observation.

6.7.4 Magnetosphere Models

Magnetosphere models are based on particle acceleration due to electric fields (see Section 2.3.3) parallel to the magnetic fields. Originally, those models have been proposed for pulsars. But, a particle-staved magnetosphere similar to those known from pulsars may also be anchored to the ergosphere of black holes (Neronov et al. 2009; Levinson & Rieger 2011; Punsly 2001). Figure 6.22 illustrates this scenario. A magnetospheric model was also proposed to explain the rapid variability observed from M87 (Levinson & Rieger 2011).

It is assumed that electric fields can exist in vacuum gaps if the density of charge carriers is low; otherwise they short-circuit. The critical density is given by the Goldreich-Julian charge

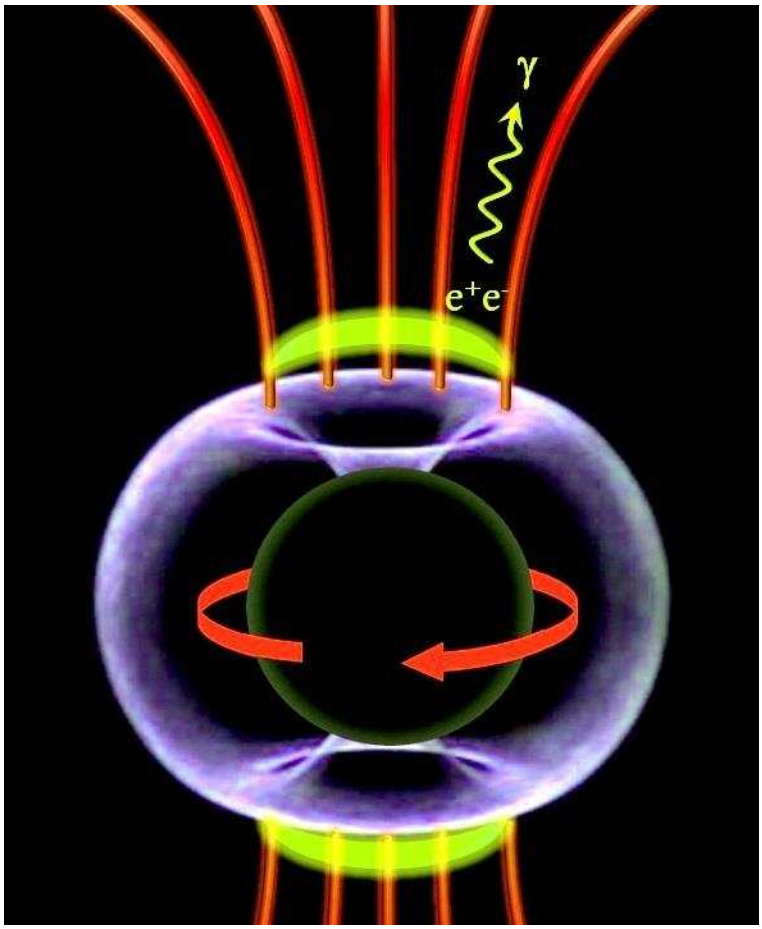

Figure 6.22: Magnetosphere anchored to the ergosphere (white/blue) of a maximally rotating black hole. The rotation induces a charge-separated magnetosphere indicated by red lines. A polar vacuum gap region is show in yellow. In this region particles are accelerated to high energies by the electric field component parallel to the magnetic field. Gamma rays are produced by inverse Compton scattering and copious pair production due to thermal photons originating from accretion of plasma. Image taken from Aleksić et al. (2014b).

density. Photon-photon collisions in a hot accretion torus or in the black hole corona may produce extra electron-positron pairs on top of the Goldreich-Julian charge density. Furthermore, it has been suggested by Neronov et al. (2009), that particles can also be injected by the reconnection of twisted magnetic loops in the accretion flow. When the accretion rate of a black hole becomes very low, it is assumed that the charges are depleted. Such a low accretion rate is expected for black holes at the end of their accretion history. Then, they should spin maximally. Following the Blandford-Znajek mechanism of Blandford & Znajek (1977) a jet is formed. The collimation of the jet is assumed to take place at a distance of $\sim 10\,R_{\rm G}$. This lies far away from the light cylinder of the black hole. Generally, gaps could be located at different angles with the jet axis. One possible location could be at the pole of the magnetosphere (see Fig. 6.22). Beams with a rather large angle could also point in the direction of the viewing angle of IC 310.

Since the observed light curve from the flare is highly variable, the emission produced in this model needs to be variable as well. The variability is characterized by the height of the gaps h. The gap heights can be smaller than $R_{\rm G}$. Therefore, rapid variability as those observed is naturally expected. According to Levinson & Rieger (2011), the gap height and the seed particle content depend on the accretion rate $\dot{m}$. For $\dot{m} \sim 10^{-4}$ in units of the Eddington rate and assuming further a maximum rotating black hole, it can be shown that $h \sim 0.2\,R_{\rm G}$.[2] The absorption via $\gamma\gamma$-pair production can be neglected in case of a radiative inefficient accretion flow. Particles accelerate in the electric field parallel to the magnetic field and produce electromagnetic cascades. This leads to an increase of the charge carrier density. Consequently, after some time the flare ends when the potential across the gap short-circuits. Then, the particles move away with the jet. The gap may reopen and produce new flares. In Mannheim (1993a) it is suggested that the unsaturated electromagnetic cascading leads to a rather stable spectrum with a power-law index of 1.9. This would be in line with the observation of the flare of IC 310.

Due to the low accretion rate in IC 310, this model provides a convincing explanation. It would be interesting to investigate the rapid TeV emission observed from the HBLs (Mrk 501, PKS 2155–304) in terms of such a model due to their low accretion rates.

6.7.5 Conclusions

The observed flare from IC 310 can not be explained with the standard shock-in-jet scenario. In order to achieve $R = R_{\rm G}$ and $\tau_{\gamma\gamma} > 1$, a large Doppler factor would be necessary. This Doppler factor would not be consistent with the results obtained from high-resolution radio measurements. Further, there exists no Lorentz factor that would be compatible with both the allowed Doppler factor range and the calculated boundaries of the viewing angle range.

Alternative models such as the interaction of clouds or stars with the jet, or the mini-jets model all fail to explain the observation. The former requires a strong Doppler boosting to be consistent with the measurement. The latter can not also explain the observed luminosity.

Particle acceleration occurring in gaps of charged-separated magnetosphere anchored in the ergosphere of a rotating black hole turns out to be one plausible explanation.

[2] The accretion rate is given in units of the Eddington rate, $\dot{m} = \dot{M}/\dot{M}_{\rm Edd}$, where the Eddington accretion rate is defined as $\dot{M}_{\rm Edd} = L_{\rm Edd}/\eta_{ff}c^2$, with $\eta_{ff} = 0.1$ and $L_{\rm Edd}$ the Eddington luminosity.

7

The First Multi-wavelength Campaign and Monitoring in the Gamma and Radio Band

Afterglow of IC 310:
From first Simultaneous Ripples
to the Search of new Radio Knots

The multi-wavelength picture presented in this chapter is partially based on the Proceeding to the 33th International Cosmic Ray Conference in 2013 (Eisenacher et al. 2013).

7.1 Multi-wavelength Campaign

The first multi-wavelength (MWL) campaign on the object IC 310 was conducted from fall 2012 to beginning of 2013 and has been organized by the author of this thesis. The aim of this project was to investigate the properties of the object in different energy bands from radio up to the gamma rays simultaneously in order to obtain the broad-band spectral energy distribution, and to study the variability behavior in different frequency ranges. The latter became of particular interest after the VHE flare in November 2012, which happened right at the beginning of the campaign.

The multi-wavelength coverage for the time range from November 2012 to February 2013 is shown in Fig. 7.1. The observations of the different telescopes have been organized to achieve the best possible temporal overlap with the observation windows of the MAGIC telescopes. The low frequency range is covered by the multi-frequency and single-frequency flux density measurements of the Effelsberg 100 m and OVRO 40 m telescope, respectively. In the optical band, the object has been monitored in the R-band by the KVA 35 cm telescope. For the UV and soft X-ray range, Target of Opportunity (ToO) proposals for the *Swift* satellite has been accepted. The hard X-ray and soft gamma-ray regime was covered by *Swift*-BAT as well as by

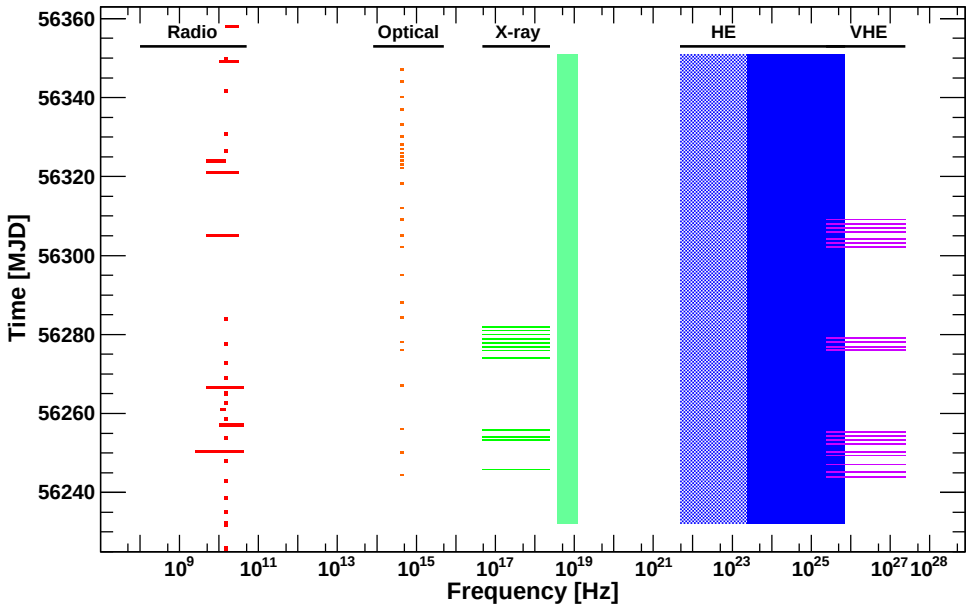

Figure 7.1: Multi-wavelength coverage from radio to gamma-ray energies between November 2012 and February 2013. Red: radio observations with the Effelsberg 100 m and OVRO 40 m telescopes. Orange: optical measurements with the KVA 35 cm telescope in the R band. Green: X-ray regime covered by *Swift*-XRT and BAT. Blue: *Fermi*-LAT observations. The shaded area indicates the energy range not accessible for IC 310, see text. Violet: MAGIC observation windows.

INTEGRAL[1] (not shown in the figure). In the gamma-ray regime, besides the MAGIC observations, the *Fermi*-LAT instrument continuously accumulates data. However, below $\sim$1 GHz the emission of the gamma-ray bright near-by galaxy NGC 1275 is too strong and the angular resolution of the instrument too poor to distinguish between the two objects.

Furthermore, from October to November 2012 the first high sensitive, high resolution radio VLBI observations were conducted with the European VLBI Network at the frequencies 1.7, 5.0, 8.4, and 22.2 GHz. The results of the 5 GHz measurement have been presented in Chapter 6[2].

7.2 MAGIC Observations and Analysis

After the VHE flare observed from IC 310 on November 12/13, 2012 with MAGIC (see Chapter 6), further observations with the upgraded system (Aleksic et al. 2014a) were carried out as part of the MWL campaign from November 2012 to February 2013 as well as for monitoring the flux level from July 2013 to March 2014. During these periods, IC 310 has been observed with the “NGC 1275 mode" described in Section 6.1, and another special wobble configuration mode called “Perseus-MA mode", see Fig. 7.2. In the latter case, the wobble center is chosen to be the central position between IC 310 and NGC 1275 in the sky. Two wobble pointings each with 0.26° offset from the wobble center were defined in a way that the offsets from the pointings to each object is always the standard wobble offset for MAGIC observations of

[1]The results from the *INTEGRAL* observations will be included in the PhD thesis of T. Beuchert.
[2]The results of the remaining frequencies will be part of the PhD thesis of R. Schulz.

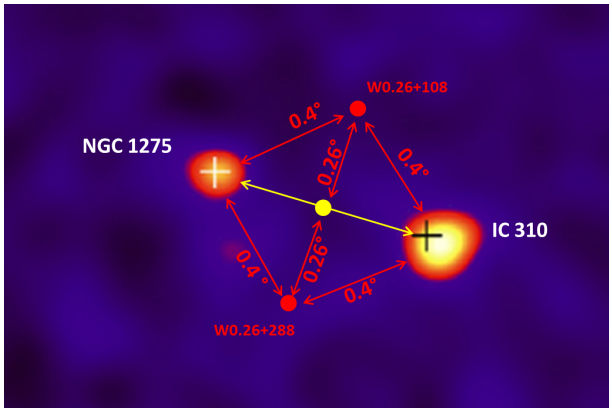

Figure 7.2: Configuration of the wobble positions during IC 310 multi-wavelength observations called "Perseus-MA mode". Two positions, W0.26+108 and W0.26+288, were used, centered around the yellow dot half way between IC 310 and NGC 1275.

$0.4°$. Hence, no additional MC simulations with non-standard wobble offset were necessary. The fraction of the data with non-standard wobble offset taken with the NGC 1275 mode during these periods is only 5% and hence could be discarded. The data cover the zenith distance range of $11° < \mathrm{Zd} < 56°$. Some of the data were taken under strong moon-light conditions. Therefore, data with a current exceeding $2\,\mu$A measured in the MAGIC-I camera were excluded from the analysis. Furthermore, data taken during bad weather or bad hardware conditions, and those affected by the dead-zone problem have been rejected, see Appendix B Table 12, 13 and 16, 17.

The data presented in this chapter have been divided into two sets, 35 h of data used for the MWL campaign covering the time range November 2012 to January 2013, and 27 h of monitoring data from August 2013 to March 2014[3]. The analysis was performed separately, as different MC simulations were used due to a change of the point-spread function during these two periods. The analysis of the data during the campaign up to the flux calculation was performed analogous to the analysis of the flare data described in Chapter 6 with the same cleaning method (see dynamical sum-image cleaning Section 4.5.2), Off data (Appendix B Table 8), and the same MC simulations. The monitoring data were analyzed as described in Aleksic et al. (2014b) and Section 4.5 using the sum-image cleaning algorithm. The Off data used is listed in Appendix B Table 18 and covers a zenith distance range of $6° - 49°$ with an effective time of $t_{\mathrm{eff}} = 13.7$ h. For this analysis, a systematic error on the flux normalization of 11% and an error of 0.15 of the photon index can be assumed for both periods (see Section 4.6). The uncertainty on the energy scale is $< 15\%$.

[3]The time ranges given here differ from the ones mentioned above due to the quality selection of the data.

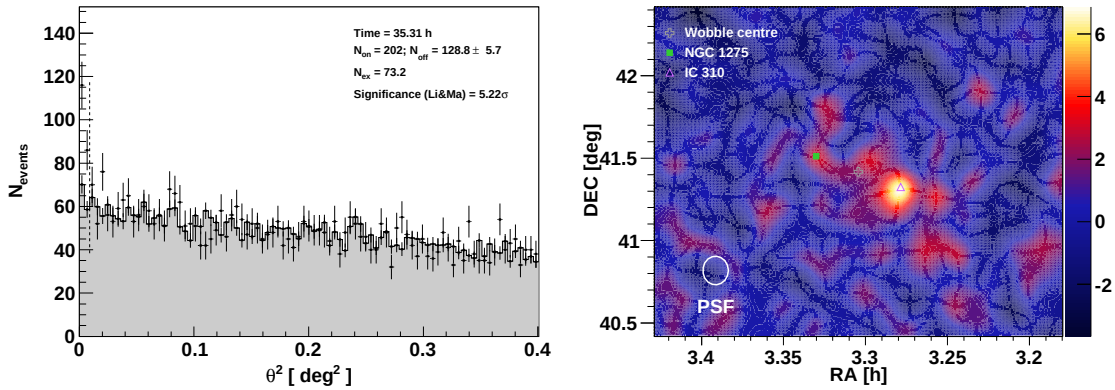

Figure 7.3: *Left panel:* θ^2 distribution above 300 GeV during MWL obervations in November 2012 to January 2013. The following cuts have been applied: HADRONNESS < 0.16, SIZE > 300 phe, $\theta^2 < 0.009$, for four OFF regions. *Right panel:* TS value map above 300 GeV with the same HADRONNESS and SIZE cut applied.

7.3 Multi-wavelength Light Curve

7.3.1 Results of MAGIC Observations during the Campaign

In the time range from November 2012 to January 2013 (MJD 56245.0–56309.1) the object could still be detected by MAGIC in $t_{\mathrm{eff}} = 35$ h of data when excluding the flare data. The measured θ^2 distribution is shown in Fig. 7.3, left, with a significance of 5.22 σ above 300 GeV. This could be verified with the skymap calculated in the same energy range (Fig. 7.3, right) showing a $\sim 6\sigma$ excess at the position of IC 310.

The light curve has been calculated assuming a simple power-law distribution with a photon index of $\Gamma = 2$. The mean flux during the MWL campaign was measured to be $F_{\mathrm{mean}} = (1.36 \pm 0.37) \times 10^{-12}\,\mathrm{cm}^{-2}\,\mathrm{s}^{-1}$ above 300 GeV. The daily and monthly binned flux results are shown in Fig. 7.4 and Appendix B Table 15. Flux upper limits have been calculated according to Rolke et al. (2005) using a 95% C.L., and assuming a systematic uncertainty of 30%. Compared to the mean flux level measured during the flare the flux decreased by a factor of 44.

From both, the daily and the monthly calculated light curve, no significant variability of the flux could be measured. A constant fit to the daily light curve yields a flux of $F_{\mathrm{CstFit}} = (0.90 \pm 0.24) \times 10^{-12}\,\mathrm{cm}^{-2}\mathrm{s}^{-1}$ with a χ^2 of 31 for 18 degrees of freedom corresponding to a probability of 2.9×10^{-2}. The upper limits were not taken into account in the fit. The monthly calculated light curve reveals a constant flux fit of $F_{\mathrm{CstFit}} = (1.30 \pm 0.27) \times 10^{-12}\,\mathrm{cm}^{-2}\mathrm{s}^{-1}$ with a χ^2/d.o.f. of 3.6/2 (probability of 1.7×10^{-1}).

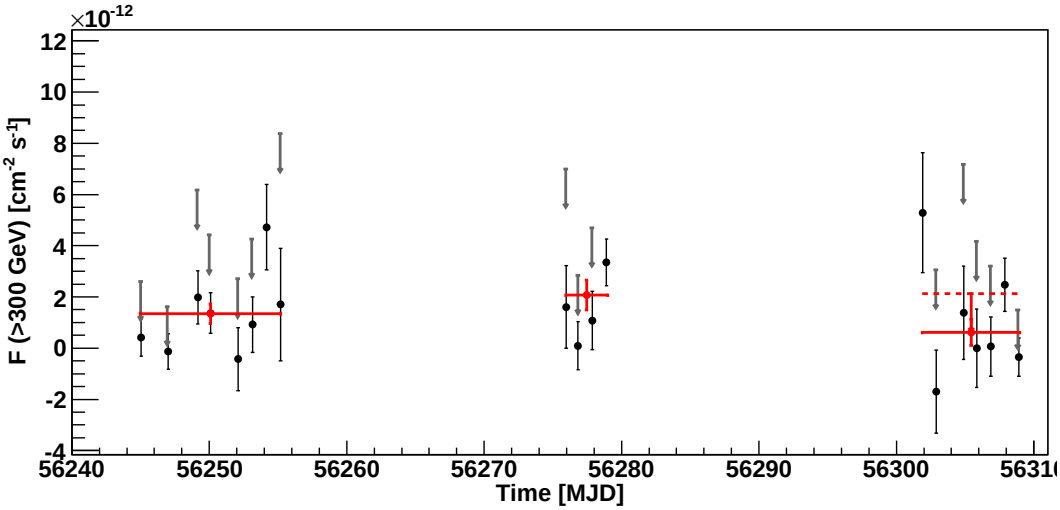

Figure 7.4: Light curve above 300 GeV during MWL observations in November 2012 to January 2013. Black and red data points show the daily and monthly calculated light curve, respectively. Gray and red-dashed arrows indicate flux upper limits.

Table 7.1: Arrival times and energies of gamma events above 1 GeV measured within a circle around IC 310 with a radius of $10.0°$ by *Fermi*-LAT during MWL campaign.

MJD	Energy [GeV]	Probability for IC 310	Probability for NGC 1275
56255.86	3.44	0.73	0.12
56298.82	8.09	0.52	0.17
56333.04	5.89	0.66	0.24

7.3.2 Results of Data in the Low Energy Bands

Figure 7.5 shows the light curve in different energy bands as measured during the campaign in November 2012 to February 2013. Except for *Fermi*-LAT, no further instrument was observing IC 310 in the night of the flare.

The light curve from *Fermi*-LAT in the second panel of Fig. 7.5 was calculated for energies above 1 GeV in order to avoid the contribution from the gamma-ray emission of NGC 1275. IC 310 could not be detected in this energy range during the campaign, although the date of the MAGIC flare was included. Only upper limits of the flux could be calculated. These are given in Appendix C Table 21. The upper limits above 1 GeV are consistent with the flux reported in the 2FGL catalog, see Chapter 5. Hence, no further conclusion can be drawn on the variability behavior of IC 310. The increasing upper limits might be connected to an increasing background produced by a rising flux of NGC 1275 and its flaring behavior as reported at end of January 2013, see ATel #4753. To further investigate the potential for a short flare, the data have been analyzed to search for individual arriving gamma-ray photons. In total, three gamma-ray event candidates above 1 GeV could be found in the time range of the campaign within a circle with a radius of $10.0°$. Those show a rather high probability to be originating from IC 310 rather than from NGC 1275 (see Table 7.1).

The *Swift*-XRT light curve is shown in the central panel of Fig.7.5. Further information of the analysis results, e.g., flux level in the energy range of 0.2–10 keV, the photon index, and N_{H} can be found in Appendix C Table 22. The temporal evolution of the flux (0.2–10 keV), the photon

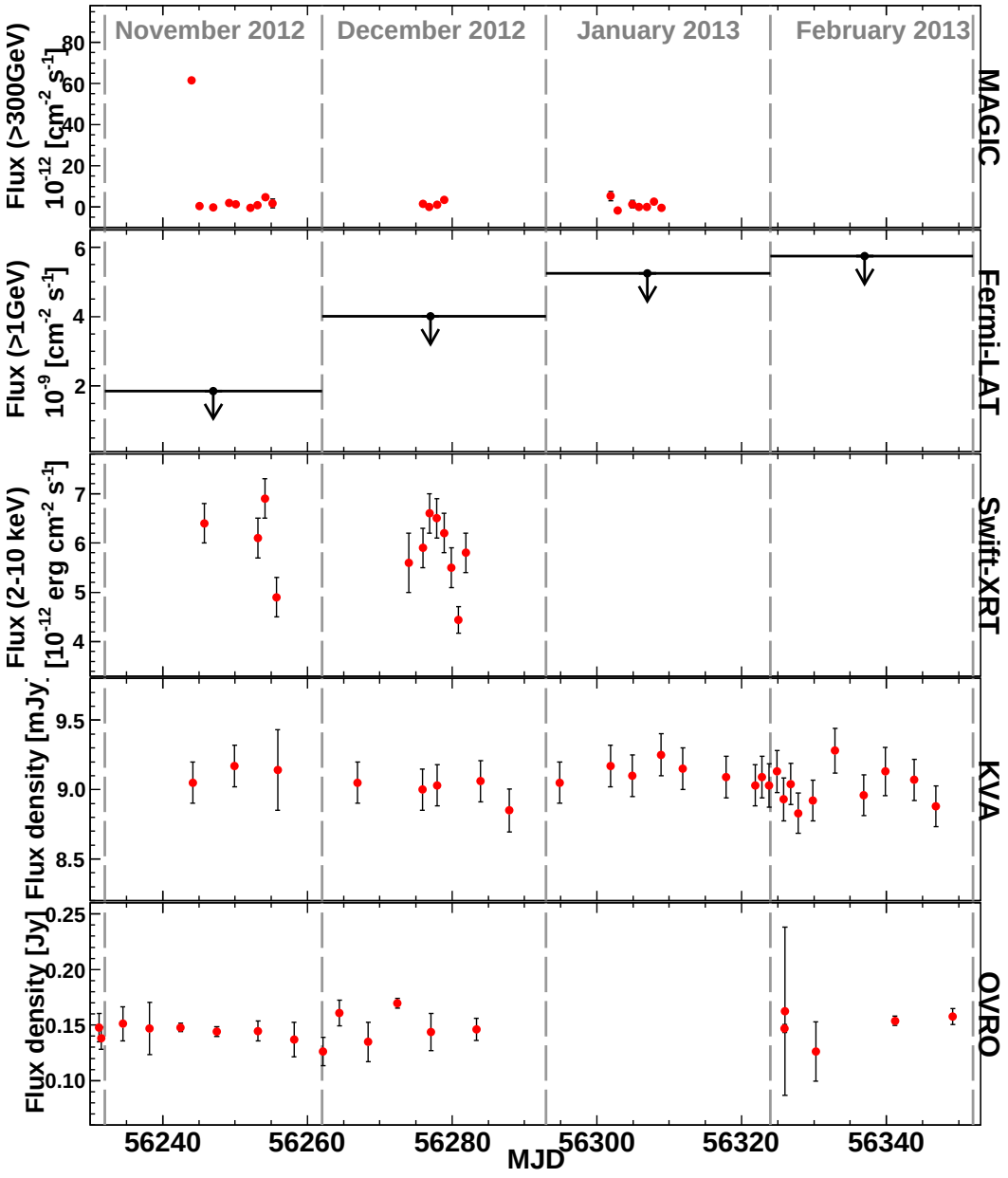

Figure 7.5: Multi-wavelength light curve of IC 310 obtained from the campaign in November 2012 to February 2013. *Top to bottom panels:* Daily MAGIC light curve above 300 GeV, *Fermi*-LAT upper limits above 1 GeV calculated monthly binned, *Swift*-XRT flux between 0.2–10 keV, KVA R-band data (not corrected for host-galaxy contribution), and OVRO measurements at 15 GHz.

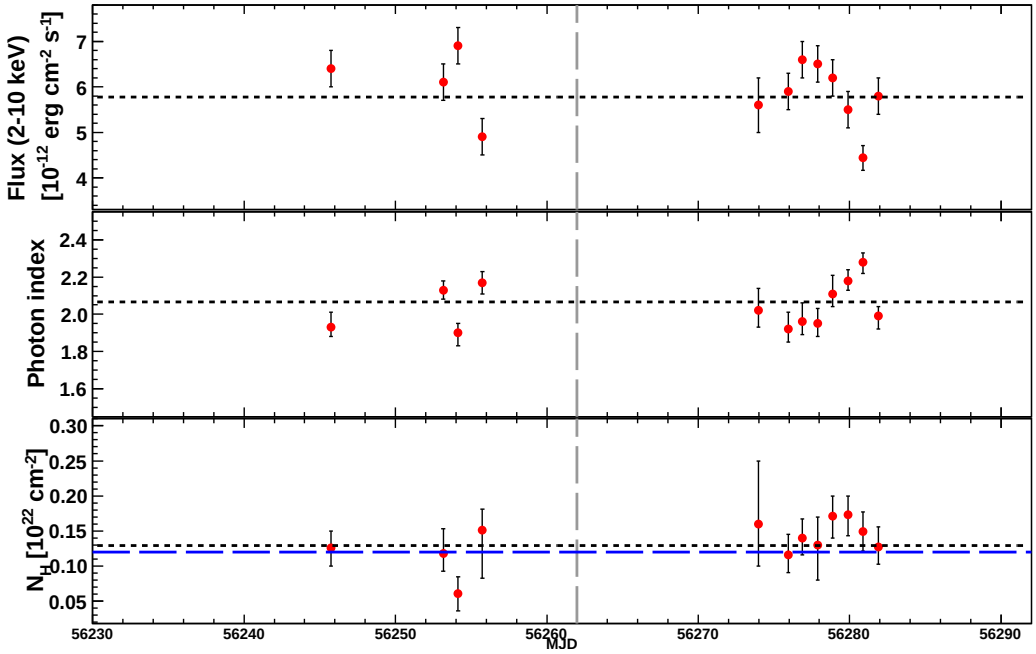

Figure 7.6: X-ray properties of IC 310 measured with *Swift*-XRT observations during the campaign in November 2012 to February 2013. Observations with XRT were only carried out in November and December 2012 (months separated by gray dashed line). *Upper panel:* Measured flux in the energy range 0.2–10 keV. *Middle panel:* Photon index Γ is defined following $F \propto E^{-\Gamma}$. *Bottom panel:* Absorption with an equivalent column of hydrogen. For comparison, the Galactic N_{H} value for IC 310 is shown in blue. All curves were fitted with a constant line (black dashed).

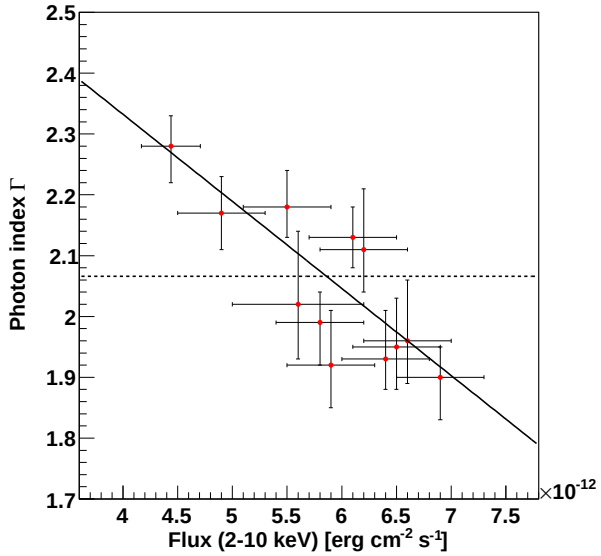

Figure 7.7: Spectral index as a function of the flux (0.2–10 keV) measured with *Swift*-XRT observations during the campaign. The dashed and solid lines represent a fit to the data with a constant and a linear, respectively.

index, and the absorption with a equivalent column of hydrogen in November to December 2012 is presented in Fig. 7.6. The mean flux has been measured to be 0.61 ± 0.01 erg cm^{-2} s^{-1} which is ~ 5 times higher than during previous measurements, see Chapter 5, and moderately higher (factor of 1.4) than in January 2012 (see Appendix C Table 23). The light curve shows variability on a daily basis. A fit with a constant linie reveals a probability of 7.3×10^{-7} for a constant flux (χ^2/d.o.f.$= 49.6/11$). However, no variation $> 3\,\sigma$ from the constant fit flux has been found. Comparing the light curve with the temporal evolution of the photon index yields evidence for a spectral hardening with increasing flux. Spectral variability is found when fitting the photon index with a constant, yielding a χ^2/d.o.f.$= 45.2/11$ (probability of 4.5×10^{-6} for a constant photon index). This evidence is also found when displaying the photon index as a function of the integral flux as shown in Fig. 7.7. A linear fit gives a χ^2/d.o.f. of $14.0/10$ and a probability of 0.17. Such a behavior was also reported for TeV bright HBLs, e.g., by Giommi et al. (2000), and interpreted in terms of a correlation between the flux state and the frequency of the peaks in the broad-band spectral energy distribution. Comparing these observations with the measurements presented in Chapter 5 no trend is found. Thus, no firm conclusion can be drawn. The hydrogen column density stayed constant during the campaign (χ^2/d.o.f.$= 13.4/11$, probability of 0.26) and is consistent with the galactic value for IC 310 (Kalberla et al. 2010). Therefore, no further intrinsic absorption can be found. To summarize the findings, a potential high, variable state in the X-ray range was found after the TeV flare complemented with spectral variability. To investigate flux variability on shorter time scales, however, more observation with more sensitive instruments such as *XMM-Newton* would be necessary.

The optical light curve shown in Fig. 7.5 has been measured with the KVA 35 cm telescope in the R-band. The data were not corrected for the contribution of the host galaxy emission. This emission is expected to be constant. If variability of the AGN would be present, this would affect the light curve. However, no hints for variability are found. The light curve in the time range of MJD 56230–56353 is consistent with a constant flux of (9.05 ± 0.03) mJy (χ^2/d.o.f.$= 13.6/26$, probability of 0.98). Monitoring in January and February 2012 (see Appendix C Table 25) resulted in a constant fit flux of 8.99 ± 0.04 mJy (χ^2/d.o.f.$= 11.7/15$, probability of 0.70). This flux is comparable within the errors of the flux measured during the campaign. Since no further historical monitoring in the optical range in the R-band was conducted for IC 310, the flux can not be compared with other measurements.

The radio data in Fig. 7.5 were collected as part of the OVRO monitoring program at 15 GHz. A fit with a constant to the light curve yields a flux of 0.151 ± 0.002 mJy with a χ^2/d.o.f. of $34.6/18$ and rather low probability of 0.01 revealing rather weak variability. Since radio flares are sometimes found a few months after a gamma-ray flare, the time period covered here is too short to draw conclusions. Therefore, further radio observations covering a larger time span beyond the campaign will be discussed in the next section.

All available flux measurements from KVA and OVRO including the data points used in this section can be found in Appendix C Table 24-29.

7.4 Multi-wavelength Variability

The combined multi-wavelength light curve in Fig. 7.5 does not show a common feature present in all bands. Such a time-correlated feature either at the same time or with a time lag could give hints on the underlying physical process causing a flare. An exceptional TeV flare was found by MAGIC in November 2012. Since IC 310 could still be detected after the flare a common low level VHE activity of the object during the campaign can be stated. The only instrument that observed simultaneous to MAGIC on November 12/13 was *Fermi*-LAT in the HE range, albeit showing no detection neither during the TeV flare nor during the campaign. Contemporaneous measurements starting after the flare indicated a high state of the object in the soft X-ray range. The variable X-ray emission was found to follow a direct correlation of the flux and the photon index with a harder index occurring during a higher flux. The optical light curve did not show a significantly higher flux nor variability, whereas rather weak variability was found in the radio band.

For investigating potential variability between the different instruments the light curves are insufficiently sampled. Time-correlation studies such as the discrete cross-correlation function method (Edelson & Krolik 1988) would lead to conclusions that are only speculative.

7.5 Radio-Gamma Monitoring

To investigate the response of the VHE flare on the radio jet, further monitoring observations in the radio and gamma-ray band have been studied. In addition to the daily flux measurements presented in Section 7.3.1, monitoring of the VHE flux was conducted with the MAGIC telescopes in August 2013 to March 2014. This data were consolidated with all available observations at 15 GHz taken by the OVRO radio telescope. After the TeV flare, radio monitoring at various frequencies with Effelsberg 100 m telescope has been successfully proposed by the author. Since early 2012, IC 310 has been included in the MOJAVE program. This will allow us to study the structural dynamics of the parsec-scale jet in detail in the future.

7.5.1 VHE Monitoring with MAGIC

During the monitoring observations in August 2013 to March 2014 (MJD 56511.1–56721.0) IC 310 could not be detected. The θ^2 distribution above 300 GeV shows a significance of $1.03\,\sigma$, see Fig. 7.8, left. In the right panel of Fig. 7.8, the TS value map at low energies above ~ 80 GeV is displayed. At this energy the central galaxy of the Perseus cluster, NGC 175, could be detected with a significance of $\sim 10\,\sigma$.

Individual flux measurements from the observation nights are shown in Fig. 7.9 and listed in Appendix B Table 20. Due to the non-detection of the object, only a flux upper limit for the full period of $< 1.13 \times 10^{-12}\,\mathrm{cm^{-2}\,s^{-1}}$ above 300 GeV was calculated, using a confidence level of 95%, and 30% systematic uncertainty.

The limit is lower than the flux level measured during November 2012 and January 2013 excluding the bright flare. This is in agreement with the variability on a yearly time-scale as reported in Aleksić et al. (2012a).

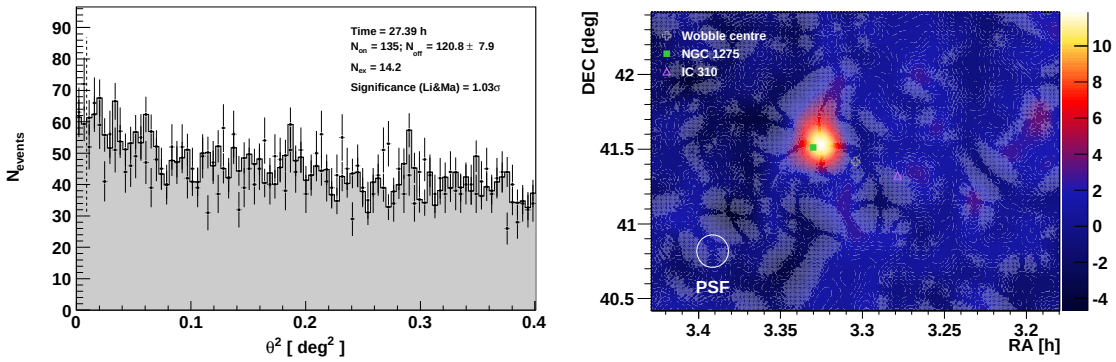

Figure 7.8: *Left panel:* θ^2 distribution above 300 GeV during monitoring obervations in August 2013 to March 2014. The following cuts have been applied: HADRONNESS < 0.16, SIZE > 300 phe, $\theta^2 < 0.009$, for two OFF regions. *Right panel:* TS value map above ~ 80 GeV. Cuts: HADRONNESS < 0.28, SIZE > 60 phe.

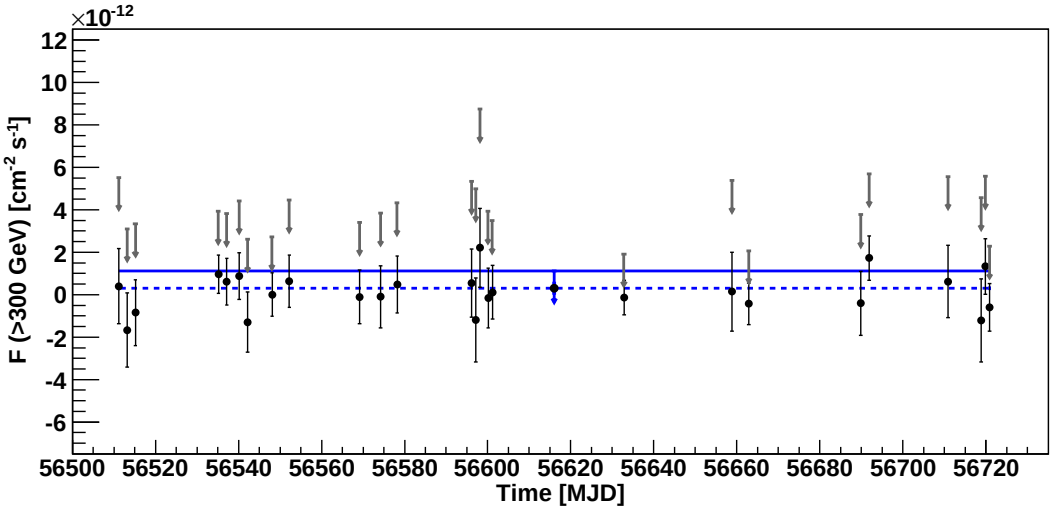

Figure 7.9: Light curve above 300 GeV during monitoring in August 2013 to March 2014. Black data points show the daily calculated light curve. The blue dashed data point shows the mean flux for the entire period and the solid arrows the corresponding flux upper limit.

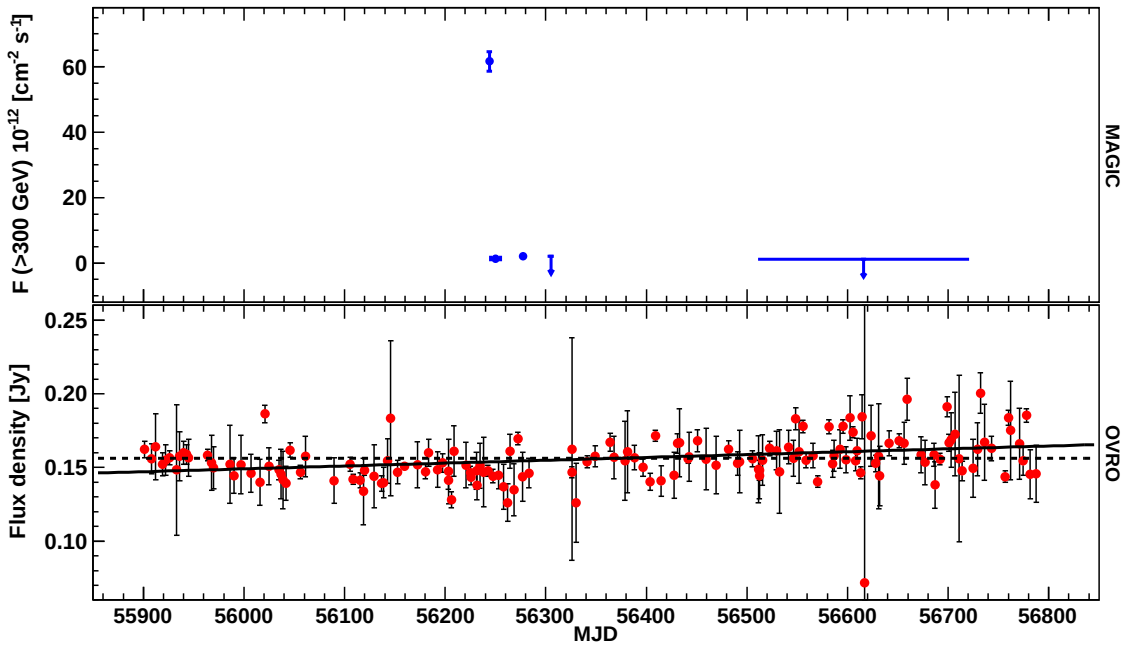

Figure 7.10: MAGIC and OVRO light curve covering the time range from December 2011 to May 2014. *Upper panel:* MAGIC light curve above 300 GeV. *Bottom panel:* OVRO light curve at 15 GHz. The dashed and solid lines represents a fit to the data with a constant and a linear, respectively.

7.5.2 Radio Monitoring

Single-dish as well as VLBI measurements in the radio band were performed. The results of the individual instruments are presented separately.

Flux Denity Measurements with OVRO

After the detection of IC 310 in the VHE range (Aleksić et al. 2010b), IC 310 has been included in the OVRO monitoring program at 15 GHz of gamma-ray loud AGN. The observations started in December 2011. The light curve up to and including May 2014 is shown in Fig. 7.10 (see also Appendix C Table 26) consolidated with the long-term VHE light curve from MAGIC above 300 GeV. The radio light curve has been fitted with a constant as well as with a linear function. The fit with the constant gives a χ^2/d.o.f.$= 506.8/151$ with an extremely low probability of 5.4×10^{-40}. The result for the linear fit improves only marginally to χ^2/d.o.f.$= 437.9/150$ (probability of 5.6×10^{-30}). As it can be seen from the linear fit, the radio flux at 15 GHz seems to increase with time. It should be noted that a re-binning of the light curve follows a decreasing trend. However, because of the large uncertainties and large scatter on the original, un-binned data points, too many binned data points' errors are consistent with the mean, and the result is that these trends do not seem to be statistically significant. The $F_{\rm Var}$-method by Vaughan et al. (2003) (see also Section 6.3.1) yields only upper limits on $F_{\rm Var}$, i.e., no variability in excess of the Poisson noise is significantly detected.

In general, the overall light curve does not show a pronounced high-state lasting for a longer period (weeks or months). To search for individual short-time flares, the distribution of the number of observations deviating from the mean flux has been calculated, see Fig. 7.11. For

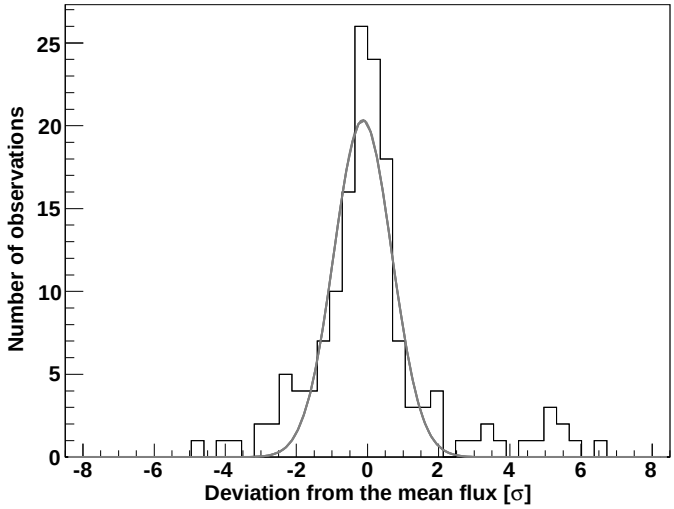

Figure 7.11: Distribution of the number of flux density measurements deviating from the mean flux in σ. Seven measurements deviate with more than $5\,\sigma$ from the mean flux.

seven measurements the flux deviates more than $5\,\sigma$ from the mean flux of 0.155 Jy[4]. Interestingly, six of these measurements were performed after the TeV flare observed from IC 310. The observation with the highest standard deviation of $6.6\,\sigma$ was found on May 1, 2014.

Figure 7.12 shows the light curve from OVRO with the temporal curve of the doubling time τ_{D}. The curve was calculated analogous to Section 6.3 and Fig. 6.6. The shortest doubling time is therefore the highest point in the curve.

Generally, variability on short as well as large time scales are found with this method. The shortest doubling times are of the order of 1 day. However, they are associated with large errors bars, i.e., they are not reliable. The most reliable shortest doubling time was found between November 17 to November 18, 2013 with a time of 4 days.

Radio Spectra with the Effelsberg 100 m telelescope

Radio spectral measurements were performed with the Effelsberg 100 m telescope. These observations were organized after the TeV flare to focus on the high frequency radio regime (> 10 GHz). Due to the low angular resolution of the telescope compared to VLBI arrays, the low frequency part of the spectrum is dominated by the extended kpc jet producing a steep radio spectrum (see Fig. 7.13, left). At higher frequencies the inner part of the jet could produce variable emission. In the left panel of Fig. 7.13, several spectra after the flare are presented. In addition, two previous measurements from Kadler et al. (2012) (see also Chapter 5) are displayed. Light curves at 4.9, 10.5, 14.6, and 32.0 GHz are shown in the left panel. Due to the snowy winter in 2012/2013 in Germany no further observations were carried out.

These measurements show that the radio flux at high frequencies is variable but no strong radio flare after the TeV flare could be identified.

[4]These measurements were performed on: MJD 56020.8, 56555.6, 56595.5, 56605.5, 56699.3, 56760.1, 56778.

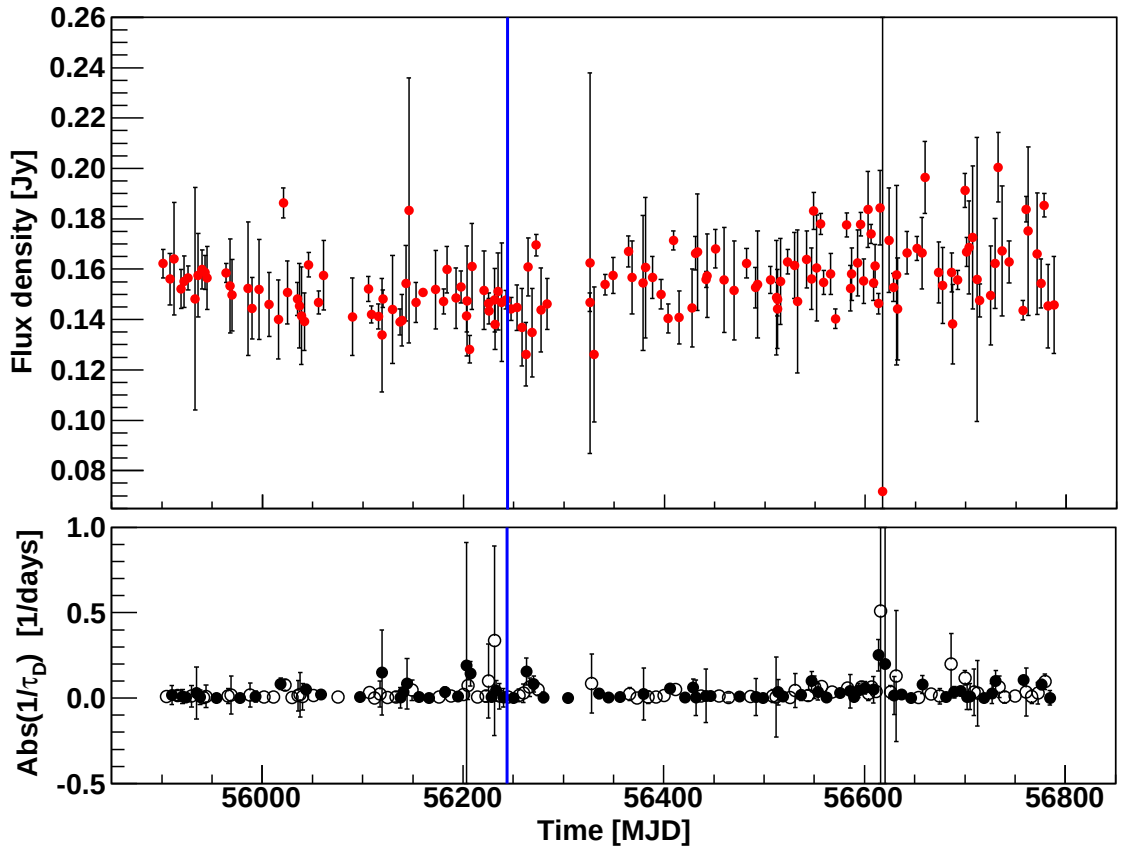

Figure 7.12: OVRO light curve and doubling time. *Upper panel:* OVRO light curve at 15 GHz. *Bottom panel:* Temporal curve of the absolute inverse doubling time. Positive doubling times are shown with filled marker whereas negative doubling times are shown with open markers. The blue line shows the date of the TeV flare.

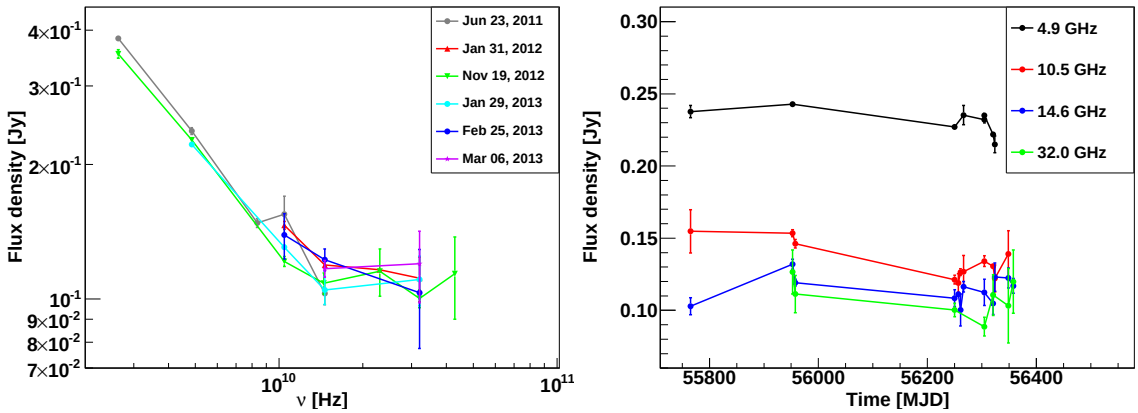

Figure 7.13: Flux density measurements at different frequencies with the Effelsberg 100 m telescope. The used colors are explained in the legends. *Left panel:* Radio spectra from different observations. *Right panel:* Light curves at different frequencies.

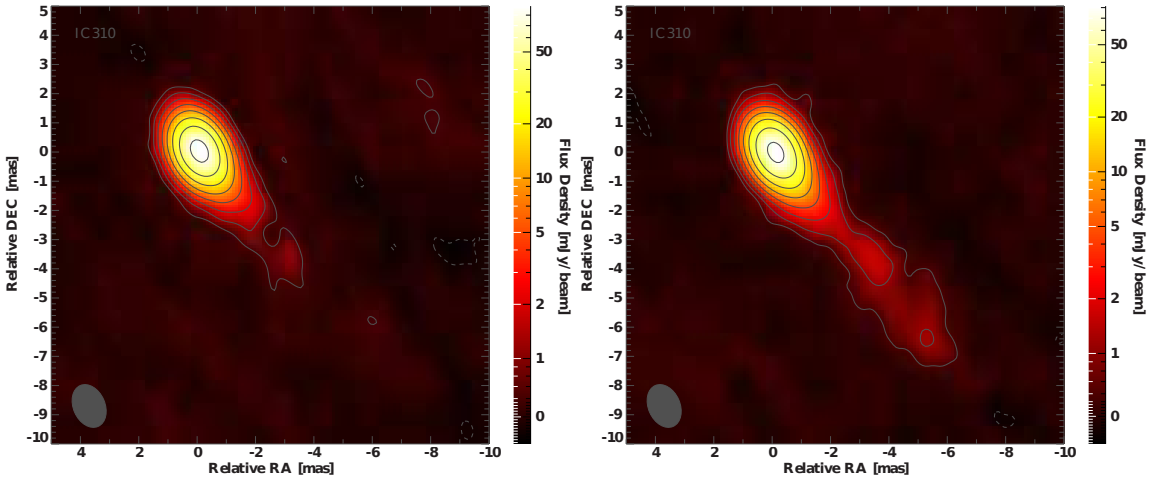

Figure 7.14: MOJAVE images at 15 GHz. Contour lines increase logarithmically by factors of 2 starting at three times the noise level. Image parameters are given in Table 7.2. *Left panel:* Combined image of the 2012-03-04 and 2012-09-27 observations. *Right panel:* Combined image of the 2012-12-10 and 2013-05-05 observations.

Table 7.2: Parameters of MOJAVE images.

Date	$S_{\mathrm{peak}}{}^{a}$ [mJy beam^{-1}]	RMS^{b} [mJy beam^{-1}]	$S_{\mathrm{total}}{}^{c}$ [mJy]	$b_{\mathrm{maj}}{}^{d}$ [mas]	$b_{\mathrm{min}}{}^{d}$ [mas]	P.A.^{d} [°]
2012-03-04 - 2012-09-27	89.77	0.196	98.96	1.53	1.08	23.65
2012-12-10 - 2013-05-05	81.58	0.185	94.22	1.53	1.08	23.65
all combined	85.28	0.140	96.59	1.53	1.08	23.65

Notes. $^{(a)}$ Peak flux density. $^{(b)}$ 1σ noise level. $^{(c)}$ Total flux density. $^{(d)}$ Major and minor axis and position angle of restoring beam.

MOJAVE

As part of the MWL campaign, IC 310 was added to the target list of the MOJAVE monitoring program. Therefore, since March 2012 the VLBI jet is observed regularly with the VLBA at 15 GHz. Up to now (2014), five measurements are available in the archive. The first two observations on March 3 and September 27, 2012 were carried out before the TeV flare, and three on December 10, 2012, May 5, and August 12, 2013 after it. In order to achieve a higher sensitivity, the images before and after the flare have been combined to the mean images shown in Fig. 7.14. A combined image of all measurements can be found in Fig. 7.15. The image parameters are summarized in Table 7.2.

Comparing the combined images of the observations before and after the TeV flare suggests no strong structural change of the parsec-scale radio jet. The peak as well as the total flux density after the flare was measured to be slightly lower than before. However, further VLBI observations are necessary to study this in more detail. In addition, more measurements are needed to investigate the kinematics of the radio components in the jet.

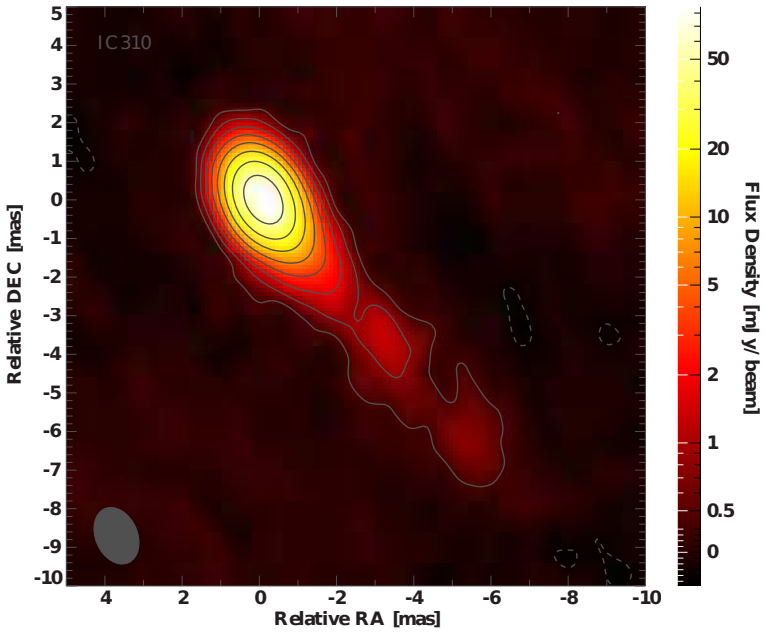

Figure 7.15: Combined MOJAVE image at 15 GHz. Contour lines start at $3\,\sigma$ and increase logarithmically by factors of 2. Image parameters are given in Table 7.2.

7.5.3 Radio-Gamma correlation

The MAGIC measurements during November 2012 to January 2013 after the VHE flare of IC 310 yield a faint, rather constant gamma-ray emission. Later observations in August 2013 to March 2014 resulted in a non-detection of the object. In contrast to this, monitoring of the radio emission at 15 GHz with OVRO suggests an increasing activity of variability after the flare occurred. This potentially coincides with a slowly increasing radio flux. From the MOJAVE and Effelsberg observations, no firm conclusions can be drawn as more data would be necessary to investigate changes of the structure of the VLBI jet (e.g., kinematics) and spectral emission.

To determine the location of the gamma-ray emission site in a jet of an AGN, it is possible to investigate the relation between the radio and gamma-ray flares (Max-Moerbeck et al. 2014). Several authors have already reported a coincidence between high-energy activity and the ejection of new radio components either directly observed with VLBI measurements or inferred from flares in single-dish observations (Jorstad et al. 2001; Marscher et al. 2008; Kovalev et al. 2009; Mahony et al. 2010; Nieppola et al. 2011; Max-Moerbeck et al. 2014). This coincidence appears with a time lag between the flares in both energy bands. Typically, such lags are between less than one month and several months (Jorstad et al. 2001; Max-Moerbeck et al. 2014). Often, the radio activity occurred after the gamma-ray flare, as found in statistical studies of many objects, e.g, Pushkarev et al. (2010), or Max-Moerbeck et al. (2014). This suggests that the gamma-ray emission originates upstream of the radio emission. Fuhrmann et al. (2014) found a correlation of the variability in both bands with a frequency-dependent radio lag. This is caused by a frequency-dependent opacity effect when a shock travels downstream.

The data in both energy bands presented in this chapter are not yet sufficient to make final conclusions on this topic. As those radio components are indicators for shock acceleration this would not conflict with the excluded shock-in-jet model being responsible for the TeV flare. The activity at the jet base caused by, e.g., gap acceleration in an magnetospheric environment similar to those in pulsars would produce electron-positron plasma clouds that move down-

stream the jet. When this emission reaches the optically thin regime, an enhanced flux in the radio band could be observed, or a new knot would appear. If the TeV flare was not energetic enough, the amplitude of the radio flare would be rather small. A weakly energetic TeV flare and/or a new component that is smeared out in time may lead to an easily missed enhancement of the radio flux due to a limited sensitivity of the radio measurement or insufficient sampling frequency of the monitoring. Note that frequent flares associated with separate emission regions during a short time period could in principle also merge to one single component when moving downstream. During the first detected gamma-ray activity in 2009/2010, three individual daily flares have been observed, see Chapter 5. Hence, a merging of small emission regions could have taken place. But since the monitoring of the VLBI structure with MOJAVE and the flux density with OVRO started in early 2012 and late 2011, respectively, no conclusion on the radio-gamma correlation can be drawn.

8

Summary and Outlook

What remains to be discovered?

The goal of this thesis was to investigate the variability behavior of the peculiar active galactic nucleus (AGN) of the galaxy IC 310 located in the Perseus cluster of galaxies. This was done by studying the light curves and spectra in different energy bands. Major emphasis was laid on measuring rapid variability in the very high energy regime covered by observations with the MAGIC telescopes. These investigations were complemented by high resolution very long baseline interferometry (VLBI) measurements.

The VLBI observations showed a blazar-like parsec-scale one-sided radio structure. This is inconsistent with the original classification of the object as a head-tail radio galaxy. Since this parsec-scale jet is closely aligned to the kilo-parsec jet, the large-scale structure is more likely determined by the parsec-scale jet rather than by the motion of the galaxy through the inter cluster medium. From the analysis of archival X-ray as well as *Fermi*-LAT (three-year) and MAGIC data from 2009/2010, several blazar-like characteristics were found. The X-ray emission demonstrates strong spectral changes as well as flux variability. Interestingly, a hint for an increased hydrogen absorption column N_{H} possibly intrinsic to the object was found. The MAGIC data revealed flux variability of daily-scales and no variability of the spectral emission.

A transitional behavior between a radio galaxy and a blazar is confirmed with the estimate of $10^{\circ} \lesssim \theta \lesssim 20^{\circ}$ for the angle between the jet-axis and the line-of-sight. The lower limit has been inferred from the length of the de-projected radio jet and the upper limit was found from high sensitive VLBI observations with the European VLBI Network. These observations were proposed by the author.

During the first deep multi-wavelength campaign in November 2012, an exceptional bright TeV flare was observed with MAGIC. This confirms the variability on daily-scales found in 2009/2010. Remarkably, the very high energy spectrum did not show significant spectral changes even if the flux raised by about one order of magnitude. Among all extragalactic objects, the TeV spectrum of the night of the flare is peculiar. It is one of the hardest spectrum measured in this energy range so far and it can be describe by a simple power-law over two order of magnitude in energy without a hint for a break. The intra-night light curve of the

TeV outburst showed several fast peaks. This motivated the search for the shortest variability time scale. The most conservative fast variability time scale of 4.8 min corresponds to 20% of the light-crossing time of the event horizon. For the first time, it was possible to observe TeV variability on minute-scales from a AGN with larger viewing angle. Several theoretical models have been consulted to explain this emission. It was found out that the findings disagree with the commonly accepted acceleration models by a sequence of shocks traveling down the jet used to explain the gamma-ray radiation for active galactic nuclei. Alternative models based on interactions of stars with the jet and small structures associated with mini-jets, fail to describe the observational findings. Instead, it was found that particle acceleration by electric fields across a magnetospheric gap close to the central engine could be a solution.

The multi-wavelength campaign from November 2012 to February 2013 opens the door to further, deeper investigations of the emission of the object. The TeV emission of the object was connected to a simultaneous high state in the X-ray band. During this period, the tendency for a harder spectrum correlated to a brighter flux of the X-ray emission was found. After the TeV flare, an increased activity of the radio emission was possibility identified from OVRO measurements. Such correlation of radio and gamma-ray light curves after high energy outbursts with a time-lagged radio flare and new appearing knots in the VLBI images were reported by many authors. A significant detection of this behavior was however not found in case of IC 310. For this, more measurements of the radio flux density as well as monitoring observations of the VLBI jet over the next years are needed.

To answer the question which of the mechanism are responsible for the ultra-rapid variability, further observations are needed. One possibility could be to measure the X-ray emission with high accuracy. The required sensitivity is provided by the *XMM-Newton* satellite[1]. The next time when IC 310 shows a TeV outburst, the flux variability at X-ray energies could be studied. In addition, variability of N_{H} could be measured. This characteristics would constrain the underlying physical processes.

So far, all explanations discussed in this thesis are based on the fact that the angle between the jet-axis and the line-of-sight of IC 310 is rather large compared to those found for blazars. Even if the probability for a smaller angle is low, measuring the counter-jet would constrain the angle with higher precision. Therefore, more sensitive VLBI observation with a larger integration time at higher frequencies are important. Likewise, measuring the counter-jet on larger scales with the Low Frequency Array (LOFAR) could be exiting.

Finally, the analysis of the broad-band spectral energy distribution (SED) is ongoing. By studying the SED with different emission models, the radiation processes relevant in the object could be explained.

In general, there are many open questions regarding the acceleration and emission mechanism in AGN jets. The observation of the ultra-rapid variability of IC 310 just showed that these processes are still not understood. This is in-line with observation of fast variability observed from other TeV loud objects. The constrained size of the emission for many those measurements are often not compatible with the horizon light-crossing time. A correlation or non-correlation between the shortest time scale and the black hole mass could possibly indicate the underlying physical scenario.

The failure of simple single-zone SSC models to explain the minute-scale variability emphasizes the importance of sub-structures in the jets. It is remarkable that these sub-structures manifest themselves with variable multi-TeV emission, because the expected higher photon

[1] A Target of Opportunity proposal has been prepared by the author.

density in these compact regions should lead to $\gamma\gamma$-pair production. This may indicate that particle acceleration occurs mainly along the magnetic field direction at a vanishing angle between the particle's velocity vector and the magnetic field. Due to the high Lorentz factors of the emitting particles, any secondary particles or photon acquire such small angles. Thus, low-energy emission and gamma-ray attenuation due to pair production will be suppressed. Such physical conditions can be found in the magnetospheres of pulsars where due to the rotation of their magnetosphere regions with electric fields parallel to the magnetic field emerge. Therefore, the flux variability on minute-scales and, especially, the results in this thesis challenge the main paradigm of shock-in-jet models.

Investigating fast variability in the high-energy band is difficult, because this events are rare and often only found by chance. Therefore, long-term monitoring at TeV energies of these objects is mandatory in order to identify bright flares where sufficient statistics allows for the search for rapid flux changes. Such a program is provided by the FACT telescope on La Palma. An extension of the program to the DWARF project (many small telescopes spread around the world) would support this investigation.

Further, the particle content of the jets that produces the high energy emission is not known. Similarly to that, the origin of the cosmic rays needs to be identified. One particular hint would be to detect the sources of the neutrinos found by the IceCube Collaboration.

In the future, a view to the insights of the jets will be provided by higher resolution VLBI measurements (EHT or space-based VLBI) and more sensitive imaging air Cherenkov telescopes such as CTA allowing for variability studies on even shorter time scales.

Appendix A: Fundamental Parameters of AGN IC 310

Some theoretical discussions presented in this thesis require the mass of the black hole located in the center of the galaxy IC 310 and the kinetic power of the jet of the AGN. Those parameters are introduced in this chapter.

1 The Mass of its Black Hole

The mass of the black hole M_{BH} of IC 310 can be inferred from the relation between the mass of a supermassive black hole and the velocity dispersion σ of the host galaxy, called $M-\sigma$ relation:

$$\log\left(\frac{M_{\mathrm{BH}}}{\mathrm{M}_{\odot}}\right) = \alpha + \beta\log\left(\frac{\sigma}{200\,\mathrm{kms}^{-1}}\right), \tag{1}$$

see, e.g., Gültekin et al. (2009). For IC 310, a velocity dispersion of $\sigma = (229.6 \pm 5.9)$ km s^{-1} has been measured by McElroy (1995) and Simien & Prugniel (2002). Adapting $\alpha = (8.12 \pm 0.08)$ and $\beta = (4.24 \pm 0.41)$ for the parameter in Eq. 1 obtained in Gültekin et al. (2009) for all types of galaxies yields a mass of $M_{\mathrm{BH}} = (2.4 \pm 0.5) \times 10^8\,\mathrm{M}_{\odot}$. For early-type galaxies such as those with Hubble-type S0, $\alpha = (8.22 \pm 0.07)$ and $\beta = (3.86 \pm 0.38)$ were found. This leads to a slightly higher mass of $M_{\mathrm{BH}} = (2.8 \pm 0.6) \times 10^8\,\mathrm{M}_{\odot}$. The intrinsic scatter of $\log(M/\mathrm{M}_{\odot})$ of the order of $\epsilon_0 = 0.44 \pm 0.06$ and $\epsilon_0 = 0.35 \pm 0.03$ for both estimates has to be taken into account as uncertainty.

Another method to obtain the mass of a black hole is based on the so-called *fundamental plane of black hole activity* (Merloni et al. 2003). This plane relates the X-ray luminosity L_{X} (2–10 keV range) and radio-core luminosity L_{R} at 5 GHz with the mass inferred from studies of stellar to supermassive black holes. The following correlation can be found:

$$\log L_{\mathrm{R}} = \left(0.60^{+0.11}_{-0.11}\right)\log L_{\mathrm{X}} + \left(0.78^{+0.11}_{-0.09}\right)\log M_{\mathrm{BH}} + 7.33^{+4.05}_{-4.07}. \tag{2}$$

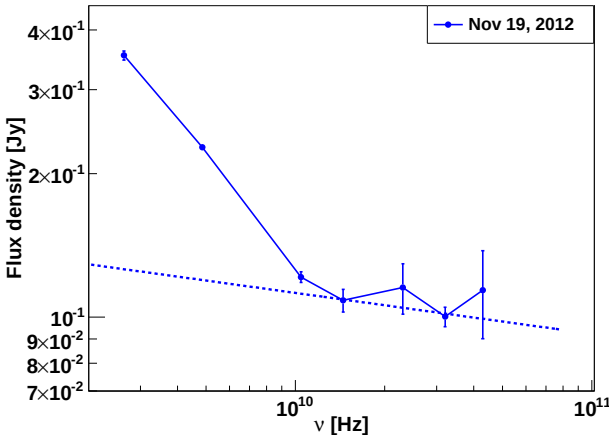

Figure 1: Effelsberg flux density measurement used for calculating the mass of the black hole of IC 310. Below 10 GHz the emission is dominated by a steep spectrum from the extended, large-scale jet emission. Above 10 GHz the spectrum flattens, caused by the dominating core emission. Therefore, the spectrum above 10 GHz has been fitted with a power-law revealing a spectral index of $\alpha = 0.09$ ($S \propto \nu^{-\alpha}$) with a χ^2/d.o.f. of $1.08/2$. The extrapolation yields a flux density of 0.119 Jy at 5 GHz.

The radio-core luminosity can be calculated from the total flux density measured at 5 GHz with EVN on October 29, 2012, see Section 6.5. Here, a total flux density of $S_{5\,\mathrm{GHz}} = 0.109$ Jy with an uncertainty of 10% was found. This results in a radio luminosity of $L_\mathrm{R} = (4.3 \pm 0.4) \times 10^{39}\,\mathrm{erg\,s^{-1}}$. The value of the total flux density has been chosen for the core to allow for a similar resolution as for the radio measurement used for the study in Merloni et al. (2003). The X-ray luminosity was calculated from the *Swift*-XRT flux measurement on November 14, 2012 of $F_{2-10\,\mathrm{keV}} = (6.4 \pm 0.4) \times 10^{-12}\,\mathrm{erg\,cm^{-2}\,s^{-1}}$ (see Chapter 7) yielding $L_{\mathrm{X},2-10\,\mathrm{keV}} = (5.0 \pm 0.3) \times 10^{42}\,\mathrm{erg\,s^{-1}}$. An independent estimate is possible from the contemporary Effelsberg spectrum on November 19, 2012 and *Swift*-XRT observation November 22, 2012 after the VHE flare of the object. The radio spectrum is shown in Fig. 1. Due to the limited resolution of a single-dish instrument the radio emission at 5 GHz is dominated by the extended jet. To obtain the core emission the flat spectrum above 10 GHz has been fitted and extrapolated down to 5 GHz. From this procedure a flux density of $S_{5\,\mathrm{GHz}} = 0.119$ Jy, and a luminosity of $L_\mathrm{R} = 4.7 \times 10^{39}\,\mathrm{erg\,s^{-1}}$ were found. The *Swift*-XRT measurement on November 22, 2012 showed a flux of $F_{2-10\,\mathrm{keV}} = (6.1 \pm 0.4) \times 10^{-12}\,\mathrm{erg\,cm^{-2}\,s^{-1}}$ (see Chapter 7) and a luminosity of $L_{\mathrm{X},2-10\,\mathrm{keV}} = (4.8 \pm 0.3) \times 10^{42}\,\mathrm{erg\,s^{-1}}$. In both cases, a mass of $M \sim 4 \times 10^8\,\mathrm{M_\odot}$ could be obtained. This is consistent with the values obtained from the $M - \sigma$ relation. However, notice that the fundamental plane shows a large scatter of $\sigma_\mathrm{R} = 0.88$ (Merloni et al. 2003), and the measurements used were not taken simultaneously.

In this thesis, the value of $M_\mathrm{BH} \simeq \left(3^{+4}_{-2}\right) \times 10^8\,\mathrm{M_\odot}$ obtained from the first method will be used.

For $M_\mathrm{BH} \simeq 3 \times 10^8\,\mathrm{M_\odot}$, the so-called Schwarzschild radius $R_\mathrm{S} = 2GM_\mathrm{BH}/c^2$ can be calculated to be 8.9×10^{13} cm valid for a non-rotating black hole with the Kerr parameter $a = 0$, and the Gravitational radius $R_\mathrm{G} = GM_\mathrm{BH}/c^2$ of 4.4×10^{13} cm for a maximally rotating black hole with $a = 1$.

Following Eq. 3 in Neronov & Vovk (2011), the light-crossing time is given by:

$$T_\mathrm{lc} = 2(1+z)\left(R_\mathrm{G} + \sqrt{R_\mathrm{G}^2 - a^2}\right)/c \tag{3}$$

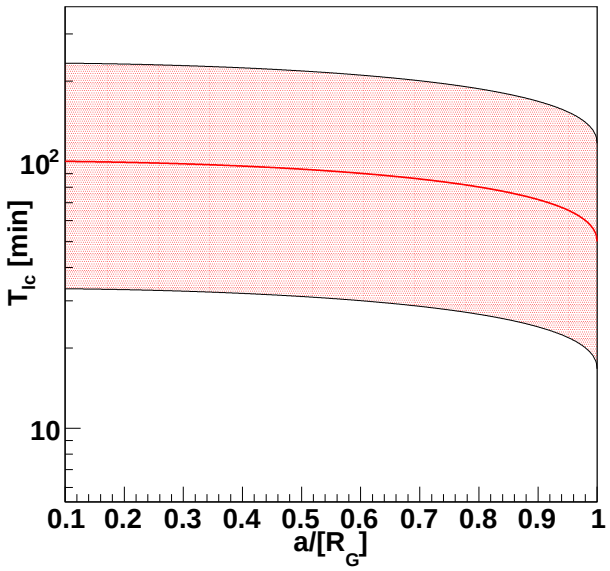

Figure 2: Light-crossing time as a function of the Kerr parameter calculated for the black hole of IC 310. The thick red line shows the light-crossing time for a of $M_{\rm BH} \simeq 3 \times 10^8\,{\rm M}_\odot$, and the thin black lines indicate the error margin.

Figure 2 shows the dependence of the light-crossing time on the rotation of a black hole indicated by the Kerr parameter for a mass found for the black hole in IC 310 of $M_{\rm BH} \simeq (3^{+4}_{-2}) \times 10^8\,{\rm M}_\odot$.

2 The Jet Power

In general, the kinetic power of the jet can be inferred from radio measurements. On possible method is based on the minimum energy assumption (Burbidge 1956) and the observed synchrotron cooling break in the radio, see, e.g., Sijbring & de Bruyn (1998). It yields a jet power of $L_{\rm jet} = 2 \times 10^{42}$ erg s^{-1}. This estimate includes only electrons. However, if protons are considered as well, the minimum energy increases by a factor $50^{4/7}$ since the ratio of the cosmic proton-to-electron energy density amounts to a total of about 50. This increases the jet luminosity by one order of magnitude.

Appendix B: Additional Details to the MAGIC Analysis

3 Analysis in Chapter 5

Table 1: Overview on MAGIC analysis

Analysis	Chapter 5	Chapter 6	Chapter 7 part I (MWL)	Chapter 7 part II (monitoring)
Time	Oct. 2009 - Feb. 2010	Nov. 13, 2012	Nov. 2012 - Jan. 2013	Jul. 2013 - Mar. 2014
Telescope config.	M-I: old camera, readout MUX-FADC M-II: readout DRS 2	M-I: new camera, readout DRS 4 M-II: readout DRS 4	M-I: new camera, readout DRS 4 M-II: readout DRS 4	M-I: new camera, readout DRS 4 M-II: readout DRS 4
Calib.	M-I: callisto Mars V1.8.8, Root v5.12/00f M-II: callisto Mars V2.0.2, Root v5.12/00g	M-I: sorcerer Mars V2.10.2, Root v5.26/00e M-II: sorcerer Mars V2.10.2, Root v5.26/00e	M-I: sorcerer Mars V2.10.2, Root v5.26/00e M-II: sorcerer Mars V2.10.2, Root v5.26/00e	M-I: sorcerer Mars V2.12.5, Root v5.34/04 M-II: sorcerer Mars V2.12.5, Root v5.34/04
Image cleaning	M-I: 6/3 level, 4.5/1.5 time M-II: 9/4.5 level, 4.5/1.5 time Mars V2.4.3, Root v5.26/00	M-I/II: dynamical sum M-I/II: 6/3.5 level, 4.5/1.5 time Mars V2.11.4, Root v5.34/03	M-I/II: dynamical sum M-I/II: 6/3.5 level, 4.5/1.5 time Mars V2.11.4, Root v5.34/03	M-I/II: dynamical sum M-I/II: 6/3.5 level, 4.5/1.5 time Mars V2.12.5, Root v5.34/04
superstar	Mars V2.7.2, Root v5.26/00e	dynamic Mars V2.12.0, Root v5.26/00e	dynamic Mars V2.12.0, Root v5.26/00e	dynamic, Mars V2.12 (unreleased) comp. Jul 24, 2013, Root v5.26/00e
coach	Mars V2.4 (unreleased) comp. Jul 6, 2011, Root v5.26/00e	dynamical WIDTH/LENGTH Mars V2.12.0, ROOT v5.26/00e	dynamical WIDTH/LENGTH RMSTimeW used Mars V2.12.3, ROOT v5.26/00e	Mars V2.13.6, Root v5.26/00e
melibea	Mars V2.7.2, Root v5.26/00e	Mars V2.12.2, Root v5.26/00e	Mars V2.12.6, Root v5.26/00e	Mars V2.13.6, Root v5.26/00e
Light curve/ spectrum	fluxlc, sim. ON-MinusOFF Mars V2.7.2, Root v5.26/00e	flute, sim. ON-MinusOFF Mars V2.12 (unreleased) comp. Jul 24, 2013, Root v5.26/00e	flute, sim. ON-MinusOFF Mars V2.12.6, Root v5.26/00e	flute, sim. ON-MinusOFF Mars V2.12.6, Root v5.26/00e
	Unfold.: Mars V2.7.2, Root v5.26/00e	Unfold.: Mars V2.13.5, Root v5.26/00e	Unfold.: Mars V2.13.6, Root v5.26/00e	Unfold.: Mars V2.13.6, Root v5.26/00e

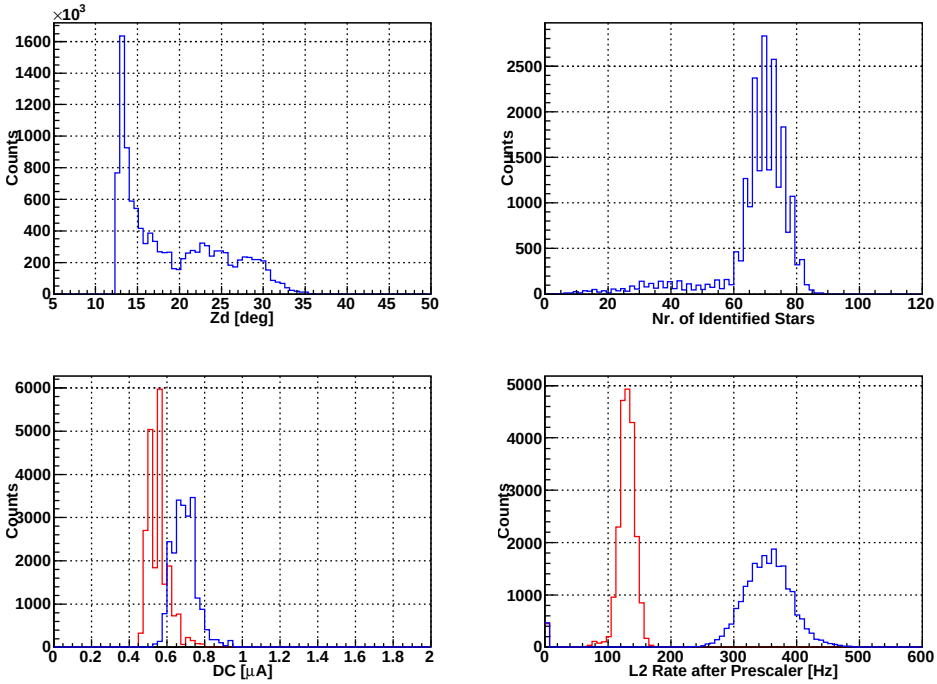

Figure 3: Quality parameters of the data taken in October 2009 to February 2010 (after quality selection). *Top left:* zenith distance. *Top right:* number of identified stars. The tail of the distribution to low numbers of stars may arises from some non-optimal weather conditions. However, the percentage of this data in the total set is rather small. *Bottom left:* currents in the MAGIC-I (blue) and MAGIC-II (red) camera. *Bottom right:* L2 rate after prescaler for MAGIC-I (blue) and MAGIC-II (red). Due to the soft stereo mode only MAGIC-I was triggering. This causes an overall lower trigger rate for MAGIC-II.

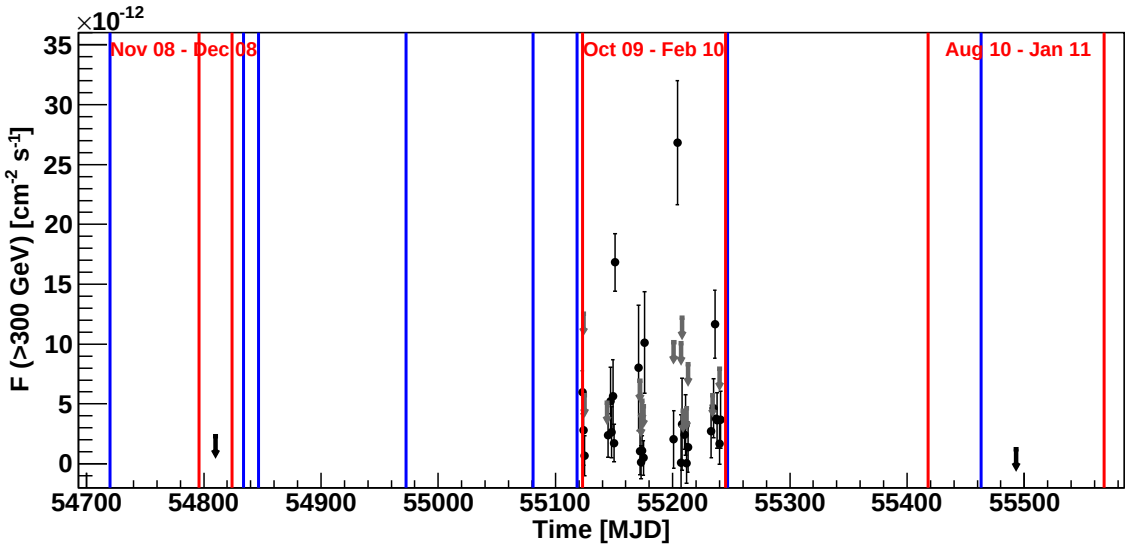

Figure 4: MAGIC light curve above 300 GeV and arrival times of gamma-like events (blue lines) measured by *Fermi*-LAT in November 2008 to January 2011. The arrows show the 95% confidence level upper limits calculated for observation compatible with no signal. The MAGIC observation times are indicated by red lines. The black upper limits were published in Aleksić et al. (2010b) and Aleksić et al. (2012a).

Table 2: Data from individual MAGIC observations in 2009/2010. The data before 2009-10-19 were excluded as both telescopes were operating in mono mode only.

data[a]	Run	MJD start	$t_{\rm eff}$ [h]	Zd [°]	DC (MI) [μ A]	Comments or excluded runs
2009-10-19	05002715-23	55123.02	2.43	12-31	0.7-0.9	
2009-10-20	05002741-44	55124.05	1.11	12-23	0.7-1.0	
2009-10-21	05002790-96	55125.02	1.58	12-29	0.7-0.9	05002787, 92: short
2009-11-09	05003257-59	55143.96	0.80	20-31	0.7-0.9	05003256: too short
2009-11-10	05003302-07	55144.97	1.19	12-27	0.6-0.8	05003297, 301: short
2009-11-12	05003393-96	55146.98	0.99	12-24	0.6-0.8	05003397: too short
2009-11-13	05003433-37	55147.98	1.17	12-24	0.7-0.8	
2009-11-14	05003480-84	55148.98	1.11	12-23	0.6-0.8	
2009-11-15	05003523-31	55149.94	2.61	12-32	0.6-0.8	
2009-11-16	05003546-54	55150.94	2.34	12-31	0.6-0.8	
2009-11-25						excl. all, moon
2009-11-26						excl. all, moon
2009-12-06	05004040-41	55170.89	0.44	23-31	0.6-0.9	
2009-12-07	05004065-69	55171.89	1.44	14-29	0.5-0.8	
2009-12-08	05004094-102	55172.88	2.51	12-31	0.5-0.9	
2009-12-09	05004143-53	55173.89	3.18	12-29	0.6-0.8	
2009-12-10	05004188-95	55174.88	2.40	12-31	0.6-0.8	
2009-12-11	05004247 05004250 05004253	55175.88	0.54	12-31	0.6-0.7	05004254: clouds

Notes. [a] Dates in MAGIC night notation, i.e., after midnight.

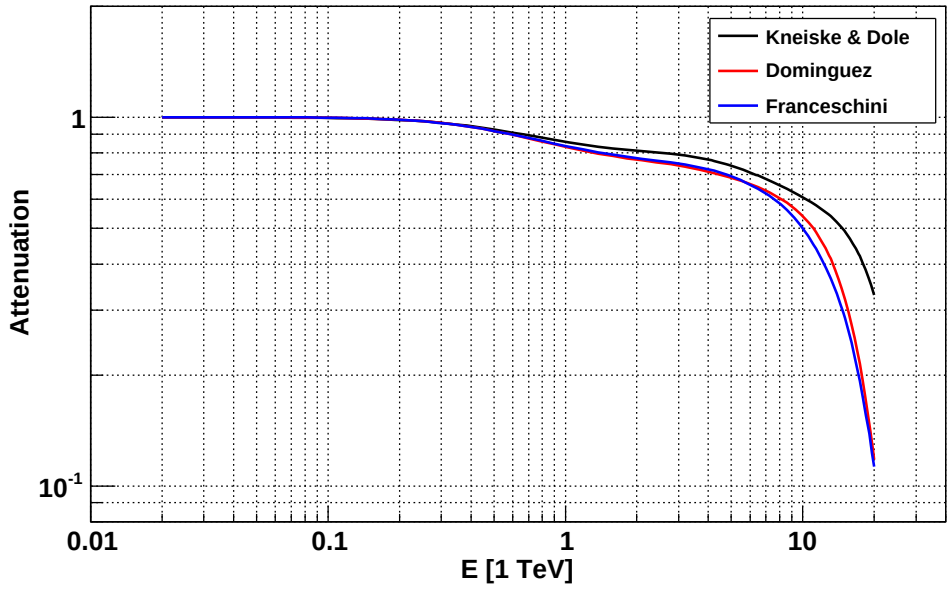

Figure 5: EBL attenuation models as used for the correction for spectra of IC 310. The black line shows the model by Kneiske & Dole (2010), the red line Domínguez et al. (2011) and the blue one Franceschini et al. (2008).

Table 3: Data from individual MAGIC observations in 2009/2010. Continued.

data[a]	Run	MJD start	$t_{\rm eff}$ [h]	Zd [°]	DC (MI) [μ A]	Comments or excluded runs
2010-01-05	05004296-99	55200.83	0.81	15-25	0.6-0.8	05004298: too short
2010-01-08	05004310-12	55203.89	0.78	12-17	0.5-0.7	
2010-01-11	05004349-50	55206.87	0.62	12-14	0.6-0.8	05004351: too short
2010-01-12	05004391-92	55207.90	0.61	13-20	0.6-0.7	
2010-01-13	05004434-37	55208.88	0.86	12-18	0.6-0.7	05004431: clouds
2010-01-14	05004471-76	55209.84	1.47	12-18	0.6-0.8	
2010-01-15	05004517-20	55210.83	1.46	12-18	0.6-0.8	05004521: clouds
2010-01-16	05004561-66, 05004575-76	55211.83	1.90	12-31	0.6-0.8	05004562: too short
2010-01-17	05004620-23	55212.84	1.22	12-16	0.6-0.8	
2010-01-18						bad weather: excl. all
2010-02-05						bad weather: excl. all
2010-02-06	05005188 05005193-96	55232.84	1.22	14-36	0.6-0.9	
2010-02-07	05005238 05005241-43	55233.87	0.60	20-33	0.6-0.7	
2010-02-08	05005285, 05005288, 05005293-98	55234.85	0.90	16-33	0.6-1.0	
2010-02-09	05005311-15	55235.85	1.38	16-34	0.6-0.8	05005307: too short
2010-02-10	05005399, 05005401	55236.87	0.62	22-30	0.6-0.8	05005398, 40: short
2010-02-11	05005497-99	55237.86	0.87	22-33	0.6-0.8	05005494: too short
2010-02-13	05005595, 05005598-600	55239.84	0.92	19-31	0.6-1.0	
2010-02-14	05005659-63 05005666	55240.84	1.24	20-36	0.6-0.8	

Notes. [(a)] Dates in MAGIC night notation, i.e., after midnight.

Table 4: Off data for analysis Chapter 5.

Source	Date	Used runs
OffCrab7	2009-11-26	05003936-40
3c454.3	2009-12-06; 12-07; 12-08; 2009-12-09; 12-10; 12-11	05004033-36; 05004061; 5004087, 89-90; 05004136, 38-40; 05004183-85; 05004242
ON-325	2010-01-24	05005042-54
CygnusLoop	2010-10-27; 10-28; 10-29; 2010-10-30; 10-31; 11-01; 2010-11-02; 11-06; 11-09	05010474-76; 05010489-97; 05010531-38 05010594; 05010638-43; 05010690-93, 95-97 05010719; 05010776, 78-81; 05010840-43

Table 5: Details on high-level analysis: Chapter 5.

Spectrum:	high and low state spectra
Dead time	5×10^{-4} s
Binning	16 bins between 10–100000 GeV
Number of OFF regions	2 (0.25° data) and 5 (1° data)
Normalization region	0.06–0.12 (0.25° data) and 0.08–0.24 (1° data)
Cuts	LEAKAGE MAGIC-I < 0.3, LEAKAGE MAGIC-II < 0.15, Number-of-Islands MAGIC-I/II < 3, SIZE > 150 phe
0.25° offset data	HADRONNESS cuts: 0.5, 0.5, 0.5, 0.42, 0.38, 0.34, 0.34, 0.38, 0.45, 0.5, 0.6, 0.6, 0.6, 0.6, 0.6, 0.6 θ^2 cuts: 0.05, 0.05, 0.05, 0.03, 0.024, 0.018, 0.014, 0.012, 0.012, 0.012, 0.012, 0.012, 0.012, 0.012, 0.012, 0.012
1° offset data	HADRONNESS cuts: 0.6, 0.6, 0.6, 0.5, 0.45, 0.4, 0.4, 0.4, 0.5, 0.6, 0.7, 0.7, 0.7, 0.7, 0.7, 0.7 θ^2 cuts: 0.05, 0.05, 0.05, 0.03, 0.024, 0.018, 0.016, 0.014, 0.014, 0.014, 0.014, 0.014, 0.014, 0.014, 0.014, 0.014
Light curve:	
Dead time	5×10^{-4} s
Binning	19 bins between 10–100000 GeV
Number of OFF regions	2 (0.25° data) and 5 (1° data)
Normalization region	0.06–0.12 (0.25° data) and 0.08–0.24 (1° data)
Cuts	LEAKAGE MAGIC-I < 0.3, LEAKAGE MAGIC-II < 0.15, Number-of-Islands MAGIC-I/II < 3, SIZE > 150 phe
0.25° offset data	HADRONNESS cuts: 0.5, 0.5, 0.5, 0.42, 0.38, 0.34, 0.34, 0.34, 0.38, 0.45, 0.5, 0.6, 0.6, 0.6, 0.6, 0.6, 0.6, 0.6, 0.6, 0.6 θ^2 cuts: 0.02 for all energy bins
1° offset data	HADRONNESS cuts: 0.6, 0.6, 0.6, 0.5, 0.45, 0.40, 0.40, 0.40, 0.40, 0.5, 0.6, 0.6, 0.7, 0.7, 0.7, 0.7, 0.7, 0.7, 0.7 θ^2 cuts: 0.02 for all energy bins

Table 6: Flux results from individual observations in 2009/2010.

used data[a]	MJD start	t_{eff} [h]	$F_{\mathrm{E>300\,GeV}}{}^{b}$ [10^{-12} ph cm^{-2} s^{-1}]	$F_{\mathrm{E>300\,GeV}}{}^{c}$ [10^{-12} ph cm^{-2} s^{-1}]
all data		43.32	3.62 ± 0.40	
2009-10-19	55123.02	2.43	5.97 ± 1.79	$3.63 \pm 1.17\,(3.06 \pm 1.65)$
2009-10-20	55124.05	1.11	$(2.80 \pm 2.93) < 12.52$	
2009-10-21	55125.02	1.58	$(0.67 \pm 1.67) < 5.74$	
2009-11-09	55143.96	0.80	$(-3.42 \pm 3.09) < 5.11$	$5.74 \pm 0.89\,(6.32 \pm 1.13)$
2009-11-10	55144.97	1.19	2.36 ± 1.83	
2009-11-12	55146.98	0.99	5.21 ± 2.86	
2009-11-13	55147.98	1.17	2.64 ± 2.14	
2009-11-14	55148.98	1.11	5.65 ± 3.03	
2009-11-15	55149.94	2.61	1.73 ± 1.57	
2009-11-16	55150.94	2.34	16.83 ± 2.40	
2009-12-06	55170.89	0.44	8.01 ± 5.25	$1.50 \pm 0.72\,(1.86 \pm 0.94)$
2009-12-07	55171.89	1.44	$(1.03 \pm 1.94) < 6.95$	
2009-12-08	55172.88	2.51	$(0.13 \pm 1.39) < 4.06$	
2009-12-09	55173.89	3.18	$(1.10 \pm 1.25) < 5.25$	
2009-12-10	55174.88	2.40	$(0.49 \pm 1.44) < 4.83$	
2009-12-11	55175.88	0.54	10.13 ± 4.23	
2010-01-05	55200.83	0.81	$(2.05 \pm 2.40) < 10.02$	$3.49 \pm 0.89\,(2.44 \pm 1.08)$
2010-01-08	55203.89	0.78	26.84 ± 5.19	
2010-01-11	55206.87	0.62	$(0.09 \pm 4.00) < 10.09$	
2010-01-12	55207.90	0.61	$(3.29 \pm 3.85) < 12.19$	
2010-01-13	55208.88	0.86	$(-2.91 \pm 2.59) < 4.42$	
2010-01-14	55209.84	1.47	2.44 ± 1.22	
2010-01-15	55210.83	1.46	3.23 ± 2.54	
2010-01-16	55211.83	1.90	$(0.03 \pm 1.66) < 4.63$	
2010-01-17	55212.84	1.22	$(1.40 \pm 2.11) < 8.33$	
2010-02-06	55232.84	1.22	2.71 ± 2.18	$4.40 \pm 0.92\,(2.95 \pm 1.24)$
2010-02-07	55233.87	0.60	$(-5.19 \pm 4.50) < 5.71$	
2010-02-08	55234.85	0.90	4.65 ± 2.47	
2010-02-09	55235.85	1.38	11.65 ± 2.84	
2010-02-10	55236.87	0.62	3.77 ± 2.91	
2010-02-11	55237.86	0.87	3.62 ± 2.32	
2010-02-13	55239.84	0.92	$(1.69 \pm 1.74) < 7.95$	
2010-02-14	55240.84	1.24	3.68 ± 2.38	

Notes. [a] Dates in MAGIC night notation, i.e., after midnight. [b] Daily measured flux above 300 GeV in units of 10^{-12} ph cm^{-2}s^{-1}. Upper limits are given with 95% confidence level for negative flux measurements, or points that are consistent with zero within the error. [c] Monthly measured flux above 300 GeV in units of 10^{-12} ph cm^{-2}s^{-1}. For comparison, the result from Aleksić et al. (2010b) is given in parentheses.

Table 7: SED points derived for MAGIC observations in October 2009 to February 2010.

state	Energy[a] [GeV]	$E^2\,\mathrm{d}N/\mathrm{d}E$ [$\mathrm{TeV}^{-1}\,\mathrm{cm}^{-2}\,\mathrm{s}^{-1}$]	$E^2\,\mathrm{d}N/\mathrm{d}E$ EBL corrected[b] [$\mathrm{TeV}^{-1}\,\mathrm{cm}^{-2}\,\mathrm{s}^{-1}$]
high	199^{+86}_{-75} / 199^{+85}_{-76}	$(3.66 \pm 1.02) \times 10^{-12}$	$(3.65 \pm 1.46) \times 10^{-12}$
	459^{+199}_{-174} / 461^{+197}_{-176}	$(4.14 \pm 0.73) \times 10^{-12}$	$(4.70 \pm 0.91) \times 10^{-12}$
	1060^{+459}_{-403} / 1064^{+456}_{-406}	$(3.88 \pm 0.79) \times 10^{-12}$	$(4.38 \pm 1.08) \times 10^{-12}$
	2450^{+1061}_{-930} / 2458^{+1053}_{-938}	$(4.72 \pm 1.11) \times 10^{-12}$	$(6.49 \pm 1.68) \times 10^{-12}$
	5659^{+2452}_{-2148} / 5678^{+2433}_{-2167}	$(4.55 \pm 1.53) \times 10^{-12}$	$(6.78 \pm 2.80) \times 10^{-12}$
low	199^{+86}_{-75} / 199^{+85}_{-76}	$(5.04 \pm 2.95) \times 10^{-13}$	$(5.18 \pm 3.03) \times 10^{-13}$
	459^{+199}_{-174} / 461^{+197}_{-176}	$(4.84 \pm 1.65) \times 10^{-13}$	$(5.22 \pm 1.78) \times 10^{-13}$
	1060^{+459}_{-403} / 1065^{+455}_{-407}	$(6.59 \pm 2.01) \times 10^{-13}$	$(7.93 \pm 2.42) \times 10^{-13}$
	2450^{+1061}_{-930} / 2460^{+1051}_{-940}	$(7.50 \pm 2.53) \times 10^{-13}$	$(9.96 \pm 3.37) \times 10^{-13}$
	5659^{+2451}_{-2148} / 5682^{+2429}_{-2171}	$(4.99 \pm 2.66) \times 10^{-13}$	$(7.40 \pm 3.94) \times 10^{-13}$

Notes. [a] Energy of the bin center at the Lafferty-Wyatt position for the measured / EBL corrected spectrum. [b] For the EBL correction of the spectra the model by Domínguez et al. (2011) has been applied.

4 Analysis in Chapter 6

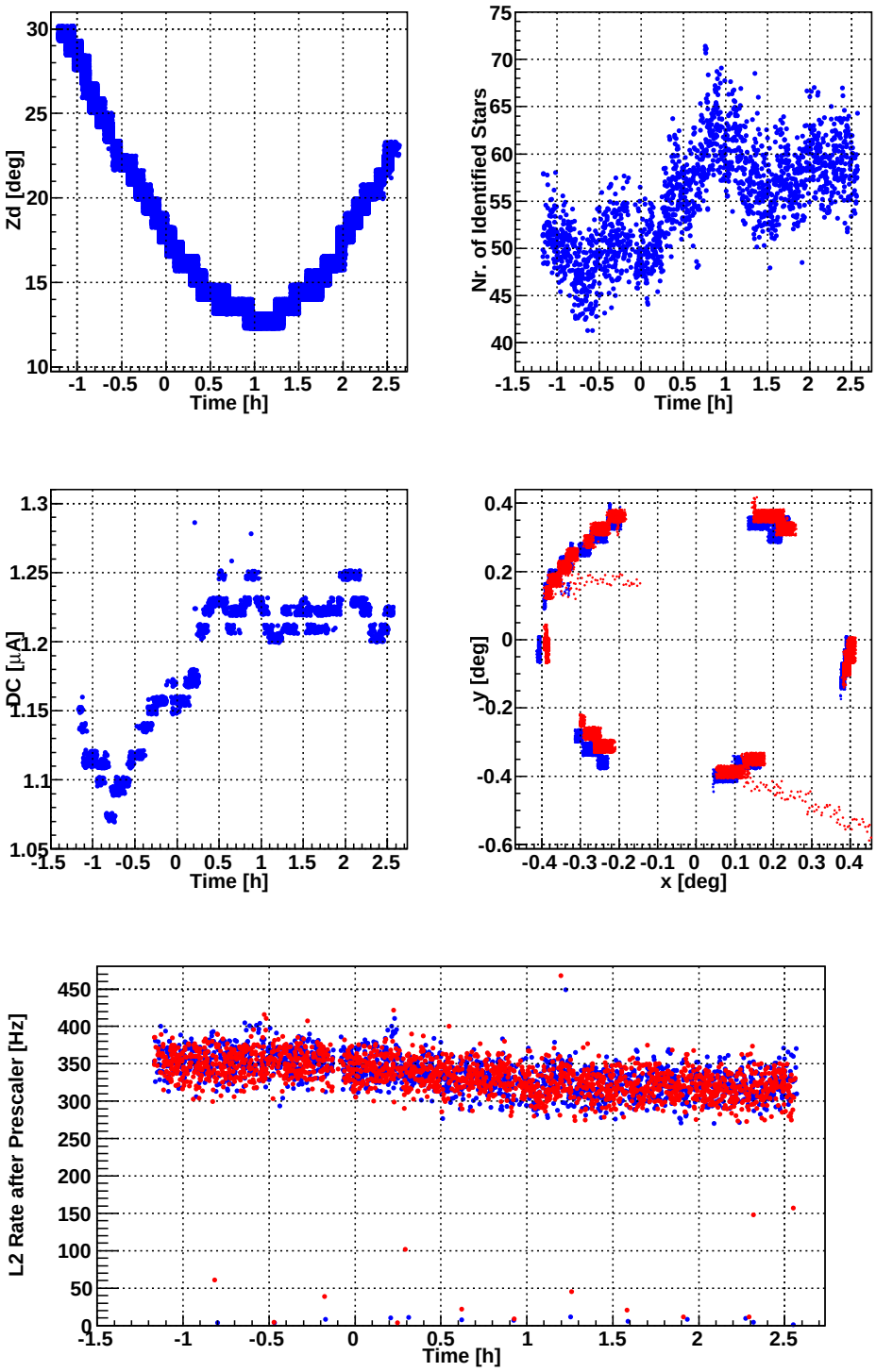

Figure 6: Quality check of the data of the night November 13, 2012. No data have been excluded for the analysis. The outliers in the middle right panel do not originate from runs in which IC 310 showed the flares. Blue data points show the measurement of MAGIC-I and red points show the measurement of MAGIC-II.

Table 8: Off data for analysis Chapter 6 and 7 (MWL data).

Source	Date	Used runs
DarkPatch18	2012-10-22	05020671-72
DarkPatch4	2012-10-22; 11-16	05020675-79; 05020992-96
DarkPatch6	2012-10-23	05020725-26
DarkPatch2	2012-11-12; 11-13	05020851-52; 05020897-900
M87	2012-12-10	05021542-48
DarkPatch22	2013-01-06	05022167-68
DarkPatch25	2013-01-08	05022192-94
2GGLJ1410+74	2013-01-17	05022681-82
DarkPatch28	2013-01-21	05022871, 74, 77, 80-82
DarkPatch29	2013-01-23	05022887
DarkPatch11	2013-02-08	05023304-06
DarkPatch31	2013-02-16	05023698

Table 9: Details on high-level analysis: Chapter 6.

Spectrum:	
Dead time	26×10^{-6} s
Binning	30 bins between 5–50000 GeV,
Number of OFF regions	4 ($0.4°$, $0.938°$ data)
Normalization region	0.1–0.4 ($0.4°$, $0.938°$ data)
Assumed index	2.0
Cuts	LEAKAGE MAGIC-I/II < 0.15,
	Number-of-Islands MAGIC-I/II < 2, SIZE > 50 phe
$0.4°$ offset data	HADRONNESS cuts: 0.8 efficiency in range 0.15-0.95
	θ^2 cuts: determined by 0.9 efficiency in range 0.01-0.2
$0.938°$ offset data	HADRONNESS cuts: 0.8 efficiency in range 0.15-0.95
	θ^2 cuts: determined by 0.9 efficiency in range 0.01-0.2
Light curve:	
Dead time	26×10^{-6} s
Binning	30 bins between 5–50000 GeV
Number of OFF regions	4 ($0.4°$, $0.938°$ data)
Normalization region	0.1–0.4 ($0.4°$, $0.938°$ data)
Assumed index	2.0
Cuts	LEAKAGE MAGIC-I/II < 0.15,
	Number-of-Islands MAGIC-I/II < 2, SIZE > 50 phe
$0.4°$ offset data	HADRONNESS cuts: 0.8 efficiency in range 0.15-0.95
	θ^2 cuts: determined by 0.9 efficiency in range 0.01-0.2
$0.938°$ offset data	HADRONNESS cuts: 0.8 efficiency in range 0.15-0.95
	θ^2 cuts: determined by 0.9 efficiency in range 0.01-0.2

Table 10: Fit parameters obtained from different power-law fits. The data has been fitted in the energy range between 70 GeV to 8.2 TeV.

Formula	Fit parameters	χ^2/d.o.f.
simple power-law: $\frac{\mathrm{d}N}{\mathrm{d}E} = f_0 \times \left(\frac{E}{1\mathrm{TeV}}\right)^{-\Gamma}$	$f_0 = (1.77 \pm 0.07)^{-11}\,\mathrm{cm}^{-2}\,\mathrm{s}^{-1}\,\mathrm{TeV}^{-1}$; $\Gamma = (1.87 \pm 0.04)$	$15.56/16$
Log-parabolic fit: $\frac{\mathrm{d}N}{\mathrm{d}E} = f_0 \times \left(\frac{E}{0.3\mathrm{TeV}}\right)^{-\Gamma + b \cdot \log 10(E/0.3\mathrm{TeV})}$	$f_0 = (1.74 \pm 0.07)^{-10}\,\mathrm{cm}^{-2}\,\mathrm{s}^{-1}\,\mathrm{TeV}^{-1}$; $\Gamma = (1.77 \pm 0.07)$; $b = (-0.13 \pm 0.09)$	$13.15/15$
Broken power-law: $\frac{\mathrm{d}N}{\mathrm{d}E} = f_0 \times \left(\frac{E}{0.3\mathrm{TeV}}\right)^{-\Gamma 1} \cdot \left[1 + (E/E_0)^{\beta}\right]^{(-\Gamma 2 + \Gamma 1)/\beta}$	$f_0 = (1.71 \pm 0.07)^{-10}\,\mathrm{cm}^{-2}\,\mathrm{s}^{-1}\,\mathrm{TeV}^{-1}$; $\Gamma 1 = (1.75 \pm 0.09)$; $\Gamma 2 = (2.45 \pm 0.90)$; $E_0 = (2.24 \pm 2.89)\,\mathrm{TeV}$; $\beta = (2.00 \pm 0.00)$	$12..12/14$

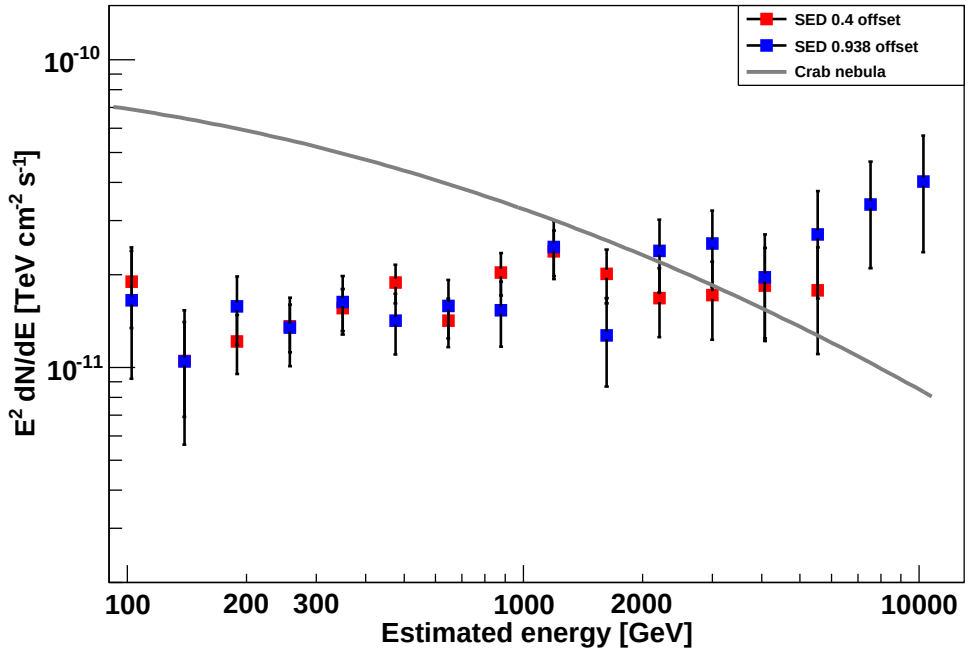

Figure 7: Spectrum energy distribution of the flare data sets with different offsets as function of the estimated energy (before the unfolding). Red and blue points denote the data with 0.4° and 0.938° offset, respectively.

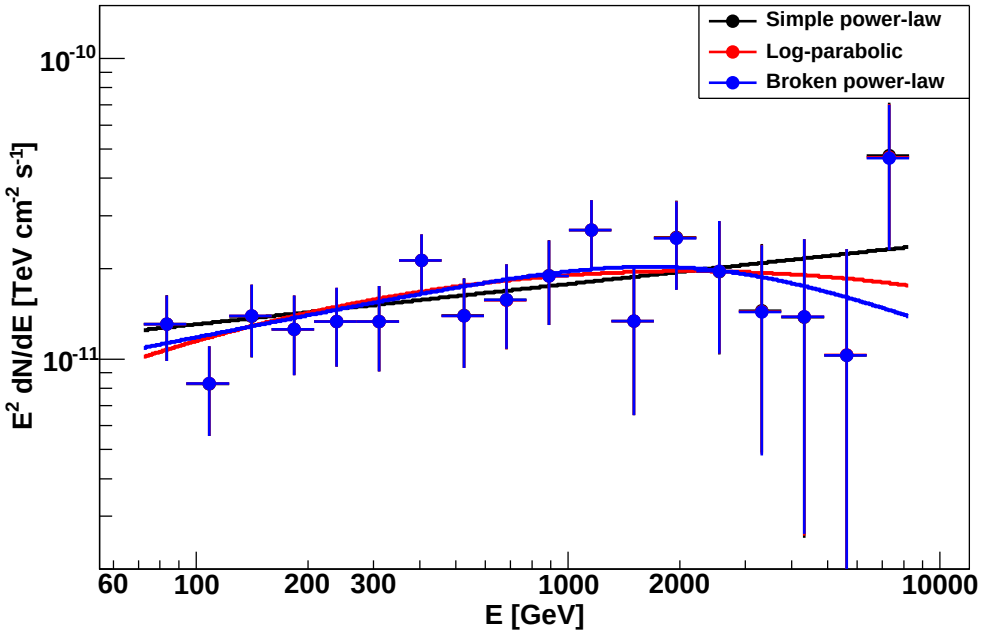

Figure 8: Unfolded spectrum energy distribution of the flare with nine bins per decade. Different power-law fits were applied. Black, red, and blue lines show the simple, log parabolic, and broken power-law fit, respectively. Since the Lafferty-Wyatt binning approach is used the data points from different fitting methods are not exactly overlaying. The significance of last data point can not be easily evaluated due to a low statistic of the observed events in this bin. The results of the parameters of the fits are given in Table 10.

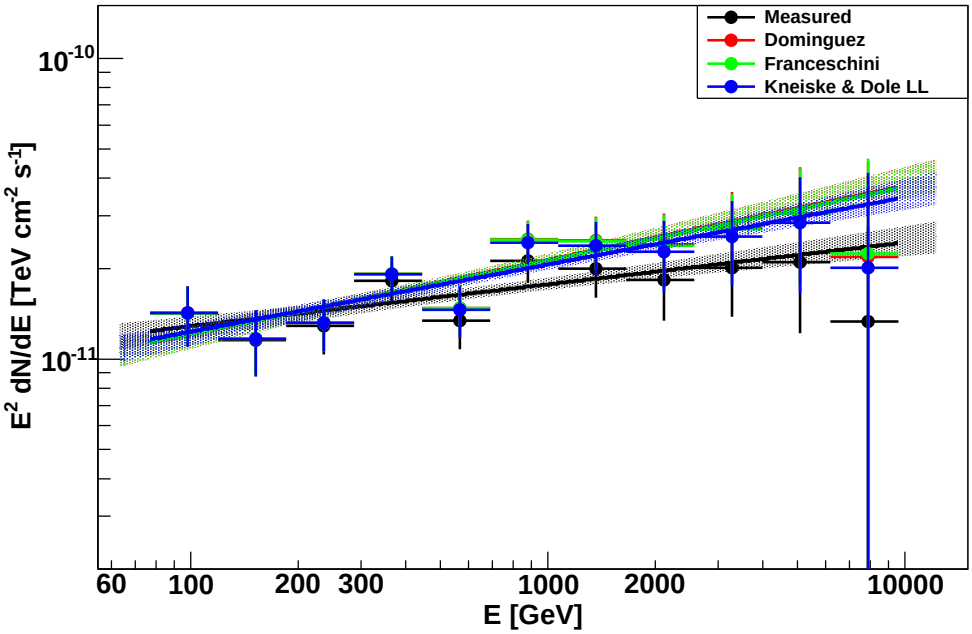

Figure 9: Spectrum energy distribution of the flare with different EBL models applied. Black: measured. Red: Domínguez et al. (2011). Green: Franceschini et al. (2008). Blue: Kneiske & Dole (2010). The unfolded (solid line and filled points) and forward folded (butterflies) results are shown, respectively. For the unfolding the Schmelling method has been applied.

Table 11: SED points of the flare.

Energy[a] [GeV]	$E^2\,\mathrm{d}N/\mathrm{d}E$ [$\mathrm{TeV}^{-1}\,\mathrm{cm}^{-2}\,\mathrm{s}^{-1}$]	$E^2\,\mathrm{d}N/\mathrm{d}E$ EBL corrected[b] [$\mathrm{TeV}^{-1}\,\mathrm{cm}^{-2}\,\mathrm{s}^{-1}$]
98^{+22}_{-21} / 98^{+22}_{-21}	$(1.43 \pm 0.32) \times 10^{-11}$	$(1.45 \pm 0.32) \times 10^{-11}$
151^{+34}_{-32} / 151^{+34}_{-32}	$(1.16 \pm 0.28) \times 10^{-11}$	$(1.17 \pm 0.28) \times 10^{-11}$
235^{+53}_{-49} / 235^{+52}_{-50}	$(1.29 \pm 0.25) \times 10^{-11}$	$(1.32 \pm 0.26) \times 10^{-11}$
364^{+82}_{-77} / 364^{+81}_{-77}	$(1.82 \pm 0.26) \times 10^{-11}$	$(1.92 \pm 0.28) \times 10^{-11}$
564^{+126}_{-119} / 564^{+126}_{-119}	$(1.35 \pm 0.26) \times 10^{-11}$	$(1.49 \pm 0.29) \times 10^{-11}$
874^{+196}_{-184} / 875^{+195}_{-185}	$(2.11 \pm 0.33) \times 10^{-11}$	$(2.49 \pm 0.39) \times 10^{-11}$
1355^{+304}_{-285} / 1357^{+303}_{-286}	$(2.02 \pm 0.40) \times 10^{-11}$	$(2.52 \pm 0.50) \times 10^{-11}$
2102^{+471}_{-442} / 2104^{+470}_{-444}	$(1.83 \pm 0.49) \times 10^{-11}$	$(2.39 \pm 0.64) \times 10^{-11}$
3259^{+731}_{-686} / 3262^{+728}_{-688}	$(2.02 \pm 0.63) \times 10^{-11}$	$(2.76 \pm 0.86) \times 10^{-11}$
5053^{+1133}_{-1063} / 5057^{+1129}_{-1067}	$(2.10 \pm 0.88) \times 10^{-11}$	$(3.06 \pm 1.28) \times 10^{-11}$
7834^{+1757}_{-1648} / 7841^{+1750}_{-1655}	$(1.34 \pm 1.42) \times 10^{-11}$	$(2.19 \pm 2.33) \times 10^{-11}$

Notes. [a] Energy of the bin center at the Lafferty-Wyatt position for the measured / EBL corrected spectrum. [b] For the EBL correction of the spectra the model by Domínguez et al. (2011) has been applied.

5 Analysis in Chapter 7

Table 12: Data from individual MAGIC observations in 2012/2013 used for the MWL campaign.

data[a]	Run	MJD start	Light Cond.	t_{eff} [h]	Zd [°]	Comments excluded runs
2012-11-13	05020909-11, 05020915-22	56243.95	dark	3.51	12-30	mode: NGC 1275, IC 310 flare detected
2012-11-14	05020956-63	56245.00	dark	2.38	12-23	05020951, 55, 64 too short
2012-11-16	05021007-17	56246.94	dark	3.49	12-30	
2012-11-18	05021023-30	56249.11	dark	2.39	27-55	
2012-11-19	05021078-81, 83-92	56249.99	m/d	4.42	12-54	05021069-75 with 0.29° wobble offset
2012-11-20						bad weather, ON-mode exclude all
2012-11-21	05021200-02, 05021205	56252.06	m/d	1.31	18-33	05021191-4, 7-9 05021203-4, 6-8: too short, low rates
2012-11-22	05021232-33, 35-38	56253.09	dark	1.96	26-54	05021234: drop in rates, cloud
2012-11-23	05021262, 64-66	56254.13	m/d	1.31	36-55	05021252-9, 63: bright moon, low rates
2012-11-24	05021288-89	56255.17	m/d	0.65	46-55	05021280-82, 85: bright moon, low rates
2012-12-11						bad weather
2012-12-15	05021691-91, 95	56275.93	dark	0.92	12-18	mode: NGC 1275, 05021694: AMC problem
2012-12-16	05021727-28	56276.82	moon	0.65	33-42	05021729-30
2012-12-17	05021773-79	56277.83	moon	2.01	15-37	
2012-12-18	05021824-34	56277.83	m/d	3.50	12-38	05021823
2012-12-19						excl. all: bad weather
2012-12-20						excl. all: bad weather
2012-12-21						excl. all: bad weather

Notes. [a] Dates in MAGIC night notation, i.e., after midnight.

Table 13: Data from individual MAGIC observations in 2012/2013 used for the MWL campaign. Continued.

data[a]	Run	MJD start	Light Cond.	$t_{\rm eff}$ [h]	Zd [°]	Comments excluded runs
2013-01-10	05022287, 89	56301.89	dark	0.62	12-20	mode: NGC 1275
2013-01-11	05022344-45	56302.88	dark	0.65	12-19	mode: NGC 1275
2013-01-13	05022444 47-48	56304.87	dark	0.80	12-16	mode: NGC 1275, AMC problems
2013-01-14	05022497-99	56305.82	moon	0.98	12-20	
2013-01-15	05022545-50	56306.83	moon	1.50	12-17	05022544
2013-01-16	05022595-602	56307.83	moon	2.51	12-28	05022594
2013-01-17	05022640-49, 52	56308.82	moon	3.35	12-38	
2013-01-18						bad weather, bright moon, excl. all
2013-01-19						new AMC: excl. all
2013-01-20						new AMC: excl. all Fermi ATel: NGC 1275
2013-01-29						new AMC: excl. all
2013-02-15						new AMC: excl. all

Notes. [(a)] Dates in MAGIC night notation, i.e., after midnight.

Table 14: Details on high-level analysis: Chapter 7 (MWL data).

Light curve:	
Dead time	26×10^{-6} s
Binning	16 bins between 10–100000 GeV
Number of OFF regions	4 (0.4° data only)
Normalization region	0.15–0.35 (0.4° data only)
Assumed index	2.0
Cuts	LEAKAGE MAGIC-I/II < 0.15, Number-of-Islands MAGIC-I/II < 2, SIZE > 50 phe
0.4° offset data	HADRONNESS cuts: 0.9 efficiency in range 0.15-0.95 θ^2 cuts: determined by 0.7 efficiency in range 0.01-0.2

Table 15: Flux results from individual observations in 2012/2013 (without flare data).

used data[a]	MJD start	t_{eff} [h]	$F_{\mathrm{E>300\,GeV}}{}^{b}$ [10^{-12} ph cm^{-2} s^{-1}]	$F_{\mathrm{E>300\,GeV}}{}^{c}$ [10^{-12} ph cm^{-2} s^{-1}]
all data		35.3	1.36 ± 0.27	
2012-11-14	56245.00	2.28	$(0.41 \pm 0.73) < 2.60$	1.35 ± 0.39
2012-11-16	56246.94	3.49	$(-0.13 \pm 0.70) < 1.63$	
2012-11-18	56249.11	2.39	$(1.98 \pm 1.04) < 6.17$	
2012-11-19	56249.99	4.42	$(1.37 \pm 0.80) < 4.42$	
2012-11-21	56252.06	1.31	$(-0.43 \pm 1.23) < 2.71$	
2012-11-22	56253.09	1.96	$(0.92 \pm 1.08) < 4.27$	
2012-11-23	56254.13	1.31	4.72 ± 1.66	
2012-11-24	56255.17	0.65	$(1.70 \pm 2.19) < 8.38$	
2012-12-15	56275.93	0.92	$(1.61 \pm 1.61) < 6.99$	2.07 ± 0.58
2012-12-16	56276.82	0.65	$(0.09 \pm 0.93) < 2.85$	
2012-12-17	56277.83	2.01	$(1.08 \pm 1.14) < 4.70$	
2012-12-18	56278.83	3.50	3.35 ± 0.92	
2013-01-10	56301.89	0.62	5.29 ± 2.34	$(0.61 \pm 0.51) < 2.14$
2013-01-11	56302.88	0.65	$(-1.70 \pm 1.63) < 3.06$	
2013-01-13	56304.87	0.80	$(1.38 \pm 1.82) < 7.18$	
2013-01-14	56305.82	0.98	$(0.00pm1.54) < 4.17$	
2013-01-15	56306.83	1.50	$(0.07 \pm 1.16) < 3.20$	
2013-01-16	56307.83	2.51	2.47 ± 1.04	
2013-01-17	56308.82	3.35	$(-0.35 \pm 0.74) < 1.48$	

Notes. $^{(a)}$ Dates in MAGIC night notation, i.e., after midnight. $^{(b)}$ Daily measured flux above 300 GeV in units of 10^{-12} ph cm^{-2}s^{-1}. Upper limits are given with 95% confidence level for negative flux measurements, or points that are consistent with zero within the error. $^{(c)}$ Monthly measured flux above 300 GeV in units of 10^{-12} ph cm^{-2}s^{-1}.

Table 16: Further data taken in 2013/2014 used for monitoring.

data[a]	Run	MJD start	Light Cond.	t_{eff} [h]	Zd [°]	DC (MI) [μ A]	Comments excl. runs
2013-07-30							strong moon: excl. all
2013-07-31							strong moon: excl. all
2013-08-01							dead zone, moon, excl. all
2013-08-02							dead zone, calima excl. all
2013-08-03							dead zone, calima excl. all
2013-08-07	05028334-35	56511.16	dark	0.44	40-46	0.9-1.0	05028334.001-011: dead zone
2013-08-09	05028407-08	56513.16	dark	0.50	38-45	0.9-1.0	05028407.001-009: dead zone
2013-08-11	05028478-79	56515.15	dark	0.49	39-46	0.9-1.0	05028478: dead zone
2013-08-28							strong moon: excl. all
2013-08-29							strong moon: excl. all
2013-08-30							AMC2 problem excl. all
2013-08-31	05028880-87	56535.10	moon	2.57	16-44	0.9-1.6	
2013-09-02	05028956-57 65-68	56537.09	d/m	1.96	13-43	0.8-1.0	
2013-09-05	05029082-84	56540.12	dark	0.98	23-35	0.8-0.9	bad PSF
2013-09-07	05029159-61	56542.19	dark	0.98	12-18	0.8-1.0	
2013-09-13	05029320-22, 26	56548.06	dark	1.30	25-46	1.0-1.1	mode: NGC 1275 and Perseus-MA
2013-09-15							excl. all
2013-09-17	05029419-21	56552.19	m/d	0.98	12-19	1.0-1.5	
2013-10-04	05029439-40, 43	56569.11	dark	0.98	12-19	0.9-1.1	mode: NGC 1275
2013-10-09	05029950, 53-54	56574.18	dark	0.84	18-35	0.9-1.1	mode: NGC 1275
2013-10-13	05030125, 29-30	56578.17	dark	0.97	17-36	1.0-1.2	mode: NGC 1275
2013-10-31	05030447, 50	56596.12	dark	0.60	18-32	1.0-1.1	mode: NGC 1275
2013-11-01	05030465	56597.11	dark	0.32	17-20	1.0-1.1	mode: NGC 1275 05030466, 69: bad weather
2013-11-02	05030512-13	56598.13	dark	0.65	21-29	0.9-1.1	mode: NGC 1275
2013-11-04	05030571, 74	56600.10	dark	0.56	16-29	0.9-1.2	mode: NGC 1275 05030577: short
2013-11-05	05030621-22 25-26, 30	56601.12	dark	1.50	19-56	1.0-1.2	mode: NGC 1275

Notes. [a] Dates in MAGIC night notation, i.e., after midnight.

Table 17: Further data taken in 2013/2014 used for monitoring. Continued.

data[a]	Run	MJD start	Light Cond.	$t_{\rm eff}$ [h]	Zd [°]	DC (MI) [μ A]	Comments excl. runs
2013-11-22							strong moon excl. all
2013-11-24							strong moon excl. all
2013-11-25							strong moon excl. all
2013-11-26							strong moon excl. all
2013-11-27							moon, bad w., excl. all
2013-12-07	05031474-81	56632.83	moon	2.25	19-46	1.0-1.9	05031474.001-008: dead zone
2013-12-08							bad weather: excl. all
2013-12-31							bad weather: excl. all
2014-01-02	05032038-39	56658.84	dark	0.64	16-23	1.0-1.1	NGC 1275
2014-01-06	05032264-69	56662.85	moon	1.96	12-18	1.4-1.9	moon: low rate
2014-01-07							strong moon excl. all
2014-02-02	05032663-65	56689.84	moon	0.74	14-20	0.9-1.1	
2014-02-04	05032754, 60 63-64, 67-68, 71	56691.85	moon	2.30	15-50	0.9-2.0	
2014-02-05							strong moon excl. all
2014-02-23	05033132-33	56710.87	dark	0.65	32-41	1.1-1.2	
2014-03-03	05033434	56718.86	moon	0.28	35-39	1.1-1.2	
2014-03-04	05033481-84	56719.85	moon	1.28	35-52	1.1-1.4	
2014-03-05	05033534-35	56720.86	moon	0.98	36-49	1.6-1.8	05033537-39: moon
2014-03-08							very low rate excl. all

Notes. [a] Dates in MAGIC night notation, i.e., after midnight.

Table 18: Off data for analysis Chapter 7 (monitoring data).

Source	Date	Used runs
1H0323+342	2013-09-01	05028919-21
TXS2320+343	2013-09-03	05028987-92
3c454.3	2013-09-28; 10-05	05029516-26; 05029760-61
1ES0229+200	2013-10-02	05029705
BZBJ0123+342	2013-10-09	05029929-47

Table 19: Details on high-level analysis: Chapter 7 (monitoring data).

Light curve:	
Dead time	26×10^{-6} s
Binning	16 bins between 5–50000 GeV
Number of OFF regions	4 (0.4° only)
Normalization region	0.15–0.35 (0.4° only)
Assumed index	2.0
Cuts	LEAKAGE MAGIC-I/II < 0.15,
	Number-of-Islands MAGIC-I/II < 2, SIZE > 50 phe
0.4° offset data	HADRONNESS cuts: 0.9 efficiency in range 0.15-0.95
	θ^2 cuts: determined by 0.7 efficiency in range 0.01-0.2

Table 20: Flux results from individual observations in 2013/2014 (monitoring data).

used data[a]	MJD start	t_{eff} [h]	$F_{\mathrm{E>300\,GeV}}{}^{b}$ [$10^{-12}\,\mathrm{ph\,cm^{-2}\,s^{-1}}$]
all data		27.4	$(0.31 \pm 0.24) < 1.13$
2013-08-07	56511.16	0.44	$(0.40 \pm 1.78) < 5.53$
2013-08-09	56513.16	0.50	$(-1.67 \pm 1.74) < 3.10$
2013-08-11	56515.15	0.49	$(-0.84 \pm 1.55) < 3.33$
2013-08-31	56535.10	2.57	$(0.96 \pm 0.91) < 3.93$
2013-09-02	56537.10	1.96	$(0.61 \pm 1.10) < 3.82$
2013-09-05	56540.12	0.98	$(0.88 \pm 1.10) < 4.43$
2013-09-07	56542.19	0.98	$(-1.29 \pm 1.41) < 2.61$
2013-09-13	56548.06	1.30	$(0.00 \pm 1.03) < 2.72$
2013-09-17	56552.20	0.98	$(0.64 \pm 1.23) < 4.47$
2013-10-04	56569.11	0.98	$(-0.11 \pm 1.27) < 3.42$
2013-10-09	56574.18	0.84	$(-0.09 \pm 1.47) < 3.84$
2013-10-13	56578.17	0.97	$(0.48 \pm 1.33) < 4.34$
2013-10-31	56596.12	0.60	$(0.55 \pm 1.60) < 5.35$
2013-11-01	56597.11	0.32	$(-1.20 \pm 1.98) < 4.99$
2013-11-02	56598.13	0.65	$(2.21 \pm 1.86) < 8.74$
2013-11-04	56600.10	0.56	$(-0.16 \pm 1.40) < 3.93$
2013-11-05	56601.12	1.50	$(0.12 \pm 1.26) < 3.48$
2013-12-07	56632.83	2.25	$(-0.13 \pm 0.81) < 1.92$
2014-01-02	56658.84	0.64	$(0.15 \pm 1.86) < 5.40$
2014-01-06	56662.85	1.96	$(-0.43 \pm 0.97) < 2.07$
2014-02-02	56689.84	0.74	$(-0.41 \pm 1.51) < 3.77$
2014-02-04	56691.85	2.30	$(1.73 \pm 1.05) < 5.70$
2014-02-23	56710.87	0.65	$(0.62 \pm 1.71) < 5.57$
2014-03-03	56718.86	0.28	$(-1.21 \pm 1.95) < 4.58$
2014-03-04	56719.85	1.28	$(1.33 \pm 1.31) < 5.59$
2014-03-05	56720.86	0.98	$(-0.60 \pm 1.12) < 2.28$

Notes. $^{(a)}$ Dates in MAGIC night notation, i.e., after midnight. $^{(b)}$ Daily measured flux above 300 GeV in units of $10^{-12}\,\mathrm{ph\,cm^{-2}s^{-1}}$. Upper limits are given with 95% confidence level for negative flux measurements, or points that are consistent with zero within the error.

Appendix C: Data for MWL Campaign

Table 21: Flux upper limits from *Fermi*-LAT observations during the MWL campaign.

MJD	$F_{1-300\,\mathrm{GeV}} \times 10^{-9}$ [$\mathrm{s^{-1}\,cm^{-2}}$]
56247.0	$<$1.90
56277.0	$<$4.01
56307.0	$<$5.14
56336.5	$<$5.89

Table 22: Results from the *Swift*-XRT observations during the MWL campaign.

Obs. ID	MJD start	Exps. [s]	$F_{0.2-10\,\mathrm{keV}} \times 10^{-11}$ [erg s^{-1} cm^{-2}]^a	Γ^b	$N_{\mathrm{H}}{}^c$ [10^{22} cm^{-2}]	χ^2/ d.o.f.
all data (0003...)		45773	0.606 ± 0.010	$2.036^{+0.022}_{-0.019}$	0.135 ± 0.008	222.4/ 240
2264007	56245.67	4977	0.64 ± 0.04	$1.93^{+0.08}_{-0.05}$	$0.126^{+0.024}_{-0.026}$	37.3/38
2264008	56253.09	3984	0.61 ± 0.04	2.13 ± 0.05	$0.118^{+0.035}_{-0.025}$	43.8/36
2264009	56253.98	3968	0.69 ± 0.04	$1.90^{+0.05}_{-0.07}$	$0.061^{+0.024}_{-0.025}$	32.9/31
2264010	56255.70	3991	0.49 ± 0.04	2.17 ± 0.06	$0.151^{+0.030}_{-0.068}$	22.3/23
2264011	56273.95	1983	0.56 ± 0.06	$2.02^{+0.12}_{-0.09}$	$0.16^{+0.09}_{-0.06}$	7.3/11
2264012	56275.88	3891	0.59 ± 0.04	$1.92^{+0.09}_{-0.07}$	$0.116^{+0.029}_{-0.025}$	29.6/28
2264013	56276.81	3878	0.66 ± 0.04	$1.96^{+0.10}_{-0.07}$	$0.140^{+0.027}_{-0.024}$	34.3/31
2264014	56277.81	3878	0.65 ± 0.04	$1.95^{+0.08}_{-0.07}$	$0.13^{+0.04}_{-0.05}$	23.2/30
2264015	56278.82	3660	0.62 ± 0.04	$2.11^{+0.10}_{-0.07}$	$0.171^{+0.029}_{-0.031}$	37.7/29
2264016	56279.82	3864	0.55 ± 0.04	$2.18^{+0.06}_{-0.05}$	$0.173^{+0.027}_{-0.030}$	23.1/30
2264017	56280.82	3856	0.44 ± 0.03	$2.28^{+0.05}_{-0.06}$	0.149 ± 0.028	47.3/28
2264018	56281.82	3844	0.58 ± 0.04	$1.99^{+0.05}_{-0.07}$	$0.127^{+0.029}_{-0.024}$	31.9/28

Notes. $^{(a)}$ Flux between 0.2 and 10 keV determined by a simple power-law fit. $^{(b)}$ Photon index: $F \propto E^{-\Gamma}$. $^{(c)}$ Absorption with a equivalent column of hydrogen.

Table 23: Results from the *Swift*-XRT observations in January 2012.

Obs. ID	MJD start	Exps. [s]	$F_{0.2-10\,\mathrm{keV}} \times 10^{-11}$ [erg s^{-1} cm^{-2}]^a	Γ^b	$N_{\mathrm{H}}{}^c$ [10^{22} cm^{-2}]	χ^2/ d.o.f.
all data (0003...)		13214	0.438 ± 0.015	$2.10^{+0.05}_{-0.04}$	$0.125^{+0.015}_{-0.029}$	58.9/ 75
2264001	55952.65	2988	0.40 ± 0.04	$2.07^{+0.10}_{-0.07}$	$0.10^{+0.06}_{-0.04}$	18.9/17
2264002	55953.58	2885	0.37 ± 0.03	$2.18^{+0.12}_{-0.09}$	0.18 ± 0.05	11.7/15
2264003	55954.12	2742	$0.48^{+0.09}_{-0.07}$	$2.10^{+0.15}_{-0.09}$	0.14 ± 0.04	9.3/17
2264004	55955.12	3094	$0.48^{+0.04}_{-0.06}$	2.13 ± 0.06	0.12 ± 0.04	24.5/22
2264005	55956.14	1504	0.45 ± 0.05	$2.03^{+0.09}_{-0.10}$	$0.11^{+0.05}_{-0.06}$	14.6/8

Notes. $^{(a)}$ Flux between 0.2 and 10 keV determined by a simple power-law fit. $^{(b)}$ Photon index: $F \propto E^{-\Gamma}$. $^{(c)}$ Absorption with a equivalent column of hydrogen.

Table 24: Results from the KVA observations in the R band during the MWL campaign.

MJD	Flux density [mJy]	Error of flux density [mJy]
56221.15005	9.10	0.15
56222.15063	9.16	0.15
56244.14379	9.05	0.15
56249.9487	9.17	0.15
56255.90087	9.14	0.29
56266.94108	9.05	0.15
56275.90372	9.00	0.15
56277.94691	9.03	0.15
56283.92947	9.06	0.15
56287.90108	8.85	0.15
56294.86696	9.05	0.15
56301.89024	9.17	0.15
56304.90712	9.10	0.15
56308.89412	9.25	0.15
56311.88023	9.15	0.15
56317.88406	9.09	0.15
56321.88795	9.03	0.15
56322.81984	9.09	0.15
56323.81855	9.03	0.16
56324.90887	9.13	0.15
56325.81984	8.93	0.16
56326.81635	9.04	0.15
56327.82454	8.83	0.15
56329.84887	8.92	0.15
56332.90643	9.28	0.16
56336.88522	8.96	0.15
56339.85226	9.13	0.18
56343.86059	9.07	0.15
56346.8553	8.88	0.15

Table 25: Results from the KVA observations in the R band during January-February 2012.

MJD	Flux density [mJy]	Error of flux density [mJy]
55934.91019	9.13	0.15
55937.92324	8.62	0.14
55940.89206	8.99	0.16
55944.88245	9.09	0.15
55947.87119	8.97	0.15
55952.91141	8.99	0.15
55954.86492	8.95	0.15
55955.8957	8.87	0.15
55958.88718	9.06	0.15
55961.8454	8.96	0.17
55965.84918	9.23	0.15
55975.8681	9.00	0.15
55979.90071	9.05	0.15
55982.84527	8.97	0.15
55989.84422	8.97	0.15
55993.8473	9.03	0.16

Table 26: Results from the OVRO observations at 15 GHz.

MJD	$S_{15\,\mathrm{GHz}}$ [mJy]
55901.1	0.162 ± 0.006
55908.1	0.156 ± 0.010
55912.1	0.164 ± 0.022
55919.1	0.152 ± 0.008
55922.1	0.155 ± 0.010
55926	0.157 ± 0.005
55933	0.148 ± 0.044
55936	0.158 ± 0.017
55940	0.160 ± 0.008
55943	0.159 ± 0.007
55945	0.157 ± 0.013
55964	0.158 ± 0.004
55967.9	0.153 ± 0.019
55969.9	0.150 ± 0.014
55985.9	0.152 ± 0.027
55989.9	0.144 ± 0.012
55996.9	0.152 ± 0.020
56006.8	0.146 ± 0.013
56015.8	0.140 ± 0.016
56020.8	0.186 ± 0.006
56024.8	0.151 ± 0.012
56034.7	0.148 ± 0.007
56036.7	0.145 ± 0.017
56038.7	0.142 ± 0.019
56041.7	0.139 ± 0.011
56046	0.162 ± 0.005
56056	0.147 ± 0.005
56060.9	0.158 ± 0.014
56089.6	0.141 ± 0.015
56105.5	0.152 ± 0.005
56108.6	0.142 ± 0.003
56115.5	0.141 ± 0.005
56118.8	0.134 ± 0.023
56119.8	0.148 ± 0.003
56129.5	0.144 ± 0.021
56136.8	0.139 ± 0.005
56138.7	0.140 ± 0.010
56142.8	0.154 ± 0.015
56145.8	0.183 ± 0.053
56152.7	0.147 ± 0.008
56159.7	0.151 ± 0.005
56172.4	0.152 ± 0.016

Table 27: Results from the OVRO observations at 15 GHz. Continued.

MJD	$S_{15\,\mathrm{GHz}}$ [mJy]
56180.4	0.147 ± 0.005
56183.6	0.160 ± 0.009
56192.6	0.148 ± 0.012
56197.6	0.153 ± 0.006
56203.3	0.141 ± 0.006
56203.6	0.147 ± 0.022
56206.3	0.128 ± 0.005
56208.6	0.161 ± 0.017
56220.5	0.152 ± 0.016
56225.2	0.146 ± 0.004
56225.5	0.143 ± 0.005
56231.2	0.148 ± 0.013
56231.5	0.138 ± 0.010
56234.5	0.151 ± 0.015
56238.2	0.148 ± 0.024
56242.5	0.148 ± 0.004
56247.5	0.144 ± 0.005
56253.2	0.145 ± 0.009
56258.2	0.137 ± 0.015
56262.2	0.126 ± 0.013
56264.4	0.161 ± 0.012
56268.4	0.135 ± 0.018
56272.4	0.170 ± 0.004
56277.1	0.144 ± 0.017
56283.4	0.146 ± 0.010
56326	0.147 ± 0.004
56326	0.162 ± 0.076
56330.3	0.126 ± 0.027
56341.2	0.154 ± 0.004
56349.2	0.158 ± 0.007
56364.2	0.167 ± 0.006
56367.9	0.157 ± 0.014
56378.8	0.155 ± 0.027
56381.1	0.161 ± 0.028
56388.1	0.157 ± 0.008
56396.7	0.150 ± 0.006
56403.8	0.140 ± 0.006
56409	0.171 ± 0.004
56414.7	0.141 ± 0.010
56427.7	0.145 ± 0.016
56431	0.166 ± 0.007
56433	0.167 ± 0.023

Table 28: Results from the OVRO observations at 15 GHz. Continued.

MJD	$S_{15\,\mathrm{GHz}}$ [mJy]
56441.6	0.156 ± 0.003
56442.6	0.157 ± 0.017
56450.9	0.168 ± 0.008
56459.6	0.156 ± 0.021
56469.6	0.152 ± 0.020
56481.8	0.162 ± 0.006
56490.8	0.153 ± 0.008
56492.8	0.154 ± 0.021
56505.5	0.156 ± 0.005
56511.5	0.149 ± 0.023
56512.4	0.148 ± 0.007
56512.5	0.144 ± 0.016
56515.5	0.155 ± 0.017
56522.7	0.163 ± 0.005
56529.4	0.161 ± 0.013
56532.4	0.147 ± 0.028
56541.7	0.164 ± 0.011
56546.4	0.156 ± 0.012
56548.6	0.183 ± 0.007
56551.6	0.160 ± 0.021
56555.6	0.178 ± 0.004
56558.6	0.155 ± 0.005
56565.6	0.158 ± 0.008
56570.3	0.140 ± 0.004
56581.6	0.178 ± 0.005
56490.8	0.153 ± 0.008
56492.8	0.154 ± 0.021
56505.5	0.156 ± 0.005
56511.5	0.149 ± 0.023
56512.4	0.148 ± 0.007
56512.5	0.144 ± 0.016
56515.5	0.155 ± 0.017
56522.7	0.163 ± 0.005
56529.4	0.161 ± 0.013
56532.4	0.147 ± 0.028
56541.7	0.164 ± 0.011
56546.4	0.156 ± 0.012
56548.6	0.183 ± 0.007
56551.6	0.160 ± 0.021
56555.6	0.178 ± 0.004
56558.6	0.155 ± 0.005
56565.6	0.158 ± 0.008

Table 29: Results from the OVRO observations at 15 GHz. Continued.

MJD	$S_{15\,\mathrm{GHz}}$ [mJy]
56570.3	0.140 ± 0.004
56581.6	0.178 ± 0.005
56585.2	0.152 ± 0.009
56586.5	0.158 ± 0.011
56592.5	0.162 ± 0.013
56595.5	0.178 ± 0.005
56598.5	0.155 ± 0.009
56602.5	0.184 ± 0.015
56605.5	0.174 ± 0.004
56608.2	0.154 ± 0.007
56609.5	0.161 ± 0.008
56613.2	0.146 ± 0.004
56614.5	0.184 ± 0.015
56617.2	0.072 ± 0.321
56623.4	0.171 ± 0.021
56628.1	0.153 ± 0.006
56631.1	0.158 ± 0.036
56632.1	0.144 ± 0.020
56641.4	0.166 ± 0.008
56651.4	0.168 ± 0.005
56656.3	0.166 ± 0.014
56659.4	0.196 ± 0.014
56673	0.159 ± 0.012
56677	0.153 ± 0.015
56686	0.159 ± 0.008
56687	0.138 ± 0.016
56692	0.156 ± 0.004
56699.3	0.191 ± 0.007
56700.9	0.167 ± 0.006
56703.2	0.169 ± 0.018
56707	0.173 ± 0.028
56711.2	0.156 ± 0.056
56713.9	0.148 ± 0.007
56724.9	0.150 ± 0.020
56729.1	0.162 ± 0.018
56732.2	0.200 ± 0.014
56736.1	0.167 ± 0.026
56743.1	0.163 ± 0.008
56756.8	0.144 ± 0.004
56760.1	0.184 ± 0.005
56762.1	0.175 ± 0.034
56771	0.166 ± 0.024
56774.7	0.154 ± 0.010
56778	0.185 ± 0.005
56781.7	0.145 ± 0.017
56787.7	0.146 ± 0.019

Bibliography

Aartsen, M. G., Ackermann, M., Adams, J., et al. 2014, ArXiv e-prints: 1405.5303

Abdo, A. A., Ackermann, M., Ajello, M., et al. 2010a, ApJ, 715, 429

Abdo, A. A., Ackermann, M., Ajello, M., et al. 2011, Science, 331, 739

Abdo, A. A., Ackermann, M., Ajello, M., et al. 2009a, ApJ, 699, 31

Abdo, A. A., Ackermann, M., Ajello, M., et al. 2009b, ApJ, 707, 55

Abdo, A. A., Ackermann, M., Ajello, M., et al. 2010b, ApJ, 719, 1433

Abdo, A. A., Ackermann, M., Ajello, M., et al. 2010c, Science, 328, 725

Abramowicz, M. A., Chen, X.-M., Granath, M., & Lasota, J.-P. 1996, ApJ, 471, 762

Acciari, V. A., Aliu, E., Arlen, T., et al. 2011a, ApJ, 738, 169

Acciari, V. A., Aliu, E., Arlen, T., et al. 2009, Science, 325, 444

Acciari, V. A., Arlen, T., Aune, T., et al. 2011b, ApJ, 729, 2

Ackermann, M., Ajello, M., Albert, A., et al. 2012, ApJS, 203, 4

Ackermann, M., Ajello, M., Allafort, A., et al. 2011, ApJ, 743, 171

Ackermann, M., Ajello, M., Allafort, A., et al. 2013, ApJS, 209, 34

Adrián-Martínez, S., Al Samarai, I., Albert, A., et al. 2012, Astroparticle Physics, 36, 204

Aharonian, F., Akhperjanian, A. G., Bazer-Bachi, A. R., et al. 2007, ApJ, 664, L71

Aharonian, F., Akhperjanian, A. G., Bazer-Bachi, A. R., et al. 2006, A&A, 457, 899

Aharonian, F. A., Akhperjanian, A. G., Barrio, J. A., et al. 1999, A&A, 342, 69

Aharonian, F. A., Hofmann, W., Konopelko, A. K., & Völk, H. J. 1997, Astroparticle Physics, 6, 343

Albert, J., Aliu, E., Anderhub, H., et al. 2008a, Nuclear Instruments and Methods in Physics Research A, 594, 407

Albert, J., Aliu, E., Anderhub, H., et al. 2008b, Nuclear Instruments and Methods in Physics Research A, 588, 424

Albert, J., Aliu, E., Anderhub, H., et al. 2007a, Nuclear Instruments and Methods in Physics Research A, 583, 494

Albert, J., Aliu, E., Anderhub, H., et al. 2007b, ApJ, 667, 358

Albert, J., Aliu, E., Anderhub, H., et al. 2007c, ApJ, 669, 862

Albert, J., Aliu, E., Anderhub, H., et al. 2008c, ApJ, 674, 1037

Aleksić, J., Alvarez, E. A., Antonelli, L. A., et al. 2012a, A&A, 539, L2

Aleksić, J., Alvarez, E. A., Antonelli, L. A., et al. 2012b, Astroparticle Physics, 35, 435

Aleksic, J., Ansoldi, S., Antonelli, L. A., et al. 2014a, ArXiv e-prints: 1409.6073

Aleksic, J., Ansoldi, S., Antonelli, L. A., et al. 2014b, ArXiv e-prints: 1409.5594

Aleksić, J., Ansoldi, S., Antonelli, L. A., et al. 2014a, A&A, 564, A5

Aleksić, J., Ansoldi, S., Antonelli, L. A., et al. 2014b, Science, 346, 1080

Aleksić, J., Antonelli, L. A., Antoranz, P., et al. 2014c, A&A, 563, A91

Aleksić, J., Antonelli, L. A., Antoranz, P., et al. 2010a, A&A, 524, A77

Aleksić, J., Antonelli, L. A., Antoranz, P., et al. 2010b, ApJ, 723, L207

Aleksić, J., Antonelli, L. A., Antoranz, P., et al. 2011, ApJ, 730, L8

Aliu, E., Archambault, S., Aune, T., et al. 2014, ApJ, 781, L11

Anderhub, H., Backes, M., Biland, A., et al. 2013, Journal of Instrumentation, 8, 6008P

Appl, S., Lery, T., & Baty, H. 2000, A&A, 355, 818

Araudo, A. T., Bosch-Ramon, V., & Romero, G. E. 2013, MNRAS, 436, 3626

Arbeiter, C., Pohl, M., & Schlickeiser, R. 2002, A&A, 386, 415

Arlen, T., Aune, T., Beilicke, M., et al. 2013, ApJ, 762, 92

Arshakian, T. G., León-Tavares, J., Böttcher, M., et al. 2012, A&A, 537, A32

Atwood, W. B., Abdo, A. A., Ackermann, M., et al. 2009, ApJ, 697, 1071

Baldwin, J. A., Phillips, M. M., & Terlevich, R. 1981, PASP, 93, 5

Barkov, M. V., Aharonian, F. A., Bogovalov, S. V., Kelner, S. R., & Khangulyan, D. 2012a, ApJ, 749, 119

Barkov, M. V., Aharonian, F. A., & Bosch-Ramon, V. 2010, ApJ, 724, 1517

Barkov, M. V., Bosch-Ramon, V., & Aharonian, F. A. 2012b, ApJ, 755, 170

Barkov, M. V. & Komissarov, S. S. 2008, International Journal of Modern Physics D, 17, 1669

Barth, A. J., Ho, L. C., & Sargent, W. L. W. 2002, ApJ, 566, L13

Bassani, L., Landi, R., Malizia, A., et al. 2007, ApJ, 669, L1

Bednarek, W. & Protheroe, R. J. 1997a, MNRAS, 287, L9

Bednarek, W. & Protheroe, R. J. 1997b, MNRAS, 290, 139

Bednarek, W. & Protheroe, R. J. 1999, MNRAS, 302, 373

Begelman, M. C. 1998, ApJ, 493, 291

Begelman, M. C., Fabian, A. C., & Rees, M. J. 2008, MNRAS, 384, L19

Beichman, C. A., Neugebauer, G., Habing, H. J., Clegg, P. E., & Chester, T. J., eds. 1988, Infrared astronomical satellite (IRAS) catalogs and atlases. Volume 1: Explanatory supplement, Vol. 1

Belloni, T. M. & Altamirano, D. 2013, MNRAS, 432, 10

Benlloch, S., Rothschild, R. E., Wilms, J., et al. 2001, A&A, 371, 858

Bernardini, F. & Cackett, E. M. 2014, MNRAS, 439, 2771

Bertaud, C., Wlerick, G., Veron, P., et al. 1973, A&A, 24, 357

Bertero, M. 1989, Linear inverse and ill-posed problems, Advances in ectronics and electron physics, 1

Bettoni, D., Falomo, R., Fasano, G., & Govoni, F. 2003, A&A, 399, 869

Beuchert, T. 2013, Of Radio-Loud and Radio-Quiet AGN – Single Dish Radio Polarimetry and X-ray Variability Study of Polar Scattered Seyfert I Galaxies, Master Thesis, Naturwissenschaftlichen Fakultaet der Friedrich-Alexander-Universitaet Erlangen-Nuernberg, Erlangen, Nuernberg, Germany

Biland, A., Garczarczyk, M., Anderhub, H., & et al. 2008, International Cosmic Ray Conference, 3, 1353

Blandford, R. & Eichler, D. 1987, Phys. Rep., 154, 1

Blandford, R. D. & Königl, A. 1979, ApJ, 232, 34

Blandford, R. D. & Payne, D. G. 1982, MNRAS, 199, 883

Blandford, R. D. & Znajek, R. L. 1977, MNRAS, 179, 433

Blasi, M. G., Lico, R., Giroletti, M., et al. 2013, A&A, 559, A75

Bloom, S. D. & Marscher, A. P. 1996, ApJ, 461, 657

Boettcher, M., Harris, D. E., & Krawczynski, H. 2012, Relativistic Jets from Active Galactic Nuclei, by M. Boettcher, D.E. Harris, ahd H. Krawczynski, 425 pages. Berlin: Wiley

Bonning, E. W., Cheng, L., Shields, G. A., Salviander, S., & Gebhardt, K. 2007, ApJ, 659, 211

Bretz, T., Dorner, D., Wagner, R. M., & Sawallisch, P. 2009, Astroparticle Physics, 31, 92

Burbidge, G. R. 1956, ApJ, 124, 416

Burke, B. F. & Graham-Smith, F. 2002, An Introduction to Radio Astronomy: Second Edition, Infrared Astronomy

Burrows, D. N., Hill, J. E., Nousek, J. A., et al. 2005, Space Sci. Rev., 120, 165

Cavaliere, A. & D'Elia, V. 2002, ApJ, 571, 226

Cavallo, G. & Rees, M. J. 1978, MNRAS, 183, 359

Celotti, A., Fabian, A. C., & Rees, M. J. 1998, MNRAS, 293, 239

Condon, J., Darling, J., Kovalev, Y. Y., & Petrov, L. 2011, ArXiv e-prints: 1110.6252

Condon, J. J. & Broderick, J. J. 1988, AJ, 96, 30

Cortina, J. 2012, The Astronomer's Telegram, 4583

Costamante, L., Ghisellini, G., Giommi, P., et al. 2001a, X-ray Astronomy: Stellar Endpoints, AGN, and the Diffuse X-ray Background, 599, 586

Costamante, L., Ghisellini, G., Giommi, P., et al. 2001b, A&A, 371, 512

Davies, J. M. & Cotton, E. S. 1957, J. Solar Energy Sci. and Eng., 1, 16

de Bruyn, A. G. 1988, in IAU Symposium, Vol. 129, The Impact of VLBI on Astrophysics and Geophysics, ed. M. J. Reid & J. M. Moran, 97

de Gouveia Dal Pino, E. M., Kowal, G., Lazarian, A., & Santos-Lima, R. 2011, ArXiv e-prints: 1107.2674

de Gouveia dal Pino, E. M. & Lazarian, A. 2005, A&A, 441, 845

Dermer, C. D. & Schlickeiser, R. 1994, ApJS, 90, 945

Doeleman, S. S., Fish, V. L., Schenck, D. E., et al. 2012, Science, 338, 355

Domingo-Santamaria, E., Flix, J., Rico, J., Scalzotto, V., & Wittek, W. 2005, International Cosmic Ray Conference, 5, 363

Domínguez, A., Primack, J. R., Rosario, D. J., et al. 2011, MNRAS, 410, 2556

Donato, D., Ghisellini, G., Tagliaferri, G., & Fossati, G. 2001, A&A, 375, 739

Dondi, L. & Ghisellini, G. 1995, MNRAS, 273, 583

Dunn, R. J. H., Allen, S. W., Taylor, G. B., et al. 2010, MNRAS, 404, 180

Edelson, R. & Nandra, K. 1999, ApJ, 514, 682

Edelson, R. A. & Krolik, J. H. 1988, ApJ, 333, 646

Edwards, P. G. & Piner, B. G. 2002, ApJ, 579, L67

Eichler, D. 1993, ApJ, 419, 111

Eisenacher, D., Colin, P., Lombardi, S., et al. 2013, in ., Proc. to the 33^{rd} ICRC, Id. 0336, Rio de Janeiro, Brazil

Fabian, A. C. 1979, Royal Society of London Proceedings Series A, 366, 449

Falomo, R., Kotilainen, J. K., & Treves, A. 2002, ApJ, 569, L35

Fanaroff, B. L. & Riley, J. M. 1974, MNRAS, 167, 31P

Farina, E. P., Decarli, R., Falomo, R., Treves, A., & Raiteri, C. M. 2012, MNRAS, 424, 393

Feretti, L., Giovannini, G., Klein, U., et al. 1998, A&A, 331, 475

Fermi, E. 1949, Phys. Rev., 75, 1169

Fomin, V. P., Stepanian, A. A., Lamb, R. C., et al. 1994, Astroparticle Physics, 2, 137

Fossati, G., Buckley, J. H., Bond, I. H., et al. 2008, ApJ, 677, 906

Fossati, G., Maraschi, L., Celotti, A., Comastri, A., & Ghisellini, G. 1998, MNRAS, 299, 433

Franceschini, A., Rodighiero, G., & Vaccari, M. 2008, A&A, 487, 837

Fromm, C. M., Ros, E., Perucho, M., et al. 2013, A&A, 551, A32

Fruck, C., Gaug, M., Zanin, R., et al. 2014, ArXiv e-prints: 1403.3591

Fuchs, M. 2008, Untersuchung der atmosphaerischen Transmission mittels Pyroskop und Lidar zur Gamma-Astronomie mit dem MAGIC Cherenkov Teleskop auf La Palma, Diploma Thesis, Fachhochschule Muenchen, Muenchen, Germany

Fuhrmann, L., Larsson, S., Chiang, J., et al. 2014, MNRAS, 441, 1899

Gabuzda, D. C. & Cawthorne, T. V. 2003, MNRAS, 338, 312

Gaidos, J. A., Akerlof, C. W., Biller, S., et al. 1996, Nature, 383, 319

Garcia, J. R., Dazzi, F., Häfner, D., et al. 2013, Proc. to the 33^{rd} ICRC, Id. 0666, Rio de Janerio, Brazil

Garmire, G. P., Bautz, M. W., Ford, P. G., Nousek, J. A., & Ricker, Jr., G. R. 2003, in Society of Photo-Optical Instrumentation Engineers (SPIE) Conference Series, Vol. 4851, X-Ray and Gamma-Ray Telescopes and Instruments for Astronomy., ed. J. E. Truemper & H. D. Tananbaum, 28–44

Gebhardt, K. & Thomas, J. 2009, ApJ, 700, 1690

Gehrels, N., Chincarini, G., Giommi, P., et al. 2004, ApJ, 611, 1005

Georganopoulos, M. & Kazanas, D. 2003, ApJ, 594, L27

Georganopoulos, M. & Kazanas, D. 2004, ApJ, 604, L81

Ghisellini, G. 1999, Astroparticle Physics, 11, 11

Ghisellini, G. 2013, in European Physical Journal Web of Conferences, Vol. 61, European Physical Journal Web of Conferences, 5001

Ghisellini, G., Celotti, A., Fossati, G., Maraschi, L., & Comastri, A. 1998, MNRAS, 301, 451

Ghisellini, G. & Madau, P. 1996, MNRAS, 280, 67

Ghisellini, G., Padovani, P., Celotti, A., & Maraschi, L. 1993, ApJ, 407, 65

Ghisellini, G. & Tavecchio, F. 2008, MNRAS, 387, 1669

Ghisellini, G., Tavecchio, F., & Chiaberge, M. 2005, A&A, 432, 401

Giannios, D., Uzdensky, D. A., & Begelman, M. C. 2009, MNRAS, 395, L29

Giannios, D., Uzdensky, D. A., & Begelman, M. C. 2010, MNRAS, 402, 1649

Gini, C. 1921, Economic Journal, 31, 22

Giommi, P., Massaro, E., Padovani, P., et al. 2007, A&A, 468, 97

Giommi, P., Padovani, P., & Perlman, E. 2000, MNRAS, 317, 743

Giommi, P., Padovani, P., Polenta, G., et al. 2012a, MNRAS, 420, 2899

Giommi, P., Polenta, G., Lähteenmäki, A., et al. 2012b, A&A, 541, A160

Giroletti, M., Giovannini, G., Feretti, L., et al. 2004a, ApJ, 600, 127

Giroletti, M., Giovannini, G., Taylor, G. B., & Falomo, R. 2004b, ApJ, 613, 752

Gordovskyy, M., Browning, P. K., & Vekstein, G. E. 2010, ApJ, 720, 1603

Graham, P. J. & Tingay, S. J. 2014, ApJ, 784, 159

Grauer, A. D. 1984, ApJ, 277, 77

Greisen, E. W. 2003, Information Handling in Astronomy - Historical Vistas, 285, 109

Grinberg, V. 2013, PhD thesis, Investigations of the long term variability of black hole binaries, Naturwissenschaftlichen Fakultaet der Friedrich-Alexander-Universitaet Erlangen-Nurrnberg, Erlangen, Germany

Gültekin, K., Richstone, D. O., Gebhardt, K., et al. 2009, ApJ, 698, 198

Harris, D. E. & Krawczynski, H. 2002, ApJ, 565, 244

Hartman, R. C., Bertsch, D. L., Fichtel, C. E., et al. 1992, ApJ, 385, L1

Healey, S. E., Romani, R. W., Cotter, G., et al. 2008, ApJS, 175, 97

Heck, D., Knapp, J., Capdevielle, J. N., Schatz, G., & Thouw, T. 1998, CORSIKA: a Monte Carlo code to simulate extensive air showers., by Heck, D.; Knapp, J.; Capdevielle, J. N.; Schatz, G.; Thouw, T.. Forschungszentrum Karlsruhe GmbH, Karlsruhe (Germany)., Feb 1998, V + 90 p., TIB Hannover, D-30167 Hannover (Germany)

Heitler, W. 1960, The Quantum Theorie of Radiation, by Walter Heitler. The International series of monographs on physics. ISBN 0486845584. Oxford, UK: Clarendon Press, 1960

Hess, V. 1912, Physikalische Zeitschrift, 13, 1084

Hillas, A. M. 1985, International Cosmic Ray Conference, 3, 445

Hofmann, W., Jung, I., Konopelko, A., et al. 1999, Astroparticle Physics, 12, 135

Holder, J., Aliu, E., Arlen, T., et al. 2011, ArXiv e-prints: 1111.1225

Homan, D. C., Lister, M. L., Kellermann, K. I., et al. 2003, ApJ, 589, L9

Houck, J. C. & Denicola, L. A. 2000, in Astronomical Society of the Pacific Conference Series, Vol. 216, Astronomical Data Analysis Software and Systems IX, ed. N. Manset, C. Veillet, & D. Crabtree, 591

Hughes, P. A., Aller, H. D., & Aller, M. F. 1985, ApJ, 298, 301

Hughes, P. A., Aller, H. D., & Aller, M. F. 1992, ApJ, 396, 469

IceCube Collaboration. 2013, Science, 342

Igoshev, A. P. & Kholtygin, A. F. 2011, Astronomische Nachrichten, 332, 1012

Ivanov, P. B., Chernyakova, M. A., & Novikov, I. D. 2003, MNRAS, 338, 147

Jansen, F., Lumb, D., Altieri, B., et al. 2001, A&A, 365, L1

Jansky, K. G. 1933, Nature, 132, 66

Jones, T. W. 1988, ApJ, 332, 678

Jorstad, S. G., Marscher, A. P., Lister, M. L., et al. 2005, AJ, 130, 1418

Jorstad, S. G., Marscher, A. P., Mattox, J. R., et al. 2001, ApJ, 556, 738

Kadler, M., Eisenacher, D., Ros, E., et al. 2012, A&A, 538, L1

Kalberla, P. M. W., McClure-Griffiths, N. M., Pisano, D. J., et al. 2010, A&A, 521, A17

Kellermann, K. I. & Pauliny-Toth, I. I. K. 1969, ApJ, 155, L71

Kellermann, K. I., Sramek, R., Schmidt, M., Shaffer, D. B., & Green, R. 1989, AJ, 98, 1195

Kirk, J. G., Guthmann, A. W., Gallant, Y. A., & Achterberg, A. 2000, ApJ, 542, 235

Klein, O. & Nishina, Y. 1929, Zeitschrift für Physik, 52, 853

Kneiske, T. M. & Dole, H. 2010, A&A, 515, A19

Koenigl, A. & Choudhuri, A. R. 1985, ApJ, 289, 173

Kohnle, A., Aharonian, F., Akhperjanian, A., et al. 1996, Astroparticle Physics, 5, 119

Komissarov, S. S., Barkov, M. V., Vlahakis, N., & Königl, A. 2007, MNRAS, 380, 51

Kovalev, Y. Y., Aller, H. D., Aller, M. F., et al. 2009, ApJ, 696, L17

Kraus, A., Krichbaum, T. P., Wegner, R., et al. 2003, A&A, 401, 161

Krauß, F. 2013, Multiwavelength Observations of Tanami sources, Master Thesis, Naturwissenschaftlichen Fakultaet der Friedrich-Alexander-Universitaet Erlangen-Nuernberg, Erlangen, Nuernberg, Germany

Krauß, F., Eisenacher, D., Kadler, M., et al. 2012, The Astronomer's Telegram, 4581

Krawczynski, H., Hughes, S. B., Horan, D., et al. 2004, ApJ, 601, 151

Lafferty, G. D. & Wyatt, T. R. 1995, Nuclear Instruments and Methods in Physics Research A, 355, 541

Lang, K. R. 1992, Astrophysical Data I. Planets and Stars. X, 937 pp. 33 figs.. Springer-Verlag Berlin Heidelberg New York

Lawrence, A., Watson, M. G., Pounds, K. A., & Elvis, M. 1987, Nature, 325, 694

Levinson, A. & Rieger, F. 2011, ApJ, 730, 123

Li, T.-P. & Ma, Y.-Q. 1983, ApJ, 272, 317

Lico, R., Giroletti, M., Orienti, M., et al. 2012, A&A, 545, A117

Lister, M. L., Aller, M., Aller, H., et al. 2011, ApJ, 742, 27

Lister, M. L., Aller, M. F., Aller, H. D., et al. 2013, AJ, 146, 120

Lister, M. L. & Homan, D. C. 2005, AJ, 130, 1389

Liu, H. T. & Bai, J. M. 2006, ApJ, 653, 1089

Lodato, G., King, A. R., & Pringle, J. E. 2009, MNRAS, 392, 332

Lomb, N. R. 1976, Ap&SS, 39, 447

Lombardi, S. 2010, PhD thesis, Development of analysis tools for the MAGIC Telescopes and observation of the Segue 1 Satellite Galaxy with the MAGIC-I Telescope., Universitá degli Studi di Padova and INFN, Padova, Italy

Longair, M. S. 2011, High Energy Astrophysics, by Malcolm S. Longair, Cambridge, UK: Cambridge University Press

Lopez, M. 2013, Proc. to the 33^{rd} ICRC, Id. 0692, Rio de Janeiro, Brazil

Lund, N., Budtz-Jørgensen, C., Westergaard, N. J., et al. 2003, A&A, 411, L231

Lyutikov, M. & Lister, M. 2010, ApJ, 722, 197

Machalski, J., Kozieł-Wierzbowska, D., Jamrozy, M., & Saikia, D. J. 2008, ApJ, 679, 149

Mahony, E. K., Sadler, E. M., Murphy, T., et al. 2010, ApJ, 718, 587

Mannheim, K. 1993a, Phys. Rev. D, 48, 2408

Mannheim, K. 1993b, A&A, 269, 67

Mannheim, K. 1995, Astroparticle Physics, 3, 295

Maraschi, L., Ghisellini, G., & Celotti, A. 1992, ApJ, 397, L5

Markowitz, A., Edelson, R., Vaughan, S., et al. 2003, ApJ, 593, 96

Marscher, A. P. 1980, ApJ, 239, 296

Marscher, A. P. 1992, in Emission Models for Compact Jets., Physics of Active Galactic Nuclei, ed. W. J. Duschl & S. J. Wagner, 510

Marscher, A. P. 2008, in Astronomical Society of the Pacific Conference Series, Vol. 386, Extragalactic Jets: Theory and Observation from Radio to Gamma Ray, ed. T. A. Rector & D. S. De Young, 437

Marscher, A. P. & Gear, W. K. 1985, ApJ, 298, 114

Marscher, A. P., Jorstad, S. G., D'Arcangelo, F. D., et al. 2008, Nature, 452, 966

Marscher, A. P., Marshall, F. E., Mushotzky, R. F., et al. 1979, ApJ, 233, 498

Mas-Hesse, J. M., Giménez, A., Culhane, J. L., et al. 2003, A&A, 411, L261

Matthews, T. A. & Sandage, A. R. 1963, ApJ, 138, 30

Max-Moerbeck, W., Hovatta, T., Richards, J. L., et al. 2014, MNRAS, 445, 428

Mazin, D., Tescaro, D., Garczarczyk, M., et al. 2013, Proc. to the 33^{rd} ICRC, Id. 1071, Rio de Janerio, Brazil

McElroy, D. B. 1995, ApJS, 100, 105

McHardy, I. & Czerny, B. 1987, Nature, 325, 696

Melia, F. & Konigl, A. 1989, ApJ, 340, 162

Merloni, A., Heinz, S., & di Matteo, T. 2003, MNRAS, 345, 1057

Miley, G. 1980, ARA&A, 18, 165

Mirzoyan, R. & Lorenz, E. 1997, Proc. to the 25^{rd} ICRC, Durban, South Africa

Moll, R. 2009, A&A, 507, 1203

Moll, R., Spruit, H. C., & Obergaulinger, M. 2008, A&A, 492, 621

Mücke, A., Protheroe, R. J., Engel, R., Rachen, J. P., & Stanev, T. 2003, Astroparticle Physics, 18, 593

Müller, C., Kadler, M., Ojha, R., et al. 2011, A&A, 530, L11

Nalewajko, K., Giannios, D., Begelman, M. C., Uzdensky, D. A., & Sikora, M. 2011, MNRAS, 413, 333

Narayan, R. & Piran, T. 2012, MNRAS, 420, 604

Neeser, M. J., Eales, S. A., Law-Green, J. D., Leahy, J. P., & Rawlings, S. 1995, ApJ, 451, 76

Neronov, A., Semikoz, D., & Vovk, I. 2010, A&A, 519, L6

Neronov, A. & Vovk, I. 2011, MNRAS, 412, 1389

Neronov, A. Y., Semikoz, D. V., & Tkachev, I. I. 2009, New Journal of Physics, 11, 065015

Nieppola, E., Tornikoski, M., Valtaoja, E., et al. 2011, A&A, 535, A69

Nolan, P. L., Abdo, A. A., Ackermann, M., et al. 2012, ApJS, 199, 31

Owen, F. N., Ledlow, M. J., & Keel, W. C. 1996, AJ, 111, 53

Padovani, P., Costamante, L., Ghisellini, G., Giommi, P., & Perlman, E. 2002, ApJ, 581, 895

Padovani, P., Giommi, P., & Rau, A. 2012, MNRAS, 422, L48

Padovani, P., Perlman, E. S., Landt, H., Giommi, P., & Perri, M. 2003, ApJ, 588, 128

Paneque, D., Gebauer, H. J., Lorenz, E., & Mirzoyan, R. 2004, Nuclear Instruments and Methods in Physics Research A, 518, 619

Parma, P., Murgia, M., de Ruiter, H. R., & Fanti, R. 2002, New A Rev., 46, 313

Piner, B. G. & Edwards, P. G. 2004, ApJ, 600, 115

Piner, B. G., Pant, N., & Edwards, P. G. 2010, ApJ, 723, 1150

Protheroe, R. J. 1998, in Origin and Propagation of the Highest Energy Cosmic Rays, Towards the Millennium in Astrophysics, Problems and Prospects. International School of Cosmic Ray Astrophysics 10th Course, ed. M. M. Shapiro, R. Silberberg, & J. P. Wefel, 3

Punsly, B. 2001, Black hole gravitohydromagnetics, by Punsly, Brian;Punsly, Brian. Black hole gravitohydromagnetics, by Punsly, Brian. New York : Springer, c2001. Astronomy and astrophysics library, 0941-7834

Pushkarev, A. B., Kovalev, Y. Y., & Lister, M. L. 2010, ApJ, 722, L7

Racine, R. 1970, ApJ, 159, L99

Rani, B., Krichbaum, T. P., Fuhrmann, L., et al. 2013, A&A, 552, A11

Rector, T. A., Gabuzda, D. C., & Stocke, J. T. 2003, AJ, 125, 1060

Rector, T. A., Stocke, J. T., & Perlman, E. S. 1999, ApJ, 516, 145

Rees, M. J. 1966, Nature, 211, 468

Reinthal, R., Lindfors, E. J., Mazin, D., et al. 2012, Journal of Physics Conference Series, 355, 012013

Reis, R. C., Reynolds, M. T., Miller, J. M., & Walton, D. J. 2014, Nature, 507, 207

Reville, B. & Bell, A. R. 2014, MNRAS, 439, 2050

Rhee, G., Burns, J. O., & Kowalski, M. P. 1994, AJ, 108, 1137

Richards, J. L., Max-Moerbeck, W., Pavlidou, V., et al. 2011, ApJS, 194, 29

Rieger, F. M. 2011, International Journal of Modern Physics D, 20, 1547

Rivers, E., Markowitz, A., & Rothschild, R. 2011, ApJ, 742, L29

Robson, I. 1999, in IAU Symposium, Vol. 194, Activity in Galaxies and Related Phenomena, ed. Y. Terzian, E. Khachikian, & D. Weedman, 3

Rohlfs, K. & Wilson, T. L. 2004, Tools of radio astronomy, 4th rev. and enl. ed., by K. Rohlfs and T.L. Wilson. Berlin: Springer

Rolke, W. A. & López, A. M. 2001, Nuclear Instruments and Methods in Physics Research A, 458, 745

Rolke, W. A., López, A. M., & Conrad, J. 2005, Nuclear Instruments and Methods in Physics Research A, 551, 493

Rosswog, S. & Brüggen, M. 2007, Introduction to High-Energy Astrophysics, by Stephan Rosswog , Marcus Brüggen, Cambridge, UK: Cambridge University Press

Ryle, M. & Windram, M. D. 1968, MNRAS, 138, 1

Sánchez Losa, A. & ANTARES Collaboration. 2013, Nuclear Instruments and Methods in Physics Research A, 725, 60

Sato, K., Furusho, T., Yamasaki, N. Y., et al. 2005, PASJ, 57, 743

Scargle, J. D. 1982, ApJ, 263, 835

Schmelling, M. 1998, Numerische Methoden der Datenanalys. MPI-K, Heidelberg

Schwarz, R. A., Edge, A. C., Voges, W., et al. 1992, A&A, 256, L11

Shang, Z., Brotherton, M. S., Green, R. F., et al. 2005, ApJ, 619, 41

Shaw, M. S., Romani, R. W., Cotter, G., et al. 2013, ApJ, 764, 135

Shepherd, M. C., Pearson, T. J., & Taylor, G. B. 1994, in Bulletin of the American Astronomical Society, Vol. 26, DIFMAP: an interactive program for synthesis imaging. Bulletin of the American Astronomical Society, 987–989

Sijbring, D. & de Bruyn, A. G. 1998, A&A, 331, 901

Sikora, M. 1994, ApJS, 90, 923

Simien, F. & Prugniel, P. 2002, A&A, 384, 371

Sitarek, J., Carmona, E., Colin, P., et al. 2013a, ArXiv e-prints: 1308.0141

Sitarek, J., Gaug, M., Mazin, D., Paoletti, R., & Tescaro, D. 2013b, Nuclear Instruments and Methods in Physics Research A, 723, 109

Skrutskie, M. F., Cutri, R. M., Stiening, R., et al. 2006, AJ, 131, 1163

Sokolsky, P. 1989, Introduction to ultrahigh energy cosmic ray physics. Frontiers in Physics, Vol. 76

Stanev, T. 2004, High energy cosmic rays, by Todor Stanev. Springer-Praxis books in astrophysics and astronomy. Chichester, UK: Springer. ISBN: 3540406530

Strüder, L., Briel, U., Dennerl, K., et al. 2001, A&A, 365, L18

Takalo, L. O., Nilsson, K., Lindfors, E., et al. 2008, in American Institute of Physics Conference Series, Vol. 1085, American Institute of Physics Conference Series, ed. F. A. Aharonian, W. Hofmann, & F. Rieger, 705–707

Tavani, M., Bulgarelli, A., Vittorini, V., et al. 2011, Science, 331, 736

Tavecchio, F. & Ghisellini, G. 2008, MNRAS, 385, L98

Tavecchio, F. & Ghisellini, G. 2014, ArXiv e-prints: 1404.6894

Tavecchio, F., Ghisellini, G., Ghirlanda, G., Foschini, L., & Maraschi, L. 2010, MNRAS, 401, 1570

Tescaro, D., Aleksic, J., Barcelo, M., et al. 2009, ArXiv e-prints: 0907.0466

Tescaro, D., López-Oramas, A., Moralejo, A., Mazin, D., & Daniela Hadasch for the MAGIC Collaboration. 2013, ArXiv e-prints: 1310.1565

Thompson, A. R., Moran, J. M., & Swenson, Jr., G. W. 2001, Interferometry and Synthesis in Radio Astronomy, by A. Richard Thompson, James M. Moran, and George W. Swenson, Jr. 2nd ed. New York: Wiley, c2001.xxiii, 692 p.: ill.; 25 cm. ”A Wiley-Interscience publication.” Includes bibliographical references and indexes. ISBN: 0471254924”

Tikonov, A. N. & Arsenin, V. J. 1979, Methods of solution of ill-posed problems.

Ubertini, P., Lebrun, F., Di Cocco, G., et al. 2003, A&A, 411, L131

Urry, C. M. & Padovani, P. 1995, PASP, 107, 803

Uttley, P., McHardy, I. M., & Papadakis, I. E. 2002, MNRAS, 332, 231

Vaughan, S., Edelson, R., Warwick, R. S., & Uttley, P. 2003, MNRAS, 345, 1271

Vedrenne, G., Roques, J.-P., Schönfelder, V., et al. 2003, A&A, 411, L63

Veilleux, S. & Osterbrock, D. E. 1987, ApJS, 63, 295

Vermeulen, R. C. & Cohen, M. H. 1994, ApJ, 430, 467

Vermeulen, R. C., Ogle, P. M., Tran, H. D., et al. 1995, ApJ, 452, L5

von Montigny, C., Bertsch, D. L., Chiang, J., et al. 1995, A&A, 299, 680

Vovk, I. & Neronov, A. 2013, ApJ, 767, 103

Wagner, S. J. 1997, in Relativistic Jets in AGNs, ed. M. Ostrowski, M. Sikora, G. Madejski, & M. Begelman, 208–216

Wagner, S. J. & Witzel, A. 1995, ARA&A, 33, 163

Weekes, T. C. 2003, Very high energy gamma-ray astronomy, by Trevor C. Weekes. IoP Series in astronomy and astrophysics, ISBN 0750306580. Bristol, UK: The Institute of Physics Publishing

Wehrle, A. E., Pian, E., Urry, C. M., et al. 1998, ApJ, 497, 178

Weidinger, M. 2011, PhD thesis, Variabilitaet entlang der Blazar-Sequenz - Hinweise auf die Zusammensetzung relativistischer Ausfluesse Aktiver Galaxienkerne, Universitaet Wuerzburg, Fakultaet fuer Physik und Astronomie, Institut fuer Theoretische Physik und Astrophysik, Wuerzburg, Germany

Weisskopf, M. C., Brinkman, B., Canizares, C., et al. 2002, PASP, 114, 1

Winkler, C., Courvoisier, T. J.-L., Di Cocco, G., et al. 2003, A&A, 411, L1

Wolter, A., Beckmann, V., Ghisellini, G., Tavecchio, F., & Maraschi, L. 2008, in Astronomical Society of the Pacific Conference Series, Vol. 386, Extragalactic Jets: Theory and Observation from Radio to Gamma Ray, ed. T. A. Rector & D. S. De Young, 302

Woo, J.-H. & Urry, C. M. 2002, ApJ, 579, 530

Zacharias, M. 2014, ArXiv e-prints: 1412.1600

Zanin, R. 2011, PhD thesis, Observation of the Crab pulsar wind nebula and microquasar candidates with MAGIC, Universitat Autonoma de Barcelona, Barcelona, Spain

Zanin, R., Carmona, E., Sitarek, J., et al. 2013, Proc. to the 33^{rd} ICRC, Id. 0773, Rio de Janeiro, Brazil

Zenitani, S. & Hoshino, M. 2001, ApJ, 562, L63

Acknowledgement

To *Prof. Karl Mannheim* I am thankful for the possibility to work in the fascinating field of high energy astroparticle physics and active galactic nuclei. at the chair of astronomy of the university of Würzburg. Especially, I would like to thank for his scientific guidance and expertise on the way towards writing this thesis.
Further sincere thanks goes to *Prof. Matthias Kadler* for the invaluable and undeniably direct impact to the results of this thesis.
I deeply acknowledge the work in the MAGIC Collaboration, especially with *Dr. Pierre Colin* and *Dr. Julian Sitarek*.
Many results in this thesis could not be achieved without the help of *Felicia Krauß* as *Gute Fe* and *Robert Schulz*.
I am also greatly thankful to many colleagues for very fruitful discussions and proposing, conducting, data analyzing of multi-wavelength observations: *Dr. Dominik Elsässer, Dr. Daniela Dorner, Prof. Eduardo Ros, Prof. Jörn Wilms, Dr. Elina Linfors, Dr. Fabrizio Tavecchio, Dr. David Paneque*, and *Dr. Uwe Bach, Tobias Beuchert, Thomas Dauser, Dr. Victoria Grinberg, Dr. Talvikki Hovatta, Dr. Alex Markowitz, Dr. Cornelia Müller, Christoph Wendel, Sven Wilbert* as well as all other colleagues from Dr. Karl Remeis-Sternwarte in Bamberg. Further, I would like to thank *Dr. Stefan Rügamer, Dr. Alexander Summa, Katja Meier, Watz, Frau Kuhns*, and many others for the great time at the chair of astronomy.
Many thanks go to the proof readers of this thesis: *Prof. Karl Mannheim, Prof. Matthias Kadler, Dr. Dominik Elsässer, Dr. Daniela Dorner, Felicia Krauß, Dr. Julian Sitarek, Katja Meier*, and *Dr. Sebastian Glawion*.
Last but not least my deepest thanks go to my family, to my friends in Mühlhausen and in Leipzig, and especially to my beloved husband Sebastian for their continuous support and understanding.